MORPHOLOGICAL TRANSITIONS IN SIMPLE ELECTROCAPILLARY SYSTEMS

TOOLS FOR MICROFLUIDIC LIQUID MANIPULATION

Promotiecomissie:

Voorzitter	prof. dr. J. Greve	Univ. Twente, TNW
Secretary	prof. dr. J. Greve	Univ. Twente, TNW
Promotor	prof. dr. F. G. Mugele	Univ. Twente, TNW
Referent	prof. dr. ir. M.M.J. Decré	Philips Research, Eindhoven
	prof. L. Limat	ESPCI, Paris
Leden	prof. dr. D. Lohse	Univ. Twente, TNW
	dr. J.G.E. Gardeniers	Univ. Twente, EWI
	prof. dr. S. Herminghaus	MPI, Göttingen

The research described in this thesis was carried out in the Applied Physics group at the University of Ulm (D), in the Physics of Complex Fluids group at the University of Twente and in the Healthcare devices and Instrumentation group at Philips Research Laboratories Eindhoven and has been financially supported by the Marie Curie Host Fellowship IST-1999-80004, the German Science Foundation within the priority program Wetting and Structure Formation at Interfaces and by the Institute of Mechanics, Process and Control Twente (IMPACT).

ISBN 90-365-2242-0

MORPHOLOGICAL TRANSITIONS IN SIMPLE ELECTROCAPILLARY SYSTEMS

TOOLS FOR MICROFLUIDIC LIQUID MANIPULATION

PROEFSCHRIFT

ter verkrijging van
de graad van doctor aan de Universiteit Twente,
op gezag van de Rector Magnificus,
prof.dr. W.H.M. Zijm,
volgens besluit van het College voor Promoties
in het openbaar te verdedigen
op donderdag 27 oktober 2005 om 15.00 uur

door

Jean-Christophe Baret
geboren op 11 april 1979
te Fontainebleau (F)

Dit proefschrift is goedgekeurd door de promotor

prof. dr. F. Mugele

Contents

Chapter 1

Introduction

Contents

1.1 "Why is Philips interested in liquid manipulation ?"

This is the question I have been asked the most during my PhD. Indeed, why would a company known for the production of lamps and electronic devices be interested in fluids ?
The first part of the answer is that a lot of industrial processes involve liquid flows. Philips has been for example producing Cathode Ray Tubes for televisions in which the photophores are deposited from a liquid film or CDs and DVDs where the protective, bonding and even optical layers are spin-coated on planar substrates or on previously structured layers. The knowledge of the fundamental properties of flow which determine the behaviour of liquid in these systems is an obvious prerequisite for the control of the industrial process. In more recent applications, Philips has developed research in ink-jet printing of the LCD-display photophores and microcontact printing of transistors with intermediate resolution from an inked and soft stamp. As one may expect, Philips is not the only company developing fluid-based processes; BASF and Kodak are also using coating techniques for photographic films, HP ink-jet for printers and IBM microcontact printing.
The second point is that independently of the industrial processes related to device manufacturing, liquid manipulation is nowadays a topic in its own right: biotechnologies have driven the research in microfluidics and the "lab-on-a-chip" concept where the need to manipulate small amounts of bio-materials usually in aqueous solutions is crucial. Due to the biological constraints on the accessible volumes of material the smallest quantity of material has to be used in order to make chemical reactions or biological tests. In this case one has to achieve some key steps like the production of a small drop, the transport of a given volume of liquid, the mixing of two drops, the splitting of a drop into two sub-drops,... Since Philips is nowadays investigating this field of research to produce health care devices liquid manipulation has become a relevant issue that has to be addressed both in the frame of fundamental research and in relation with industrial and practical constraints.
Finally, in some technological applications, fluid is a key element in the device principle: the oldest example are Liquid Crystal Displays (LCD) but more recently Philips has been the first to demonstrate a working display

using fluid actuation in the pixels based on electrowetting[1]. Electrowetting is also the key feature of the lenses with adaptative focal length which has been developed independentely by Philips[2] and Varioptic[3].

1.2 Capillarity

An interface is the limit between two different media 1 and 2 and associated to this interface an interface energy E_S is defined. The classical representation of this energy is achieved by considering a molecule of medium 1 close to the interface. The interactions of the molecule with its neighbours of medium 1 are different from the interactions with its neighbours of medium 2. This asymmetry results in a net force counteracted at equilibrium by the surface force. The interfacial energy is proportional to the number of particles close to the surface and thus to the area of the surface S ($S = a^2N^2$, N being the number of molecules in one direction, a the mean distance between two molecules). The proportionality coefficient is the surface tension[4] γ: $E_S = \gamma \times S$. For comparison a body force acts on the total number of molecules in a volume N^3. For a macroscopic particle of volume V and surface S the number of molecules at the surface is a fraction of the total number of molecules which decreases when the size of the particle increases. Surface forces will thus dominate at "small" scales while body forces dominate at "large" scales. Considering gravity as the body force acting on a volume $V \propto L^3$ (L is the typical size of the particle) the potential energy associated to this force reads $E_V \propto \rho g L^4$ where ρ is the density of the material and g the acceleration of gravity. The surface energy reads $E_S \propto \gamma L^2$. Surface contribution becomes relevant when $E_S > E_V$ which means that

$$L < \sqrt{\frac{\gamma}{\rho g}}$$

$L_c = \sqrt{\gamma/(\rho g)}$ is named the capillary length: for typical sizes larger than L_c the surface energies are negligible compared to gravity while they dominate

[1] `www.research.philips.com/technologies/display/electrowetdisp/`

[2] `www.research.philips.com/technologies/light_dev_microsys/fluidfocus/`

[3] `www.varoptic.com`

[4] An estimate of the surface tension is obtained by the balance of the surface energy per molecule $\gamma S/N^2$ with the thermal energy $k_B\Theta$: $\gamma = k_B\Theta/a^2$

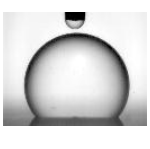

for sizes below L_c[5]. For water in air for example, $L_c \approx 3$ mm. For sub-millimeter dimensions which is the typical situation we will consider in the following the relevant energy is thus surface energy: we will consider capillary systems where surface energy dominates and gravity will be neglected most of the time.

1.3 Problems of liquid manipulation

The problem we consider in the following is liquid manipulation at small scales (*i.e.* in the capillary framework). In those conditions we are confronted to the intrinsic behavior of surfaces.

1.3.1 Surface Minimization

At small scales capillary forces dominate and the natural tendency for the liquid at scales below the capillary length is to form drops as first studied by Lord Rayleigh [2, 3, 4]. In a capillary problem the liquid morphology minimizes the free-energy of the system which means that the liquid minimizes its surface. In the absence of a solid substrate, for a free drop, the minimal surface is a sphere while in contact with a substrate the minimization of the free-energy is performed according to the constraint of the solid substrates leading to two conditions for the shape of the liquid structure: Laplace's equation (1.1) giving the difference of pressure between the drop and its surrounding ΔP as a function of the local mean-curvature M and the surface tension γ:

$$2\gamma \times M = \Delta P \tag{1.1}$$

and the Young-Dupré equation [5] defining the contact angle θ_Y of the liquid / vapor interface with the solid substrate:

$$\gamma \times \cos\theta_Y = \gamma_{\mathrm{sv}} - \gamma_{\mathrm{sl}} \tag{1.2}$$

where γ_{sv} (resp. γ_{sl}) is the interfacial energy of the solid / vapour (resp. solid / liquid) interface. On a planar and homogeneous substrate the liquid volume forms a spherical cap which gives only a little freedom for liquid manipulation. However, using composite surfaces, the deviation of the wetting properties

[5]For more details see e.g. the book by de Gennes, Brochart-Wyart and Quéré [1]

from this ideal case creates a wide range of shapes accessible to the liquid structures and thus opens the door to liquid manipulation.

1.3.2 Real surfaces

When dealing with real substrates the first practical observation is contact angle hysteresis. In practical cases a surface is never planar nor homogeneous and the contact angle θ is undetermined between two values defining the contact angle hysteresis: $\theta_a > \theta > \theta_r$ where θ_a (resp. θ_r) is the maximal (resp. the minimal) angle for which the contact angle is static and the contact line is not advancing (resp. not receding). Young's equilibrium angle is also within the hysteresis $\theta_a > \theta_Y > \theta_r$. The first consequence, interesting for fluid manipulation is that the shape of the drop can differ from a simple spherical cap and take more complicated stable morphologies, defined as local minima of the complex free-energy landscape. Indeed the boundary condition on the contact angle is partially relaxed and gives a certain degree of freedom. On the contrary a perturbation to the drop free-surface does not automatically involve a motion of the pinned contact line: thus, in order to move the drop it becomes necessary to overcome the contact angle hysteresis. The force that has to be applied to move the drop depends then on the substrate hysteresis. [6, 7, 8].
Using rough substrates, it has also been observed that the wetting properties of the solid are modified by its roughness, the contact angles being different than those of the same planar substrate [9, 10]. For instance on such topographies the water repellency is enhanced: the drop / substrate interaction decreases and the drop is hardly deposited on the substrate. This effect is used in nature by many plants as observed in the simple "garden-experiment" presented on the Fig. 1.1 showing water repellency of plant leaves [11]. This effect corresponds to a natural evolutionary advantage for the plant in the removal of dust and solid particles deposited on the leaves [12] which would otherwise reduce the amount of incident light required for the photosynthesis. Because of their practical interest as self-cleaning surfaces, these textured surfaces, called superhydrophobic surfaces are studied intensively nowadays [13, 14, 15, 16]. They also have the property to display several local minima of the free-energy landscape leading for example to the so-called Cassie and Wenzel drops depending on the wetting or not of the substrate

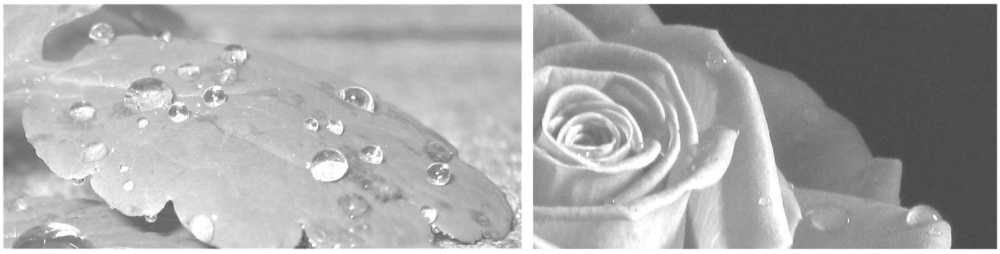

Figure 1.1: Example of roughness-induced water repelency and self-cleaning surface: in the garden, the textured surface of the weed leaves (left) or roses petal (right) decreases the wettability of the surface. Rain drops slide on the surface and remove dusts and particles deposited on the surface.

microstructures. Unfortunately the switch from one minimum to the other is not a reversible transition due to a large hysteresis [14] which is a major drawback since reversible and controlled transitions between two shapes would represent a nice tool for fluid manipulation.
The strategy for fluid manipulation we will consider in the following is based on the active control of the surface wettability and the accessibility of the local minima of the free-energy on heterogeneous substrates: the surfaces are designed to display different morphologies in different regimes of parameters based on recent studies. On heterogeneous chemically treated flat substrates extended morphologies and bulges have been observed and studied by Brinkmann and co-workers [17, 18], Gau *et al.* [19, 20] and several other authors [21, 22]. The chemical heterogeneities will produce a surface with heterogeneous contact angles for a given liquid. The liquid can for instance be confined along stripes or other structures. On chemically homogeneous but topographically structured substrates, the first analysis made on surface roughness has been done by Cassie [9] and Wenzel [10]. The problem of drop shapes on solid structures has been studied more recently by Patankar [23], Parry [24] or Seemann *et al.* [25]. They studied theoretically and experimentally liquid morphologies on open microchannels and showed a full morphological diagram of the liquid structure on these substrates. The transitions observed give a nice starting point for fluid manipulation. Finally the ultimate idea would be to combine topographies and chemical heterogeneities [26] in order to offer the widest range of choices to fulfil specific requirements. In addition an active control of the wetting heterogeneities

would provide the most versatile tool for fluid manipulation.

1.3.3 Finding a driving force

The second problem we are confronted to is to find the active control for fluid actuation: liquid flow or a switch between two stable states requires a driving force. The transport of large volumes of liquid using gravity has been known for ages: Roman aqueducts work on this principle, the flow along the pipes being gravity-driven. In our case gravity cannot be used as a driving force since it is too weak. A technological solution exists to artificially supplement gravity: in spin-coating [27], a centrifugal force is used to produce thin layers of material. This is a non-reversible passive method used for patterning and combined with additional photo-lithography steps. The method requires mechanical parts and the flow is influenced by previously deposited layers [28] which strongly limit its interest. Yet the technique has been extended to microfluidics to actuate the liquid in channels made in a circular disc using a CD drive mechanism [29].
Different strategies are known to actuate liquid depending on the system or on the geometry [30]. The surface can be passively treated to display microstructures [31] or gradient of wettability [31] or of surface roughness [32]: in this case a drop deposited on the surface will move from the least to the most wettable area; real-time control is however preferable: the surface tension of a liquid can be tuned for instance using Marangoni effect. Increasing the liquid temperature locally results in a net capillary force which produces a liquid motion. A working device has already been proposed by Darhuber *et al.* [33]. The interest is clear in terms of scalability: a system working on that principle should be scalable to any size contrary to the actuation by a body force which vanishes when the size decreases. Indeed to have a scalable system the requirement is to have the same scaling (in terms of length) between the driving force and the opposing force. This is for instance not the case for a gravity / capillary system: gravity scales as L^4 and capillarity as L^2. A thermocapillary system uses only capillarity as driving and opposing force. However in the presence of contact angle hysteresis the scalability vanishes: contact angle hysteresis acts as an opposing contribution proportional to the length of the contact line L while capillarity acts as a surface energy L^2: scalability should vanish below a certain length scale [8]. In this case, it is

thus important to have systems with the smallest hysteresis possible. Other systems based on acoustic waves have also been studied [34] but one of the most interesting idea is to use surface electric forces and the electrowetting effect [35]. Due to its ease of use and especially the control of the fluid by a simple voltage, this technique is used in many systems.

1.4 Liquids in an electric field

1.4.1 Electrostatic and electrokinetics

The influence of electric forces on liquid structures can be observed in simple "bathroom-experiments" when a plastic rod (a hair-brush) charged by friction on clothes is approached to a flowing liquid filament and deviates the flow as displayed in Fig. 1.2. The interaction between the charges in the liquid and the charges at the surface of the plastic rod results is a force which bends the interface. The field also has an influence on the production of small droplets downstream similarly to the experiment described by Feynman [36]. Using an electric field, liquid can be actuated in confined geometries such as channels, capillaries [37] or parallel plates [38]; using the terminology from Tabeling book [39] (p.178), an electric field can move an ionized liquid (electro-osmosis), charged particles in a steady liquid (electrophoresis), or neutral particles (dielectrophoresis). On capillary structures like droplets, an electric field can deform the shape by elongating the drop along the direction of the field [40, 41] and an external electrostatic field has been used to move droplets on planar substrates on-demand [42, 43]. Finally the electric force also acts on the contact angle of a drop, this effect being named electrowetting. The so-called electrowetting effect is linked to dielectrophoresis as shown by Jones [44] and has already been used to actuate liquid in a wide variety of systems, in particular to reach droplet motion [45, 43], switches between droplet morphologies [46, 47, 48] or actuation in confined systems [37, 49]. This effect will be presented in more details in the following section and has been used as the basis of this thesis.

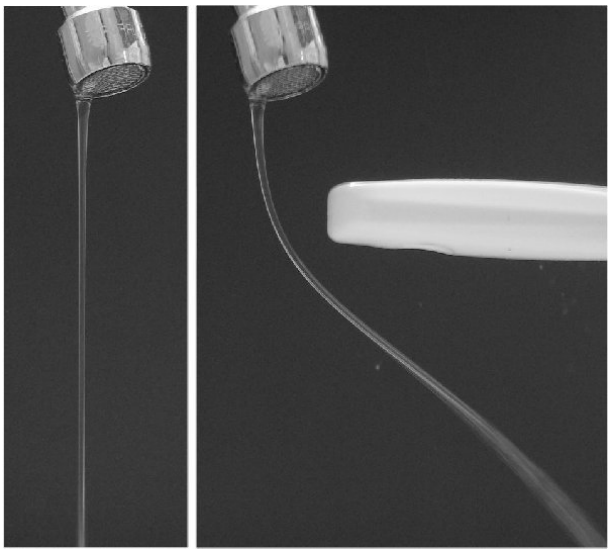

Figure 1.2: Example of the influence of an electric field on a liquid structure. The water flowing from the tap in a bathroom is deviated by the electric field produced by a plastic hair-brush electrostatically charged by friction on a sweater.

1.4.2 Electrowetting

The basis of electrowetting has been first described more than one century ago by Lippmann[6] [51] who observed that the surface tension of the interface between acidic water and mercury is a function of the potential difference at this interface. He used this effect to develop a capillary electrometer and several other applications based on his findings. The study has been continued when Froumkine [52] studied droplets in electric fields: a conducting drop wets a metallic plate better in the presence of an electric field. He related this electrocapillary effect to the capacitance of the electric double layer at the surface. In practical cases, the main limitation in electrowetting has been for a long time the breakdown current through the double layer resulting in a heating of the drop by Joule effect. This problem has been solved in the early 90's by the use of an insulating layer between the drop and the substrate [53, 54]: the capacitance of the double layer is replaced by a controlled dielectric capacitance. The systems are then better controled and therefore

[6]Lippmann's paper has been written in French in 1875. An English translation is available in the Appendix of Mugele & Baret [50]

used for industrial applications like optical lenses [55, 56], electrowetting displays [49] or in droplet microfluidics [45, 57].
In a classical electrowetting on dielectric experiment (EWOD) a voltage is applied between a sessile drop and a substrate. The drop is insulated from the substrate by a homogeneous insulating layer made out of a dielectric material. When the voltage is applied, the electrical charges in the drop and the opposite charges in the substrate interfere positively generating an additional surface term in the energy balance and therefore changing the drop contact angle to a smaller value depending on the applied voltage named Lippmann's angle as displayed in Fig. 1.3. The voltage dependent contact angle is given

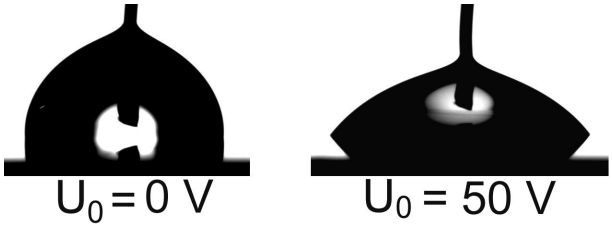

Figure 1.3: Example of the electrowetting effect. The contact angle of a conducting drop on an insulated conducting substrate is modulated by an applied voltage.

by Lippmann's equation:

$$\cos\theta_L = \cos\theta_Y + \left(\frac{U_0}{U_L}\right)^2 \tag{1.3}$$

where $U_L = (2T\gamma/\varepsilon_0\varepsilon_r)^{1/2}$ is the characteristic voltage of the system named Lippmann's voltage, γ being the surface tension, ε_r and T the dielectric constant and thickness of the insulating layer. The value $(U_0/U_L)^2$ is the Lippmann number Li. The quadratic variation of Lippmann's equation is however not valid at high voltages and small contact angles. For any system a saturation voltage is found above which the contact angle does do not depend quadratically on the voltage any longer. This angle is usually of the order of 30 – 70 degrees depending on the system. The origin of this saturation is still under debate with different interpretations [58, 59, 60, 61]. The electrowetting effect has already been used in order to induce morphological transitions between liquid structures [62, 47, 48, 46, 63]. For a review on

electrowetting the interested reader should refer to the review by Mugele and Baret [50].

1.5 Thesis subject

In the following we will use the variation of the contact angle on the substrate in different systems in order to dynamically vary the wettability of the substrate. In a first part we will study how such variations influence the deposition criterion for a droplet from a syringe. Then we will observe how this simple system can be used in order to induce oscillatory motion of a drop by a modulation of the contact angle. Finally we will extensively study the influence of the wettability in a confined system consisting of parallel open microchannels, the equilibrium situation (third part) and the dynamics (fourth part). The active change of wettability studied here provides a reversible fluid actuation that has potential interest to provide microfluidic devices, such as a mixer with the oscillating drops or a cooling device for chips with the actuation of flow in the microchannels.

Two "Daumenkino" [7] are printed on the bottom of each page. On the right hand side (odd pages), the movie represents the oscillations of a glycerol / water / salt droplet in electrowetting (1.4 ms between two frames, the voltage is 85 V rms at 10 kHz); on the left hand side (even pages) the movie represents the filling and emptying of an open-channel of width 40 μm and depth 20μm in electrowetting conditions (85 V rms at 20 kHz, 25 ms between two frames).

[7] From German: Daumen = *Thumb*, Kino = *Movie theater*

Chapter 2

Drop deposition on hydrophobic substrates

Jean-Christophe Baret and Martin Brinkmann

Contents

2.1 Introduction

Dealing with droplet manipulation the first problem is drop deposition: how to produce small volumes of liquid on a surface in a controlled way. Depending on the meaning of 'small' different solutions are used to extract a drop out of a reservoir. The simplest way is to use a syringe and increase the volume of the drop hanging at the tip of the syringe until an instability occurs which will force the drop to fall down. The detachment criterion has been studied for a long time as the dripping faucet problem (see for example Eggers [64] or Finn [65]). This technique gives rather large volumes since the deposited volume scales with the internal radius r_e of the syringe times the square of the capillary length L_c [1]:

$$V \propto L_c^2 \times r_e$$

Under those conditions, the typical sizes of the drops are hardly smaller than one millimetre. For example a small syringe of 10 μm radius would produce a water[1] drop of about 0.3 mm, and only a small improvement is achieved with nozzle shape modifications [66].

A technological evolution from the previous solution is to push the liquid

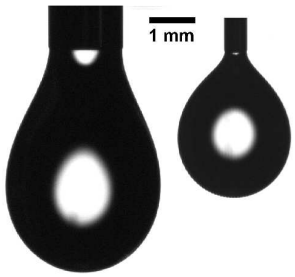

Figure 2.1: Production of a drop from a syringe of radius r_e. The volumes V are close to the maximal volume. V/r_e is approximately constant: 29 mm^3 /0.82 mm $\approx$ 35 mm^2 (Left), 9.5 mm^3 /0.26 mm $\approx$ 36 mm^2 (Right).

faster in such a way that inertia becomes significant (see Fig. 2.2). Under the conditions of ink-jet printing liquids flow when inertia overcomes the surface forces. In this case, drop sizes as small as 10 μm are produced but the limitations come from viscosity which cannot exceed 20 mPas.

Using an electric field, another type of instability of the liquid surface is in-

[1] the capillary length of water is of order 2 mm

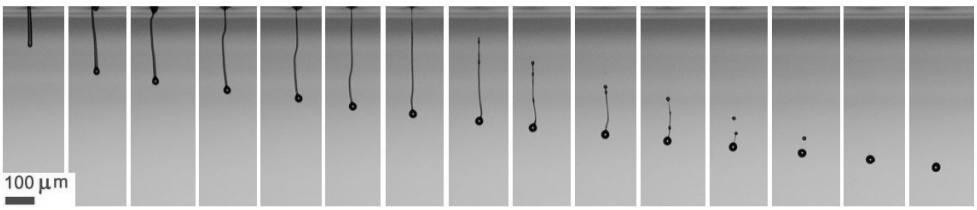

Figure 2.2: Inkjet printing of a light emitting polymer in organic solvent (diameter ≈ 20 μm, $\eta \approx 10$ mPas, Spectra SX print head, nozzle diameter 24 μm). The liquid is pushed out of the nozzle at 3 m/s by a piezo-actuation of ≈ 5 μs. (Experiment by Martin Hack, Philips Research)

duced via the so-called Taylor cone which emits small droplets above a critical threshold [67, 68]. Using this technique named electrospraying the droplets formed are charged which can be a drawback for some applications. To create smaller structures, microcontact printing[2] – or its "nano-sister" nanoimprint lithography – is used: in offset printing liquid brought in to contact with a surface is deposited on a wettable substrate [70]. A last technique is also starting to be implemented, dip-pen lithography which takes advantage of capillary condensation on an AFM tip to produce liquid structures[3].

In the following we consider a special case of offset printing where drops hang from a syringe: we investigate the conditions of deposition of the drop in contact with a flat surface. Contrary to the faucet problem the volume at which the droplet detaches from the tip of the syringe is not determined by the comparison of gravity force acting on the drop and capillary forces but by capillary forces only.

When the drop is brought into contact with a surface the caillary forces depend on the wetting properties of the surface. In the limiting case of full wetting the liquid will detach easily from the syringe while spreading. On the other hand for complete non-wetting with contact angle equal to 180 °, the drop will detach only when gravity forces dominate (the faucet problem). One is therefore interested in the intermediate case of partial wetting. The problem has been studied in the limit of zero gravity, both experimentally and theoretically by searching the criterion which determines the detachment process. We performed experiments using electrowetting which gives a sim-

[2] for a review see Xia *et al.* [69]

[3] see `www.nanoink.net`

ple way to tune the wettability of the surface. The theoretical model is based on analytical solutions of the capillary problem while the influence of gravity is studied using numerical minimization with surface evolver [71].
In the following we present the capillary model based on the description of drop shapes which will be also used in Chapter 3

2.2 Experiments: Drop deposition

2.2.1 Electrowetting

We used electrowetting on dielectric as a way to continuously modulate contact angles [53] in the following configuration. The substrate is a n–doped As conductive silicon wafer (Wacker Siltronics AG – resistivity $1.0 - 5.0$ m$\Omega\times$cm) on top of which a silicon oxide insulating layer (thickness $T = 1\ \mu$m) has been thermally grown. An additional hydrophobic coating (Octadecyl-Tetrachloro-Silane, OTS) has been produced from the liquid phase following standard protocol[72]. We used water drops with NaCl (0.3 % mass concentration) to increase the electrical conductivity. The surface tension of the liquid mixture has been measured in air using the pendant drop method (Dataphysics – OCA30 apparatus and software): $\gamma_{L/air} = 72.5 \pm 0.5$ mN/m and its density $\rho_{\rm L} = 10^3$ kg/m^3. The whole system is immersed in silicone oil (Fluka DC200, density $\rho_{\rm oil} = 937$ kg/m^3, viscosity $\eta_{\rm oil} \approx 10$ mPa$\times$s) to reduce the effect of evaporation on the time of the experiments, increase the capillary length by reducing the effect of gravity and decrease the contact angle hysteresis to a value of the order 2 degrees. The surface tension of the liquid in oil has been measured on the pendant drop ($\gamma_{\rm L/oil} = 38 \pm 1$ mN/m) which gives a capillary length $L_c = \sqrt{\gamma_{\rm L/oil}/(\rho_{\rm L} - \rho_{\rm oil})g} = 8$ mm. For a millimetre drop of water in oil the Bond number characterising the effect of gravity is Bo< 0.1 for which gravity is expected to be negligible. The variation of the apparent contact angle θ_L of a millimetre liquid drop of the mixture as a function of the applied voltage U_0 under oil follows Lippmann's equation:

$$\cos\theta_L = \cos\theta_Y + (U_0/U_L)^2, \qquad U_L = \left(\frac{2T\gamma_{L/oil}}{\varepsilon_0\varepsilon_r}\right)^{1/2} \tag{2.1}$$

as shown in Fig. 2.3. The apparent contact angle at zero voltage (Young's

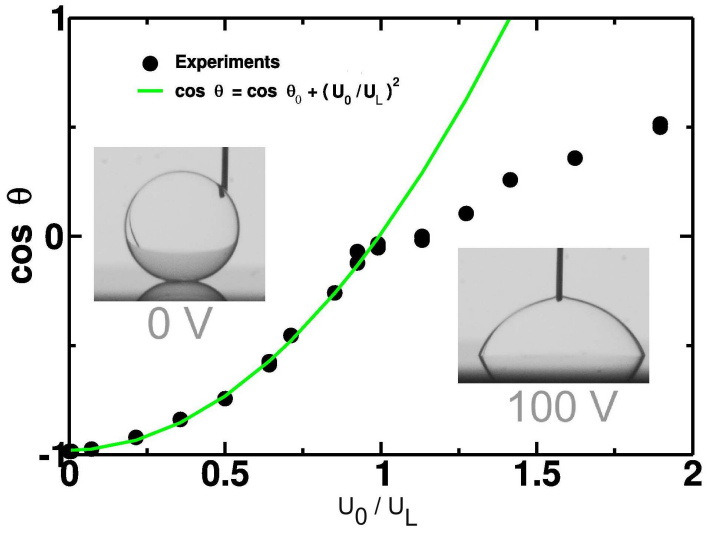

Figure 2.3: Electrowetting curve at 10 kHz ac voltage for a water-salt drop in silicon oil (The electrode diameter is 100 μm). The Lippmann regime is observed below 50 V. The fit with the Lippmann equation gives $\theta_Y \approx 155$ degrees and $U_L = 50$V.

contact angle) is $\theta_Y = 155^\circ$ and the scaling voltage $U_L = 50$V is in good agreement with Eq. 2.1. The dependence of the apparent contact angle as a function of the applied voltage displays the expected quadratic behaviour (Lippmann's regime) until a saturation voltage above which the contact angle follows a system-dependent behaviour. In our case the presence of charges in the insulating layer and the corona instability of the contact line are the most probable explanations for the observed behaviour. In the following all the applied voltages are below the saturation voltage which correspond to a decrease of the contact angle down to 90 degrees. The expression "contact angle" will refer to the apparent contact angle measured at the scale of drop size.

2.2.2 Deposition / Detachment

The experiments have been performed as follows. A voltage is applied between the electrode and the substrate. A drop of volume V is produced out of a syringe (EFD - precision stainless tips, external radius $r_e = 255\mu$m,

internal radius $r_e^i = 125\mu$m). The substrate is approached to the drop and the contact is established at a distance d_c given by the geometry: for droplet diameter much larger than the electrode, the spherical drop touches the substrate when

$$d_c = 2 \times \left(\frac{3V}{4\pi}\right)^{1/3}$$

The drop spreads until its contact angle on the surface has reached the equilibrium contact angle. In order to prevent any confusion in the following Young's angle will refer to the equilibrium contact angle in the absence of voltage, Lippmann's angle will refer to equilibrium angle in the presence of an applied voltage. The substrate height is then decreased step by step ($\Delta z = 10\mu$m) and pictures of the drop are registered. After the break-up a picture is taken which gives the maximal distance $d_{\max}$ (with the accuracy Δz) for which a connected state exists between the drop and the syringe.
Increasing the distance d the drop shape elongates in the vertical direction as displayed in Fig 2.4 and the area of the solid / liquid interface decreases. These surfaces are also obtained in a simple "kitchen-experiment" with soap and water bubbles, an aluminium foil as a flat substrate and a plastic bottle as shown in Fig. 2.5. The two systems are similar because they are both pure capillary systems. The drop is smaller than the capillary length which makes the gravity negligible and a soap bubble is only sensitive to capillary forces. The main differences in these experiment is that the contact angle of the bubble is always fixed at 90 degrees independent on the surface while drops can display different contact angles and that gravity limits the typical drop sizes to the millimetre scale.

At a critical distance $d_{\max}$ depending on drop volume and contact angle the liquid / vapour interface breaks. Two situation are observed: in the case of "large" contact angle and "small" volumes, prior to the breakup, the area of the solid / liquid interface decreases significantly and the drop detaches from the solid substrate: the final state obtained is then a drop hanging at the tip of the syringe. We will refer to this situation as **"detachment"**. During the detachment process a tiny liquid drop has been deposited on the solid surface (see Fig. 2.6). The presence of this tiny drop is likely a consequence of the dynamics which is not resolved by the camera used here. This effect and especially the dependence of the drop size as a function of the parameters has

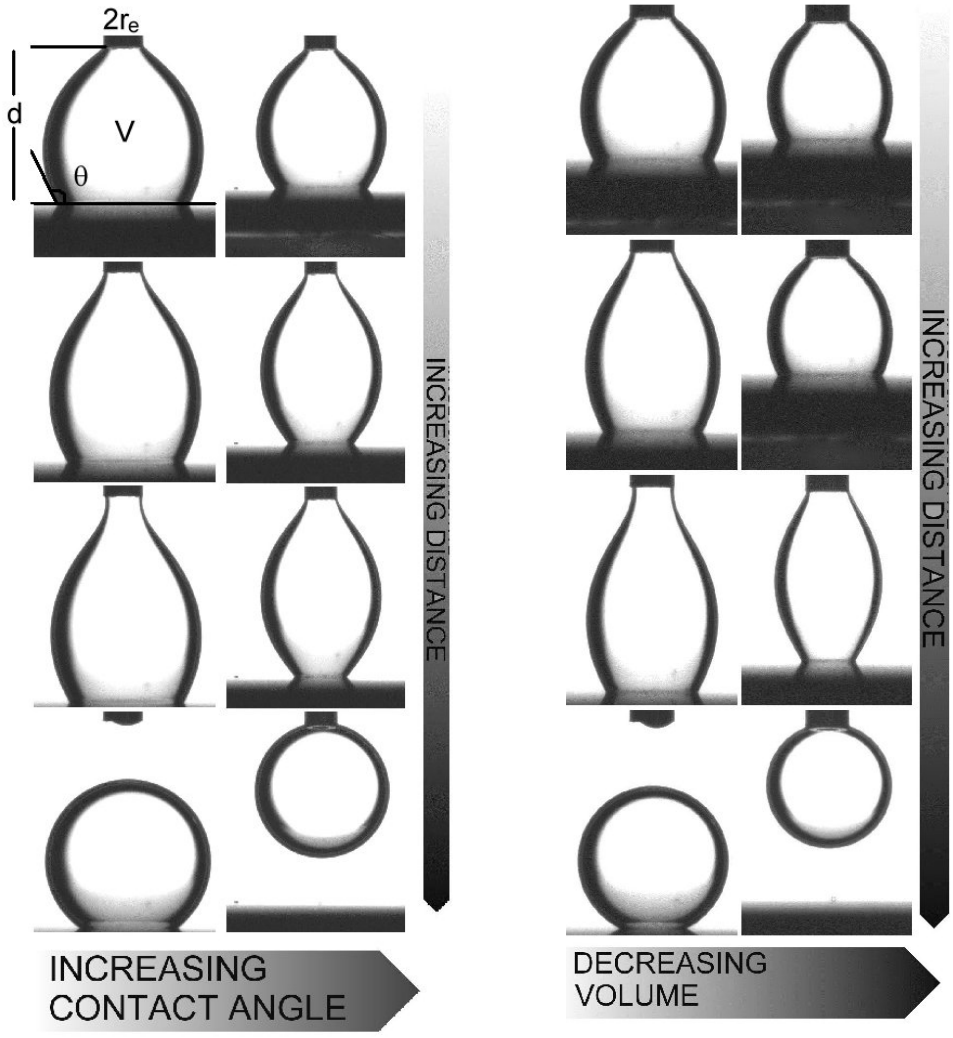

Figure 2.4: Two modes of rupture for a drop in between a syringe and a surface. At constant volume (Left): At small contact angle the drop is deposited on the surface, at small contact angles it detaches from the surface. At constant contact angle (Right): Increasing the volume helps to deposit the drop.

not been studied but could be of interest for the production of small drops on substrates.

In the case of "small" contact angle and "large" volumes, before the breakup a capillary neck is formed between the body of the drop and the electrode. This neck is the weakest point of the structure and breaks when the distance

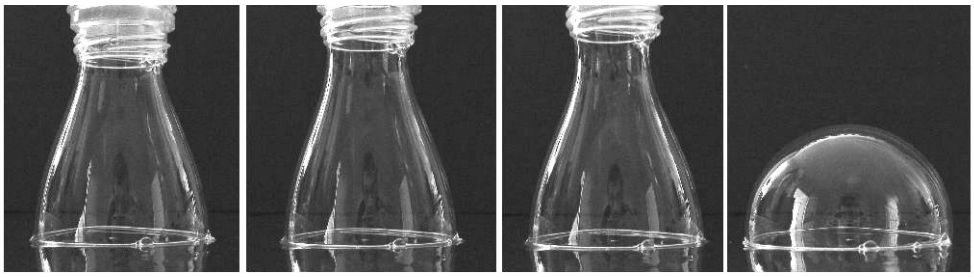

Figure 2.5: Capillary surfaces obtained with water soap and a plastic bottle. The shapes are similar to the droplet shapes of Fig. 2.4.

Figure 2.6: The detachment process leads to the deposition of a tiny drop on the surface, likely as a result of the dynamic of the instability process.

is large enough leading to a deposited drop on the solid surface. We will refer to this situation as **"deposition"**. The contact angle observed in the experiments displayed above after the deposition is close to Young's contact angle meaning that after the breakup no electrical charges are present in the drop. However it is possible to have a control on the charge of the drop after the breakup by playing with the electrical parameters of the system. The contact angle of the drop after the break-up is then close to Lippmann's contact angle. This phenomenon will be studied in details in the chapter 3. In the following, the dynamics of the break-up process is not studied and is expected to have little influence on the limits between the two regimes deposition and detachment at least when the syringe moves quasi-statically (with a speed smaller than the typical speed of the interfaces).
By varying the voltage we tune the contact angle and this way study the

limit between deposition and detachment. For each contact angle a critical volume is determined separating both regimes as shown in Fig. 2.7.

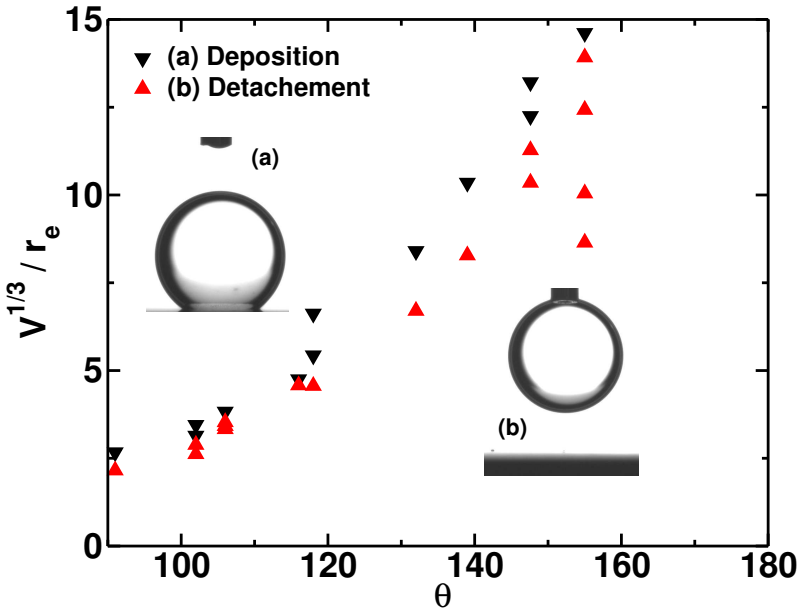

Figure 2.7: Experiments: Two regimes of break-up are observed as a function of volume and contact angle. The deposition (a) occurs at small contact angle and large volumes, the detachment (b) occurs at large contact angle and small volumes. A clear limit is found for the two regimes.

As expected, the critical volume is increasing with increasing contact angle: indeed, the wettability acts in favour of deposition while the liquid / vapour surface tension acts in favor of detachment. Thus decreasing the wettability will be favourable for the detachment process.

2.3 Capillary model

In order to determine the regimes of distances between the syringe and the surface for which a connected configuration of the liquid / vapor interface exists we investigate the shape of the drop undergoing surface forces only (capillary model) in the particular geometry presented in Fig 2.8.

We will consider the following conditions:

1. the geometry is axi-symmetric: in our experiments, the drops exhibit elongated shape. In this situation one expects that the axisymmetric

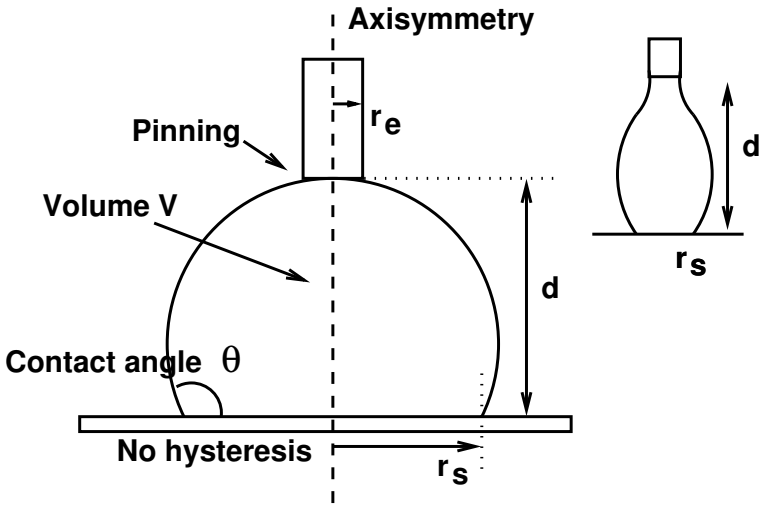

Figure 2.8: Geometry considered in the following: An axi-symmetric drop in contact with (i) an ideal substrate (No contact angle hysteresis) and (ii) an ideal syringe (full pinning at the edges)

modes of instability dominate over the non-axisymmetric modes. In the opposite case, not studied here, where the drop is pressed by the syringe, the non-axisymmetric modes become relevant.

2. gravity is neglected: the model is thus purely capillary, the only length-scale is the radius of the syringe r_e that will be used to scale all the distances. The model is universal in the sense that it can be applied to any liquid and any syringe provided that the dimensions makes gravity negligible.

3. full pinning at the edge of the syringe, which correspond to 0 degree contact angle on the bottom of the syringe and 180 degrees on the sides. This condition allows some simplification in the class of solutions which are studied here but has no influence on the result as soon as the distance d is larger than the height of a sessile drop at its equilibrium contact angle. The influence of the wetting properties of the syringe becomes relevant for distances smaller than this height which correspond to a situation where the droplet is pressed by the syringe. Since we are studying the opposite situation, our pinning condition is well justified.

4. no contact angle hysteresis on the substrate. It is clear that in the case where contact angle hysteresis is included in the model it will favour the deposition of the drop. The model without hysteresis is thus the extreme situation for which deposition is the most difficult to reach.

2.3.1 Unduloids

The drop is an axi-symmetric constant mean curvature surface. Delaunay studied these surfaces in the XIX$^{\text{th}}$ century [73] and showed that they form a family of surfaces parametrized by two numbers, which are usually taken as the minimal radius r_1 and the maximal radius r_2. As soon as these two parameters are fixed, the surface (named Delaunay surface) is fully defined. The Delaunay surfaces are periodic surfaces and include nodoids, unduloids, catenoids, cylinder and sphere. The sphere, cylinder and catenoid are limiting shapes of the unduloids and nodoids. In the following we will focus on stretched surfaces which are then represented by the family of the unduloid (see Fig. 2.9) for which mathematical expressions are given in Appendix C. The unduloid shape parametrized by $\{r_1, r_2\}$ will be noted $r_{r_1,r_2}(z)$. The origin of the axis $z = 0$ is taken at a position where $r = r_1$. From a physical

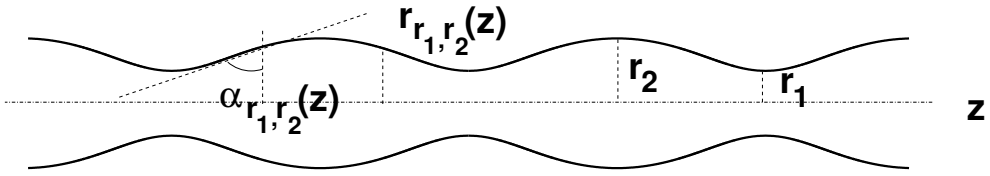

Figure 2.9: Typical section of an unduloid. The 3 dimensional shape is obtained by rotation around the horizontal axis of symmetry.

point of view we observe as stable surfaces only portions of these shapes. Indeed an unduloid longer than one period is unstable due to the Rayleigh instability [65, 74]. For nodoids since the shape intersects itself only portions are observed [17, 75]. Here we observe a portion of the unduloid limited on one side by the solid substrate and on the other side by the electrode. The solid substrate intersect the unduloid shape at the coordinates (r_s, z_s) and the electrode at the coordinates (r_e, z_e).

2.3.2 Method

The idea in the following is to solve the system of equations:

$$\begin{cases} r_{r_1,r_2}(z=z_e) &= r_e \\ \alpha_{r_1,r_2}(z=z_s) &= \theta \\ \int_{z_s}^{z_e} \pi r_{r_1,r_2}^2 \mathrm{d}z &= V \\ z_e - z_s &= d \end{cases} \tag{2.2}$$

where $r_{r_1,r_2}(z)$ is the unduloid shape, $\alpha_{r_1,r_2}(z)$ the unduloid tilt angle (see Appendix C), $\{r_1, r_2, z_s, d\}$ are unknowns[4] and r_e (radius of the electrode), θ (drop contact angle)and V (drop volume) are the constraints. Using these three equations for the four unknowns does not give a single set of solution but an ensemble of parametrized solutions. Moreover, since the problem is non-linear with respect to the unknowns several groups of solutions are expected, corresponding to different shapes. All these solutions will be extrema of the free-energy. The first condition represents the pinning at the edge of the syringe, the second the contact angle constraint and the third the volume constraint. A first study of these conditions determines the range of parameters $\{r_1, r_2\}$ which provides solutions:

Pinning – $r_{r_1,r_2}(z=z_e) = r_e$ – The pinning at the tip gives already limits for the values of r_1 and r_2. Indeed according to Fig. 2.9 it is clear that $r_1 \leq r_{r_1,r_2} \leq r_2$ and thus

$$r_1 \leq r_e \leq r_2$$

The minimal (resp. maximal)radius r_1 (resp. r_2) has to be smaller (resp. larger) than the radius of the electrode r_e. The unduloid being symmetric with respect to the position of the minimal radius, two possibilities exist: the position of the electrode is either above (Fig. 2.10, label 1) or below (label 2) the position of the minimal radius, defining two sub-classes of solutions, the necked unduloids and the un-necked unduloids.

Contact angle – $\alpha_{r_1,r_2}(z=z_s) = \theta$ – The inflexion point $\mathrm{P_{inf}}$ of the unduloid defines a maximal $\alpha^{(\max)}$ and a minimal $\alpha^{(\min)}$ value for the tilt

[4] One can also use the set $\{r_1, r_2, r_s, d\}$

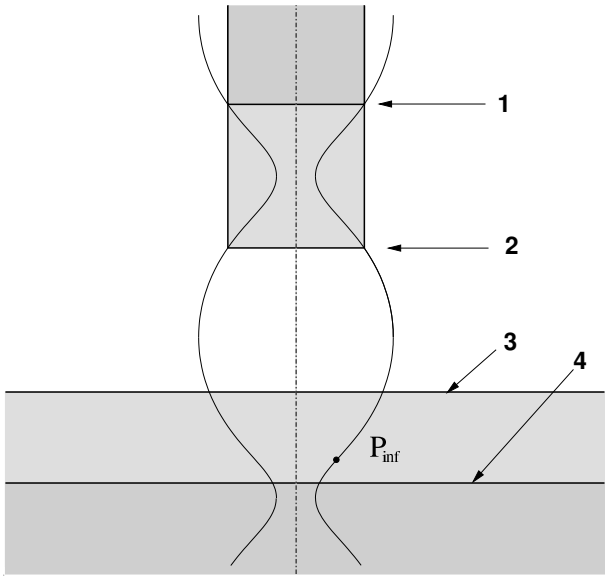

Figure 2.10: Four unduloids fulfilling the contact angle and pinning constraints is found.

angle of the unduloid[5] defined by

$$\cos\alpha^{(\min)} = -\cos\alpha^{(\max)} = \frac{r_2 - r_1}{r_2 + r_1} \tag{2.3}$$

Thus

$$|\cos\alpha_{r_1,r_2}| \leq \frac{r_2 - r_1}{r_2 + r_1} \tag{2.4}$$

Three cases arise:

1. when the contact angle is such that $|\cos\theta| \geq (r_2 - r_1)/(r_2 + r_1)$ (*i.e.* θ too small or too large) no solution exit with the set of parameters $\{r_1, r_2\}$;

2. when $\cos\theta = (r_2 - r_1)/(r_2 + r_1)$ a single solution is found: the solid surface is located at the altitude of the inflexion point P_{inf};

3. when $|\cos\theta| \leq (r_2 - r_1)/(r_2 + r_1)$ two solutions exist defining two positions for the solid substrate located on each side of the inflexion point (see Fig. 2.10, labels 3 and 4); two sub-classes of unduloid solutions are thus defined, the one with an inflexion point above the substrate surface (named "long unduloids", label 4) and the one with inflexion point

[5]Note that $\alpha^{(\max)} + \alpha^{(\min)} = \pi$

below the surface (named "short unduloids", label 3). The two radii on the substrate r_s and their corresponding altitude z_s are determined analytically as a function of θ, r_1 and r_2.

The existence of a solution fulfilling the contact angle constraint requires then

$$|\cos\theta| \leq (r_2 - r_1)/(r_2 + r_1)$$

which also reads

$$r_2 \geq \frac{1 + |\cos\theta|}{1 - |\cos\theta|} \times r_1 \tag{2.5}$$

This equation defines a region in the map $\{r_1, r_2\}$.

Consequences – Combining the first two constraints the solutions are defined in a domain of s$\{r_1, r_2\}$ which is represented in Fig. 2.11. The two

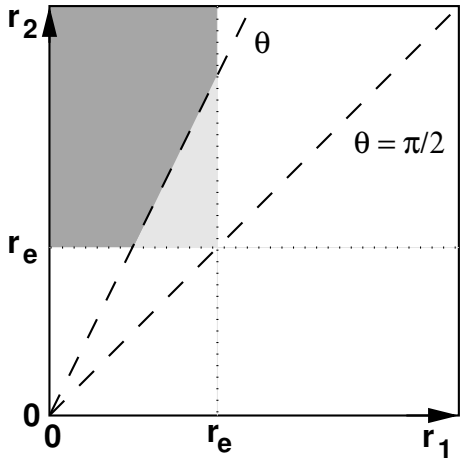

Figure 2.11: Region of the parameter $\{r_1, r_2\}$ where the first two constraints are fulfilled. For a given θ the slope of the dashed line is determined according to Eq. 2.5. The solutions have to be found in the dark gray area. The light gray area vanishes only for the special case $\theta = \pi/2$.

constraints give for a given set of $\{r_1, r_2\}$ the limit of the shape. In the region where the two constraints are fulfilled the combination of the two conditions with two solutions gives four possible solutions which correspond then to four classes of solutions: Short-un-necked, long-un-necked, short-necked and long-un-necked. The stability of these shapes, provided they exist can be summarize in the table 2.1.

unduloid	Un-Necked	Necked
Short	Always Stable (a)	Stable or Unstable (b)
Long	Stable or Unstable (c)	Always Unstable (d)

Table 2.1: Stability of the different subclasses of solutions provided the parameters $\{r_1, r_2\}$ are in the range of admissible values. The labels (a) - (d) refers to the example shown in the following.

Note – Two other solutions exist as displayed in Fig. 2.12. They however correspond to a peculiar case of small volumes and small distances not accessible in the experiments and will not be considered in the following without any influence on the general character of the discussions.

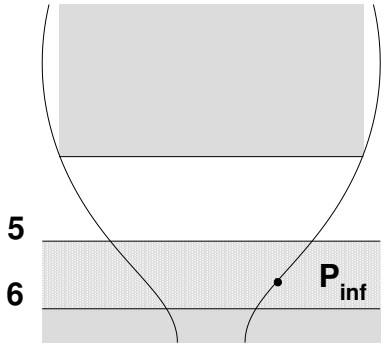

Figure 2.12: Two additional unduloids fulfilling the contact angle and pinning constraints at small volumes.

Volume – $\int_{z_s}^{z_e} \pi r_{r_1,r_2}^2 \mathbf{d}z = V$ – For a set of parameters $\{r_1, r_2\}$ it is clear that the volume is determined when two extremities of the shape are given. Here these extremities are given by the two previous boundary conditions, the radius r_e and the radius on the substrate r_s. The volume of the unduloid is thus determined by $\{r_1, r_2\}$, two additional radii which delimit the shape and also the knowledge of the class of the unduloid (see Appendix C). Indeed depending on the class of unduloid studied the expression of the volume differs and the volume constraint has to be applied successively to the four classes of unduloids with the corresponding expression for the volume. Finally the volume constraint leads to four different unduloids with four different sets of

parameters $\{r_1, r_2\}$: the distance d, the radius wetted by the drop r_s and any other geometrical quantity defined by the knowledge of r_1 and r_2 are then fully determined.

Distance $z_e - z_s = d$ – This last condition is self-explanatory and corresponds to the constraint that fixes the distance d between the substrate and the electrode.

Numerical solutions – The numerical resolution of the system of equation with four unknowns $\{r_1, r_2, z_s, z_e\}$ requires four constraints $\{\theta, V, r_e, d\}$. Instead of solving the non-linear system of four equations with four unknowns, we varied the parameters $\{r_1, r_2\}$ in order to fulfil the first three constraints (Eq. 2.2.1-3) in the different classes of solution leaving the distance d as a free parameter and looked at the parametrization of the solution in a $\{r_s, d\}$ diagram. The representation in the $\{r_s, d\}$ diagram is arbitrary and other representations are also possible, for instance a diagram $\{r_1, d\}$ can also been used. However the representation $\{r_s, d\}$ gives the most readable view, especially for comparison with experimental data since r_s and d are directly accessible by the experiments contrary to r_1 which can be obtained only indirectly in some cases. r_s becomes thus an order parameter in this system.

Let us illustrate the case of the short-un-necked unduloid: r_s is expressed analytically from the contact angle constraint as a function of r_1, r_2 and θ. For a given r_1 the volume is a function of r_2 only. Under those conditions fulfilling the volume constraint is a problem at only one variable r_2, numerically determined by the equation $\Omega(r_1, r_2, r_s(r_1, r_2, \theta)) = V$. From the knowledge of the set $\{r_2, r_1, \theta\}$, the set $\{r_s, d\}$ is determined. In the end for a given set $\{r_1, \theta, V\}$ one obtained a solution defining $\{r_2, d\}$ and as a consequence $\{r_s, z_s\}$ and a single point in the $\{r_s, d\}$ diagram. The same operation is repeated for the three other class of unduloids which thus leads in the end to four points in the $\{r_s, d\}$ diagram. In Fig. 2.13 (a) an example is displayed for $r_1 = 0.5$, $V/r_e^{1/3} = 100$ and $\theta = 100$ (top) or $\theta = 130$ (bottom) showing the four unduloids matching the boundary conditions. It is clear on the example that all four solutions have the correct contact angle. The volume is the same and the distance d and the radius r_s differ from one solution to the

other.
The operation is repeated for other values of r_1 between 0 and r_e. In order to represent the results when r_1 varies, the solutions are plotted in a $\{r_s, d\}$ diagram of Fig. 2.13 (b) for the previous example $V/r_e^{1/3} = 100$ ($\theta = 100$ and $\theta = 130$). The positions of the solutions in the $\{r_s, d\}$ diagram are a function of r_1: the four different classes defines 4 branches of solution. The position of the points obtained at $r_1 = 0.5$ are displayed with their labels. For a fixed drop volume the shape of the branches and their position in the diagram depend on the contact angle:

1. at the small contact angle (100 degrees) the branches define two independent lobes constructed by the union of two branches of solutions (short-un-necked and short-necked on one hand and long-un-necked and long-necked on the other hand)

2. at large contact angle (130 degrees) one lobe only is defined.

A more complete diagram for different contact angle between 45 to 166 ̊is displayed in Fig. 2.14 showing how the lobes merge when θ increases. When the contact angle increases the two lobes gets first closer and then merge at the bifurcation point. In this case the bifurcation between two lobes to one lobe occurs between 121 and 136 degrees. The bifurcation occurs at different contact angle depending on the volume as displayed in Fig. 2.15. Reducing the volume increases the size of the lobes and thus increases the interaction between the two lobes. Thus when θ increases the bifurcation from two lobes to one is reached for increasing volumes. These diagrams show how the different shapes interact when the constraints are changed. The lobes are not independent and move in the diagram. They do not intersect simply but instead merge or split into new structures indicating bifurcation phenomena controlled by the two parameters volume and contact angle. Moreover the bifurcation is observed in all the possible diagrams $\{r_s, d\}$, $\{r_s, r_1\}$, $\{r_s, r_2\}$, $\{r_1, r_2\}$ as displayed in Fig. 2.16 which indicates that the choice made of the representation $\{r_s, d\}$ do not influence the observations. Complex and interesting phenomena occur close to the point where the two lobes merge into one which defines two values $\{\theta_c, V_c\}$ of contact angle and volume. In the following we will refer to this special point where the two lobes merge into one as the **bifurcation point**. The full description of the bifurcation [76]

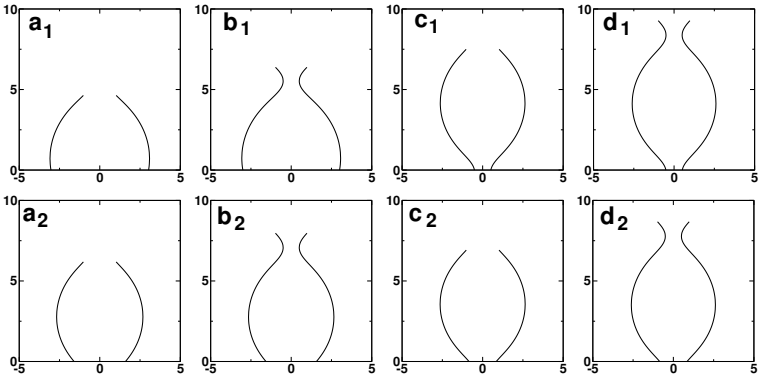

(a)

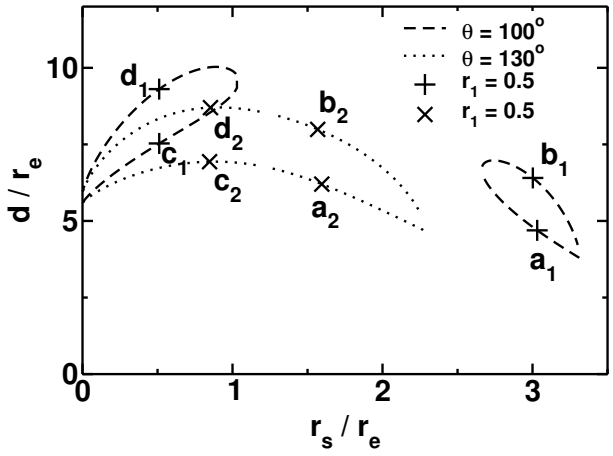

(b)

Figure 2.13: Solutions of the capillary problem (a) At $V/r_e^3 = 100$, for $\theta = 100$ degrees (Top) and $\theta = 130$ degrees (Bottom), fixing $r_1 = 0.5$ four solutions are found with different values of d and r_s. From left to right, the solutions are respectively called short-un-necked, short-necked, long-un-necked and long-necked unduloids. (b) Varying r_1, the solutions define four branches in the $\{r_s, d\}$ map. For $\theta = 100$ degrees, the branches define two independent lobes (dashed line), for $\theta = 130$ degrees, a single lobe is defined (dots).

is not required here since most of the complex features of the bifurcation are restricted to a very narrow region around the bifurcation point $\{\theta_c, V_c\}$ not accessible within the usual experimental accuracies of the wetting experiments. Indeed in Fig. 2.17 one can see that the bifurcation from two lobes

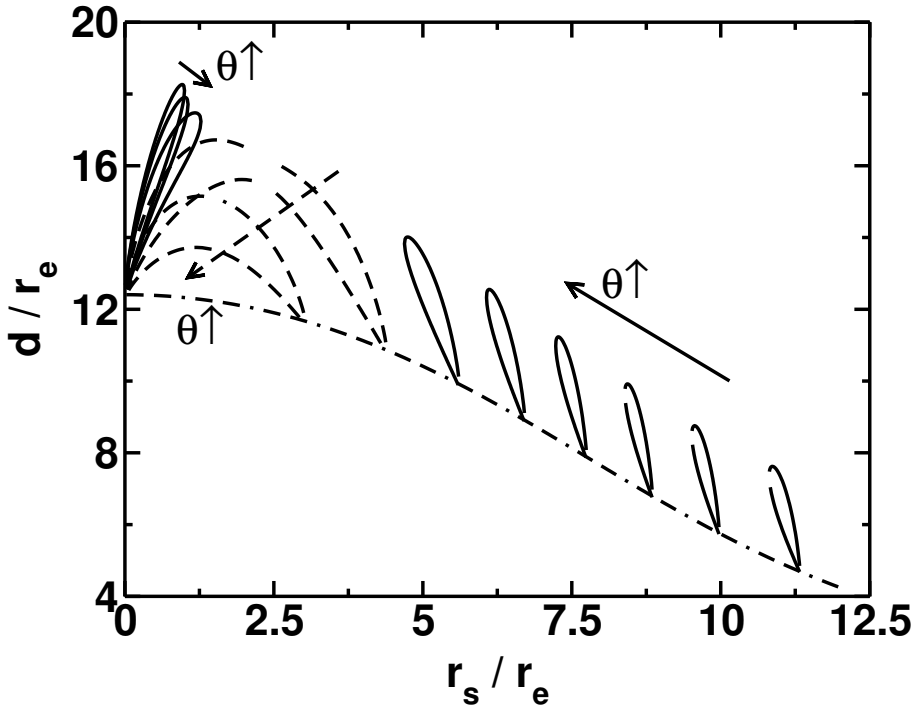

Figure 2.14: $V/r_e^3 = 10^3$, the shapes of the lobes as a function of contact angle: at small contact angles (full line) two lobes are defined ($\theta \in \{45, 60, 75, 91, 106, 121\}$). At larger contact angle a single lobe exists $\theta \in \{151, 166\}$. The dot-dashed line corresponds to the height of a sessile drop of volume $V/r_e^3 = 10^3$.

to one is complete within 1.5 degrees which is already around the maximal accuracy that one can expect for the measurement of drop contact angles.

Diagrams – In the following we will used $\{r_s, d\}$ diagrams which link the order parameter r_s to the control parameter d via the Eq. 2.2. In order to determine the exact shape of the unduloid, it is necessary to determine either r_s or d. The problem is thus fully solved by fixing the distance d: the solutions are given by the intersections of the different branches with the horizontal line corresponding to the constant d. The stable unduloid has to be searched in this intersections. But this does not give the solution since the stability of the shape is not warranted. Starting at small distances, the stable branch is the one called (a). When the distance inreases, the radius of the stable unduloid shrinks (r_s decreases). A distinction has to be made

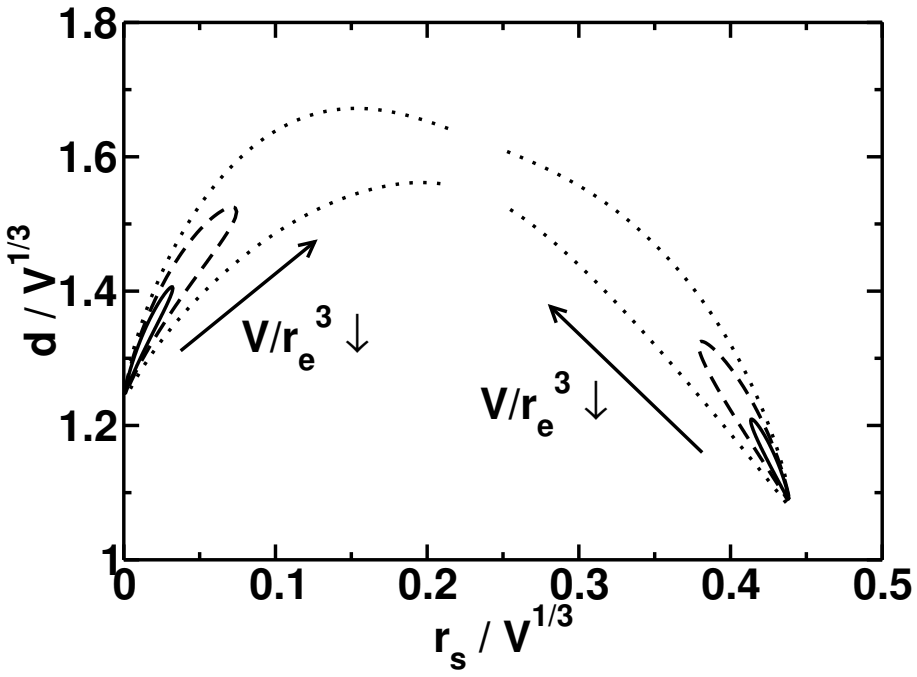

Figure 2.15: Bifurcation at different volumes: at fixed contact angle (here $\theta = 121^\circ$), the transition is reached by increasing the volume ($V/r_e^3 \in \{10^3, 10^4, 10^5\}$). The distances are now rescaled by the volume to fit on the graph.

between the behaviour at 100 and 130 degrees. At 100 degrees, the decrease of r_s stops at the moment where the stable shape becomes necked. Then for increasing distances r_s increases again up to a final point where no solution exist in this classes. At large contact angle (here 130 degrees) r_s decreases continuously while going from the class (a) to the class (c). At a maximal distance no stable solutions are found in this class. The instability process during the break-up is thus fundamentally different in the two situations. The break-up will occur at the weakest point, *i.e* the capillary neck for small contact angles or the substrate surface for large contact angles in agreement with the experimental observations.

In Fig. 2.14 we can follow different characteristic points. The meeting point of two branches gives the bifurcation from the basic shape short-un-necked unduloid to the shape which will destabilize by an increase of d, either a short-necked or a long-un-necked unduloid. The extremum of each lobe give the limits of stability of the unduloid binding the syringe to the substrate.

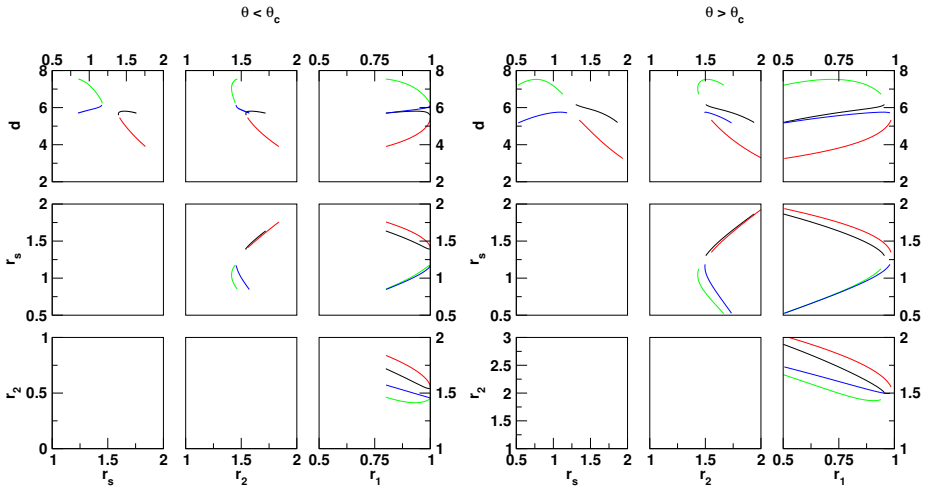

Figure 2.16: Bifurcation for a given volume $V/r_e^3 = 32$: the bifurcation is observed in all the possible diagrams $\{r_s, d\}$, $\{r_s, r_1\}$, $\{r_s, r_2\}$, $\{r_1, r_2\}$. Left: $\theta = 100.5^\circ$, right: $\theta = 102^\circ$.

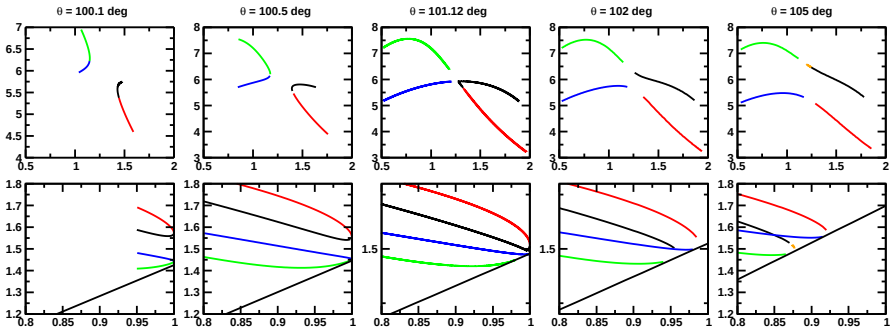

Figure 2.17: Bifurcation for a given volume $V/r_e^3 = 32$: the bifurcation is complete in less than 1.5°. Top: $\{r_s, d\}$ diagram showing the bifurcation from two lobes to one. Bottom: $\{r_1, r_2\}$ diagram. The full black line is given by Eq. 2.5 showing that no couple $\{r_1, r_2\}$ is found below this line.

By changing the contact angle the variation of the position of the extremum $d_{\max}$ is determined and displays a cusp (see Fig. 2.18): this cusp represents the bifurcation between the two modes of rupture. When the other limiting shapes are added to the graph, the cusp appears to be a meeting point for all the different shapes (see Fig. 2.19). At the transition the shape of the

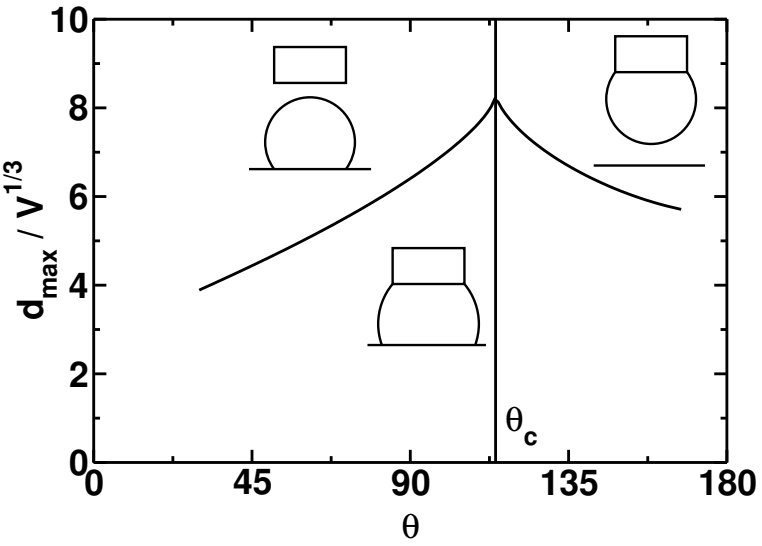

Figure 2.18: Limit of existence of an unduloid of volume $V/r_e^3 = 100$. The cusp separates the two modes of rupture: at the tip of the syringe ($\theta < \theta_c$) or at the solid surface ($\theta > \theta_c$)

drop has to be consistent with the 4 different branches of solution: this corresponds to a situation where the inflexion point is on the surface and the neck radius is exactly equal to the radius of the syringe. Due to the complex scenario of the bifurcation, this argument is only an approximation. However for a fixed volume, the contact angle $\theta_c^{(1)}(V/r_e^3)$ at the bifurcation obtained by this argument is always very close to the one obtained by looking at the contact angle $\theta_c^{(0)}(V/r_e^3)$ for which the lobes merge [76]. The discrepancy $\delta\theta^{(1)} = |\theta_c^{(1)} - \theta_c^{(0)}|$ are displayed in Table 2.2 showing that the error made on the determination of the contact angle at the bifurcation is within 0.5 ° for all rescaled volumes above 16 and within 0.1 ° above 64 which gives an error much smaller than the experimental error that can be made on the determination of a contact angle.

The height of the sphere delimits the area between nodoids and unduloids. It has to be noticed that close to 180 degrees the nodoid shape has to be taken into account since the unduloid limit intersects the sphere for contact angle smaller than 180 degrees which can be interpreted as a geometrical effect on the volume due to the size of the syringe (see Fig. 2.20). This effect concerns however a small area of the diagram and is not investigated in more details in the following. Moreover the contact angles and volumes required to observe

V/r_e^3	$\theta_c^{(1)}$	$\theta_c^{(0)}$	$\delta\theta^{(1)}$
16	91.207	91.65 ± 0.05	0.5
32	100.967	101.15 ± 0.05	0.2
64	109.371	109.45 ± 0.05	0.1
128	116.805	116.83 ± 0.01	0.03
256	123.453	123.46 ± 0.01	0.02
512	129.427	129.43 ± 0.01	0.01
1024	134.794	134.80 ± 0.01	0.01

Table 2.2: Values of contact angle (in degrees) at the bifurcation obtained by looking at which value $\theta_c^{(0)}$ the two lobes merge into one and values of contact angle $\theta_c^{(1)}$ (in degrees) by using the argument that the transition is obtained for a unduloid with a minimal radius equal to the radius of the electrode and an inflexion point located on the solid surface. The error is always smaller than 1 degree.

it are not reached in our experiments reducing the interest of the analysis. The same argument is valid for the area below 45 degrees.

The value of the critical contact angle corresponding to the cusp depends on the volume of the drop considered. Varying the volume the curves $d_{\max}(\theta)$ are plotted and displayed in Fig. 2.21. When the volume decreases the cusp moves to smaller values of the contact angle which represents the fact that the deposition / detachment limit is shifted to smaller contact angles. The extremum is also increasing to converge at 90 degrees to a value close to the limit of stability of a liquid cylinder. From the Rayleigh instability a liquid cylinder will become unstable when its height is larger than its circumference. Here this condition gives a volume $V_{\pi/2} \approx 14.289$. For volumes smaller than the critical volume $V_{\pi/2}$ another bifurcation has been observed with another subclass of unduloid and the bifurcation occurs for contact angles smaller than 90 degrees. In this situation however, a liquid drop will always be deposited on the surface since the wettability is favourable. The volume of the drop compared to the volume of the drop still hanging at the tip will likely depend on the dynamics of the instability, the competition between the speed of motion of the contact line and the pinch-off of the capillary neck. This problem has not been studied but could be of interest in problems linked to

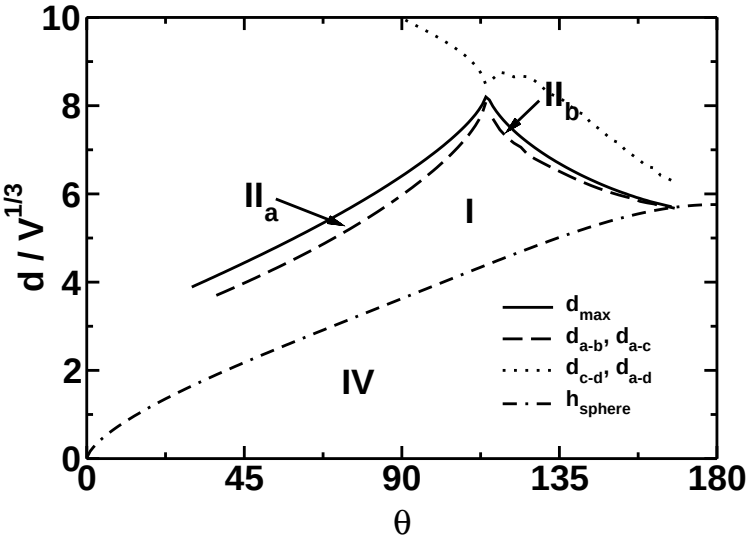

Figure 2.19: Limits of existence of the different Delaunay surfaces for a volume $V/r_e^{1/3}$=100. (IV) nodoid, (I) short-un-necked unduloid, (II_a) the locally stable short-necked unduloids and (II_b) the locally stable long-un-necked unduloids. The maximal distance for which a stable unduloid can be found is represented by the full line and the cusp appears to be at the meeting point of the four classes of solutions.

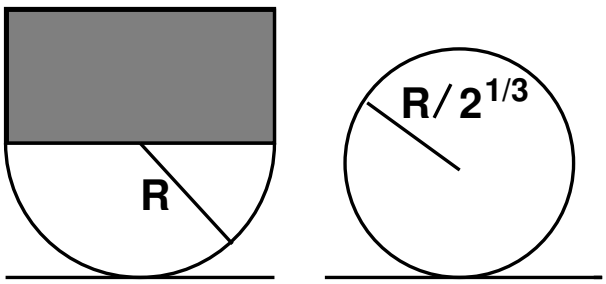

Figure 2.20: Close to 180 degrees $d_{\max}$ is smaller than the height of the sphere. Sketch of such a situation in an extreme case. The contact angle is 180 degrees. Both spheres have the same volume ($2\pi/3$) and the detachment occurs below the sphere height.

offset printing [70].

Since the cusp is the meeting point of all the different classes of unduloids

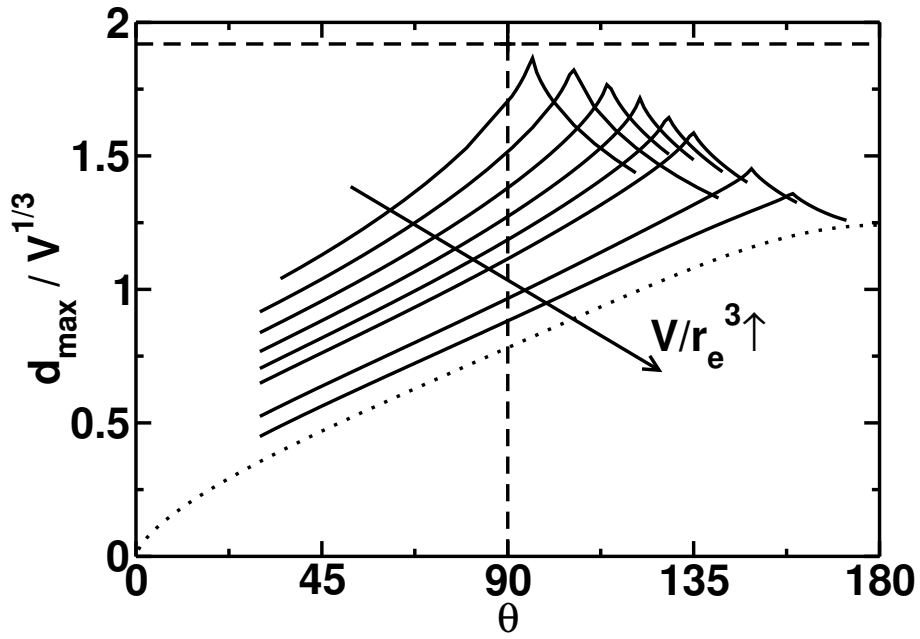

Figure 2.21: Calculated $d_{\max}$ as a function of the contact angle for different volumes $V/r_e^3 \in \{10^{4/3}, 10^{5/3}, 10^2, 10^{7/3}, 10^{8/3}, 10^3, 10^4, 10^5\}$. For large volumes $d_{\max}$ is gettting closer to the height of a spherical cap (dots).

solution the unduloid at this very point is expected to be defined by $r_1 = r_e$ and the inflexion point P_{inf} on the substrate; the radius on the substrate is thus given by $r_s = \sqrt{r_1 \times r_2}$. The volume of such a shape is then computed and the variation of the critical contact angle as a function of the volume is obtained and displayed in Fig. 2.22. The transition displays a divergence at 180 degrees where a simple scaling has been found giving a close approximation of the bifurcation limit (See Fig. 2.23).

This scaling is obtained by looking at the shape of the drop at the meeting point of all the branches. The contact angle at the surface is obtained by the argument that the inflexion point is located on the substrate surface:

$$\cos\theta = \frac{r_2 - r_1}{r_2 + r_1} \tag{2.6}$$

which is rewritten using the fact that the pinning condition at the tip is fulfilled for $r_1 = r_e = 1$:

$$r_2 = \frac{1 - \cos\theta}{1 + \cos\theta} \tag{2.7}$$

At large contact angles the transition occurs for a volume such that $r_2 \gg r_1$.

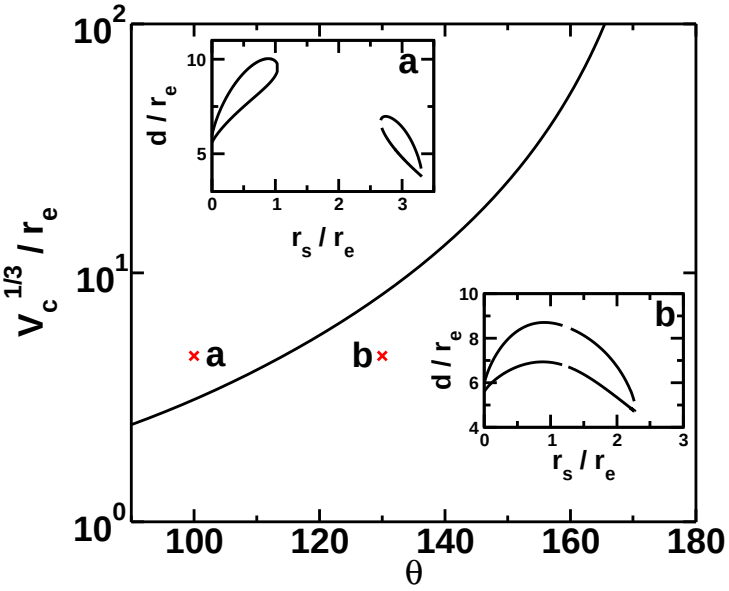

Figure 2.22: Relationship between the volume and the contact angle that separates the two modes of rupture (deposition (a) or detechment (b)). For increasing volume the cusp is located at increasing contact angle.

For such an almost spherical cap, the relation between the volume of the drop and r_2 is given by the geometry:

$$r_2 = \left(\frac{3V}{4\pi}\right)^{1/3} \left(2 - 3\cos\theta + \cos^3\theta\right)^{-1/3} \tag{2.8}$$

Combining both equations this leads to:

$$V_c^{1/3} \approx 2 \times \left(\frac{4\pi}{3}\right)^{1/3} \times \frac{1}{1+\cos\theta} \tag{2.9}$$

The transition occurs close to 180 degrees and on a relative broad extension. Considering the full capillary problem this expression gives a really good approximation of the volume that is possible to deposit. We can calculate the contact angle at the bifurcation $\theta_c^{(2)}$ using Eq. 2.9 and the error $\delta\theta^{(2)} = |\theta_c^{(2)} - \theta_c^{(0)}|$ made and the error made compared to compared to the previous $\theta_c^{(1),(2)}$: the results are summarized in Table 2.3 and show that the simple scaling argument is valid for contact angles larger than 130 degrees within 2 degree accuracy.

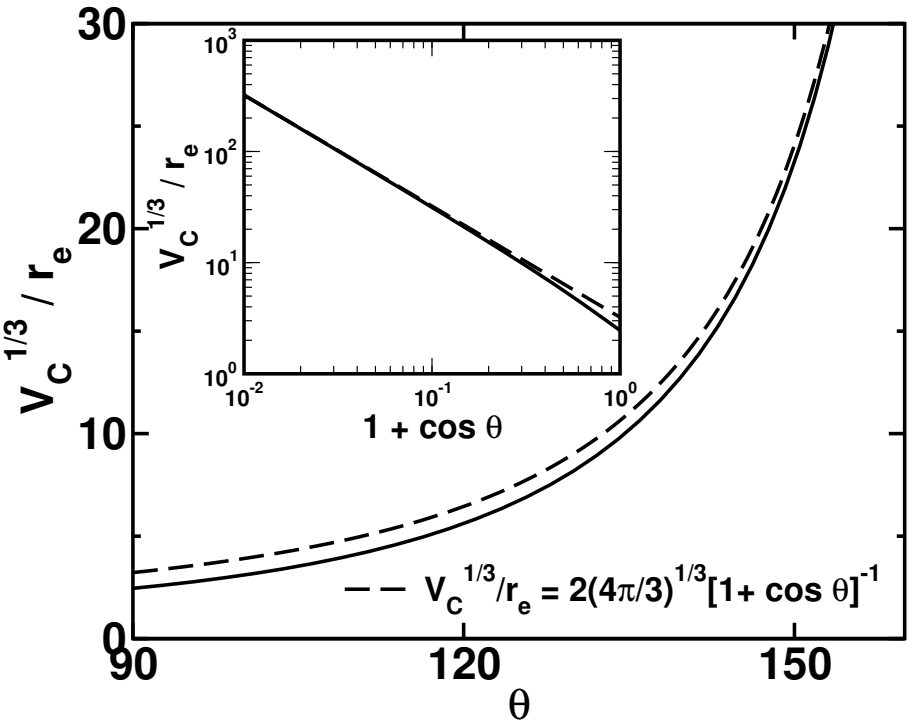

Figure 2.23: Comparison of the result of the model (solid line) with the power-law found from the scaling analysis (dashed line).

V/r_e^3	$\theta_c^{(2)}$	$\theta_c^{(0)}$	$\delta\theta^{(2)}$
16	73.77	91.65 ± 0.05	17
32	89.11	101.15 ± 0.05	12
64	101.19	109.45 ± 0.05	8
128	111.11	116.83 ± 0.01	5
256	119.49	123.46 ± 0.01	4
512	126.66	129.43 ± 0.01	3
1024	132.85	134.80 ± 0.01	2

Table 2.3: Contact angle $\theta_c^{(2)}$ (in degrees) at the bifurcation obtained from the scaling argument compared to $\theta_c^{(0)}$. The error is significant close to 90 degrees but is less than 2 degree for contact angle larger than 130 degrees.

2.4 Comparison with the experiments

For U_0=35.7 V ($\theta = 118 \pm 2$ degrees), the profile of the drop has been extracted (see Fig. 2.24). The profiles are correctly described by unduloids

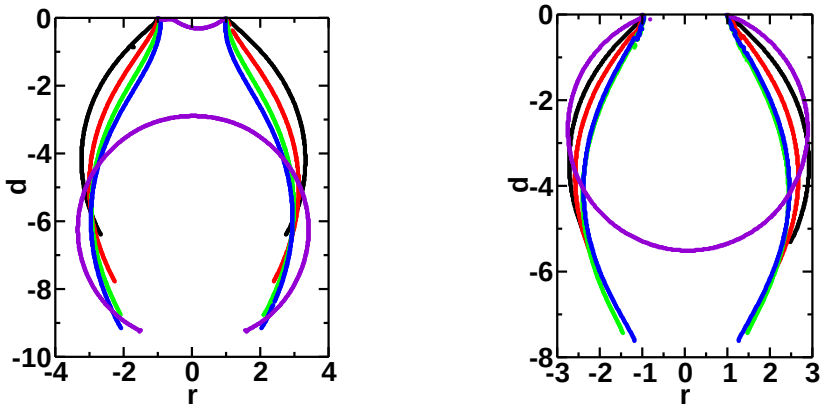

Figure 2.24: Experimental profiles obtained in the case of the droplet deposition (left) or detachment (right). U_0=35.7 V ($\theta = 118 \pm 2$ degrees)

as shown in Fig. 2.25 for $U_0 = 35.7$ V ($\theta = 118 \pm 2$ degrees) and $V = 13\mu$L. However a slight asymmetry is visible on the profiles since the parameters fitting the left and the right profiles are not equal. This slight asymmetry is evaluated as the difference between the maxima radii of the unduloids fittig the left and right profiles. In this case, the asymmetry is of the order of 3% since the relative error on the maximal radius r_2 is $\Delta r_2/r_2 = \pm 1.5\%$ which is expected to have only a small influence compared to an ideal symmetric case. The asymmetry gives also the error made on the determination of the volume which is calculated on the images assuming a symmetric profile. The relative error on the determination of the volume $\Delta V/V$ is then $\Delta V/V \approx 3\Delta r_2/r_2 = \pm 4.5\%$. As expected, as long as the size of the drop is small compared to the capillary length, the profiles are in good agreement with the predicted unduloid.

To better compare the experimental data with our model the distance d and the radius r_s have been extracted on the pictures. These measurements are rescaled by the radius of the electrode and plotted as a function of

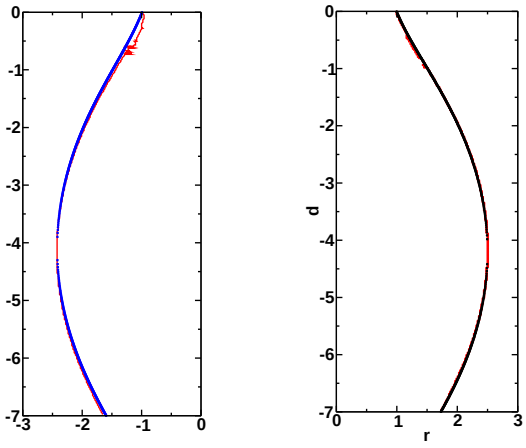

Figure 2.25: Comparison of extracted profiles and unduloids. The profile are slightly asymmetric which is confirmed by the values of the parameter of the unduloid fitting the profiles: for the left hand profile $r_1 = 0.85$ and $r_2 = 2.42$ while for the right hand profile $r_1 = 0.85$ and $r_2 = 2.50$

contact angle and volume as displayed in Fig 2.26. It should be mentioned that the model curves are obtained without any fitting parameters. The contact angles and volumes measured on the pictures are used to calculate the unduloid shapes and produce the $\{d, r_s\}$ graphs. The main features of the model curves are reproduced by the experimental curves: the curvatures of the different lobes and the transition between the two different scenarios of rupture.

The experimental limits between deposition and detachment have been plotted and compared to those predicted by the transition shape of the unduloid (Fig. 2.27). The limits are found in extemely good agreement in the range 90 to 120 degrees. Above this value the capillary model departs from the experimental data. Indeed the volume at the transition increases which therefore increases the influence of gravity on the drop shape. This point is confirmed by numerical simulation (Surface Evolver) using the capillary length $L_c \approx 8$ mm. The experimental and numerically modelled data are found in good agreements and show that gravity influences the transition from volumes as small as $V_c^{1/3}/r_e \approx 7.5$. This dimensionless volume corresponds to $V \approx 10$ μL. This value gives a Bond number Bo ≈ 0.02. In our case gravity plays a role from values of the Bond number as small as 0.02, mainly due to the

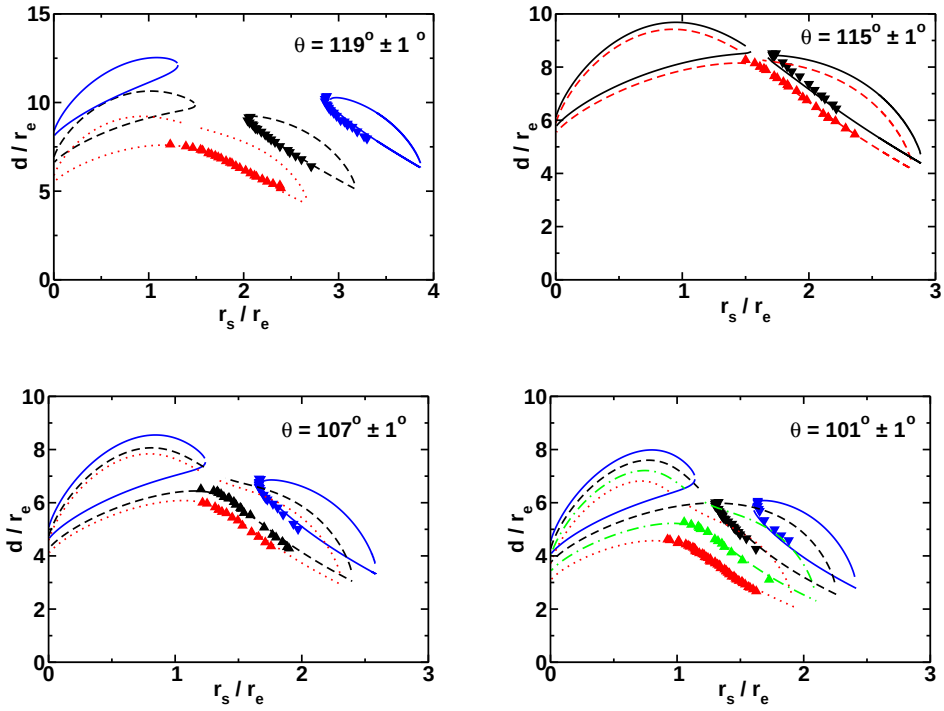

Figure 2.26: $\{d, r_s\}$ diagrams. No fit parameter have been used in the comparison: volumes and contact angle used in the calculation are within the range of accuracy of the experimental values. Top-left: $V/r_e^3 = \{290, 160, 118\}$; top right $V/r_e^3 = \{108, 96\}$; bottom left: $V/r_e^3 = \{56, 54, 40\}$; bottom right: $V/r_e^3 = \{41, 31, 24, 18\}$ ▲ correspond to detachment, ▼ correspond to deposition.

vertical extension of the drop shape during the removal of the syringe: the influence of gravity is enhanced on such an extended shape. The consequence is that the deposition / detachment transition is extremely sensitive to gravity effects. From a physical point of view it is clear that the deposited volume at a contact angle of 180 ° is obtained by the balance of gravity force and surface forces and thus leads to the volume of a dripping drop [5]:

$$V^{1/3}/r_e \approx \left(10 \times (L_c/r_e)^2\right)^{1/3} \approx 21$$

Thus one expect a crossover from the capillary regime at contact angle close to 90 ° to the dripping regime at contact angle close to 180 °. This crossover is observed in particular in Fig. 2.28 where experimental data obtained for

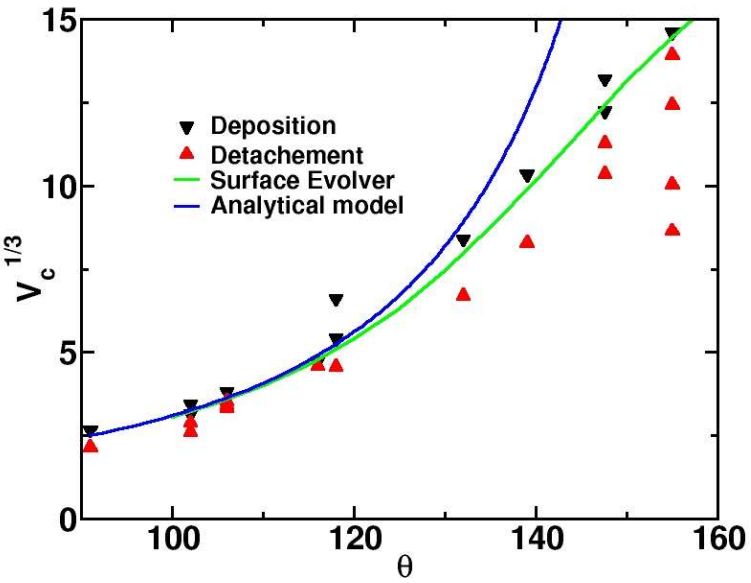

Figure 2.27: Comparison of the model with the experimental data. The agreement is correct as long as gravity is negligible. Gravity effects have been modeled using Surface Evolver.

L_c/r_e have been added.

2.5 Conclusions and discussions

A capillary model has been developed to study the deposition of a drop on a hydrophobic substrate of variable wettability. The wettability is experimentally modulated using the electrowetting effect and Lippmann's angle is used as a boundary condition in the capillary model: electrowetting acts only as a capillary term following Lippmann's equation. We restrained ourselves to contact angles larger than 90 degrees for which the quadratic relationship of Lippmann's equation is correctly reproduced experimentally. Under these conditions the limit between the deposition and detachment regimes is in agreement with our capillary model. In the model the limit is given by the point where there exist no stable unduloid surface fulfilling the boundary constraints of volumes and contact angle. More generally the model fully determines the static shape of the drop in the conditions of axi-symmetry and pinning at the edge of the syringe when the syringe is slowly pulled away

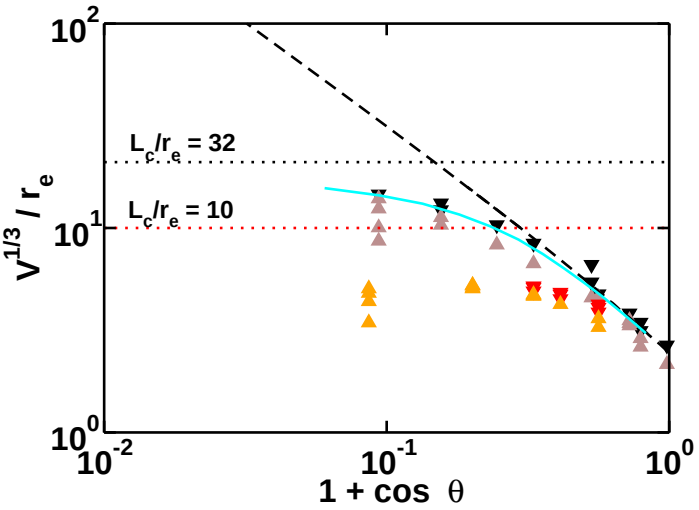

Figure 2.28: Crossover from the offset printing regime to the dripping drop regime. The black and gray triangles correspond to $L_c/r_e = 32$, the red and orange to $L_c/r_e = 10$. The blue line corresponds to surface evolver calculations at $L_c/r_e = 32$.

from the substrate. The capillary model shows three different levels:

1. model 0, the rough model describes the drop in the limit of large contact angles. In this case the results are in reasonable agreement with the experimental data. It gives the minimal volume that can be deposited as

$$V_c = \frac{32\pi}{3} \frac{1}{(1+\cos\theta)^3} \times r_e^3$$

   The accuracy of the model is within 2 degrees for volumes larger than $10^3 r_e^3$.

2. model 1, the approximated model: it gives the minimal volume that can be deposited for all contact angle but only as a numerical result. The error made with this model is less than 0.5 degrees for contact angles larger than 91 degrees;

3. model 2, the exact model [76]: it describes the details of the scenario of the bifurcation.

Depending on the level of understanding required one can refer to the results coming from the different model.
It has been shown that the volumes deposited with this method scale with the radius of the syringe to the power three:

$$V \propto r_e^3$$

which is a huge improvement compared to the dripping faucet problem where the capillary length imposes an additional scaling:

$$V^{1/3}/r_e \approx 2.1 \times (L_c/r_e)^{2/3}$$

This value is expected to be recovered for a contact angle of 180 degrees which determines the crossover between the capillary assisted deposition (offset printing) to the gravity driven dripping drop.

The analysis made here is of potential interest in microfluidics, for instance to determine the minimal volume that can be deposited by a syringe in the case of spotting of microarrays on a surface of known wettability.

Chapter 3

Self-excited Drop Oscillations in Electrowetting Experiments

Jean-Christophe Baret and Frieder Mugele

Contents

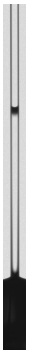

3.1 Introduction

In a classical electrowetting experiment the electrode used to apply the voltage to the drop is immersed inside the drop for any value of the voltage. In our experiments a cylindrical electrode is placed at the top of the drop at a distance d from the substrate surface. When the voltage is applied the drop spreads and can detach from the electrode. The detachment will occur when the spreading of the drop is sufficiently large to destabilize the capillary neck which forms between the drop and the electrode. It is clear that the limit for the drop detachment depends on the values of U_0 and d. The goal in the experiments described in the following is to study the behaviour of the drop after the breakup. Our system displays the same type of behaviour as already observed by Klingner *et al.* [47] the drop oscillating between a connected and a disconnected state as sketched in Fig. 3.1. In contrast however, the electrode introduces an additional length-scale, the diameter of the electrode which was not present for a drop between two plates.

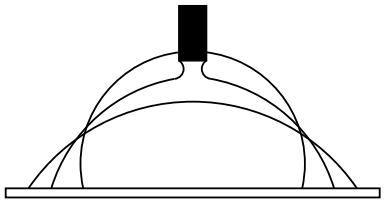

Figure 3.1: Sketch of the experimental set-up. The drop at zero voltage spreads when the voltage is applied and display a capillary neck which leads to a disconnected state when the neck becomes unstable.

3.2 Materials and methods

3.2.1 System

The material used is a typical electrowetting material made of a conductive substrate, an insulating layer, a drop of a conductive liquid and a platinum electrode immersed in the drop and the voltage is applied between the electrode and the solid substrate. The solid substrate is a conductive n^+ arsenic doped silicon wafer (conductivity 1-5 mSm) on top of which a 1 μm thick

silicon oxide insulating layer has been thermally grown. An additional hydrophobic layer has been deposited on the surface (OTS monolayer) from the liquid phase following Sagiv [72]. The liquids used are mixtures of water, glycerol and NaCl in various composition which allows to change the viscosity and conductivity of the drop without modifying significantly its surface tension. The whole set-up is immersed in a silicon oil bath (Wacker silicone oil AK 5, viscosity $\eta = 5$ mPas) in order to prevent evaporation on the time of the experiment, to reduce contact angle hysteresis and to increase the capillary length. The contact angle of the solution under oil measured using a side view of sessile drop is 155 $^\circ$ on the OTS layer with less than 5 degrees hysteresis in both cases and about 140 $^\circ$ for glycerol. The relative density of the liquids in the silicone oil is ρ =0.2-0.3 10^3kg.m^{-3}, for viscosities η ranging between 1 to 100 mPas. The voltage U_0 applied between electrode of radius $r_e = 125$ μm and the substrate goes typically from 0 to 100 V rms at a frequency ranging from 1 to 20 kHz. A R_m=10 kΩ resistance has been included in series with the drop and the current through the circuit is measured via the potential difference at the boundaries of the resistance (see Fig. 3.2).

At a given voltage U_0 when the drop is in contact with the electrode the

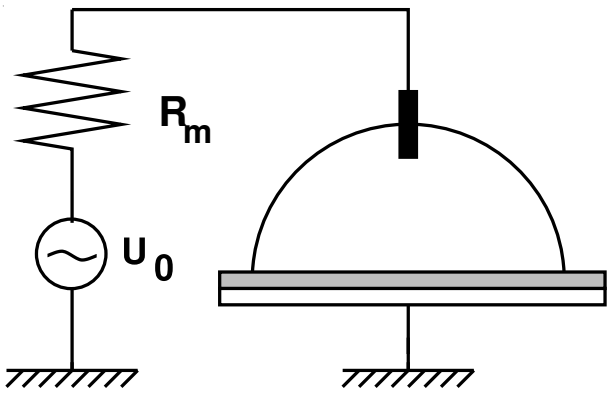

Figure 3.2: Sketch of the experimental set-up. The drop at zero voltage (dashed line) spreads when the voltage is applied and display a capillary neck (full line) which can be unstable leading to a disconnected state (dot-and-dashed line). R_m = 10kΩ is used to measure the current through the circuit.

electrowetting effect forces the drop to spread from Young's contact angle θ_Y to Lippmann's contact angle θ_L [51, 53] as displayed in Fig. 3.3 for a water

drop.

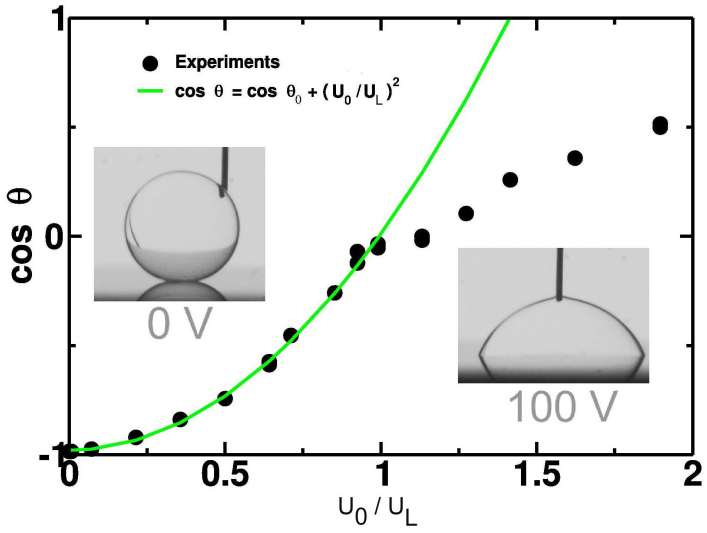

Figure 3.3: Electrowetting curve for a water drop on a silicon wafer coated with an 1 μm insulating layer and additional OTS hydrophobic coating. U_L = 50V

The experimental variation of the contact angle follows Lippmann's equation (2.1) and the fit of the experimental data with a parabolic function of the voltage gives $U_L \approx 50$V in reasonable agreement with the physical properties of the system.

3.2.2 Electrical properties of the drop

The drop behaves in the system as an electrical component [60] with a finite conductivity and a capacitive contribution due the solid / drop interface. A leakage current is usually modelled by a large resistance R_L in parallel to this capacity [60]. For simplicity in our case the insulating layer is modelled as perfect insulator ($R_L = \infty$; no leakage current) defining a capacitance C depending on the surface wetted by the drop on the substrate (Fig. 3.4); the effects of the leakage currents will be invoqued when necessary. The drop electrical resistance is modelled by a resistance R_d^0 which depends on the exact shape of the free-surface and has two parts, an intrinsic part representing the

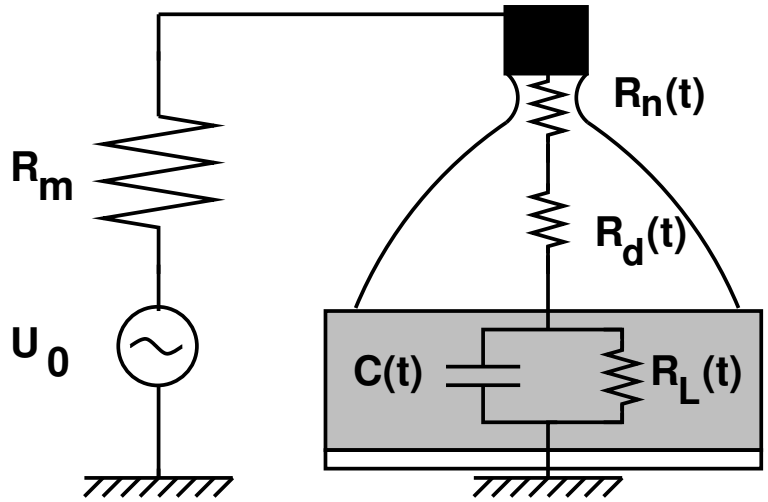

Figure 3.4: Sketch of the electrical properties of the system. Most of the impedances are time-dependent.

resistance of the drop body R_d and a part representing the neck resistance when this one exists R_n. The system has thus three major electrical parts, the resistances R_m and R_d^0 and the capacity C. The typical values of this three major impedances of the system are now discussed. The typical value for the drop resistance, in the case where the electrode is completely immersed (no neck, $R_n = 0$) in the drop is roughly given by:

$$R_d \propto \frac{h}{\sigma r_0^2}$$

where r_0 and h are the typical radius and height of the drop. Since $h \sim r_0$ for a spherical drop this leads to

$$R_d \propto \frac{1}{\sigma r_0} \sim 1 - 10\text{k}\Omega$$

for the range of parameters used in the following. On the other hand, the capacitive impedance reads:

$$Z_C \propto \frac{1}{C\omega} \sim \frac{T}{\varepsilon_0 \varepsilon r_s^2}$$

$r_s \approx r_0$ is most of the cases, and thus for a microliter drop $Z_C \sim 100$ kΩ for the maximal frequency used here (20 kHz). Considering the figures obtained here, the electrical circuit is mainly driven by the properties of the

capacitance which is in agreement with the shape of the electrowetting curve which showed that resistances were negligible ($R_d \ll Z_C$). Moreover, the exact evaluation of the resistance of body of the drop is not relevant since it is negligible compared to the capacitive impedance. In the following we will see that the electrode is not immersed in the drop for every voltages but that the connection drop - electrode involves a capillary neck. The electrical circuit is now modified. Assuming that the capillary neck is a cylinder of radius equal to the electrode radius and of length proportional to its diameter, this very piece of fluid behaves as a resistance R_n in series with the capacitance and the resistance of the body of fluid which can be neglected compared to the drop capacitance. The evaluation of the resistance reads now:

$$R_n \propto \frac{r_e}{\sigma \times r_e^2}$$

The typical value of R_n is close to 100 kΩ which becomes comparable to the capacitive impedance. In the presence of a capillary neck, the electrical circuit is modified as displayed in Fig. 3.5. Finally in the absence of a connection between the drop and the substrate, the system is once again changed. The capacity is present but the resistance of the connection is infinite. There is still a capacitive link through the air or oil gap but the corresponding impedance can be seen as infinite compared to the solid surface impedance. As a consequence all these cases are included in a single electrical circuit, a capacitance in series with a resistance, both function of the drop geometry, the capacitance typical values being borned while the resistance varies between R_d^0 =0 (limiting case of an electrode immersed in the drop) and $R_d^0 = \infty$ (limiting case of an electrode disconnected from the drop); in the presence of a capillary neck $0 < R_d^0 < \infty$.

3.2.3 Variation of the electrical current

The electrical current through the circuit is given by the values of the different impedances and varies during the spreading due to the change in the surface drop/substrate and the variation of the neck size.

During the spreading – Assuming a drop spreading in the fully connected state, the circuit is made of a resistance in series with a capacitance. The resistance and the capacitance define the time-scale $R_m \times C \approx 10^{-6}$s

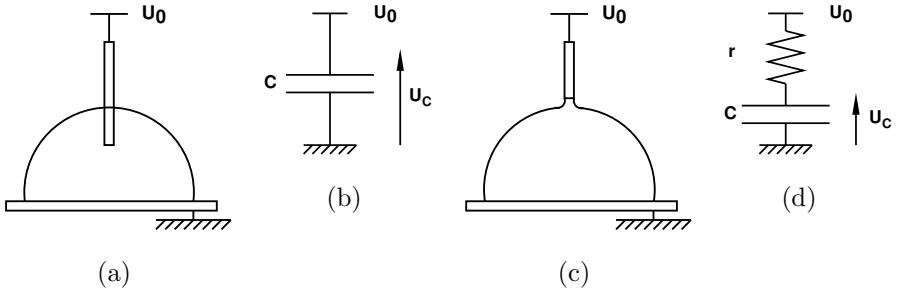

Figure 3.5: Extremal model for the drop electrical properties. The only interesting impedances are the neck resitance function of time and the drop capacitive impedance.

at which the circuit follows the forcing. Assuming the capacitance constant during this time-scale (which is a fair approximation since the contact line moves according to an hydrodynamic time-scale at least 3 orders of magnitude slower than $R_m \times C$), the charge q in the capacitance is given by $q = C \times U_0$. Since the current i is simply $\mathrm{d}q/\mathrm{d}t$ and using a sinusoidal forcing then the current is proportional to the capacitance and thus to the surface of the drop. Since the drop spreads under the influence of the voltage, the current increases during the spreading.

$$i(t) \propto C(t)$$

During the pinchoff – Assuming now that the drop detaches from the electrode through the break-up of a capillary neck. Now the electrical resistance R_n at the capillary neck decreases and gives the time-scale of the variation of the electrical parameters. Since the resistance diverges at the pinchoff (at $t = t_0$), there will be a time $t_1 < t_0$ above which the resistance dominates over the capacitance. In this case the capacitance is taken constant and equal to zero. In this state, the system is simply a resistance plugged at the boudaries of a voltage source. The current is inversely proportional to the resistance and goes to zero. The variations of the current are determined in the latest stage by the pinch-off hydrodynamics **coupled with** the electrical properties of the neck.

$$i(t) \propto \frac{1}{R_n(t)}$$

In the disconnected state – In the disconnected state, the switch is off, the current is zero except for a small noise.

$$i(t) = 0$$

The variation of the current between connected and disconnected state provides thus information on the state of the drop and is used as an electrical measurement of drop oscillations frequency. The current is recorded using a National Instruments Acquisition Board at $4{\times}10^6$ samples per second which gives sufficient time resolution of a 20 kHz signal.

3.2.4 Influence on the electrowetting effect

Not only the electrical circuit is modified by the resistance of the neck but the electrowetting effect in itself also: the contact angle is in principle a consequence of the applied voltage U_0; here it will be determined by the voltage across the capacitor which is the residual of the applied voltage after the loss caused by the electrical resistance. In consequence when the loss of voltage in the capillary neck becomes significant, the electrowetting effect is influenced and the contact angle will be modified (*a priori* larger than expected): the visualisation of the contact angle of the drop will then give a good indication of the relative values of the different impedances and an estimate of the number of charges present in the drop.

In the following we will study the two requirements to have oscillations: first, a simple geometrical condition and then and electrical condition that arises from the capillary break-up .

3.3 Geometrical conditions for the oscillations

When a drop smaller than the capillary length is deposited on the solid surface its shape is a spherical cap since gravity is negligible; the height of the apex of the drop $h(U_0 = 0)$ corresponds to the height of a drop of Young's contact angle on a planar substrate (see Appendix C.2) since no voltage is applied between the drop and the substrate.
A platinum electrode of radius r_e is positioned at the top of the drop at

a distance d of the substrate surface. In order to have contact between the drop and the electrode d has to be smaller than $h(U_0 = 0)$. When a voltage U_0 is applied the drop spreads, its contact angle following Lippman's equation. The associated height $h(U_0)$ of a sessile drop with Lippmann's contact angle is computed from the volume V of the drop and its contact angle always assuming a spherical cap shape of the drop. When the distance from the electrode to the substrate is larger than $h(U_0)$, a liquid capillary neck is formed between the electrode and the drop. When the distance d is increased at fixed voltage the capillary neck becomes unstable and breaks at a distance $d_{\max}(U_0)$. This distance $d_{\max}(U_0)$ is determined experimentally by quasi statically removing the electrode from the drop. After the break up, the discharged drop relaxes back to its equilibrium shape, a spherical cap with Young's contact angle.
It is clear that in the case where $d_{\max}(U_0)$ is smaller than the height of the drop at zero voltage at some point of its relaxation to equilibrium the drop will touch the electrode, charge and spread again. The apparition of an oscillating regime in this system is thus expected from a simple geometrical point of view when

$$d_{\max}(U_0) < d < h(U_0 = 0) \tag{3.1}$$

Such a situation is presented as an illustration in Fig. 3.6 for a 1 μL drop of glycerol water and salt under a voltage of 72 Vrms at 10 kHz. The diameter of the electrode (250 μm) gives the scale. The drop oscillates at about 20 Hz between the connected state (spreading at Lippmann's angle) and the disconnected state (receding at Young's angle). The shape of the drop in the oscillating regime depends on the hydrodynamic and electrical parameters of the system and will be discussed later.

3.3.1 Phase diagram

For a given drop the parameters of the experiments are the distance d between the electrode and the substrate and the applied voltage. By varying these two parameters a phase diagram is plotted. A drop of diameter $V \approx 3\mu$L of the solution is deposited on a silicon substrate coated with an OTS monolayer. The electrode is immersed in the drop and slowly pulled-up. The distance $d_{\max}$ for which the connection between the electrode and the drop is broken is measured. The voltage is increased to obtain the curve $d_{\max}(U_0)$. The

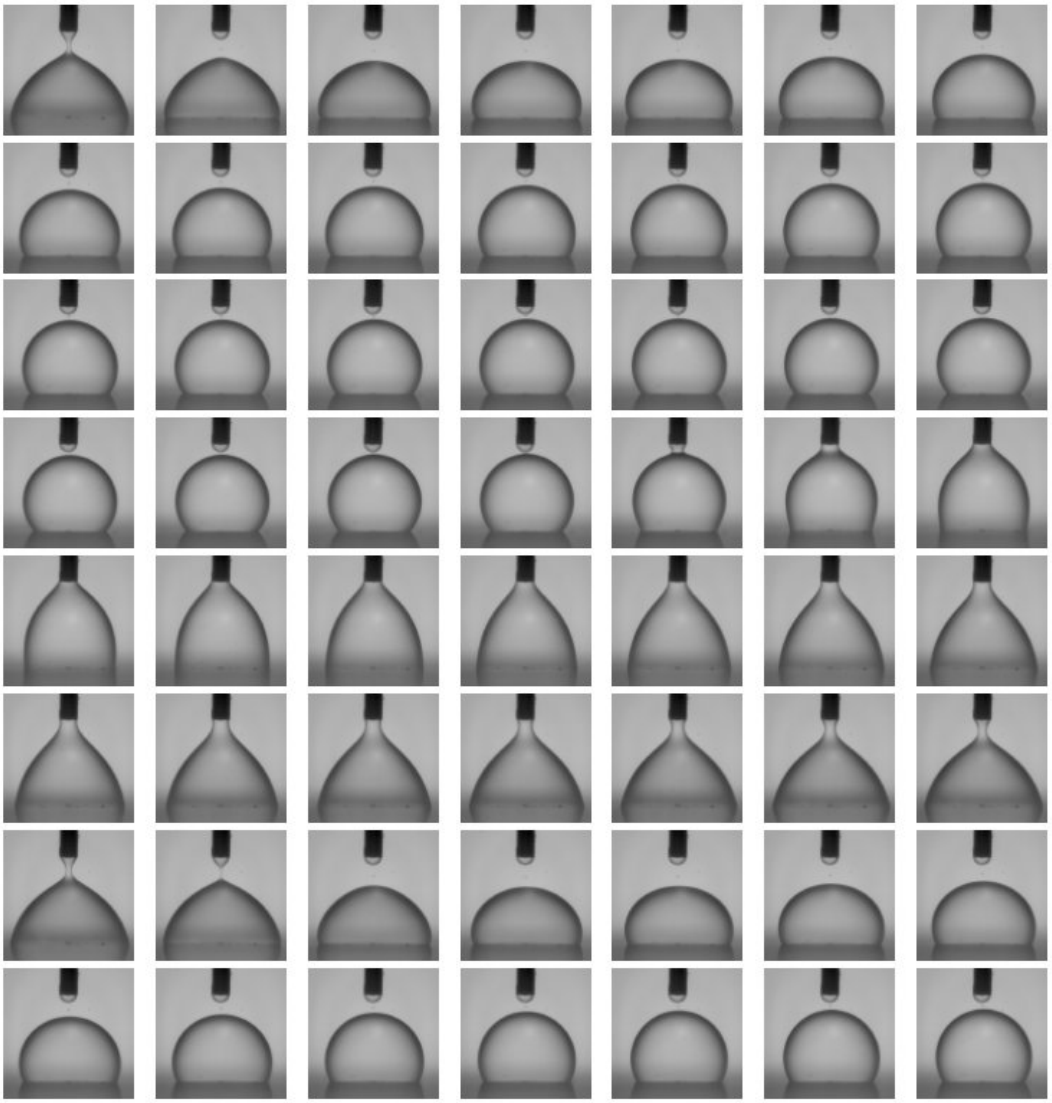

Figure 3.6: Oscillations of a drop at 70 V rms and 10 kHz; the frequency of the oscillations is about 20 Hz. (2000 fps)

oscillations are expected for voltages U_0 and distances such that $d_{\max}(U_0) < d < h(U_0 = 0)$ where $h(U_0 = 0)$ is the height of the drop at zero voltage. In Fig. 3.7 the variation of $d_{\max}(U)$ is displayed as well as the height of the drop at zero voltage. The oscillations are expected in the right corner defined by the curves $d_{\max}(U_0)$ and $h(U_0 = 0)$. The stars represent the points where the oscillations have been experimentally observed. Oscillations have not

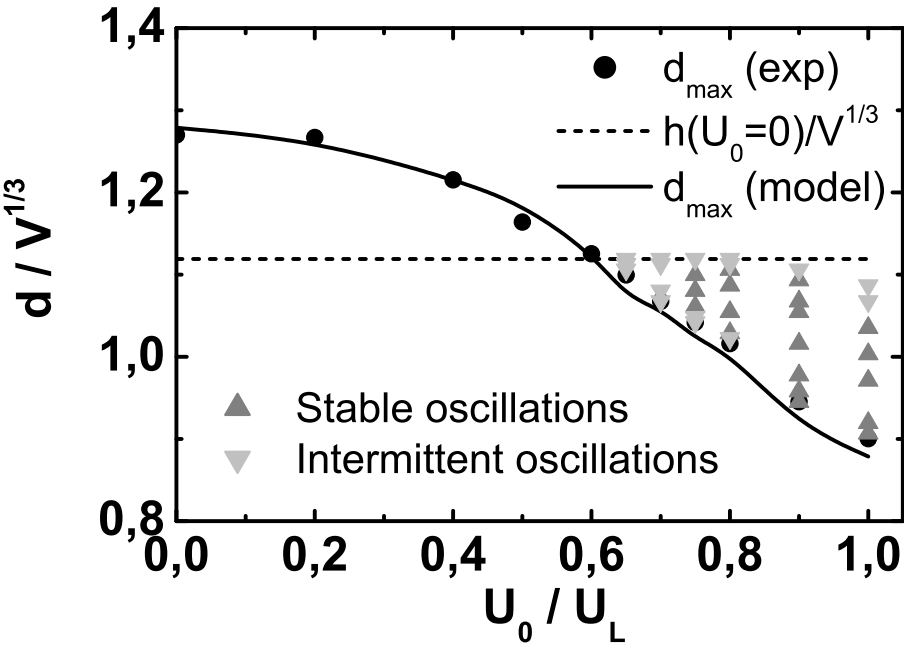

Figure 3.7: Phase diagram of the system. The voltage is normalised by $U_0 = 50$V and the distances by the volume of the drop to the third. The model predicts an oscillating regime above the full line ($d > d_{\max}$) and below the dashed line ($d < h(U = 0)$). The triangles represent the point where oscillations have been observed.

been observed anywhere else. The graph shows distinctly an oscillating area above a threshold voltage U_T. This voltage is the intersection of the curve $d_{\max}$ with the curve $d = h(U_0)$ as expected from the simple model. In the following we will present two models for the determination of the threshold voltage, a simple model and a more general one based on the stability of the unduloids as described in Chapter 2.

3.3.2 Modeling the threshold

In order to determine the threshold voltage it is necessary to determine the variation of $d_{\max}$ with the applied voltage and to solve the equation

$$d_{\max}(U_0) = h(U_0 = 0) \tag{3.2}$$

As it can be seen in Fig. 3.7, a model curve of $d_{\max}(U_0)$ has been calculated and added to the graph. It has been obtained by using the argument that

the capillary neck breaks when its height is of the order of its width. The height of the capillary neck at the break-up is estimated as $d_{\max}(U_0) - h(U_0)$ with $h(U_0)$ the height of the sessile drop at Lippmann's contact angle for the voltage U_0 obtained from the experimental electrowetting curve. The width of the capillary neck is of the order of the electrode diameter which means that $d_{\max}(U_0) = h(U_0) + kr_e$ where k is a parameter that has to be adjusted to fit the experimental curve and r_e is the radius of the electrode. In the present case the experimental curve and the modelled curve with $k = 5$ are in a good agreement. Indeed two simple argument explain that this threshold voltage has to be strictly positive:

- the height of the drop is a decreasing function of the applied voltage: $h(U = 0) - h(U_0) > 0$. Since one has to equal $h(U_0 = 0) - h(U_0)$ with a strictly positive value ($k \times r_e > 0$) then U_0 at the threshold is positive.
- what would mean a 0 V threshold ? Simply that an energetically insulated drop / substrate system would produce a motion without external driving which is energetically not consistent

The oscillations are thus promoted by the external force and especially by the fact that this external driving force changes during the cycle between the connected state and the disconnected state.

3.3.3 Consequences: Size effect and downscaling

This model also explains the variations of the threshold with the diameter of the electrode: U_T is increasing when the electrode diameter. The threshold voltage depends only on the geometrical parameters of the drop (θ_Y and V) and on the electrode diameter r_e: fixing the contact angle of the system, if the ratio of the drop size to the electrode diameter is kept constant and as long as gravity is negligible compared to surface tension U_T is constant. Since

$$h(U = 0) - h(U_0) = \left(\frac{3V}{\pi}\right)^{1/3} \times (f(\theta) - f(\theta_Y))$$

where f is a function of θ written in the Appendix C.2 whose expression is not required here, it is obvious that solving $h(U_0 = 0) - h(U_0) = k \times r_e$ to determine the threshold only involves θ_Y and $V^{1/3}/r_e$. The diameter of the electrode becomes then just the length scale of the system. The variations

of the threshold voltage have been measured as a function of the drop size for two different electrode radii in order to test this scaling at a fixed contact angle. The results are displayed in Fig. 3.8. The drop size $V^{1/3}$ has been

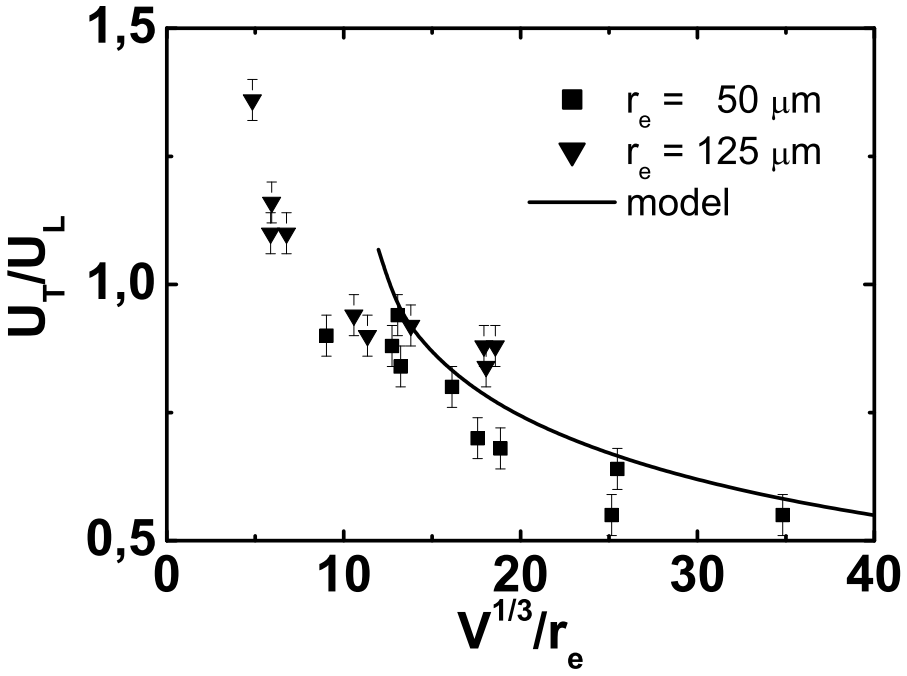

Figure 3.8: Variation of the threshold voltage U_T as a function of the aspect ratio of the size of the electrode and the size of the drop. The full line correspond to the determination of the threshold voltage from the static model with a fit parameter equal to 5 (see Fig. 3.7)

scaled by the electrode radius r_e. All the data points are collapsing on a single curve which confirms that the relevant scale is the electrode radius. The model curve of the dependence of U_T with drop size is obtained by solving for U_0 the equation $h(U_0) - h(U_0 = 0) = kr_e$ with $k \approx 5$. The tendency of the threshold voltage to increase with the electrode size (or decrease with the drop volume) is consistent with the expectations. The model curve is found to be in good agreement with experimental data, especially in the case of the smallest electrode for which the volume of the neck keeps being negligible compared to drop volume. The curve obtained from the model is not in agreement with the experimental data at small volumes. In this regime of parameters, the volume of the neck is not negligible compared to

drop volume which is an implicit condition in the model when we derive that $d_{\max} = h(U_0) + k \times r_e$. This will be improved in the following using the model based on the unduloids.

3.3.4 Contact angle saturation

Since θ saturates at a non zero value due to the saturation of the contact angle, h also saturates. A maximal value of electrode diameter is found for which the oscillations can occur: this value depends on the maximal variation of the contact angle when the voltage is applied and explains the divergence of the model curve at small $V^{1/3}/r_e$. If one would plot θ_T the threshold contact angle as a function of $V^{1/3}/r_e$ one would observe no divergence but simply an experimental cut-off at small θ_T.
However, the model based on stability of the capillary neck is not valid for small values of $V^{1/3}/r_e$. The decrease of drop size means that the drop can not be considered as a spherical cap with a neck any more but the neck and the drop are linked in a single shape. The whole drop shape must be calculated using the argument that any axi-symmetric constant mean curvature surface is a Delaunay surface [73] as studied in the Chapter 2. This full capillary model is now presented.

3.3.5 Application of the unduloids model.

The drop shape is an unduloid for which the stability limit with increasing distances has to be calculated. Taking the volume from the experimental conditions the variations of $d_{\max}$ have been calculated according to the method described in Chap. 2. The contact angles have been converted from the applied voltage using the electrowetting curve. In those conditions, the comparison of the experimental data and the modelled data are displayed in Fig. 3.9. This model is consistent with the approximate model: indeed in the regime we are working in the curve representing $d_{\max}$ is parallel to the height of the drop. This confirms that one can write $d_{\max} = h(U_O) + k \times r_e$. The parameter k that has been taken equal to 5 by a fit is recovered in the model. The advantage of the unduloid model is double:

1. there is no fit parameter;

2. there is no restrictions on drop volume.

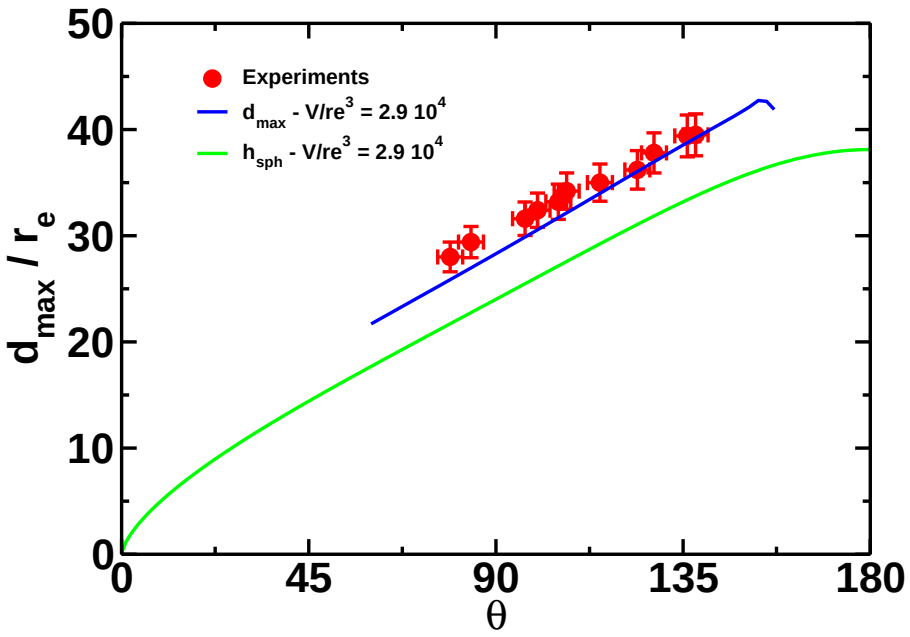

Figure 3.9: Use of the unduloid model to predict $d_{\max}$. The experimental points are the same as in Fig. 3.7. They are compared with $d_{\max}$ obtained for a rescaled volume of 29×10^3 given by the experiments.

The drawback is that the mathematical derivation of the model is more complicated. Using the unduloid model the size effect has been studied and compares quite well with the experimental observations. The model based on the unduloid has also been extended here to determine which Lippmann angle θ has to be reached in order to have the oscillations for different drop volumes as a function of Young's contact angle. The drop volumes are rescaled by the the cube of the electrode radius r_e^3. For each drop volume the variation of $d_{\max}(\theta)$ was calculated in a range of θ accessible by the electrowetting experiments (45-180 degrees). Then writing $h_s(\theta_Y)$ as the height of a spherical cap at Young's contact angle, Eq. 3.2

$$d_{\max}(\theta) = h_s(\theta_Y) \tag{3.3}$$

has been solved. The results are displayed in Fig. 3.11 and can be used for the determination of the oscillating area in the presented geometry as a function

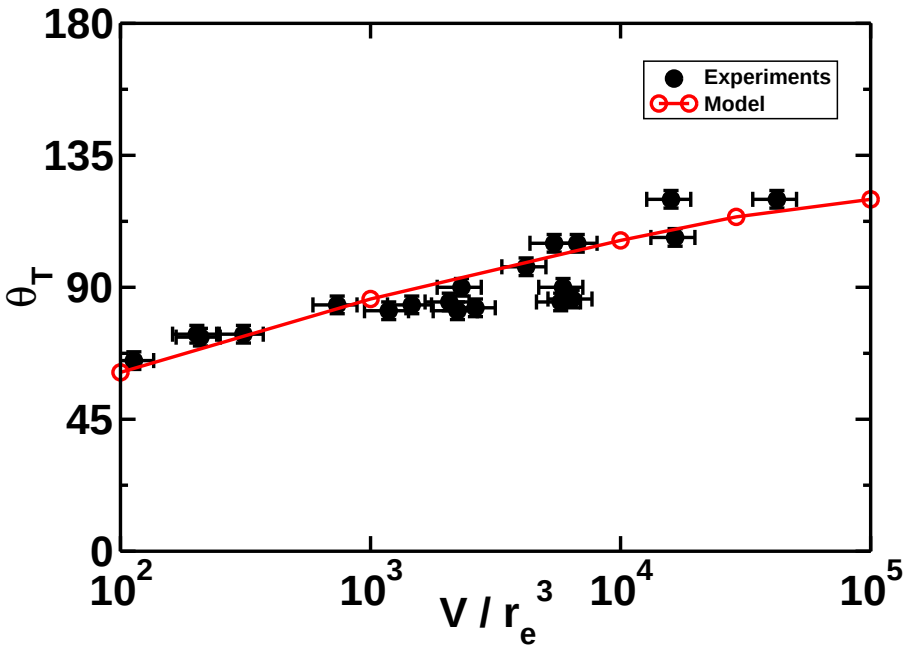

Figure 3.10: Extension of the unduloid model to determine the effect of the size of the drop on the threshold voltage. The experimental points are the same as in Fig. 3.8

of Young's contact angle and the volume of the drop. Some features can be discussed:

1. When the volume is increased, the threshold voltage gets closer to Young's contact angle. This is the same result as the one obtained with the simple model: the threshold voltage decreases with decreasing electrode diameter. The smaller the electrode is the easier the oscillations are obtained.

2. For a given volume, the shift of contact angle required to have oscillations is increasing when Young's contact angle is going close to 180. This can be seen as a simple geometrical effect due to the small variations of h_s close to 180 degrees. In the rest of the range of θ the relation is almost constant which is the result of the fact that h_s is almost linear in a wide range of θ, so is $d_{\max}$.

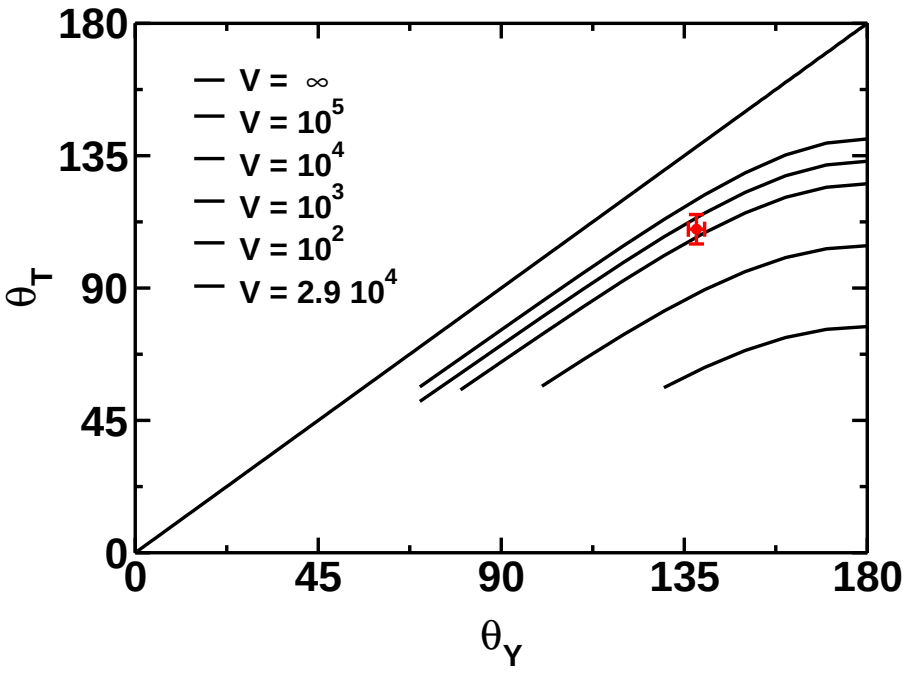

Figure 3.11: Full diagram for the predition of the threshold contact angle as a function of drop volume and Young's contact angle. In abscissa Young's contact angle, in ordinate the contact angle that has to be reached to have oscillations. The red point corresponds to the case of Fig. 3.7

For drops with diameter smaller than the electrode diameter oscillations have also been observed. However in this case the whole drop must be considered as a single capillary neck pinned at the edge of the tip and the whole oscillating process is different because the small drop left at the tip after the break-up plays also a role in the apparition of the oscillations. This geometry reminds the geometry used in the two plates geometry [47]. The oscillating regime should in this case be determined by argument close to those given in this two plates case. In the rest of the paper we will not consider these oscillations.

3.4 Influence of the pinchoff on the oscillations

In the oscillations observed by Klingner *et al.* [47] one of the ingredient of the oscillations was the presence of an electric field which was helping the relaxation. In our case, in the previous experiments the influence of the electric field on the oscillations is not observable in the experiments and thus not part of the model. However, it has been observed that the electrical properties of the system have an influence of the oscillations; in the case where detachment occurs, different situations have been observed, stable oscillations or erratic behaviour. This influence of the electrical effect are now studied, and in particular at the critical moment of the pinch-off.

3.4.1 Experiments

The experiments were performed as follows. Solutions were prepared with various proportions of glycerol, water and sodium chloride in order to vary the viscosity and the conductivity of the drop. The voltage is applied between a platinum cylindrical electrode and the substrate at different frequencies in the range 1 - 20 kHz, 70 - 85 V (rms). In those conditions, when the electrode is placed at the top of a microlitre drop the spreading due to electrowetting leads to the detachment of the drop from the electrode. The drop is observed via a standard or high speed camera. The current flowing through the electrical circuit is measured via amplification of the voltage at the boundary of a resistance in series with the drop. This method gives an electrical characterisation of the state of the drop: when the drop is connected to the electrode the current is given by the electrical properties of the drop and the insulating layer; when the drop is disconnected, the current is almost zero.
Upon detachment from the electrode two limiting phenomena have been observed. Either the drop bounces back to the electrode with a contact angle close to Young's contact angle (regime I) or the drop keeps the Lippmann contact angle and relaxes slowly to the electrode, the contact angle changing slowly (regime II). In the first case the relaxation to the electrode leads to an oscillatory regime since the drop touches the electrode again, spreads again and detaches again. In the second case, the behaviour is less predictable: either the drop relaxes to the electrode with a large time-scale or after a

short time the drop moves away from the field of view and never touches the electrode again. The two different regimes have been observed for the same drop, the same voltage but different frequencies of the voltage source (1 kHz and 10 kHz), using a high speed camera at 2000 frames per second. Snapshots of the break-up are displayed in Fig. 4.10(a).

At 1 kHz, after the break-up the drop keeps a small contact angle which in-

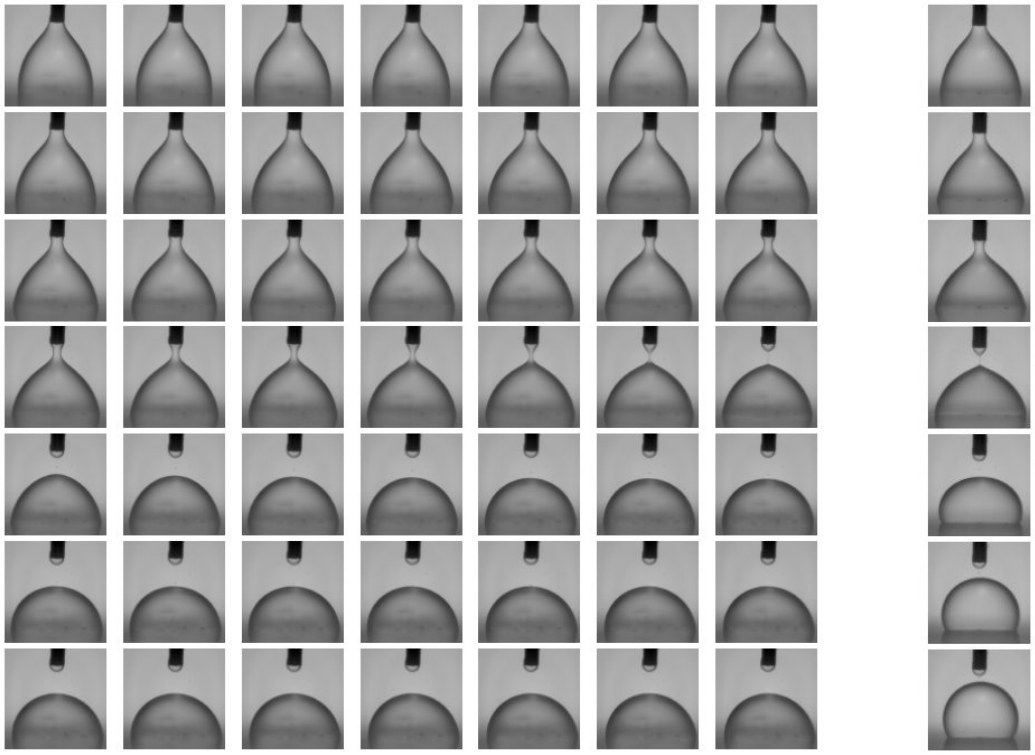

Figure 3.12: Pinch-off at 1 kHz (2000 fps movie). The oscillations are not present: the drop contact angle after the breakup is still close to Lippmann's contact angle. For comparison, the right sequence gives the pinch-off at 10 kHz showing a contact angle close to Young's contact angle after the pinch-off (See also Fig. 3.6). In both cases the electrode diameter is 250 μm

creases slowly while the drop moves away out of the field of view. At 10 kHz (see snaphshots in Fig. 3.6, page 57) stable oscillations have been observed. A noticeable difference in the variation of the contact angles is observed. The contact angle have been measured and are displayed in Fig. 3.13. It should however first be noticed that these contact angles are dynamics con-

tact angles; their value depends strongly on the speed of the contact line and on the scale at which they are measured. They give however a good indication of the state of the drop in terms of electrical charges but should not be taken as absolute and accurate values. At 10 kHz the contact angle

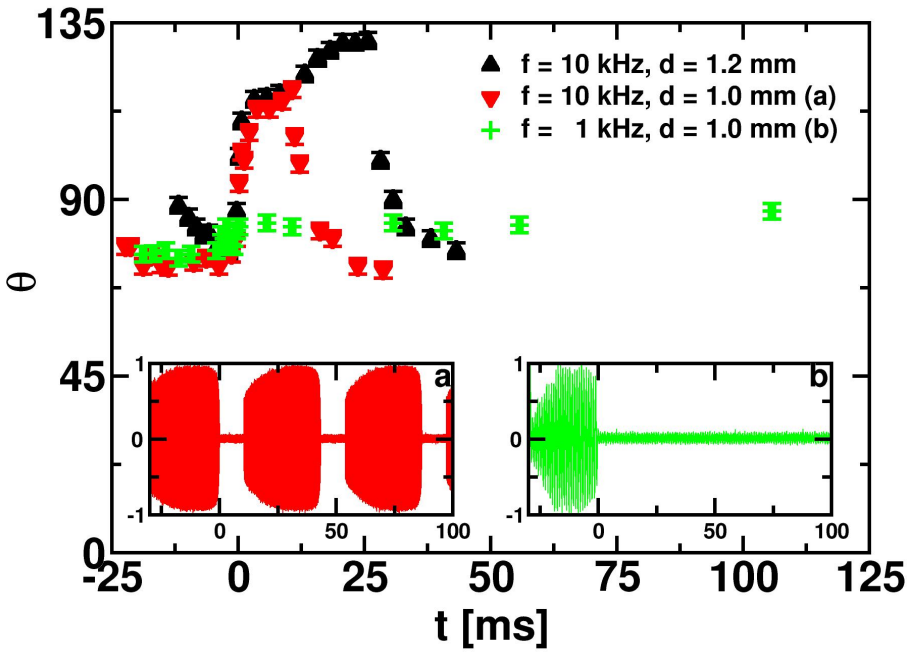

Figure 3.13: Measurement of the contact angle of the drop close to the pinch-off. At 10 kHz, the contact angle changes from Lippmann's contact angle to Young's and the oscillations occur. At 1 kHz, the contact angle is always close to Lippmann's contact angle: No oscillations. The inset are the measurements of the current in both situations showing stable oscillations (10 kHz) or no oscillations (1 kHz)

changes suddenly even before the break-up while in the case of the 1 kHz signal the contact angle is roughly Lippmann's angle after the break-up. The difference in contact angles is the result of remaining charges in the drop after the capillary break-up, the value of the contact angle after the break-up being the signature of the charges. In the regime I, the contact angle shows that no charges are kept inside the drop while in the regime II a significant number of charges is kept in the drop. These charges can leave the drop only

via the insulating layer. The time-scale of the relaxation will be driven by the electrical defects in the insulating layer and is a function of the number of charges. The charged drop is sensitive to the heterogeneous electric field in the environment and to the presence of trapped charges or holes in the insulating layer [77] which can produce a lateral driving force on the drop. The value of the contact angle after the breakup is not exactly the same as before. One argument that can be invoqued to explain this effect is that the contact line is advancing before the breakup and receding after. Since the contact angle is increasing after the breakup (and not decreasing) the change is more likely an electrical consequence of a small loss of charges during the breakup.
At 10 kHz, the contact angle varies following a master curve: at d =1.0 or 1.2 mm the relaxation of the contact angle is the same. The only difference is that the drop touches the electrode earlier when the distance is smaller: the contact angle decreases again earlier for d =1.0 mm (down triangles compared to up triangles). On the other hand when the distance is smaller the contact line has more time to spread; the contact angle even reaches a plateau close to the real Lippmann angle (see the down triangles just before the pinch-off) while the detachment occurs when the drop is still spreading significantly for a larger distance (up triangles). These two competing effect have of course an influence on the frequency of the oscillations.

The limit between regime I and regime II has been studied experimentally and shows a dependence on the electrical parameters of the system. For a given drop (conductivity and viscosity constant) the boundary depends on the frequency of the voltage source: at "high" frequency the drop oscillates regularly (regime I) and the oscillations are not present any more below a threshold frequency (regime II). For given frequency and viscosity the oscillations stop when the conductivity of the solution increases. Finally, for a given conductivity and frequency the regime I is obtained at "high" viscosities while regime II is obtained at "low" viscosity. These results are summarized in Fig. 3.14 which shows the evolution of the threshold frequency for different viscosities and conductivities.

In order to understand the influence of the electrical parameters we studied the variation of the current flowing through the circuit as a function of the electrical and hydrodynamical parameters of the set-up, with a special

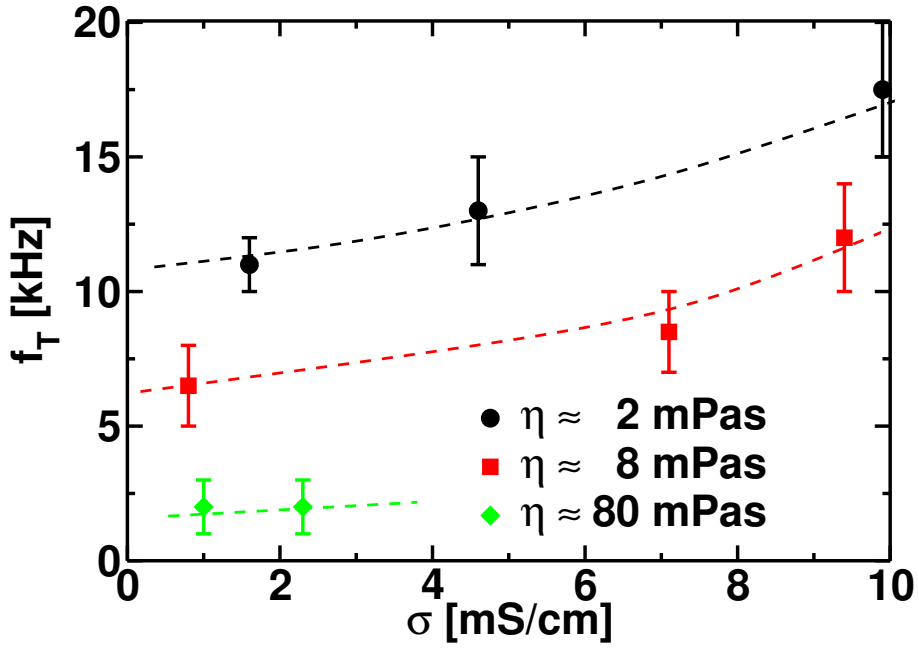

Figure 3.14: Experimental limits of the oscillating regime: influence of the electrical parameters. The drops considered here are 1 μL drops with an electrode of 250 μm diameter. The dashed lines are guides for the eye.

attention to the snap-off. The electrical analysis of the current is coupled to the determination of the geometrical parameters of the drop during the oscillations via the measurement of the drop radius on the surface and of the minimal diameter of the capillary neck using a high speed camera. As expected when the oscillations are stable, the current is alternating from a non-zero value when the drop and the electrode are in contact to a zero value in the disconnected state. The current has also a shape closely linked to the evolution of the geometrical parameters as displayed in Fig. 3.15. In a first regime, after the electrical connection is re-established, the current is increasing due to the increase of the drop surface πr_s^2. Then in the latest stage of the oscillations, the capillary neck diameter goes to zero as well as the current. A close look at the current during the breakup shows the influence of the frequency ω on the decrease of the current: when ω decreases the time-scale of the decrease of the current is ≈ 4 times larger at 20 kHz (≈ 2 ms) than at 5 kHz (≈ 0.5 ms) as displayed in Fig. 3.16. The way the current drops to zero depends then on one hand on the electrical impedances which involve the drop conductivity, the frequency of the voltage source, and

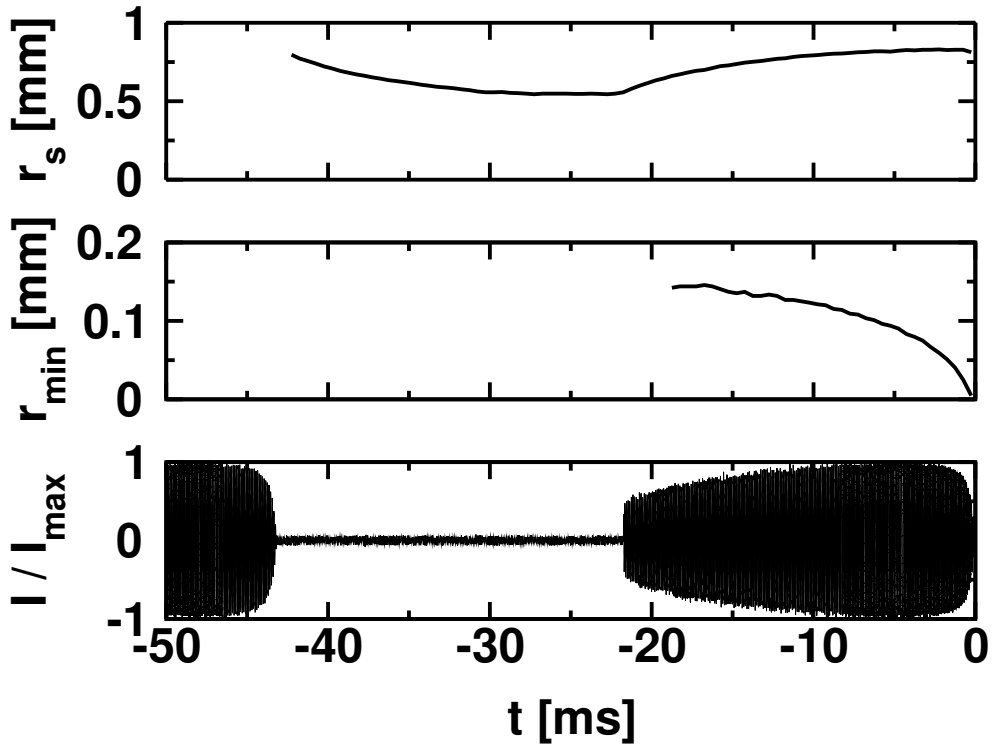

Figure 3.15: Relationship between geometrical parameters and intensity measurement (a) radius of the drop on the solid surface (linked to the capacitive impedance), (b) Minimal radius of the capillary neck (linked to the electrical resistance). (c) Variation of the electrical current through the circuit between zero (disconnected state) to a non-zero value. The current first increases following the increase of r_s and decreases at the end following the decrease of $r_{\min}$

the insulating layer parameters and on the other hand on the time-variation of these quantities determined by the hydrodynamics of spreading and the break-up.

3.4.2 Electrical model

In order to understand the interplay of these parameters, an electrical model has been developed with the minimum of fundamental ingredients:

- A capacitance C modelling the liquid / solid interface
- A resistance R_n diverging with the neck diameter.

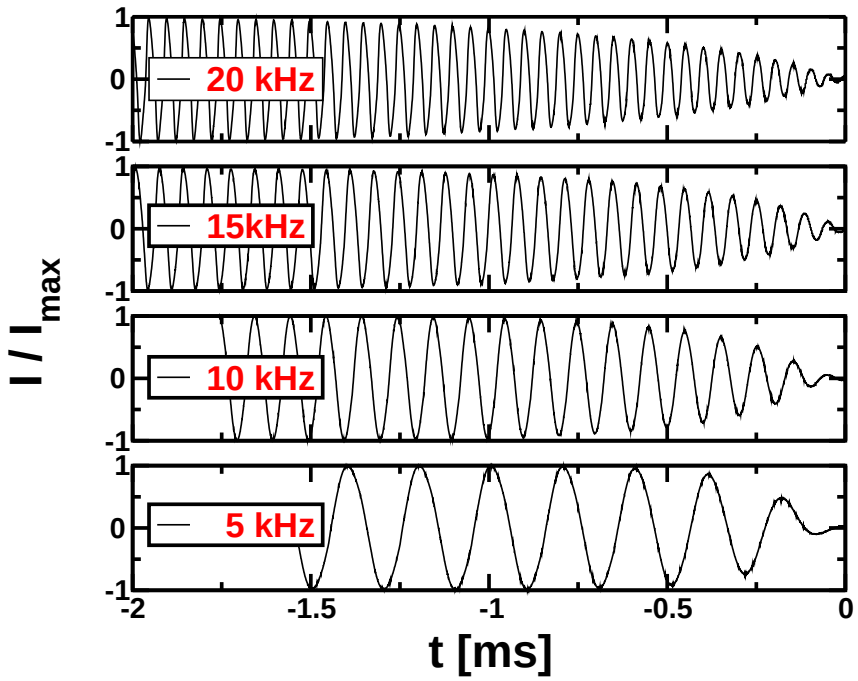

Figure 3.16: Variation of the electrical current close to the breakup when the frequency changes. The typical time of decrease of the current is shorter when the frequency is smaller. (η =7mPas, σ =1.8 mS/cm).

For simplicity the capacitance is taken constant which is a fair approximation according to the results of Fig. 3.15. The resistance divergence is due to the decrease of $r_{\min}$. The divergence of the resistance already explains the results of Fig. 3.16. Indeed, in terms of electrical impedances, the resistance dominates over the capacitance when:

$$r_{\min}(t) \ll \frac{\omega \varepsilon_0 \varepsilon_r r_s^2}{T\sigma} \tag{3.4}$$

assuming a cylindrical neck. Since $r_{\min}(t)$ diverges one can always find a time t^* above which Eq. 3.4 holds. Depending on the value of $\omega\varepsilon_0\varepsilon_r r_s^2/(T\sigma)$, t^* is more or less close to the time of the breakup. In particular when the frequency of the voltage source increases, t^* decreases.
According to previous work on capillary breakup [64, 78], the late stage

of capillary breakup displays power law variation of the neck radius as a function of time. Depending on the physical balance of stress on the neck, different exponent are expected. Assuming that the resistance of the neck is linked to its shape the power law variations of the neck should reflect on the resistance variations: the divergence of the resistance at the break-up ($t = 0$) is modelled using:

$$R_n(t) = R_0 \times \left(\frac{t}{t_0}\right)^{-\mu}, \ \mu > 0 \tag{3.5}$$

R_0 represents the typical resistance of the neck inversely proportional to the conductivity $R_0 \propto 1/\sigma$ and t_0 is a typical time coming from the physics of the break-up. μ is the exponent of resistance divergence which is linked to the exponent of capillary breakup and the shape of the neck. The driving voltage is written as $U_0 \sin(2\pi f t + \phi)$ where ϕ is an arbitrary phase and the equation followed by the electrical charge q in the capacitance is simply given by the differential equation:

$$R_n(t) \times q'(t) + \frac{q}{C} = U_O \times \sin(2\pi f t + \phi) \tag{3.6}$$

Using $q_0 = CU_0$, $\tau = 1/(2\pi f)$ the equation is written using the dimensionless variables $Q = q/q_0$, $T = t/\tau$:

$$\chi^{1+\mu} \times T^{-\mu} \times Q' + Q = \sin(T + \phi) \tag{3.7}$$

with a dimensionless number:

$$\chi = 2\pi f \times (R_0\, C\, t_0^{\mu})^{1/(\mu+1)}$$

This equation is solved numerically using a Mathematica routine. The interesting value is the charge Q at the breakup. This charge depends of course on the phase ϕ but we will focus on its maximal value $Q_{\max}$ for the different phases. The charge kept in the drop at the breakup for a given phase ϕ will thus be $0 \leq |Q| \leq Q_{\max}$. The charge at the break-up is distributed between 0 and $Q_{\max}$; in these conditions, because the phase is *a priori* randomly distributed the charge will be random leading to erratic behaviour after the break-up. It is clear that if $Q_{\max} \ll 1$ the drop charge is almost zero after the break-up. The results of the calculation are given in Fig. 3.17 showing that the maximal charge is significant for $\chi < 1$ and negligible for $\chi > 1$ The variations of $Q_{\max}$ do not depend strongly on the choice of the expo-

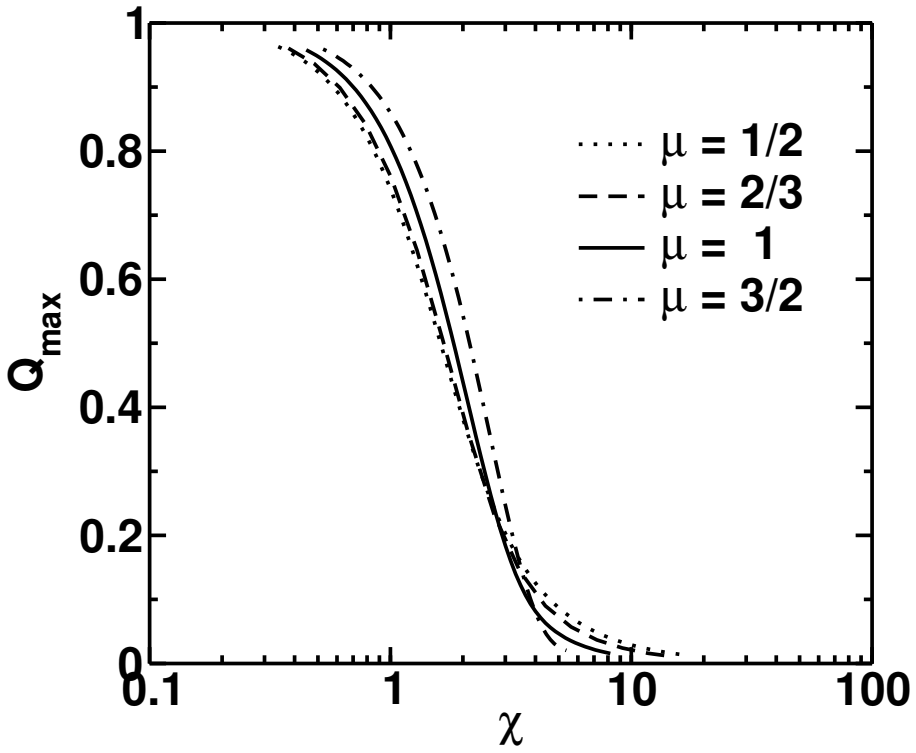

Figure 3.17: Calculation of the maximal charge in the drop at the breakup according to Eq. 3.7 for different exponent of resistance divergence μ.

nent μ at least in the range where this parameter is expected (0.5 - 2). The only important ingredient of the model is thus the presence of a divergence, regardless to the exact way the divergence takes place.

3.4.3 Comparison with experiments

In addition to the charge, the model also provides the variation of the current by a simple derivation of the charge. In order to determine the value of the parameter χ the experimental measurements of the current are fitted using χ as a fit parameter for different exponent μ between 0.5 and 2. The quality of the fit usually does not depend strongly on the value of the exponent μ and the experiments are well fitted by the model as displayed in Fig. 3.18. In most of the cases, for each $\mu \in [1.0, 1.3]$ a corresponding χ can be found that provides an excellent fit of the experimental data as displayed in Fig. 3.19 for the same electrical measurement at 15 kHz. The decrease

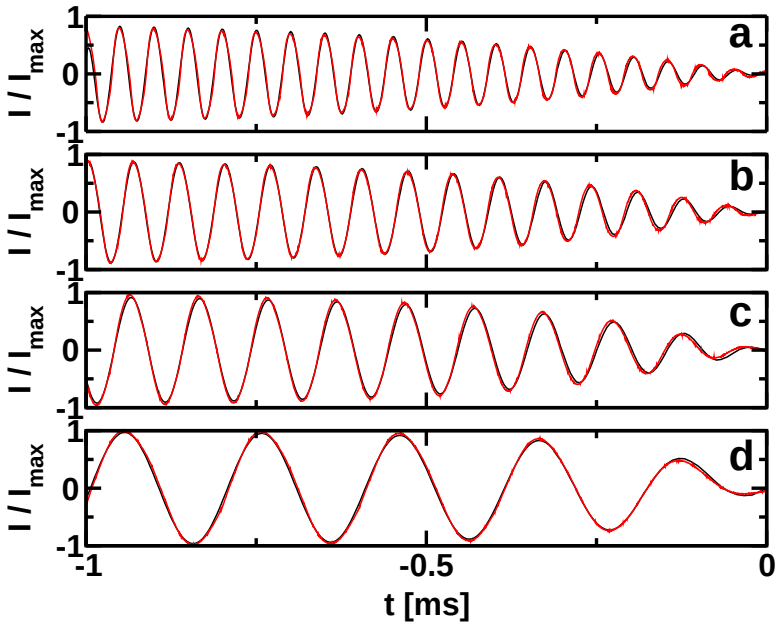

Figure 3.18: Comparison of the experimental data and the fit obtained from the model using μ=1 showing that the fit and the experimental data are undistinguishable.

to zero is well described by the resolution of the equation: the fit and the experimental data are almost indistinguishable. The parameter χ does not depend significantly on the choice of the power law exponent μ. A relatively large range of exponent can be used to fit the data; the model is thus not very sensitive to the divergence as expected from the resolution of the equations in the previous section. However, a relation independent on μ exists between χ and the frequency f of the voltage source: it follows a linear scaling with the frequency of the voltage source all the other parameters being constant:

$$\chi \propto f$$

The values of χ obtained from fits of experimental current obtained for different mixtures have been plotted as a function of the applied frequency leading to Fig. 3.20 including the error bars obtained for the different exponents. The expected linear behaviour as a function of the frequency of the voltage source

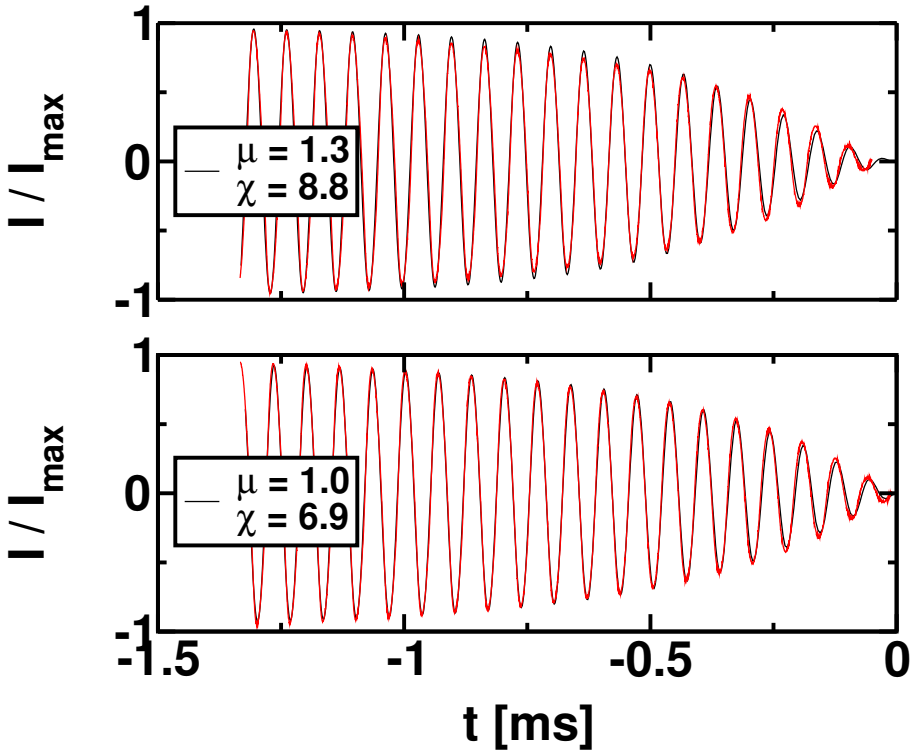

Figure 3.19: Two different fits on the same electrical signal. Different values of the expoent μ give different values of χ giving the error bars in the determination of χ. $f = 15$ kHz.

is obtained for all the mixtures used. When the conductivity σ of the drop increases, the parameter $R_0 \propto 1/\sigma$ decreases which as a consequence decreases the slope as observed. Concerning the effect of viscosity, increasing the viscosity increasing t_0 which as a consequence increases the slope. Finally the oscillations stop close to the horizontal line $\chi \approx 1$ which correspond to the point where the charges kept in the drop becomes important. Our model captures thus correctly the physics of the breakup: the most important ingredient is the divergence of the resistance more than the exact value of the exponent. An accurate determination of the exponent of the resistance is not possible experimentally. The method used here give a range of μ= 1.0 - 1.3 which can be compared to the expectations coming from the hydrodynamics of the pinch-off.

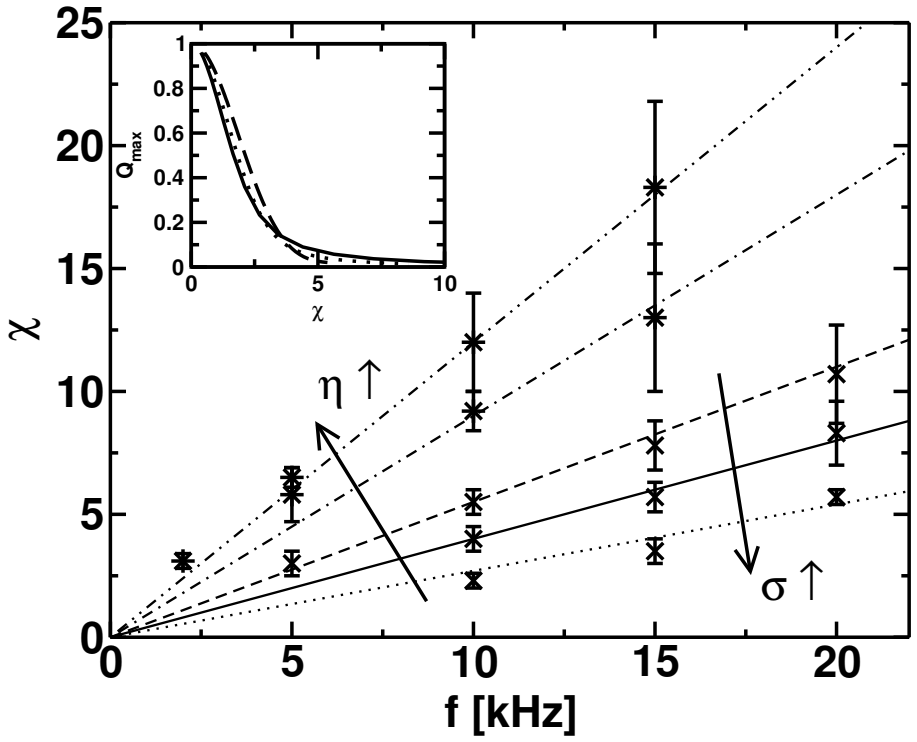

Figure 3.20: Values of χ obtained for different frequencies on several solutions. For a fixed solution the linear behavior as a function of the applied frequency is correctly observed within the accuracy of the experiments (* : $\eta = 80$ mPas, $\times$: $\eta = 7$ mPas, from top to bottom $\sigma \in [1.0, 2.3]$ mS/cm and $\sigma \in [0.8, 1.8, 7.1]$ mS/cm. Inset: $Q_{\max}$ as a function of χ.

3.4.4 Power law exponent at the pinchoff

Hydrodynamics exponents

As discussed above, the electrical measurements did not allow for an exact determination of μ. In order determine a correlation between the divergence of the resistance and pinchoff dynamics we studied with a high-speed camera the break-up process of different liquids at different frequencies of the voltage source. The spatial resolution on the images was 64×256 pixels at 16000 fps which was not enough to resolve fully the latest stage of the break-up. The minimal radius of the capillary neck has been measured on the images. We studied the influence of a change in viscosity at 10 kHz and approximately constant conductivity and the influence of frequency at constant viscosity. In

order to have a high time resolution this latter case was studied on a viscous drop. Moreover it is important to notice that we are not interested in the exponent of the dynamics at the latest stage of the capillary breakup but at a time-scale of order $1/f$ (≈ 0.05 to 1 ms). The capillary breakup in air or in inviscid fluids was studied earlier by several authors [64, 79, 80, 81]. They found power law behaviours for the minimal radius of the neck as a function of time $r_{\min} \propto t^{\nu}$; the regime of breakup (and the exponent ν) is determined by the dimensionles Oh number equal to $\eta/\sqrt{\rho r_{\min}\sigma}$. Various exponents ν for the breakup are found: the neck radius shrinks to zero in time as $r_{\min} \propto t^1$ in the case of a balance between capillarity and viscous dissipation ($Oh > 1$ – Egger's universal law [82]) or $r_{\min} \propto t^{2/3}$ in the case of a balance between capillarity and inertia ($Oh < 1$) [83]. Since the radius shrinks during the breakup a wide range of Oh is obtained during the pinchoff. Usually both regimes are observed. In the beginning of the experiment, Oh is initially small and grows above 1 in the time of the pinchoff. The transition $Oh = 1$ is obtained when the minimal radius fulfils

$$r_{\min} \sim \frac{\eta^2}{\rho\gamma}$$

Using water in air the crossover is obtained when $r_{\min}$ is smaller than one nanometer. Therefore it is not observed as shown by Burton *et al.* [81]. For glycerol at 100 mPas this radius is significantly increased. For breakup in air the crossover would be close to the millimetre. However the problem we are dealing with here is the breakup in a surrounding fluid which has also been studied by different authors [84, 85, 86]. In this case the behaviour depends on the different viscosities and in particular on the ratio of the viscosities of the two fluids [84]. In the present experiments this ratio goes from 2/5 (pure water in oil) to 80/5 (Glycerol-water 80:20 in oil). In the Stokes regime a law in $r_{\min} \propto t^1$ is recovered with a universal bi-conical shape of the neck [84, 86]. It can be shown that inertia is then always negligible [78]. The system exhibits a transition from the viscous thread to the Stokes flow or from the potential flow through the inertial-viscous thread to the Stokes flow. In those conditions the exponent is expected to crossover from 2/3 to 1 close to the experimental observations in the latest stage of the breakup (see inset of Fig. 3.21). At low viscosity the fluid behaves as inviscid on the time scale we are looking; for the viscous case the viscous thread regime is obtained. This is confirmed by numerical simulations (Volume of Fluid, see

below in Fig 3.21) which gives the correct exponents for simulation parameters comparable to the one used in the experiments.

"Electrohydrodynamic" exponent

It is clear that the exponent we are studying is not directly the exponent of the hydrodynamical breakup ν. The exponent of the electrical resistance μ depends on ν and on the shape of the neck:

$$R_n \approx \frac{1}{\pi\sigma r_e}\int \frac{\mathrm{d}z}{r(z)^2} \tag{3.8}$$

For various shapes different exponents are expected:

1. for a cylindrical neck, the relationship between the exponent of the hydrodynamics ν is simply linked to the exponent of the resistance divergence μ by: $\mu = 2\nu$.
2. for a conical neck, the relationship becomes $\mu = \nu$ [81, 87].
3. for the universal shape of Egger's solution the exponent of the resistance would follow $\mu = 3/2$.

Moreover the hydrodynamics crossover will be reflected in crossover for the μ. We used the experimental data to find the contour $r(z)$ where z is the height and r the neck radius. Then we calculated the resistance of the neck via:

$$R_n \approx \frac{1}{\pi\sigma r_e}\int_{r<r_e} \frac{\mathrm{d}z}{r(z)^2} \tag{3.9}$$

both for the experimental data in the viscous and inertial case and for the simulations in the viscous case. The results are displayed in Fig. 3.21. The inset displays the variations of the minimal radius of the capillary neck which is close to the expectations: a power law of 2/3 for the inviscid fluid and 1 for the viscous. The resistance calculation shows a nice agreement between the numerical results and the experiments. The resistance does not vary universally as a simple power law but the slope of the curves is between 1 and 1.5, consistent with the exponents obtained from the fit of the electrical current. The measurement of the divergence of the electrical resistance of the capillary neck gives then the same results with the two methods, with roughly the same accuracy.

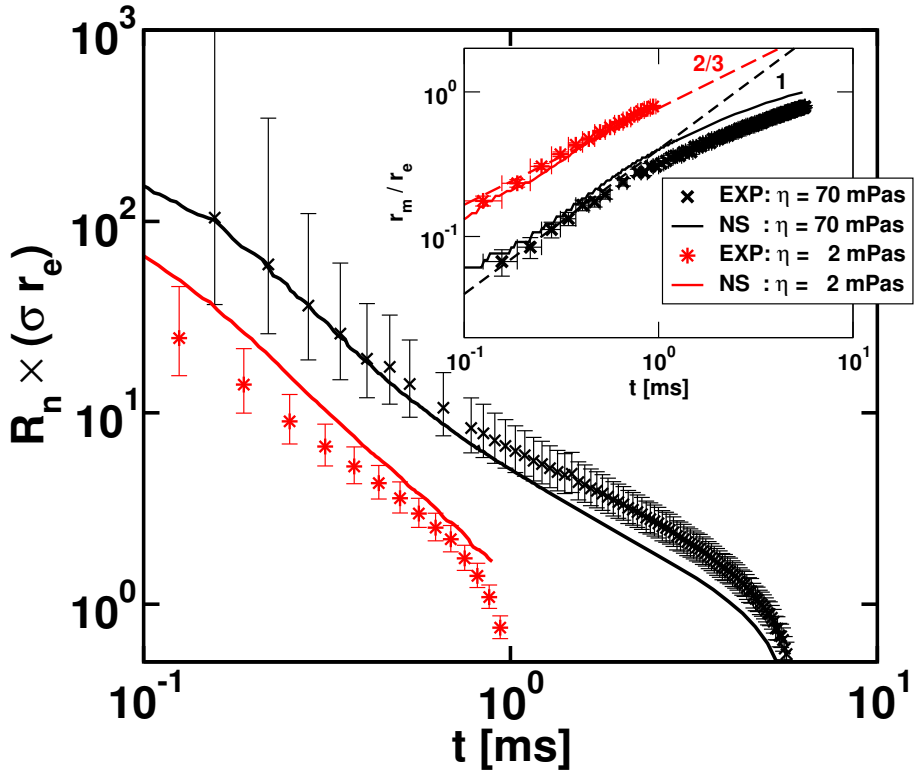

Figure 3.21: Divergence of the resistance of the capillary neck. Experiments and numerical simulations for two viscosities. The errors bars come from the lack of accuracy in the determination of the radius of the neck when its sizes reaches the pixel size of the camera. Inset: the power law exponent for the decay of the minimal radius are recovered for the experiments and the numerical simulations.

3.4.5 Influence of electric field on the pinch-off.

The influence of the frequency of the voltage source on the break-up has been studied briefly. The idea was to determine if the voltage frequency ω had an influence on the dynamics of the breakup itself. These questions have been studied on the same drop changing simply the frequency of the voltage source in order to be in the oscillating regime at 10 kHz and out of this regime at 1 kHz. The pictures of the breakup were recorded at 16000 fps and are displayed in Fig. 3.22. The pictures show a huge difference between the two situations. Indeed in the 1 kHz signal a long thread is produce which is not the case at 10 kHz. The difference is underlined when the minimal radius of

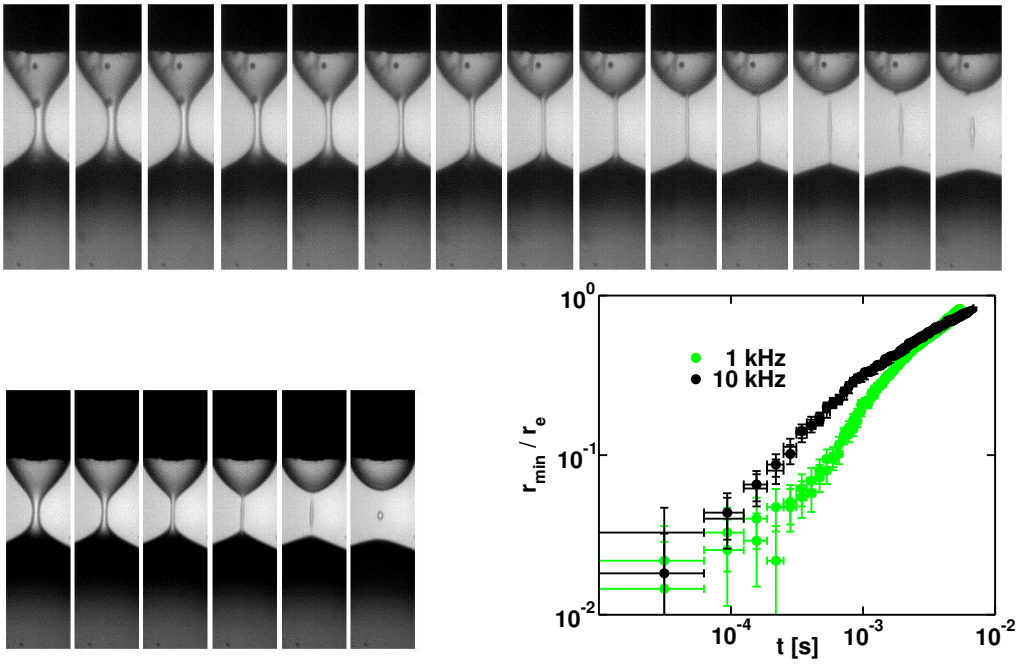

Figure 3.22: Pinchoff at 1 kHz (top snapshots), and at 10 kHz (bottom snapshots). The time between two successive pictures is 62 ms. The log-log graph represents the minimal neck diameter as a function of time. The presence of an electric field parallel to the axis of the neck has obviously an influence on the rupture of the neck.

the thread is plotted as a function of time in the two cases. There is clearly a difference in the two situations. The capillary neck seem to be stabilized for a longer time at 1 kHz compared to the situation at 10 kHz. There is thus a deviation to the classical capillary breakup in the presence of an electric field.

What could be the reason for the difference ? – The difference between 1 and 10 kHz is the presence of electrical charges in the drop after the breakup at 1 kHz. As we have previously seen at 1 kHz, the charges are frozen in the drop by the rapid change in the neck diameter. In the electrowetting system, there is no electrochemistry: the total number of charges present in the liquid volume is always zero. But in the presence of an electric field the charges are separated, the positive charges are for instance at the solid

surface and the negative charges close to the tip of the electrode. We have seen previously that at 10 kHz, 1 ms before the breakup the drop is discharged (more exactly the capacity is discharged) which means that no charges are left neither in the drop deposited on the surface nor in the droplet hanging at the tip of the electrode. No charges on each side of the capillary neck means that the capillary neck has been broken in the absence of electric field. On the other at 1 kHz some charges have been frozen in the drop and the opposite charges have been frozen in the drop hanging at the tip of the electrode. The breakup has thus involved electrical charges which could not flow through the neck (the value of voltage period is larger than the time-scale of rupture). There is thus an electric field along the neck in this case. Electric field have the property to stabilize liquid structures (see Mugele [88]). In Fig. 3.23) we present an example of the well-known instability of the contact line[1] which leads to the production of small drops at the periphery of the mother drop in which the voltage is applied. The necks bind the mother drop to satellites and satellites in cascade: the structures are stable for long times, at least much longer than time-scales expected from a pure capillary point of view. It is also known that a longitudinal electric field can stabilize a liquid jet [90] and also modify the way a drops falls from a tap [91]. This effect could then explain the long thread observed in our experiments at 1 kHz where electric fields are presumably becoming important compared to capillary forces. But it is also known that the stability of liquid cylinders is strongly influenced by electric fields [92] and depending on the electrical properties of the fluids (perfect dielectric / non perfect dielectric [93], charges [94]), the perturbation considered (axi-symmetric / non-axi-symmetric, wavelength of the unstable mode [95]) the stability limits can differ. The influence of the resistivity of the liquids used and the frequencies of the AC fields applied has also shown in some other set-up different regimes in the droplet breakup [96, 97]. All these elements may then complicate the analysis of the breakup and our simple electrical model and would make a promising subject for further investigations. For instance the electric field should influence in some regime of parameters via the surface stress the rupture exponents. It should be

[1]This instability has been observed in many experimental setups and its origin is still the subject of investigations. Coulomb explosion due to an excess of charge at the contact line is likely driving the mechanism. This effect could be linked to the instability observed in electrospraying of a rotating drop which shows similar structures [89]

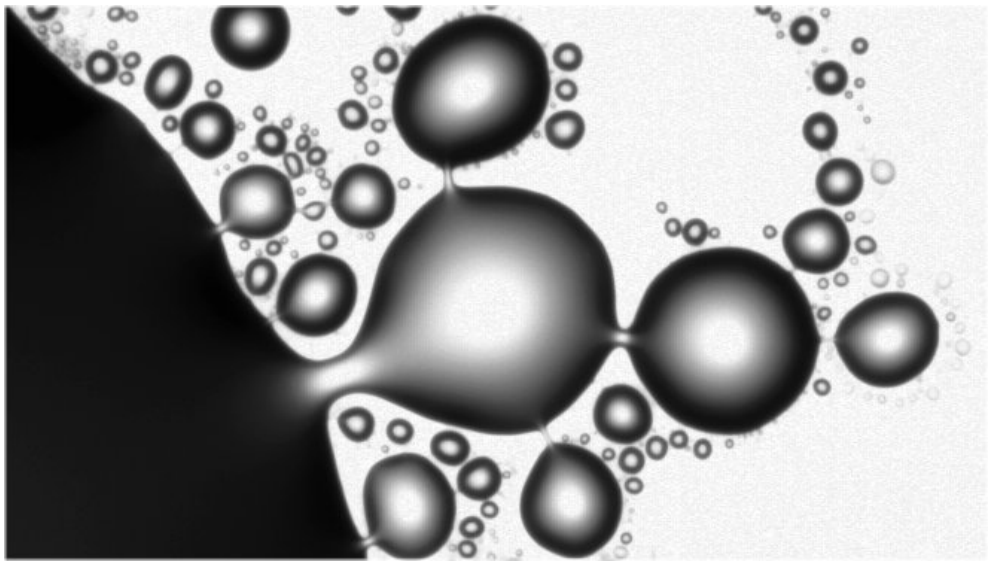

Figure 3.23: The instability of the contact line: the electric field is responsible for the stabilization of the liquid micostructure on timescales much larger than in a pure capillary frame.

noticed that in the cases we have presented here, the influence of the electric field on the breakup should be negligible since the exponents of the breakup are the one expected for the capillary rupture of free-surface flows.

3.4.6 Conclusions

During the breakup of the capillary neck under electrowetting conditions, the interplay of electrical and hydrodynamical effect determines the final charge of a drop. This has consequences on the oscillations expected from a geometric viewpoint: stable oscillations require a switch from Lippmann' angle to Young's angle at the breakup. When charges are kept in the drop the contact angle keeps its Lippmann's value: relaxation at Young's angle cannot occur and the oscillations are not stable.
We observed that two regimes occur depending on the dimensionless χ; the decay of the electrical current during the breakup is sharp at $\chi < 1$ and continuous at $\chi > 1$. The experimental observations of the electrical current show the importance of the divergence of the electrical resistance during the breakup. Measuring the electrical current it has been shown that the electrical resistance of the capillary neck diverges: the divergence is consistent

with a power law scaling with a typical exponent in the range 1 to 1.5.
This exponent is on the other hand consistent with the evaluation of the resistance of the capillary neck determined from the shape of the drop during the breakup and with expectations coming from the hydrodynamic analysis of capillary breakup.
The different regimes do not depend critically on the value of the power law exponent of the resistance. The electrical model captures thus correctly the physics of the interplay of electrical and hydrodynamic effects at the breakup.
Finally it has also been observed that the frequency of the electric field has an influence on the capillary breakup. This effect does not influence our analysis and would be an interesting subject of future investigation.

3.5 Hydrodynamics during stable oscillations

The oscillating area is well defined by the limits given by the static model however in the oscillating regime the oscillations do not look everywhere the same.

3.5.1 Intermittency: Experiments

The study of the time sequences corresponding to the stars of Fig. 3.7 has been performed. Two typical time sequences are found, depending on the position in the (U,d) graph. Close to the boundaries of the oscillating regime and especially in the vicinity of the threshold voltage, intermittency is observed as displayed on Fig. 3.24. The oscillations are bursted: for a certain time the oscillations are well defined and stop for a while. In conditions near the upper limit the drop switches between an oscillating state and a temporary disconnected state while near the lower limit the drop switches between oscillating state and temporary connected state. Far away from these boundaries, the sequence is stable and the frequency of the oscillations is well defined.

3.5.2 Modeling the intermittency

The intermittency is probably the result of the discharge at the pinchoff. As we saw earlier, in any range of electrical parameters, some charges (more

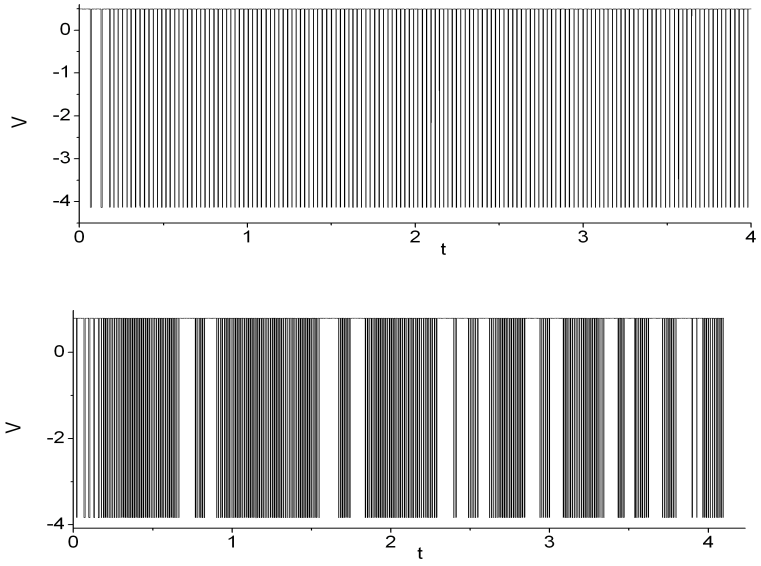

Figure 3.24: Time sequence of drop connection to the electrode in the oscillating regime: (Top) Stable oscillations at a well defined frequency, (Bottom) Intermittent oscillations close to the boundaries of the oscillating regime. For more details on the intermitency, see [98]

or less depending on the electrical parameter χ) are left in drop. Let us assume a viscous drop whose shape during the relaxation after the breakup is close to a spherical cap. Its contact angle is determined by its number of charges $Q < Q_{\max}$. If $Q = 0$, it is Young's contact angle. If $Q = Q_{\max}$ it is Lippmann's contact angle[2]. The drop will thus relax to a spherical cap of height $h(\theta(Q))$. The minimum h is obtained for a charge $Q_{\max}$:

$$h(Q_{\max}) < h < h(Q = O)$$

Let us assume now that we are in the regime of stable oscillations $Q_{\max} = \epsilon$ where ϵ is a small parameter. Since ϵ is small, $\theta(Q_{\max}) = \theta(Q = 0) - o(\epsilon^2)$ and $h(Q_{\max}) = h(Q = 0) - o(\epsilon^2)$. If the distance d is smaller than $h(Q_{\max})$, then for any phase of the voltage source we have $d < h(Q)$: the drop will always touch the electrode during the relaxation. Moreover the relaxation is driven by the wettability since the contact angle is Young's contact angle

[2]The link between Lippmann equation at fixed voltage or at fixed charge is simply given by the relation $q = CU$

(neglecting the small correction): the number of charges will not change the time-scale of the relaxation and the oscillations are stable.
On the other hand, for the case $h(Q_{\max}) < d < h(Q = O)$ the equilibrium height $h(Q)$ of the receding drop can be smaller or larger than the distance d. If it is larger, the drop will touch the electrode, if not it will not. Taking into account the leakage current through the insulating layer, the drop will discharge slowly and recede to the tip with a time-scale depending on the leakage current and the initial charge, source of the intermittency.

For any value of $Q_{\max}$ intermittency appears within a certain range of d. This size of this regime is given by $Q_{\max}$. In those conditions, we expect erratic oscillations when the distance is larger than $h(Q_{\max})$ which means *close to the horizontal line* $d = h(U_0 = 0)$. The extension of the erratic area depends on the value of $Q_{\max}$ and thus on the value of the electrical parameters: the larger $Q_{\max}$ the more intermittency will be observed.

Consequence – When $Q_{\max} \approx 1$ the intermittent area is extended all over the oscillating regime: it is the discharge through the insulating layer which drives the relaxation. The electrical model presented above has thus the advantage to explain also the intermittency observed in the experiments at large χ without having to introduce any new assumption. Intermittency is thus a consequence of the incomplete electrical discharge through the capillary neck during the capillary breakup.

Note – Close to the transition non-linear dynamics phenomena are also expected. The analysis of the intermittency in terms of non-linear dynamics has not been performed: here we restricted ourselves to the macroscopic description of the intermittency. A non-linear dynamic analysis for the intermittency could be an interesting subject of future investigations.

3.5.3 Influence of viscosity

Phase diagram

The evolution of the frequency in the oscillating area is displayed in Fig. 3.25. The frequency increases with voltage as a result of an increase of driving force.

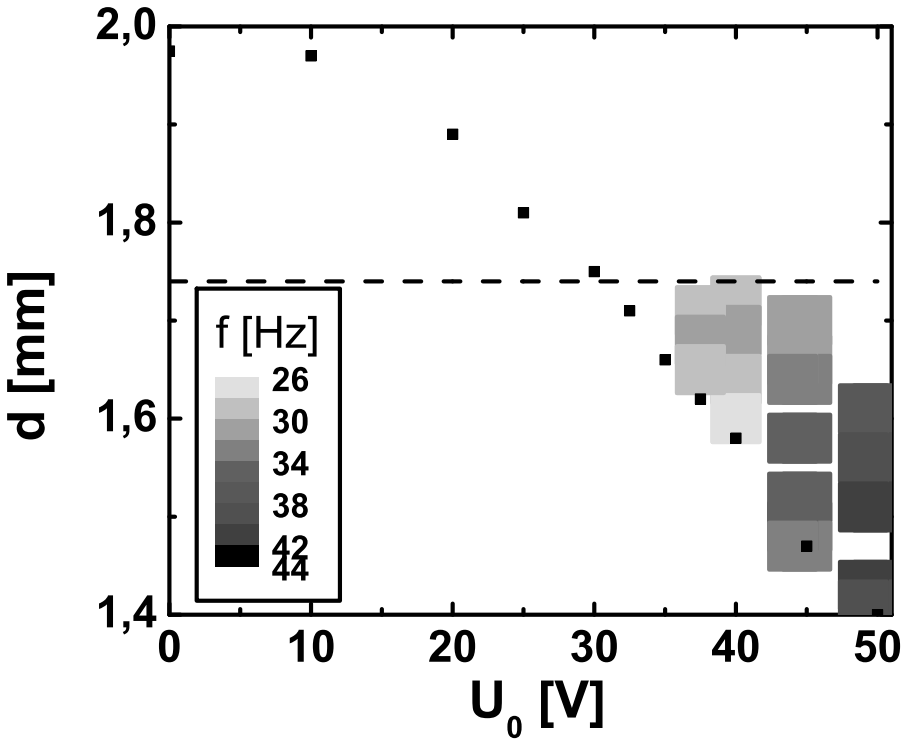

Figure 3.25: Variation of the frequency with the parameters d and U_0. The frequency has been measured on the stable oscillations displayed in Fig.3.7. ($V \approx 4\mu$L)

When the viscosity decreases, the phase diagram is modified by the effect of inertia (see Fig. 3.26). In this case the oscillations are also observed beyond the limits obtained by the static argument: Once initiated d can be increased above $h(\theta_Y)$: stable oscillations are still observed as a result of the inertial overshoot of the oscillating droplet: the maximal height of the drop during the oscillations $h_{\max}$ is larger than $h(\theta_Y)$. The oscillations stop for distance larger than $h_{\max}$. When the distance is decreased the oscillation start again when $d < h(\theta_Y)$. There is thus a dynamic hysteresis as the result of the inertial overshoot. The influence of inertia is clearly observed on the high speed movies (see Fig. 3.27 and 3.28) when the viscosity of the drop is varied.

Drop shapes during oscillations

In the viscous and in the inertial cases, the oscillating regime display three phases. In the connected state, the drop spreads with a contact angle close to

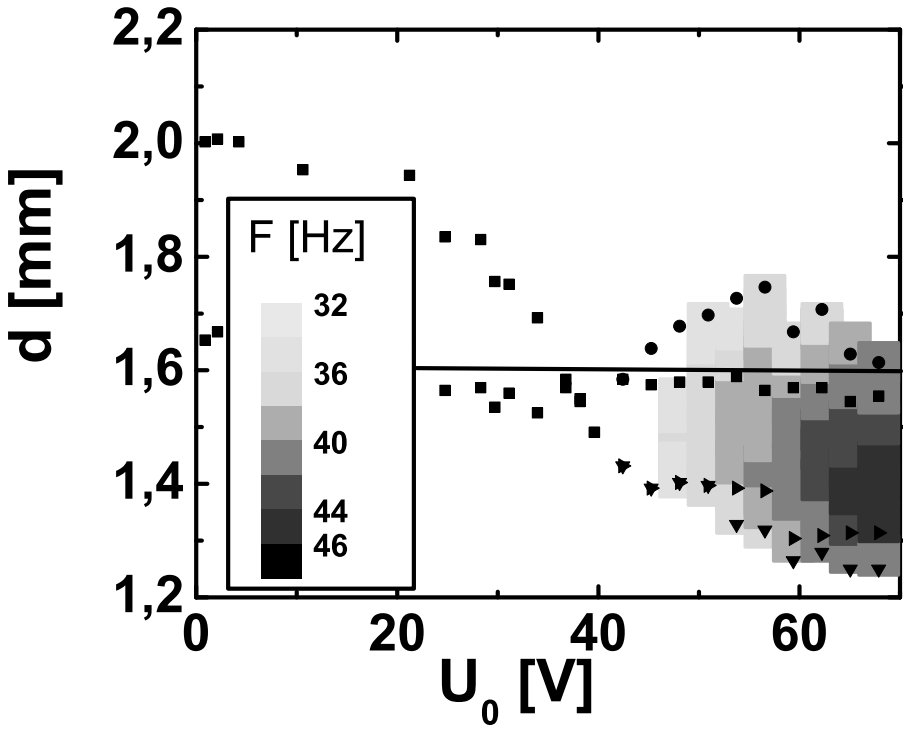

Figure 3.26: Variation of the frequency with the parameters d and U. The frequency has been measured on stable oscillations using stroboscope.

the Lippmann angle. The apprarent contact angle is a dynamic contact angle due to the speed of the contact line. In the disconnected state the contact angle of the drop has a large value close to Young's angle. The contact line is now receding and the contact angle is somewhat smaller than its value at equilibrium. The transition between connected to disconnected state involves the breakup of a capillary neck described in the previous section.
The oscillations of two drops at the same voltage and at the same AC frequency are studied using a high speed camera. The drop in the viscous case display a shape close to a spherical cap (Fig. 3.27) and its height does not exceed its maximal static height. The oscillation frequency is close to 20 Hz. On the other hand for a less viscous drop, the shape is far from a spherical cap: surface waves travel along the surface. The contact line in particular moves faster than the body of the drop. The frequency of the oscillations is close to 70 Hz which is much larger than is the previous case of the viscous drop. Moreover it can be shown that the frequency is almost independent on

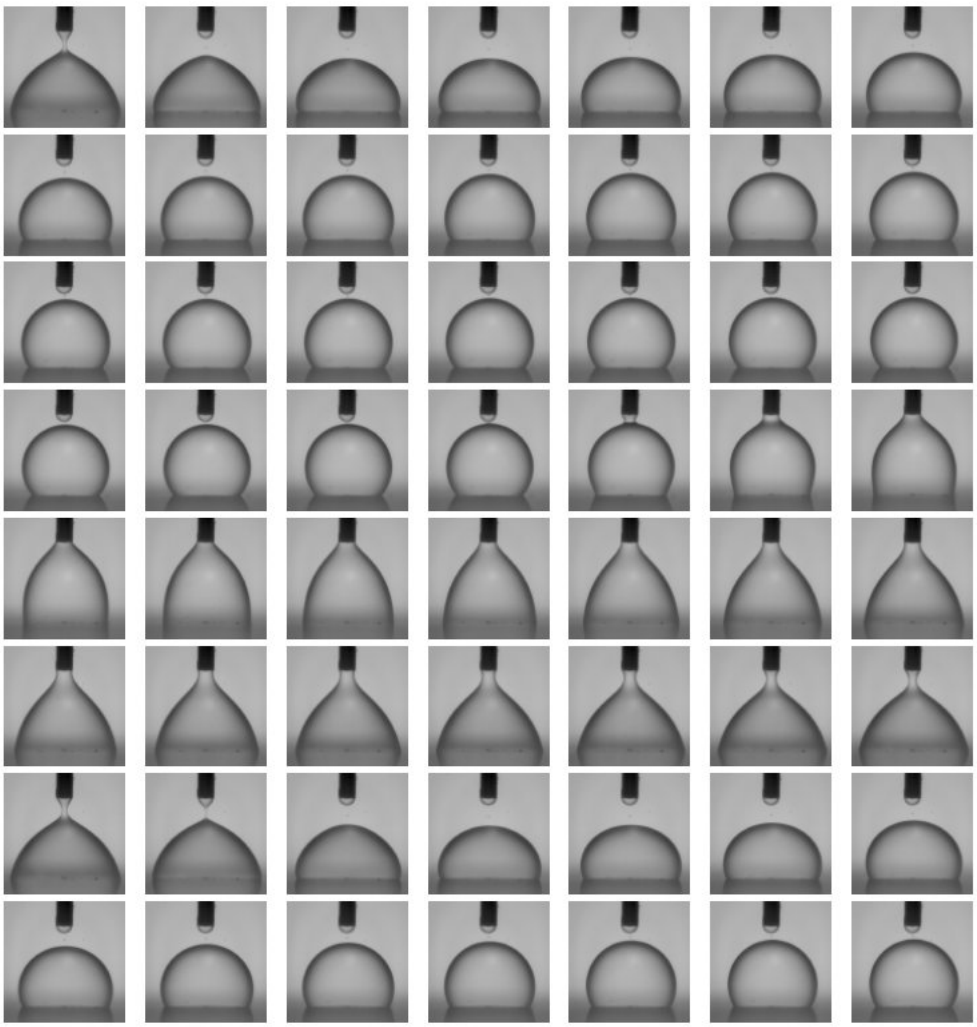

Figure 3.27: Oscillations of a viscous drop $\eta \approx 80$ mPas in a surrounding fluid ($\eta = 5$ mPas). The drop shape is spherical ($V \approx 1\mu$L, Oh ≈ 1). The frequency is about 20 Hz.

the conductivity of the drop, but depends strongly on drop size: the smaller the drops the faster they oscillate. Hence oscillations dynamics is not a function of the electrical properties but rather a function of the hydrodynamical parameters of the drop.

Discussions

Influence of physical parameters The frequency variations obtained here are in qualitative agreement with the expectations; we will now try to

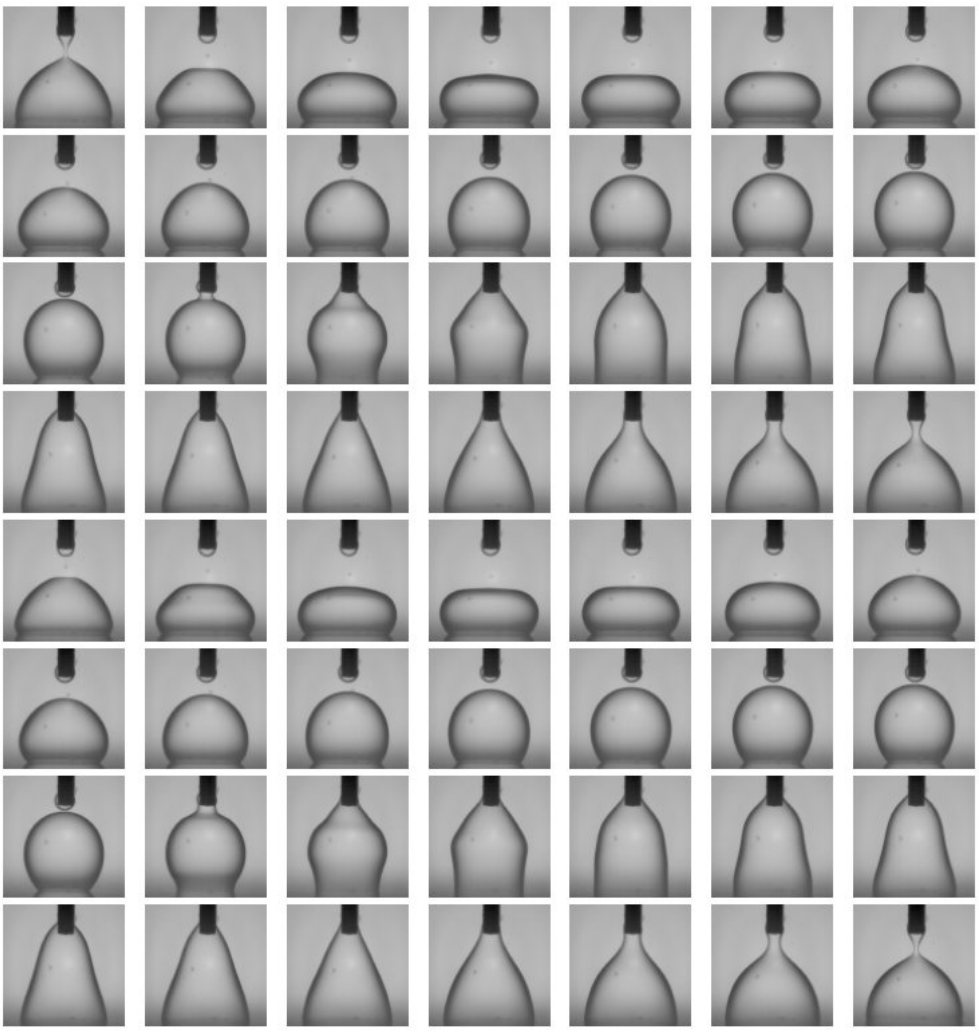

Figure 3.28: Oscillations of a non-viscous drop $\eta \approx 3$ mPas in a surrounding fluid ($\eta = 5$ mPas) in the same conditions as in Fig. 3.27. The drop is defomed by inertia ($V \approx 1\mu$L, Oh $\ll 1$). The frequency is close to 71 Hz.

discuss the values of the frequencies. Three physical phenomena are present in the oscillations; capillarity, inertia and viscous dissipation for a drop of size r_0, surface tension γ, viscosity η, density ρ. The dynamics of the oscillations is determined by the balance of these forces represented by dimensionless numbers. The capillary number Ca compares the influence of viscosity and capillarity:

$$\mathrm{Ca} = \eta v/\gamma \tag{3.10}$$

where v is the typical speed of the motion. To compare the effects of capillarity to inertia, the Weber We number is used:

$$\mathrm{We} = \rho v^2 r_0/\gamma \tag{3.11}$$

and the Reynolds number Re compares the effects of inertia and viscosity:

$$\mathrm{Re} = \rho v r_0/\eta \tag{3.12}$$

One of the drawback of all these numbers is that their evaluation requires the input of a typical speed v which is in our experiments the result of the dynamics. In order to solve this problem, one would like to make the speed disappear using combinations of these numbers. Doing so, one can write the speed as a function of the Weber number:

$$v = \sqrt{\frac{\gamma \mathrm{We}}{\rho r_0}}$$

Reporting this speed in the capillary number, one obtain:

$$\mathrm{Ca} = \frac{\eta}{\sqrt{\gamma \rho r_0}} \times \sqrt{\mathrm{We}}$$

The number $\eta/\sqrt{\gamma \rho r_0}$ is the Ohnesorge number Oh, that is besides used to determine the regime of rupture of a capillary neck as already described above. The same number arises because the same physical ingredients are relevant: inertia, capillarity and viscous dissipation.

Evaluation of Oh – In our two previous experiments, the Ohnesorge number can be simply evaluated taking the drop size, surface tension and viscosity and densities. In Fig. 3.28, Oh ≈ 0.05 while in Fig. 3.27, Oh ≈ 1 which is in agreement with the shapes observed during the oscillations. When Oh $\ll 1$ the oscillations are the result of the balance of inertia and capillarity only. Since the capillary term is balanced by inertia, one has

$$\mathrm{We} \approx 1$$

This leads to a frequency of the oscillations F obtained by taking $v \approx r_0 \times F$:

$$F \approx \sqrt{\frac{\gamma}{\rho r_0^3}}, \qquad \text{for Oh} < 1$$

The evaluation is close to 100-200 Hz which is sligthly higher than the observations but still in the correct order of magnitude. The expression of F is the one also obtained by looking at the frequency of an inertial surface wave of wavelength equal to the drop size (first mode). This value is independent on the viscosity since inertia is the opposing force.
On the other hand when Oh > 1 the oscillations are the result of the balance of capillarity and viscous dissipation. In this situation Ca ≈ 1 which leads to:

$$F \approx \frac{\gamma}{\eta r_0}, \qquad \text{for Oh} > 1$$

In this case the frequency decreases with increasing viscosities and correspond to the situation of viscous damping of a perturbation of a capillary surface of wavelength equal to drop size (first mode). No experimental data correspond to this situation but the "viscous drop" we have seen corresponds to Oh ≈ 1. The evaluation of the frequency at Oh $= 1$ by viscous dissipation or inertia gives here a value of order 100 Hz also slighlty higher than the observations but still in the correct order of magnitude[3]. The Ohnesorge number seem to underestimate slightly the viscous dissipation. However it gives a good indication of the regime of oscillations.

Conclusions The dimensionless number which determines the shape of the drop during the oscillations is thus the Ohnesorge number. The evaluation of this number gives an idea on the variations of the frequency as a function of Oh. Indeed, at small Oh the frequency does not depend on η and thus on Oh while at large Oh the frequency changes as 1 / Oh. The crossover is obtained at Oh $= 1$. This is summarized in Fig. 3.29.

3.5.4 Numerical simulations

In order to study the previous arguments in more details, some numerical simulations have been performed for different values of the parameters. We used a commercial numerical code CFD-ACE which runs in the Volume of Fluid (VOF) package.

[3]In other systems (impact of drop) the crossover regime has been obtained experimentally close to 0.1 [99] which is close to our experimental results where inertia is vanishes at Oh $= 1$

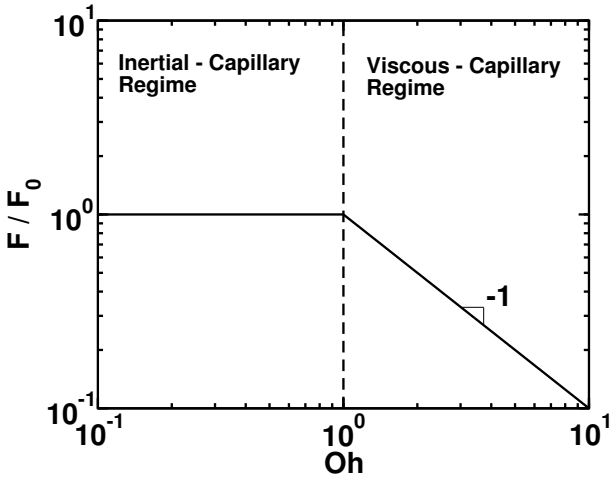

Figure 3.29: Expectations of the frequency variations according to the variation of the Oh number. A power law $F \propto \mathrm{Oh}^{-1}$ is expected for $\mathrm{Oh} > 1$. $F_0 = \gamma/\eta r_0 = \sqrt{\gamma/\rho r_0^3}$

Conditions of the simulations

The system is represented by a box of roughly 75 × 75 cells in an axisymmetric configuration (see Fig. 3.30). The electrowetting effect is modelled only by its influence on the wetting properties: when there is a contact between the drop and the electrode, the contact angle is set to Lippmann contact angle varying from 50 to 90°. As soon as the drop is disconnected the contact angle is set to Young's contact angle (140°). For simulation stability, the contact angle on the electrode is 45°at the bottom and 90°on the side. A no-slip boundary conditions is applied on the walls of the cell in non-wetting conditions (180°contact angle). The surrounding fluid (fluid 1) is oil with viscosity 5 mPas and density 0.9. The drop (fluid 2) has a viscosity ranging from 2 mPas to 70 mPas close to the viscosities used in the experiments. The surface tension of the fluid 2 in 1 is 38 mNm.

Results: Oscillations

The shape of the drop during the oscillations is well rendered by the simulation as displayed in Fig. 3.31 and 3.32. In particular the inertial effects are correctly reproduced and can be compared to the experimental observations. The viscous drop remains almost spherical while the non viscous drop un-

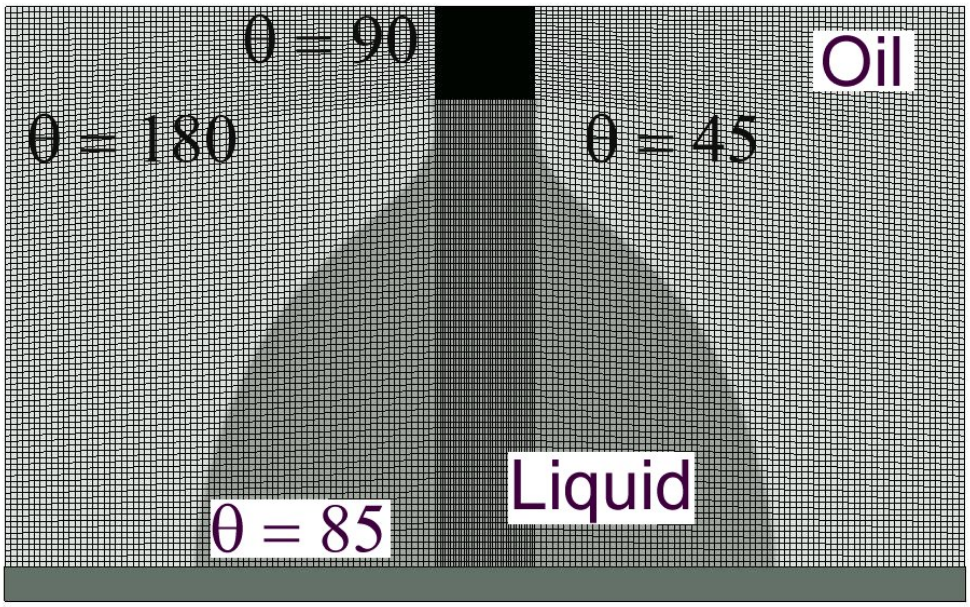

Figure 3.30: Grid used for the numerical simulations.

dergoes large deformations. The viscous drop correspond to Oh $\ll 1$ while the non-viscous drop is at Oh $= 1$. The observed features like the inertial waves are thus obtained for the correct value of the Oh number which is then confirmed to select the regime of oscillations.

Comparison with experimental data

The connected and disconnected times t_{ON} and t_{OFF} have been measured for a microlitre viscous drop on the simulations as a function of distance and contact angle and are displayed in the Table 3.1. The error on the values given below is about $\pm$ 1 ms due to the error on the determination of the breakup time. At fixed distance t_{ON} increases when the contact angle increases: this is expected since the driving force of the motion decreases. At fixed contact angle, t_{ON} decreases when the distance increases. The driving force is constant but the neck break earlier.
On the other hand, at fixed distance t_{OFF} is almost constant: the driving force of the relaxation is constant since every runs have been performed at fixed θ_Y which explains this effect. At fixed contact angle, t_{OFF} increases with the distance: the drop has to relax more to touch a higher electrode.

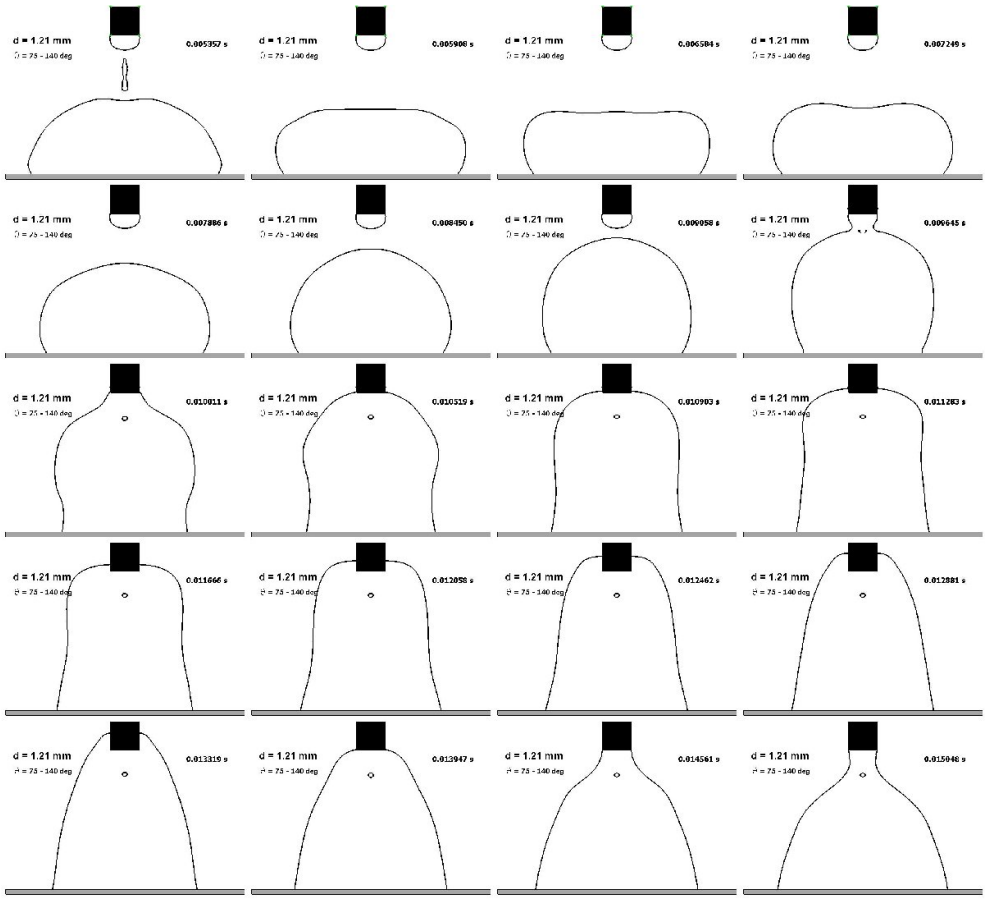

Figure 3.31: Numerical results for the drop dynamics during the oscillations. Inertia-capillary oscillations.

All these numerical results are thus in qualitative agreement with the expectations and the experimental observations. Moreover the variation of the oscillations frequency $1/(t_{\mathrm{ON}} + t_{\mathrm{OFF}})$ is of the order of the values obtained experimentally for the same drop. A direct comparison is however difficult since the times of the connected state and disconnected state vary strongly in the numerical simulations as a function of d or θ. The idea here is not to obtain a full quantitative agreement between the numerical simulations and the experiments but to reproduce the observed phenomena qualitatively. This allows us to conclude that a contact angle switch reproduces the experimental observations obtained when the switch is electrically induced. In this case the oscillations are obtained regardless of the complex scenario at the breakup which acts here simply as a trigger of the contact angle modula-

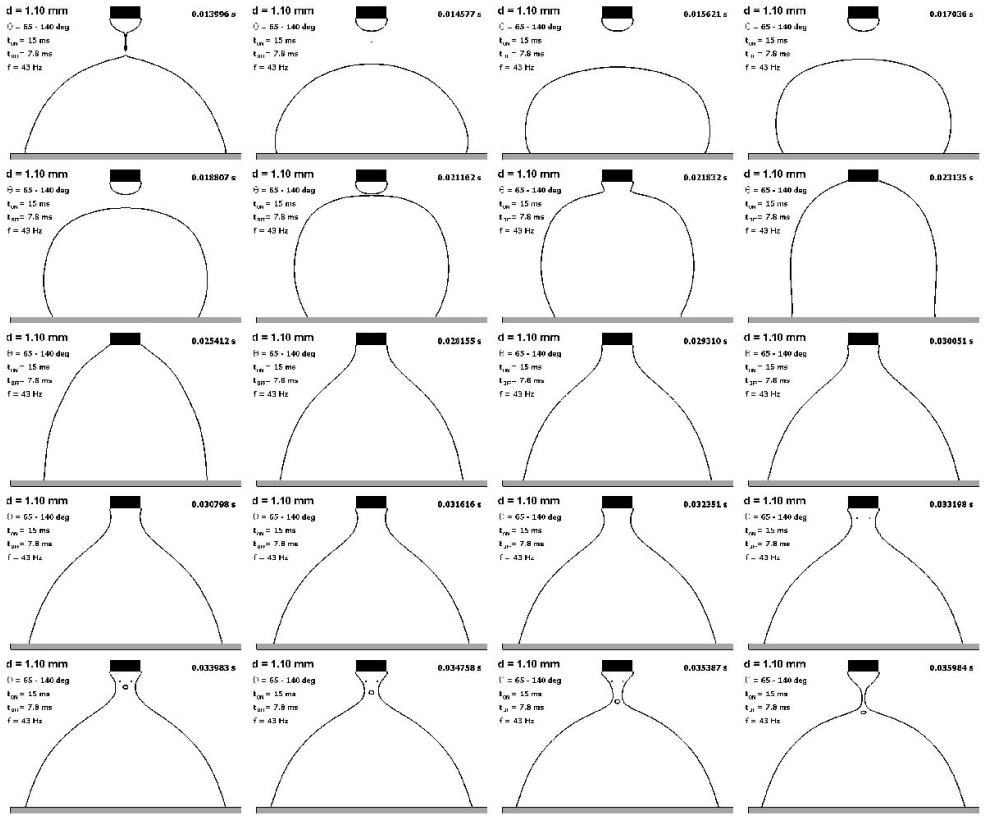

Figure 3.32: Numerical results for the drop dynamics during the oscillations. Viscous-capillary oscillations.

tion. In this situation of course, the simulation can not explain the unstable oscillations nor the electrical process at the breakup.

3.5.5 Application to mixing

The large amplitude oscillations obtained in the oscillation regime are an interesting property for drop mixing at small scales. Indeed mixing in these confined system is an issue: the Reynolds number being usually small the flows are usually reversible and the mixing is difficult. Some other electrowetting- based systems for drop mixing have been proposed by other authors [100, 101] based on drop motion on arrays of electrodes. Here it is not necessary to use an additional patterning by electrode since the oscillations will act as the source of the mixing. As a proof of principle we show the mixing of a microlitre water-like drop presented in Fig. 3.33. In the begining,

θ (deg)	ON/OFF	d (mm)					
		0.90	1.00	1.10	1.15	1.17	1.20
50	ON	40					
	OFF	7					
65	ON	∞	51	14	13	13	9
	OFF		6	8	9	10	13
75	ON		∞	25	16	14	
	OFF			8	9	10	
85	ON			∞		32	
	OFF					10	

Table 3.1: Numerical simulations results: time in the connected state (ON) or disconnected state (OFF). The times are in ms

a drop of water and dye is merged with a drop of water and glycerol. The fluorescent dye is thus at the top of the merged drop. The voltage is applied and the drop oscillates at about 80 Hz, in the inertia-capillary regime: mixing is obtained in about two secondes, at least 2 orders of magnitude faster than the diffusive mixing.

Downscaling

Downscaling is a constant concern in microfluidics. How does our mixing device behaves when the sizes shrinks ? We have seen above that two regimes of stable oscillations are observed depending on the value of the dimensionless number Oh $= \eta/\sqrt{\rho\gamma r}$. When Oh is larger than 0.1 the oscillations are capillary-viscous while they are capillary-inertial at Oh < 0.1. For a water drop Oh $= 1$ is reached at

$$r = \frac{\eta^2}{\rho\gamma} \approx 10^{-6}\text{m}$$

The drop size can decrease up to the micron and the mixing will still be capillary-inertial driven. The frequency of the oscillations is then given by the balance of inertia and capillarity which leads to and increasing frequency with a decreasing drop size $F \approx \sqrt{\gamma/(\rho r^3)}$. This result holds for low viscosities but for a viscous drop of glycerol at 100 mPas, the crossover in size is at 1

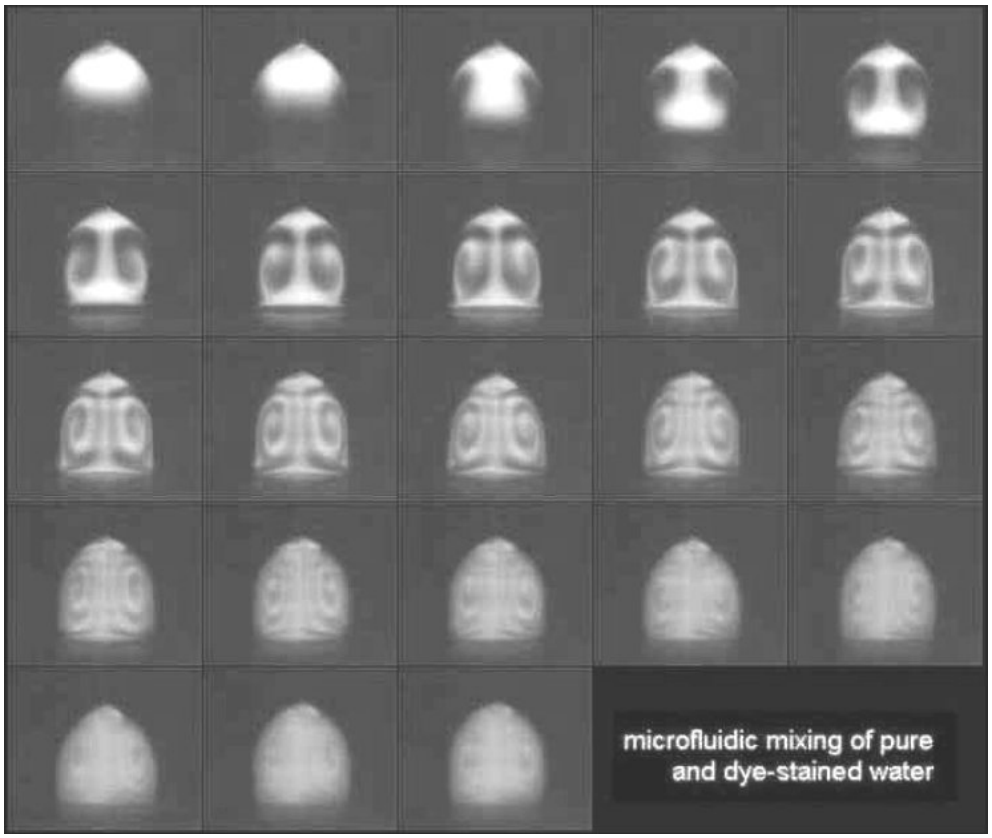

Figure 3.33: Microfluidic mixing using an oscillating drop. An heterogeneous drop (Water and dye at the top, water and glycerol at the bottom) oscillates at 80 Hz leading to full mixing in about 2 s, 100 times faster than the diffusive mixing. Experiment done by Dagmar Steinhauser (See Steinhauser [102].)

cm ! For glycerol independent of the size the oscillations will be capillary-viscous. In this situation the speed is determined by the capillary speed and the mixing efficiency is expected to decrease due to the decrease of surface waves amplitude. But mixing is still expected: indeed there is an asymmetry in the oscillations between spreading and receding which makes the flow in the drop irreversible. In the absence of this asymmetry the mixing should vanish due to flow reversibility.

3.6 Conclusions

Experiments – An oscillatory regime has been found in a simple electrowetting experiment and a static model based on the stability of the capillary neck is found to be in good agreement with the experimental observations. For each drop size a threshold voltage exists above which oscillations are present. The dependence of the threshold voltage as a function of neck and drop size is in good agreement with the simple static model as long as the volume of the neck is negligible with respect to the volume of the drop. The frequency of the oscillations is driven either by the hydrodynamical relaxation (fast oscillations) or by the electrical relaxation (slow oscillations). These two different regimes are determined by the dynamics of the capillary neck break up and by its electrical resistivity. When the hydrodynamic process of the break up is fast compared to the flow of charge through the neck some charges are left in the drop. The amount of charge is determined by the phase of the voltage at the very moment of the break up and can be considered as a random distribution. The charges have to flow through the insulating layer and the charge in the drop determines the time of drop relaxation. The oscillations thus obtained are erratic and slow. On the other hand, when the charge carriers have the time to flow out of the drop during the break up, the drop will be discharged at the moment of the break up and the oscillation process is hydrodynamically driven. The time-scale of such a relaxation are for the drop sizes we consider of the order of 10-100 ms which is in good agreement with experimental measurement of the frequency.

Comparison with previous systems – The oscillations presented here can be compared to the oscillations previously obtained in another set-up [47]. There is no fundamental difference between the two systems except the introduction of an additional length-scale in our case which is the electrode diameter.

Application – This simple system based on electrowetting is convenient to use in electrowetting based devices. The flow pattern inside the drop and the large amplitude variations of the free-surface can be used to promote mixing in drops for microfluidic devices.

The threshold voltage is a simple function of the ratio of electrode radius over drop size. Decreasing drop size and electrode size with this ratio constant will not modify the threshold voltage which is a nice property to mix small drops. Moreover the frequency of the oscillations is increasing with decreasing drop size which is an advantage when drop size usually reduces Reynolds number and then reduce the mixing possibilities.

Outlook – A number of problems are still unsolved and represent interesting subject of research. First the capillary breakup in DC and AC electric field can be studied. The influence of the electric field has been observed and one can study the influence of the electric field on the time of the breakup, on the power law exponents, on the shape of the neck... Then, the non-linear dynamics at the threshold of oscillations can be studied in order to give a better description of the transition. Finally the flow patterns in oscillating drops can be studied in order to find the optimum of mixing efficiency. This should be performed using a sheet of light and a non-diffusing dye in order to track the patterns on larger time-scales.

Chapter 4

Electrowetting-Actuation of fluid in microchannels Part 1: Statics

Jean-Christophe Baret, Michel Decré, Stephan Herminghaus and Ralf Seemann

Contents

4.1 Introduction

Fluid actuation in microchannels has received a lot of attention lately driven by the needs of microtechnology, e.g the lab-on-a-chip concept. The objective is to provide a device for substances manipulation in the liquid phase that is downscaled to the micrometer range, fast and reversible using a low power-consumption electrical source. Electrowetting seems to be a suitable solution. The actuation of liquid in closed channels has already been demonstrated using electrowetting [37], the fluid being actuated by the electrocapillary pressure induced by the electrical charges or between two parallel plates in the Pellat experiment [44]. Electrowetting is also nowadays commonly used as a way to manipulate droplets for digital microfluidic applications [57, 100, 101], the droplets motion being induced by an heterogeneous electrical field produced by patterned electrodes. Using patterned electrode on flat surfaces morphological transitions have been obtained between drops and liquid filaments [46, 48]. These transitions provide a nice tool for microfluidic since they fulfill the basic requirements of fluid actuation. In addition they are based on the active control of wettability which should provide the downscalability.

In the capillary framework, the interactions between substrate structures and liquid shapes have been initially studied by Cassie [9] and Wenzel [10] who first studied how the contact angle of a drop is modified by the roughness of the substrate. The effect of geometrical topographies on the wettability is now used to create superhydrophobic surfaces [14] which are fully non-wetting with contact angle of about 180 degrees. These surfaces have a technological interest to create self-cleaning surfaces. The interactions of solid structures and liquid is studied nowadays by several authors: Jopp *et al.* [15] showed recently that the wetting behaviour of a surface can be determined by free-energy calculation. Extensive studies have been performed in order to determine the liquid morphology on composite surfaces with patterns of wettability [19, 20, 18], with topographies [24, 21, 23] or combinations of wetting and topographic structures [26]. Seemann *et al.* [25] extensively studied experimentally and theoretically the case of open-air channels with a rectangular cross-section which has potential applications for eletrospray sources [103]. They predicted the possible morphologies for a liquid drop deposited on a groove in a complete morphological diagram and compared them

to the experimental observations (see Fig. 4.1). Contrary to the case of flat

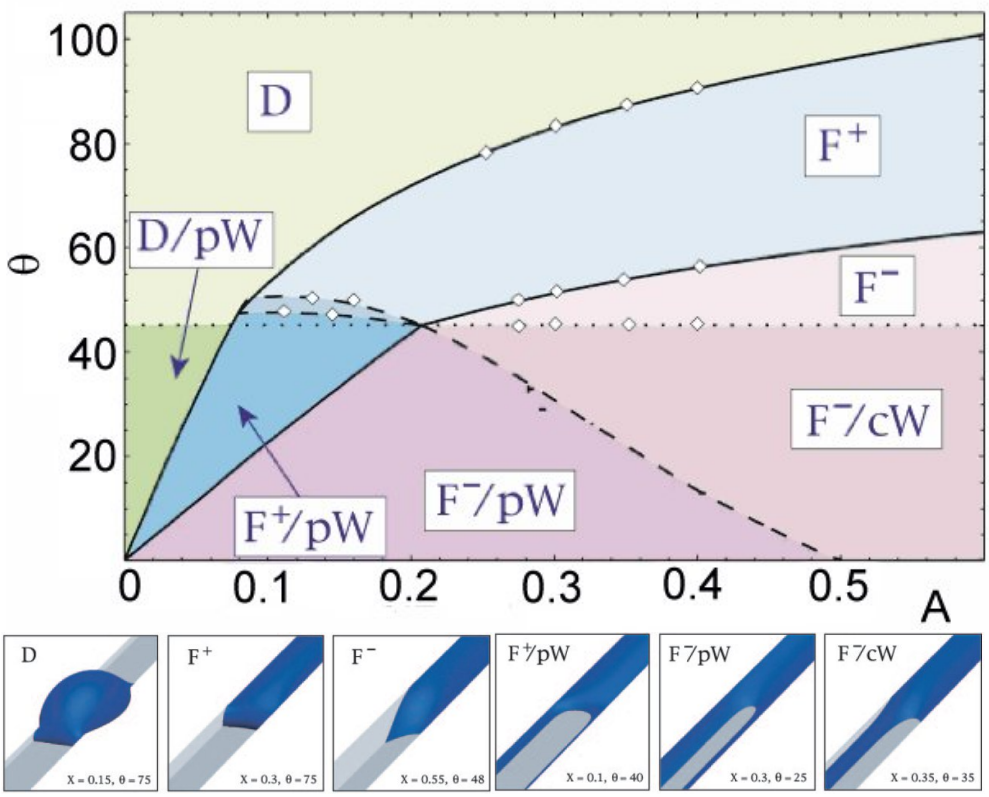

Figure 4.1: Drop shape on on rectangular channels. Top: morphological diagram for a drop on rectangular channels. A is the aspect ratio D/W of the channels and θ the contact angle on the flat surface. (Courtesy of Ralf Seemann and Martin Brinkmann, see [25]). Bottom: Corresponding shapes; droplets (D), filaments with positive pressure (F+), with negative pressure (F-), pW and cW refers to filament wetting the corners of the channels.

substrate, the liquid morphology can exhibit a negative Laplace pressure [22] which is expected to suck the liquid out of a reservoir. In these previous experiments, the surface wettability was chemically modified and determined once and for all by the surface energies of the substrate and the liquid. Here we investigate an actively induced morphological transitions between a drop and a liquid filament wetting the channels using electrowetting as a way to modify the wettablity of the substrate.

In electrowetting experiments on flat substrates a modulation of the con-

tact angle θ of a drop on a substrate is achieved by depositing drops of a conducting liquid on a conducting substrate on top of which an insulating layer has been previously formed [53]. The voltage is applied between the conducting substrate and an electrode immersed in the drop as shown in Figure 4.3(a) and the modulation of the contact angle is described by Lippmann's equation [104]:

$$\cos\theta = \cos\theta_Y + \left(\frac{U_0}{U_L}\right)^2 \tag{4.1}$$

where $U_L = (2T\gamma/\varepsilon_0\varepsilon_r)^{1/2}$ is a caracteristic of the system, γ being the liquid / vapor interfacial energy, ε_0 the dielectric permittivity of vacuum and ε_r the dielectric constant of the insulating layer and θ_Y is Young's contact angle of the liquid on the substrate which is recovered at zero voltage. Lippmann's equation (4.1) accounts for the energy contribution of the electrical field as an additional surface energy related to the solid / liquid interfacial energy which decreases when the applied voltage is increasing. In this frame electrowetting is included in capillary theory using a modified interfacial energy of the solid / liquid interface and is the right tool to modulate the contact angle of the drop on the substrate in order to investigate the morphological transitions expected from a theoretical point of view. However this ideal behaviour stops above a saturation voltage for which the contact angle remains more or less constant, the physics of the saturation being still subject of investigations.

4.2 System

Among the possible substrates used for electrowetting experiments [60], silicon wafers are the most versatile and convenient to process substrates for technological reasons. We used conducting arsenic-doped silicon wafer as solid substrates. Rectangular channels have been produced using anisotropic ion etching on the native silicon wafers. A silicon oxide dielectric layer of thickness $T = 1.1 \pm 0.1\mu$m has then been thermally grown on top. Using this process channels of width W and depth D ranging respectively from 15 to 50 μm $\pm$ 1 μm for a fixed depth of 20 μm $\pm$ 1μm have been produced (see Figure 4.2).

The aspect ratio A of the channel, defined as D/W goes then from 0.40 to 1.33. In order to have contact angles with water or glycerol larger than 90 de-

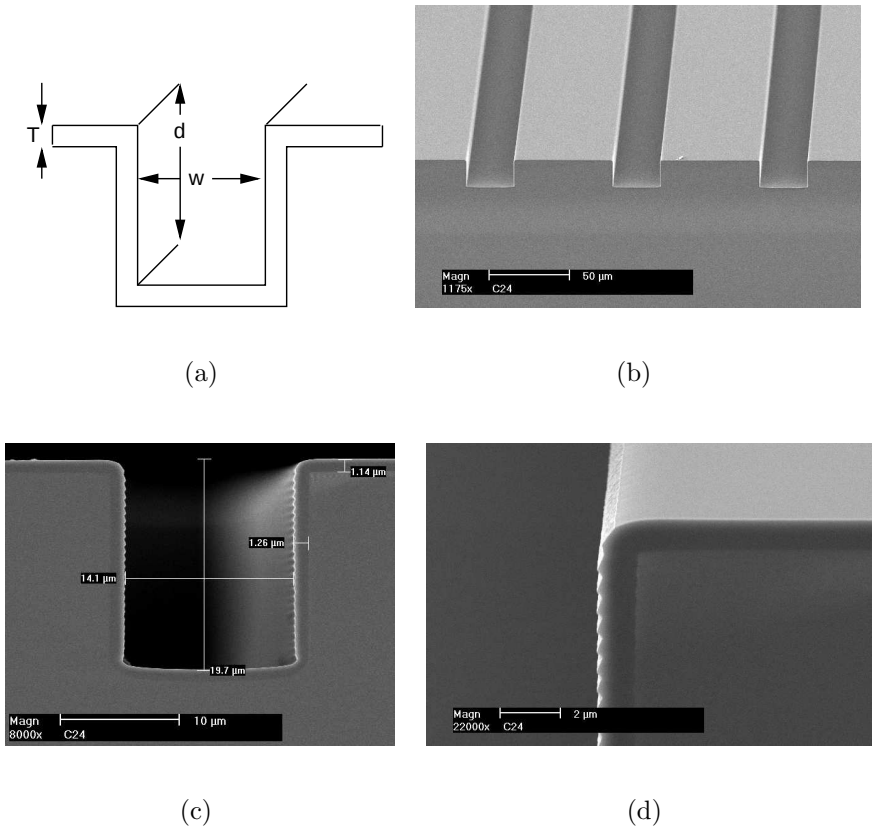

Figure 4.2: Channel etched in silicon wafer. (a) Sketch of the rectangular channels: W= 15 - 50 μm, D= 10 - 20 μm, T =1 μm. (b) SEM picture of an array of rectangular channel $W \approx 30$ μm, $D \approx 20$ μm,(c) SEM picture of the rectangular channel $W \approx 14$ μm, $D \approx 20$ μm, (d) zoom on the top corner of the groove showing the insulating layer $T \approx 1$ μm.

grees at zero voltage an additional monolayer of OTS (OctadecylTrichloroSilane) used as an hydrophobic coating has been deposited on top of the silicon oxide layer from a liquid phase following a standard protocol [72].

The liquid used is a mixture of glycerol (46.7% in weight), water (51.7%) and salt (1.6%). The viscosity η of the solution, measured using a stress-controlled rheometer (Rheometric Scientific SR-5000) is $\eta = 5$ mPa×s in agreement with the viscosity tables of the mixture and do not show variation with the applied shear stress in the measurement range 10 - $10^3 s^{-1}$. Glycerol is used to reduce the effect of evaporation of water and salt (NaCl) to

increase the conductivity of the liquid ($\sigma = 0.7$ S×m measured with Hanna HA8733 conductimeter). However, dealing with small drops a significant fraction of water evaporates after deposition leading to a drop composition at equilibrium which depends mainly on the local humidity and hygroscopy of the glycerol. Since the humidity range is 45 to 55% in our experiments the final composition is not fully controlled and can vary which leads to daily variations of the conductivity or viscosity of the drop. Measuring drop volume after deposition it is however possible to estimate the final composition assuming that only water evaporates. After a few minutes the drop is at equilibrium with about 80% glycerol confirmed by NMR measurement. The AC voltages U_0 ranging from 0 to 120 V (rms value at frequency f between 1 and 30 kHz) are applied between the drop and the substrate. In those conditions a liquid mixture at a composition close to the estimated equilibrium composition (glycerol (80.4% in weight), water (16.8%) and salt (2.7%) - σ =0.14 mS/cm, $\eta = 82$ mPa×s, $\gamma \approx 65$ mN/m) has been prepared and the Lippmann curve $\cos\theta$ as a function of the applied voltage U_0 has been measured on flat areas of the sample. The contact angle measurements do not show significant variations with the position on the wafer indicating a good uniformity of the OTS layer, confirmed by a contact angle hysteresis of 5-7 degrees of water in air. The curve shown in Figure 4.3(b) displays the classical quadratic behaviour below 50 V, called Lippmann's regime and a saturation regime above 50 V where the contact angle varies in a quasi-linear fashion.

The influence of gravity on the experiments is neglected since the typical sizes of the channels and drops are smaller than the capillary length of water or glycerol $L_c = (\gamma/\rho g)^{1/2}$, γ and ρ being the surface tension and densities of the liquid in air. The sizes are however large enough to neglect the effects of line tension or edge effects [105] which become non negligible below the micrometer scale and to estimate the capacitance of the 3-dimensional structure of the channel as combination of planar capacitances.

4.3 Experiments

According to the work done by Seemann *et al.* [25] the morphology of a drop on a channel depends only on two parameters, the contact angle of

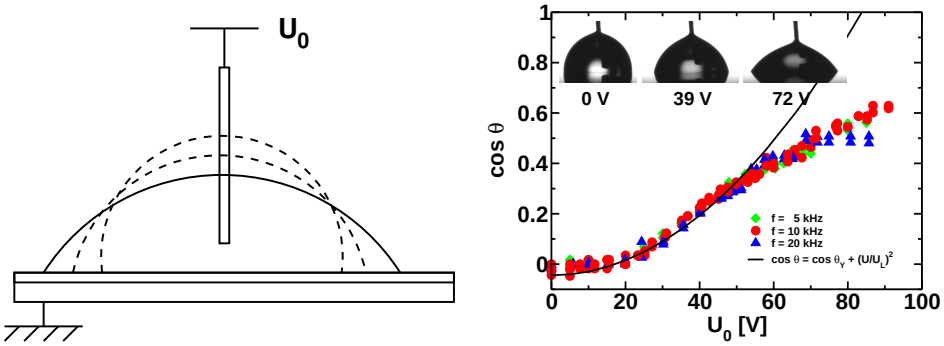

(a) (b)

Figure 4.3: (a) Principle of electrowetting on dielectric (EWOD). A voltage is applied between an electrode immersed in a conducting drop and the substrate. A dielectric layer insulates the drop from the substrate. (b) Lippmann curve for the experimental set-up used. The contact angle typically varies between 105 to 50 degrees for voltages between 0 to 50 V. The fit in the region below 50 V gives $\cos\theta_Y$ = -0.04 and U_L = 82 V.

th

the drop on the planar substrate and the aspect ratio of the channel. We are interested in the morphological transition expected from drops on the channel ((D) according to their notation) to liquid filament (F).

4.3.1 Preliminary experiments

The wetting case – On our structured surfaces, various morphologies were observed when a glycerol drop is deposited on the channels before deposition of the hydrophobic layer (θ for glycerol on silicon oxide is close to 45 degrees, wetting case) as displayed in Fig.4.4. On the wetting surface a drop has different possible states (Fig. 4.4). For a drop on top of the rigdes out of the channels (a and a') the contact line is pinned at the edge of the channel. The drop spreads preferentially in between the two channels leading to an anisotropic shape. Increasing the volume of the drop above a critical volume will destabilize it. For a drop in the channels, at a volume smaller than the total volume accessible in the channel, the drop has an elongated shape (the filament F (b)). Increasing the volume will result in the apparition of a bulge

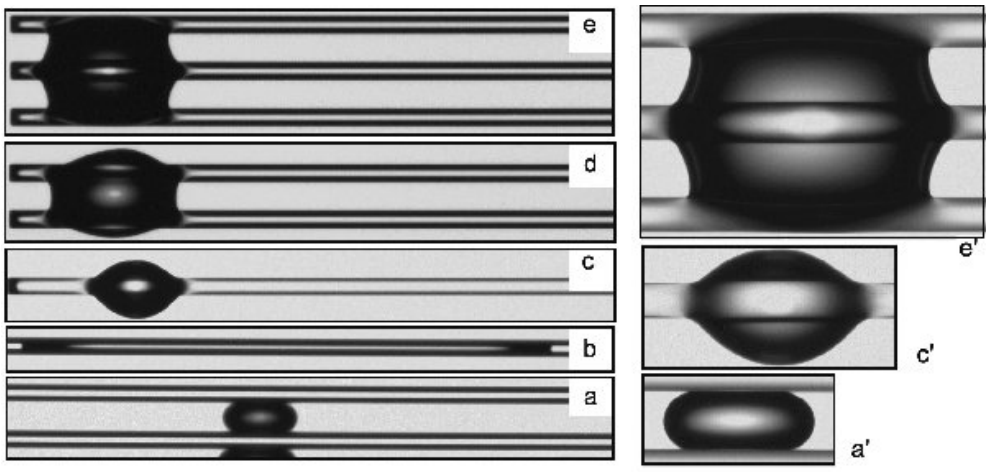

Figure 4.4: Top view of a droplet on a surface with grooves: morphologies observed in the wetting case: the typical volume of the liquid structure increases from bottom to top.

similar to the one obtained by Gau *et al.* [19] which coexists with the filament because of the finite length of the channel (c, c'). Indeed if the channels were infinitely long the bulge would disappear in the channel in a configuration similar to (b). At even higher volumes the drop will spread in a neighbouring channel with a bulge linking two channels (d), three channels (e, e') or even more (not displayed). It has to be noticed that only one bulge can exist for a given channel. Indeed two bulges can coexist only if they have the same size which is an unstable situation: the smaller will disappear in the biggest due to the excess of pressure as displayed in Fig. 4.5.

The non-wetting case – On the non-wetting surface (see Fig.4.6, on the OTS layer θ for glycerol on OTS is close to 90 degrees) the situation is different: the wetting in the channel is difficult to observe. Indeed at small volumes the drop sits in between two channels (a, b). When the volume is increased the drop bridges above the channel without wetting it: this is a fakir drop with air entrapped underneath also called a Cassie drop (c, d, e). This situation is metastable [14] and the liquid can be pushed in the channel leading to a Wenzel drop which wets partly the channel. The bulge is in this case a stable shape. This bulge can be mechanically extended to the end of

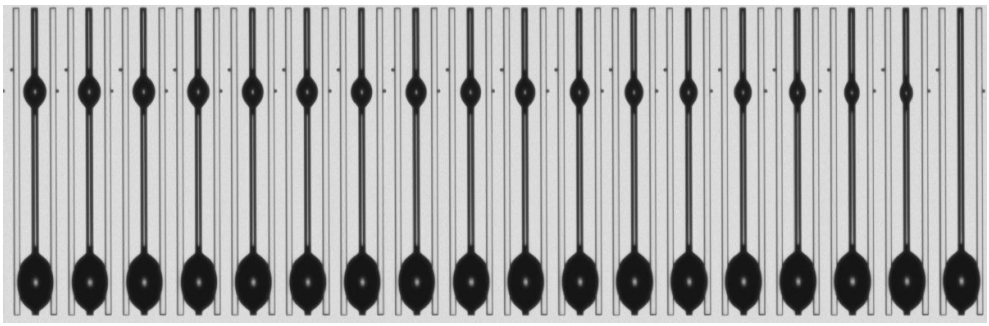

Figure 4.5: Unstable situation for a drop on a channel: the smallest drop disappears in the largest due to the excess of the Laplace pressure. The time step between two succesive pictures is 72 ms. The total length of the grooves is 2 mm.

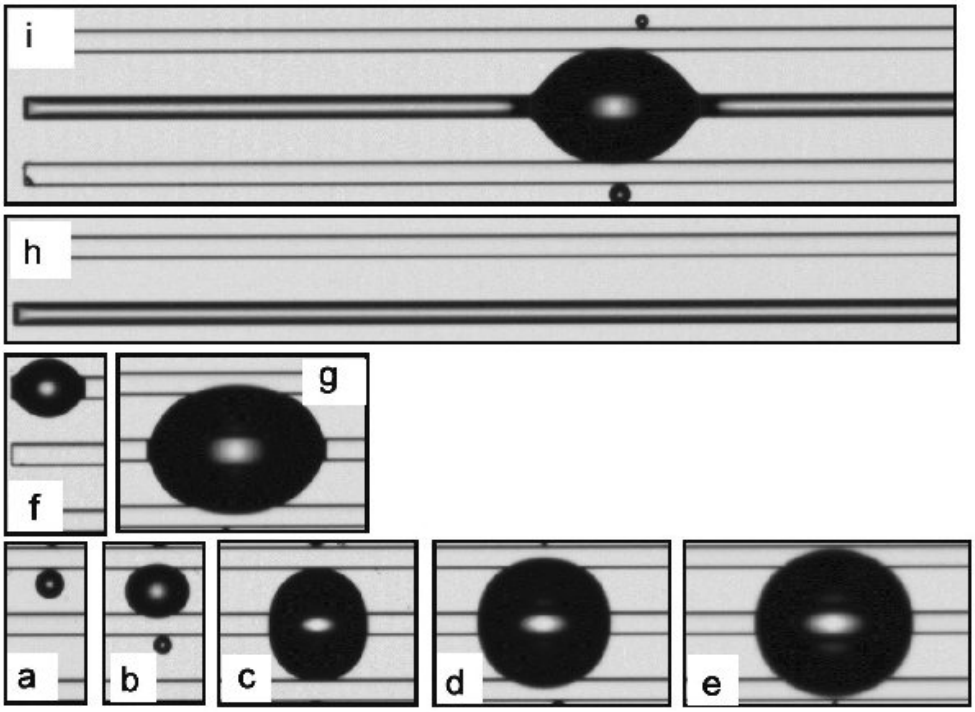

Figure 4.6: Top view of a droplet on a surface with grooves: morphologies observed in the non-wetting situation. The volume of the liquid structure increases from bottom to top.

the channels where it becomes pinned: a stable liquid finger is thus formed due to the pinning condition and and increase of the volume will lead to the

formation of a bulge (i).

4.3.2 Electrowetting experiments: metastable states

In these last experiments we changed the contact angle by chemically changing the surface. However the only important parameter is the contact angle. While changing the contact angle using electrowetting from a value larger than 90 degrees to a value close to 50 degrees, the transition line between (D) and (F) is expected to be crossed for channels of aspect ratio of order 1. In other words we expect to make a transition between the two states of the figure 4.7. In order to have a reversible transition it is necessary to avoid the

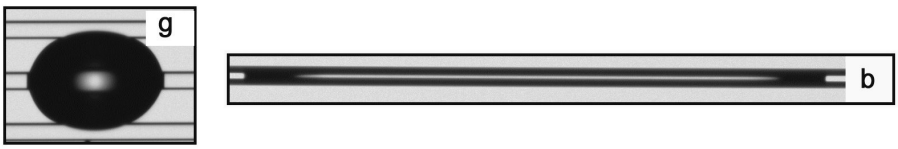

Figure 4.7: Principle of the actuation studied: an active control of the surface tension via electrowetting is used to induce the filling transition observed in the passive situation.

states involving pinning. Pinning leads to metastable shapes which reduces reversibility. The experiments were performed as follows: a drop of the solution was deposited on an array of channels. The droplet is in a metastable Cassie state. When the voltage is applied directly to the drop a family of metastable shapes is observed. They destabilize at high voltage leading to a Wenzel drop (Fig. 4.8, top). Surprisingly the Cassie state survives even at 50 V which corresponds to a contact angle close to 75 degrees. When the voltage is set to zero and re-increased the shape involve only Wenzel drops (Fig. 4.8, bottom). The drop exhibits an anisotropic shape similar to the one already observed on flat chemically patterned surfaces by Morita *et al.* [106]. The wetting anisotropy in our case has the same origin namely the anisotropy of the solid surface. Since the Cassie drop is metastable the transition from Cassie to Wenzel drop will depend on the way the experiment is performed and thus will reduce the reproducibility of the results. It is thus necessary to start the experiments with a Wenzel drop.

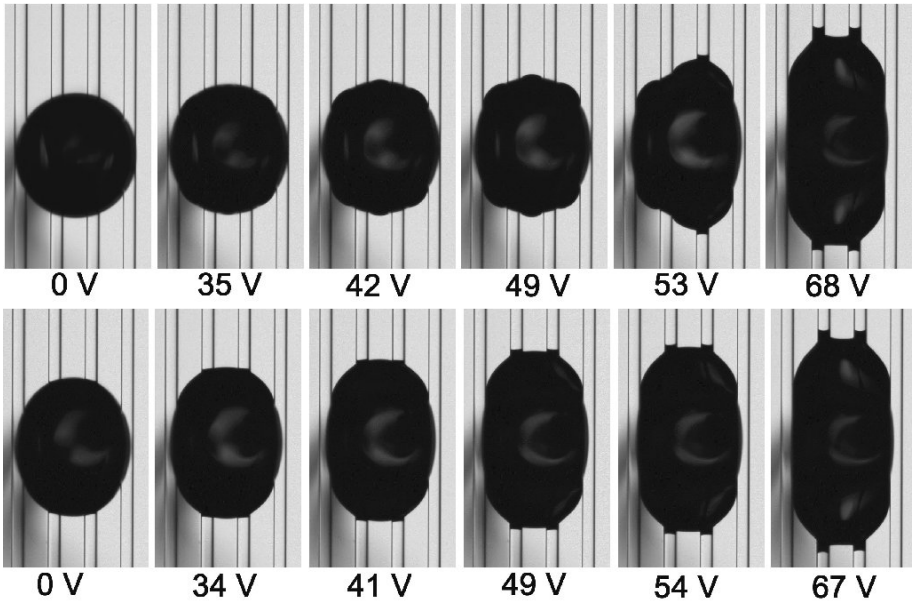

Figure 4.8: Metastable Cassie drops. The width of the channel is w=50μm and the depth d=20μm

4.3.3 Reversible electrowetting induced transitions

In the following, at the beginning of the experiments, the drop is pushed in the channels either mechanically by pressing with the electrode or by a small voltage pulse. Once the drop is in the Wenzel state, the voltage U_0 between the drop and the substrate is increased by steps. Top views of the drop are acquired using optical microscopy with a CCD camera (Philips DICA). The liquid filament is not directly observable in the channel due to the low curvatures and slopes of the interface along the channels. At the end of the filament where the curvature of the free-surface is large enough the light is deflected and the end of the filament appears black which gives the possibility to measure the length of the liquid filament as a function of the applied voltage (Fig. 4.9).

In the case of a drop deposited on channels with aspect ratio of 1.33 (D=20 μm, W=15 μm), the typical images obtained are displayed in Figure 4.10(a) with the corresponding rms value of the AC voltage at 20 kHz. Below a threshold voltage U_T= 43 V $\pm$ 2 V, a short liquid filament is growing with increasing voltage. The liquid filament becomes much longer above the

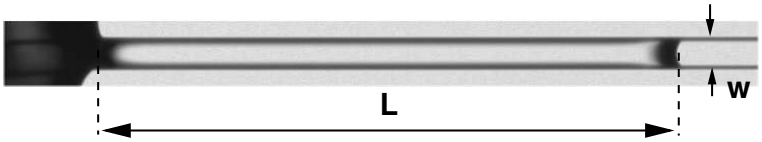

Figure 4.9: Measurement of the length of the liquid filament. In this case, W =40μm, D =20μm,U_0=85 V at 20 kHz. The length is L =0.81 mm $\pm$ 5 %.

critical voltage. In order to study the influence of the capillary pressure and the electrical properties the experiments were repeated on the same drop for several frequencies and for a fixed frequency with various drops. The results are displayed in Figure 4.10(b). The voltage was increased gradually and the equilibrium length L_∞ was measured on the pictures. In the following L_∞ will refer to the equilibrium length and L a length which does not necessarily correspond to equilibrium. When the voltage is turned down to 0 the drop nicely recedes to the mother drop: the transition is thus reversible.
In these experiments, the threshold voltage does not depend on the applied frequency but the equilibrium length of the liquid channel is a function of the frequency: the key feature here is that the length decreases with an increasing frequency.
Fixing the frequency at 20 kHz the experiments were carried out as follows for different drop sizes on channels of aspect ratio 0.66: the voltage was increased by a single step from 0 to a value U_0. The steady state value of the length L_∞ was measured using an image processing routine in Matlab. The end of the channel is detected as the point where the grey level is the mean value of the maximum and the minimum gray level which gives an accuracy of about 10μm on the determination the length. The experiments are performed for different values of U_0 and for various drop sizes. The results are displayed in Figure 4.11. Two parameters characterize the mother drop. The ratio of the size of the drop over the size of the channel ($V^{1/3}/W$) and the number of channels wetted by the drop N_c. A drop deposited on an heterogeneous substrate does not have a single possible configuration but different morphologies defined as local minima of the free-energy [23]. The two parameters have an influence on the pressure of the drop. The effect of a decrease of the size of the drop is to decrease the threshold voltage as

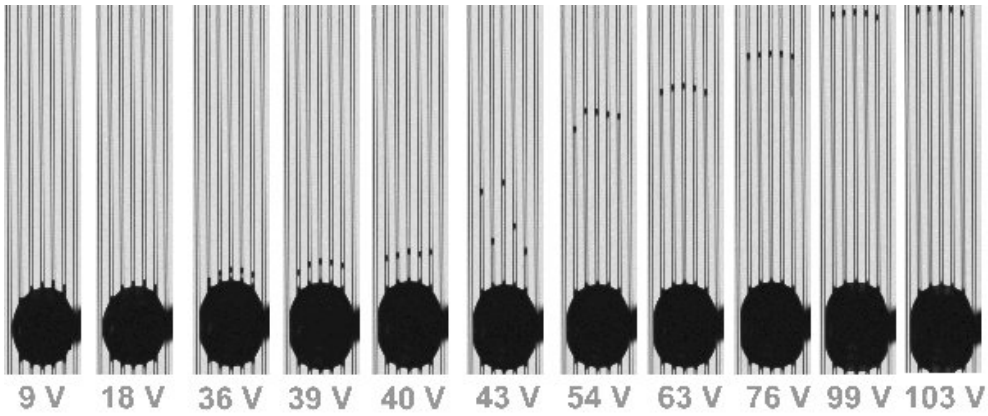

(a)

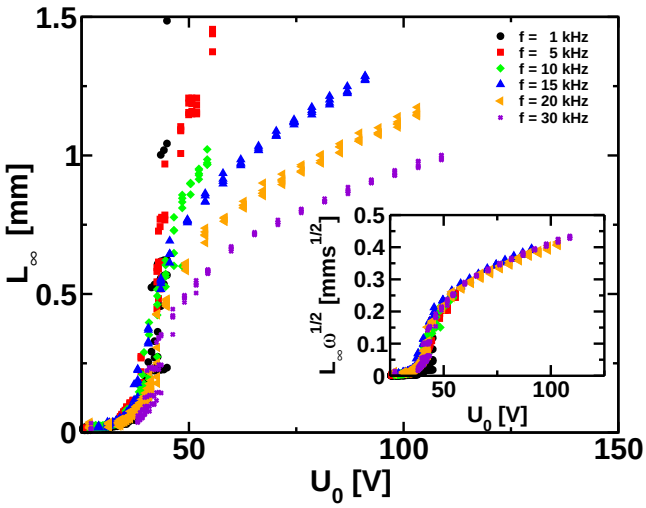

(b)

Figure 4.10: (a) Top-view of the channels for different voltages. The frequency of the voltage is 20 kHz and the drop wets 5 channels. On the right of the drop one see the contacting electrode. (b) Measurements of the length as a function of the applied voltage for different frequencies. The threshold voltage is obtained at 43 V. Inset: rescaling of the data by $\omega^{1/2}$ showing the collapse on a single master-curve.

displayed in Figure 4.11 (circles, squares and diamonds). For a fixed drop

size ($V^{1/3}/W = 9$) the drop confined to three channels (diamonds) has a threshold smaller than the drop confined to four channels (triangles). These observations are compatible with pressure argument: the Laplace pressure of the small drop pushes the liquid in the channels more than a large drop. The confinement of the drop over three channels increases also the pressure in the drop compared to a confinement over four channels which also pushes the drop in the channels. When the voltages are rescaled by the threshold voltage (see inset) the length does not show any dependence on the drop size: the equilibrium length is not obtained by a balance of capillary pressure of the drop and the pressure of the liquid in the channel. According to

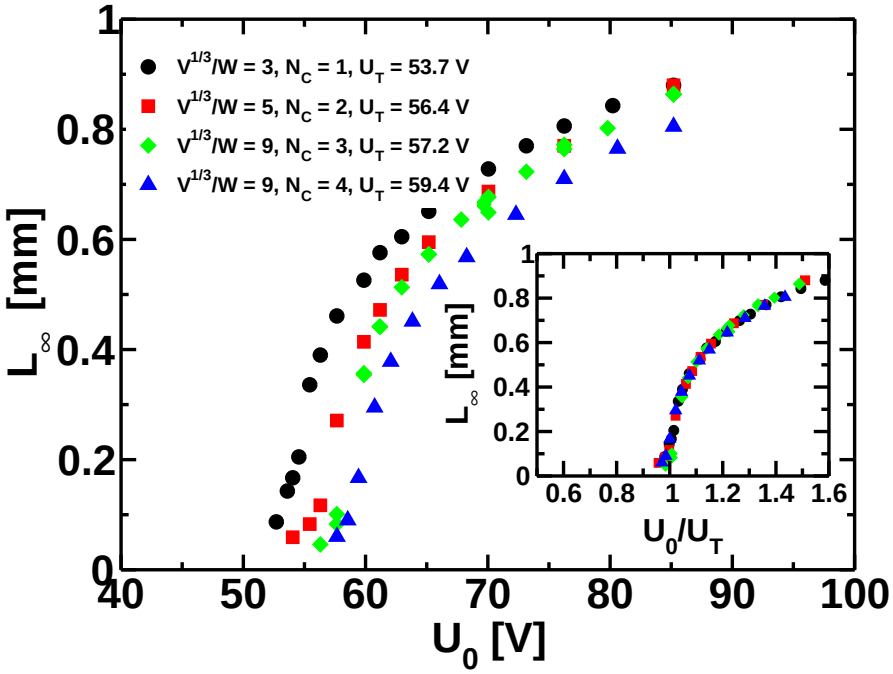

Figure 4.11: Measurements of the length as a function of the applied voltage for different drop sizes. N_c is the number of channels the drop wets. The threshold voltage depends on the reservoir pressure. Inset: rescaling of the voltages by the threshold voltage U_T showing that the length does not depend on the reservoir pressure.

the work of Seeman *et al.* the threshold voltage is expected to depend on the geometry of the channels and more precisely on the aspect ratio of the

channels. The experiments were performed for the different aspect ratios at approximately constant $V^{1/3}/W \approx 10$ and for a fixed voltage frequency of 20 kHz. The equilibrium length is measured and plotted versus the applied voltage and the results are displayed in Figure 4.12. The threshold voltage is a function of the aspect ratio which agrees with Seeman *et al.* analysis based on a capillary model. The length after the transition depends also on the aspect ratio via a simple scaling in $(1+2A)^{1/2}$ (see inset) which shows the influence of the channel dimensions on the electrical properties of the liquid filament.

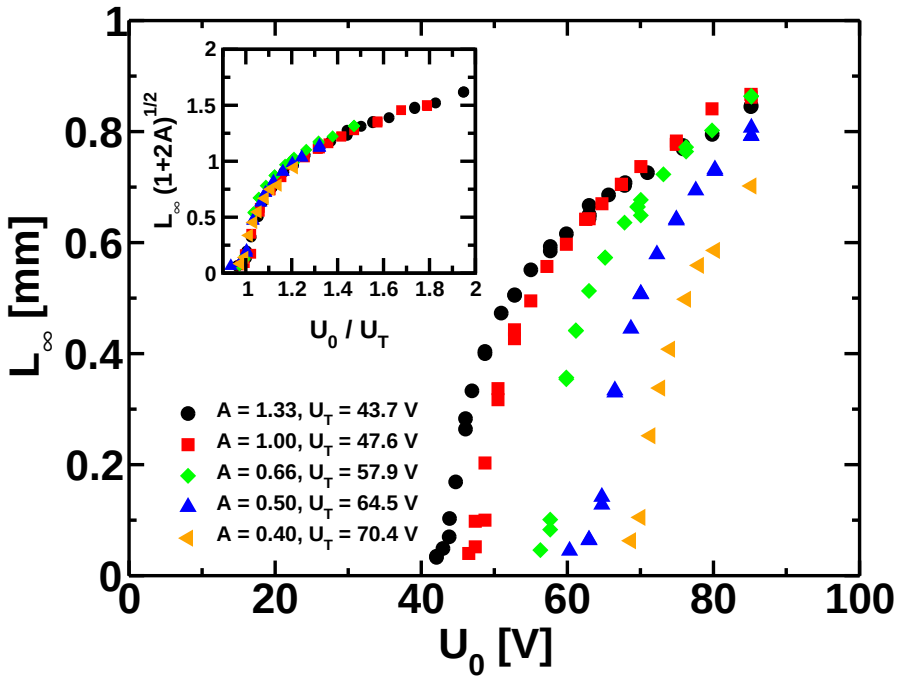

Figure 4.12: Measurements of the length as a function of the applied voltage for different aspect ratio. The threshold voltage depends on the aspect ratio. Inset: rescaling of the voltages by the threshold voltage U_T showing that the length does also depend on the aspect ratio of the channel via a scaling $(1+2A)^{1/2}$.

In summary, we experimentally observed a capillary driven transition and a finite length behaviour beyond the transition:

1. the transition voltage depends only on capillarity and Laplace pressures

and not on electrical properties. The threshold voltage depends on the way the drop is placed on the substrate even if the size is always fixed. However the effect in terms of voltage is only a few percent;

2. the behaviour of the liquid beyond the transition depends on the electrical properties of the liquid and the solid substrate and not on the capillary pressures. On a capillary view point one does not expect any equilibrium length: a balance of pressure (or energetic arguments) predicts that the drop vanishes entirely in the channel. Indeed, below a threshold contact angle the pressure in the channel is smaller than the pressure in the drop. The equilibrium length is thus a consequence of electrical phenomena;

3. the dimensions of the channel also have an influence on the equilibrium length.

In the following section we will model the electrical properties of the liquid in order to explain these experimental observations.

4.4 Modelling

4.4.1 Transition

Assuming a channel in equilibrium with a reservoir at zero Laplace pressure, increasing the length L of the liquid filament by $\mathrm{d}L$ requires a capillary energy $\mathrm{d}E^{\mathrm{c}}$:

$$\frac{\mathrm{d}E^{\mathrm{c}}}{W\gamma \mathrm{d}L} = 1 - (1+2A)\cos\theta \tag{4.2}$$

The wetting of the channel is reached when $\mathrm{d}E^{\mathrm{c}} < 0$ i.e. $\theta < \theta_T^0 = \arccos 1/(1+2A)$. This equation is represented by the line of equilibrium between F^+ and F^- in the θ vs A morphological diagram. This description corresponds to a capillary situation where only interfacial energies have been considered. In the case of electrowetting an additional electrical term is introduced in order to take into account the influence of the electrical field. This term assumes that the capacitance of the channel is evaluated as the sum of three planar capacitances, two corresponding to the edges and one to the bottom of the channel which is a fair approximation as long as $T \ll D, W$. In this situation, Eq. 4.2 holds provided that the contact angle is Lippmann's

angle: the transition occurs when the Lippmann's angle of the mother drop equals the transition contact angle θ_T^0 of the capillary model. The effect of electrowetting is thus to act as an additional term in the capillary theory as usually described. This capillary description is not sufficient to describe the behaviour beyond the transition: a capillary model predicts that the drop vanishes entirely in the channel.

4.4.2 Equilibrium length

In order to explain the finite length effect, we have to come back on the implicit assumption that the voltage is constant along the liquid finger. Let us assume that a liquid filament exists and that the voltage along the channel is a decreasing function of the position X as the result of the finite electrical conductivity of the liquid. At the entrance of the channel the voltage is equal to the applied voltage U_0. The energy $\mathrm{d}E(X)$ corresponding to a modification of the length of the channel by a infinitely small length $\mathrm{d}L$ is the sum of capillary and electrical energy and depends on the position X:

$$\frac{\mathrm{d}E(X)}{W\gamma \mathrm{d}L} = \frac{\mathrm{d}E^{\mathrm{c}}}{W\gamma \mathrm{d}L} - (1+2A)\left(\frac{U(X)}{U_L}\right)^2 \tag{4.3}$$

$\mathrm{d}E(X)$ is thus minimal at the entrance of the channel and increases along the channel. When $U_0 = 0$, $\mathrm{d}E(X=0)/\mathrm{d}L > 0$ and thus $\forall X\ \mathrm{d}E(X)/\mathrm{d}L > 0$: no liquid finger is formed; if there is one it will recede entirely to the mother drop. Increasing U_0 in the drop, $\mathrm{d}E(X=0)/\mathrm{d}L > 0$ until U_0 reaches the threshold U_T defined as $\cos\theta_Y + (U_T/U_L)^2 = 1/(1+2A)$ for which $\mathrm{d}E(X=0) = 0$. At $U_0 > U_T$, $\mathrm{d}E(X=0)/\mathrm{d}L < 0$: wetting becomes favourable. A liquid finger starts to leak in the channel. At the tip of the liquid finger the voltage $U(X=L)$ is smaller than U_O (according to our assumption of voltage decay). The energy $\mathrm{d}E(X=L)/\mathrm{d}L$ is negative as long as the voltage at L is larger than U_T. Thus beyond the threshold, assuming a loss of voltage along the liquid finger, one finds an equilibrium length L for which the voltage at position $X = L$ is equal to the threshold voltage of filling U_T. For this equilibrium position, at the tip $\mathrm{d}E(L) = 0$. In the case of a infinitely conducting liquid, the voltage is constant: beyond the transition U_T the liquid finger length would be increase continuously until the reservoir is empty since for all L, $U(X=L) = U_0 > U_T$. In the case of an infinitely conducting liquid, one find that the length L_∞ diverges to infinity: the drop

would entirely vanish in the channels. The length of the liquid finger is then expected to be increasing with increasing conductivity. The quantitative determination of the length as a function of the applied voltage requires then the knowledge of the variation of the voltage as a function of the position, depending on the electrical properties of the system and will be derived in Sec. 4.4.4.

4.4.3 Pressure effects

The results obtained for a reservoir at zero pressure are slighlty modified when the reservoir has a positive Laplace pressure like in the case of a drop reservoir. In this case the energy has to take into account the work of the pressure forces which requires the computation of the liquid - vapor interface shape at the given pressure. For a drop, the problem is not so simple since the pressure of the reservoir is not constant for three reasons: i) Some liquid flows out of the mother drop: the Laplace pressure increases since the drop size decreases due to the outflow, ii) the confinement of the drop along the stripes has an influence on the Laplace pressure and the shape deviates from the spherical cap [23] as it can be seen on the Figure 4.10(a) where the mother drop elongates along the stripes and iii) the contact angle of the drop is decreasing while increasing the voltage leading to a decrease of the Laplace pressure. The first effect is neglected as soon as the drop volume V is larger than the volume of the channels which is the case in most of the practical cases we deal with here ($V \ll L_\infty \times W \times D$). The second point could be solved by calculating completely the pressure of the drop at a given voltage which would impose the pressure. The energy balance has then to take into account the curvature of the interface in the channel determined by the pressure and the work of the pressure forces. Ignoring the second point, the third effect is solved calculating the variation of the Laplace pressure with contact angle under the spherical cap assumption. However the results have to be taken with care since the spherical cap assumption does not hold for small drops:

$$\frac{\mathrm{d}E_V^{\mathrm{C}}}{W\gamma \mathrm{d}L} = \frac{V^{1/3}/W}{f(\theta)} \arcsin \frac{f(\theta)}{V^{1/3}/W} - (1+2A)\cos\theta + 2A\frac{f(\theta)}{V^{1/3}/W} \qquad (4.4)$$

where $V^{1/3}/W$ is the size of the drop rescaled by the width of the channel, and

$$f(\theta) = (3/\pi)^{1/3}(2 - 3\cos\theta + \cos^3\theta)^{1/3}$$

(see Appendix C). The wetting of the channel is reached for equation for $\mathrm{d}E_V < 0$. The coexistence of a drop and a liquid filament is reached at a given A for θ such as $\mathrm{d}E_V^{\mathrm{c}} = 0$. The numerical solution shows the increase of the transition contact angle θ_T^V when the drop size decreases (see Fig. 4.13). Asymptotically for $V^{1/3}/W \to \infty$ the value $\cos\theta_T^0 = 1/(1+2A)$ is recovered which correspond in practical case to $V^{1/3}/W > 20$. However this resolution does not take into account the effect of grooves of the drop shape. The size effect was calculated for the different drops and compared to the experiments. The relationship between the contact angle and the voltage has been obtained using the electrowetting curve. The results are displayed in Figure 4.13. The dashed lines correspond to the transition expected at zero pressure and the curve show the transition expected from the spherical cap assumption of the reservoir drop. The points correspond to the experiments. The values of the contact angle at the transition observed in the experiments are in a region close to the one expected from the previous analysis. The size effect are also in qualitative good agreement with the experimental observations but the quantitative comparison, and in particular the size effect. The main reasons for the mismatch can be attributed to the effect of the electrode on the drop shape which is critical for small drop size and the validity of the spherical cap assumption.

4.4.4 Electrical model

The finite length effect is caused by the decay of voltage along the liquid finger. In order to predict the length as a function of the applied voltage the determination of the function $U(X)$ is required. The electrical dependence above the threshold it explained by looking at the liquid filament as an electrical component. The liquid filament is a conducting material surrounded by an insulating layer. In terms of electrical properties, it is equivalent to a coaxial cable which is known to display a voltage loss [107]. In our case, the end of the filament is free to move which means that we have here a free-ended coaxial cable of length L_∞. This system is modelled by a string of capacitance and resistance along the direction X of the channel, as displayed in Figure 4.14.

$\mathrm{d}R$ is the resistance per unit of length of the liquid filament and $\mathrm{d}Z_C$

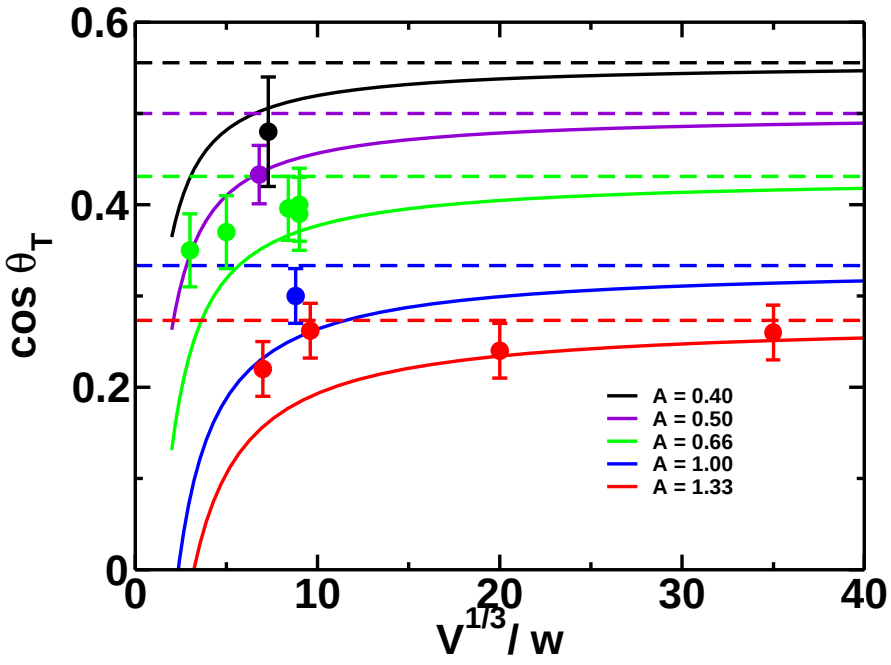

Figure 4.13: Comparison of the experimental transition contact angle with the capillary models. The dashed line correspond to the transition expected at zero pressure and the full line is obtained including pressure effects via a spherical cap assumption for the reservoir drop. Experiments show good agreement with the model.

the capacitance per unit of length of the channel. The exact value of $\mathrm{d}R$ and $\mathrm{d}Z_C$ depends on the geometry of the channels and on the shape of the liquid / air interface. In the model the cross-section of the liquid filament is approximated as constant and flat all along the channel giving a rectangular cross-section for the liquid filament which simplifies the expression of $\mathrm{d}R = \mathrm{d}X/(\sigma W D)$ and $\mathrm{d}Z_C = T/(j\omega\varepsilon_0\varepsilon_r(2D+W)\mathrm{d}X)$. For such a system the relationship between the voltages $U(X)$, $U(X-\mathrm{d}X)$ and $U(X+\mathrm{d}X)$ leads to the differential equation (see Appendix D):

$$\frac{\mathrm{d}^2U}{\mathrm{d}X^2} = 2j\frac{U(X)}{\lambda^2} \tag{4.5}$$

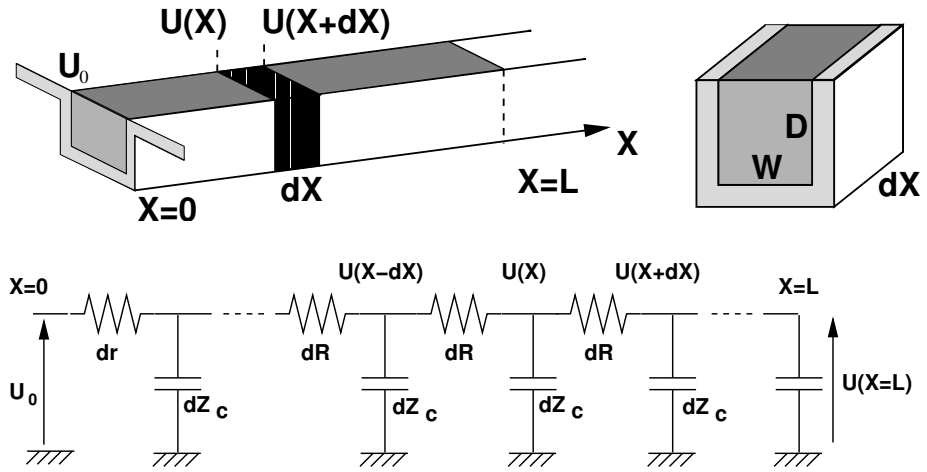

Figure 4.14: Top: sketch of the liquid channel. A slice dx of the channel has displays a resistance linked to the area of the cross-section and a capacitance linked to the wetted area of the substrate. Bottom: equivalent electrical circuit for the liquid filament: the voltage along the drop is not constant

where j is the complex unit and λ the only lengthscale of the problem:

$$\lambda = \sqrt{\frac{1}{\omega}\frac{2T\sigma}{\varepsilon_0\varepsilon_r}\frac{WD}{W+2D}}$$

λ^2 is the product of two length-scales, an electrical length-scale $2T\sigma/(\omega\varepsilon_0\varepsilon_r)$ depending on the material properties and on ω and a geometrical length-scale $WD/(W+2D)$ (the ratio of area of crossection over perimeter of wetted surface). For cylindrical channels or triangular grooves one will find the same electrical length-scale and different expression for the geometric length-scale. In our case, the geometric length-scale is of order the typical size of the channel and always limited by the smallest dimension: if $D \ll W$, $WD/(W+2D) \sim D$ and $W \ll D$, $WD/(W+2D) \sim W/2$

In order to solve Eq. 5.23, the lengths are rescaled by λ: $x = X/\lambda$, $l_\infty = L_\infty/\lambda$ and the voltages by the threshold voltage U_T: $u(x) = U(x)/U_T$, $u_0 = U_0/U_T$, U_0 being the voltage applied in the drop. Before solving the equation we notice that λ gives the length-scale for experiments performed at different frequencies for a given drop on given channels. Scaling the results of Figure 4.10(b) according to the power-law $\omega^{1/2}$ shows the collapse on a single master curve (see inset). One consequence of this analysis is that at

zero frequency the length scale is diverging which means that the whole drop will vanish in the filament: the complete morphological transition is then expected for direct current provided that the volume accessible in the channel is of the order of the volume of the drop. The scaling of λ with $(1+2A)^{1/2}$ is also demonstrated by the collapse on the master curve displayed on Figure 4.12. Moreover λ does not depend on the reservoir pressure which explains that the data of Fig. 4.11 obtained for different drop sizes collapse on a master curve when the voltage only is rescaled by the threshold voltage. The electrical model reproduces correctly all the experimental observations.

4.4.5 Comparison with experiments

A quantitative study is now performed solving Eq. 4.5. Three boundary conditions are required to solve this second order differential equation with unknown length l (the voltages are rescaled by threshold voltage $u = U/U_T$ and length by λ):

$$\begin{cases} u(x=0) &= u_0 \\ \frac{\mathrm{d}u}{\mathrm{d}x}(x=l_\infty) &= 0 \\ u(x=l_\infty) &= 1 \end{cases} \tag{4.6}$$

The first two conditions are purely electrical: the voltage at the entrance of the channel is the voltage in the drop U_0 and the current at the end is zero (electrical equilibrium). The third one is obtained by the argument developed above: the voltage at the end of the channel is the threshold voltage: $U(L_\infty) = U_T$. This condition creates the link between the capillary theory of the transition and the influence of the electrical properties on the behaviour after the threshold. Using these three boundary conditions, the length of the liquid channel is calculated. An analytical expression of the voltage along the channel is obtained (see Appendix D):

$$u(x) = \sqrt{\cosh^2(l_\infty - x) - \sin^2(l_\infty - x)} \tag{4.7}$$

The length l_∞ as a function of u_0 is given by equation 4.6 which cannot be inverted analytically: the inversion has been performed numerically. The asymptotics for $l_\infty \sim 0$ and for $l_\infty \to \infty$ read:

$$l_\infty \sim \quad 3^{1/4}(u_0 - 1)^{1/4} \quad , l_\infty \sim 0 \tag{4.8}$$

$$l_\infty \sim \qquad \ln(2u_0) \qquad , l_\infty \to \infty \tag{4.9}$$

These two equations stands for:

1. the sharp transition which occurs with an exponent of 1/4;

2. the absence of saturation of the length with the applied voltage: the length is increasing logarithmically with the voltage. In practical cases, this increase is stoped by the break-up of the insulating layer in the regions where the electric field becomes larger than the electrical strength of the insulating material. Moreover it is noticeable that the saturation of the length of the liquid finger is independent on the saturation of contact angle. Indeed, the length of the liquid finger does not show any saturation even of the contact angle is in the saturation regime. This effect is due to the fact that the length is only determined by the electrical behaviour of the liquid finger and not by the actual value of the contact angle. Indeed as soon as the contact angle is smaller than the threshold, the length of the liquid finger becomes infinite in the capillary frame. Here due to voltage loss there is a finite length. However as long as the breakup is avoided the voltage can be increased indefinitely, the length will continue to grow.

The model curve is then compared to our previous experimental results on the Figure 4.15. The shape of the curve is well rendered by the model curve as well as the value of the scaling with λ which is in reasonable agreement with the expectations considering the lack of accuracy in the determination of σ: with σ=0.14S$\times$m, $\lambda\omega^{1/2} = 0.21$ m$\times$ s$^{1/2}$ which compares well with the 0.26 found experimentally. The threshold voltage is in reasonable agreements with the values expected from the capillary transition.

4.4.6 Discussions

The model is not valid in the case where the volume of the drop is changing significantly during the filling of the groove the variation of the length as a function of the applied voltage does not follow the model behaviour. It is clear that in the case where the whole drop vanishes in the channel the length of the filament will be asymptotically smaller than the one expected from the model. The case of drops of volume of the order of the channel volume gives

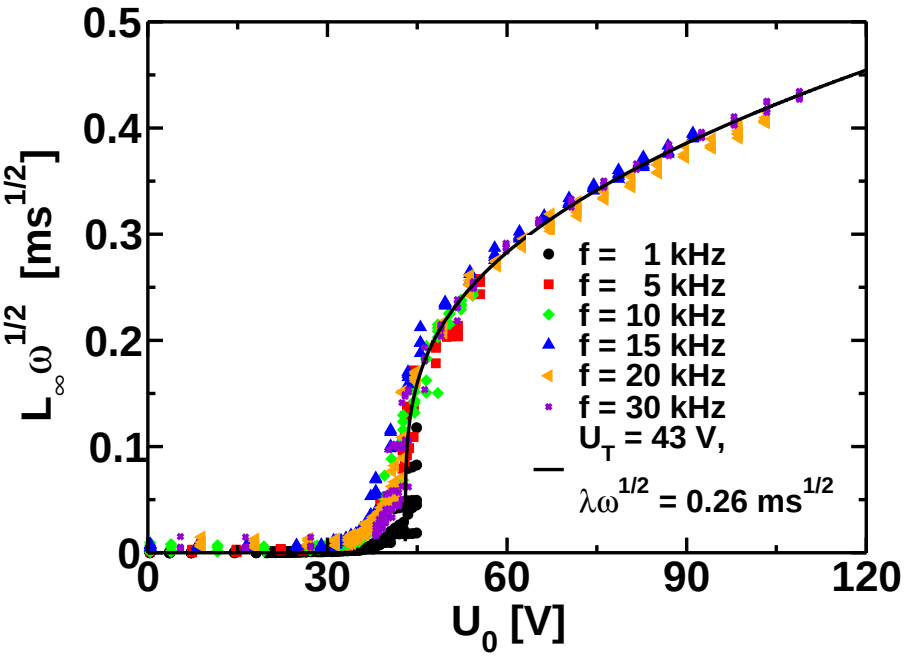

Figure 4.15: Comparison model - experiments. The electrical model gives nice agreement with the experimental data.

also a regime for which the drop vanishes entirely in the channel. A drop will vanish entirely in the channel for volumes V such that $V < WD\lambda$.

4.5 Conclusions

Electrowetting was used to induce morphological transitions on topographically structured substrates between a reservoir drop and a liquid filament in the channels. Above a threshold depending on the drop size and on the aspect ratio of the channels, the length of the filament depends on the applied voltage and its frequency in agreement with an electrical model. The threshold voltage is shown to depend on the reservoir pressure and on the geometrical parameters of the channels. The length of the liquid filament above the threshold depends on the frequency of the voltage source and on the conductivity of the liquid and not on the drop pressure. It is moreover shown that this length is independent on the contact angle saturation.

This system can be used for microfluidic actuation of liquid in channels: here a channel is wet on demand by a liquid using a simple voltage actuation. The transitions are reversible with aqueous drops in air. An actuation system using this phenomenon would be an easy to use system since the drop has just to be deposited on the channels. Moreover, the electrode used in all these experiments can be replaced by a syringe in order to have a direct control on the drop volume or composition.

Chapter 5

Electrowetting-Actuation of fluid in microchannels Part 2: Dynamics

Jean-Christophe Baret, Michel Decré, Stephan Herminghaus and Ralf Seemann

Contents

5.1 Introduction

In the Chapter 4 we studied the static properties of the electro-actuation of fluid in microchannels. We have showed that the liquid spreads to an equilibrium position determined by the penetration length of the electric voltage in the liquid finger λ.

$$\lambda = \sqrt{\frac{1}{\omega}\frac{2T\sigma}{\varepsilon_0\varepsilon_r}\frac{WD}{W+2D}}$$

This lengthscale discriminates two different regimes: when the length of the liquid finger is much smaller than the equilibrium length, *i.e.* $L \ll \lambda$ the voltage along the finger is constant and equal to the voltage applied to the drop. On the other hand, close to equilibrium $L \approx \lambda$ the voltage decreases along the liquid finger and cannot be considered as homogeneous. This implies that the description of the electric loss in the dynamics of the latest stage of the spreading ($L \approx \lambda$) is required.

We used the same experimental set-up as in the Chapter 4 to study the dynamics of the filling at different voltages. The channels are etched in a native conducting silicon wafer. An additional silicon oxide insulating layer and an hydrophobic OTS monolayer have then been processed using standard procedures. The idea in the following is to determine the time-scales of the filling dynamics and the relaxation to the equilibrium position both experimentally and theoretically based on previous work on capillary spreading. The actuation principle is based on capillary flow and the dynamics will thus be compared to related systems, mainly the capillary rise and capillary spreading in confined systems.

One of the first to study the spreading in confined system is Washburn who examined how a liquid was rising in a cylindrical tube and reaches its maximal static height named Jurin's height [108] z_J, determined by the balance of capillary and gravity forces:

$$z_J = \frac{2\gamma}{\rho g r_t}\cos\theta \tag{5.1}$$

with ρ, γ the density and surface tension of the liquid, g gravity acceleration, r_t the inner radius of the tube and θ the contact angle of the liquid on the

tube. From Washburn's analysis based on the balance of viscous dissipation, gravitational and capillary forces arises the so-called Washburn law[1] which determines the dimensionless height $\tilde{z} = z/z_J$ of the liquid front as a function of the dimensionless time $\tilde{t} = t/t_0$ in the absence of inertia [109],:

$$\tilde{z}\frac{\mathrm{d}\tilde{z}}{\mathrm{d}\tilde{t}} = 1 - \tilde{z} \tag{5.2}$$

where

$$t_0 = \frac{16\eta\gamma\cos\theta}{\rho^2 g^2 r_t^3} \tag{5.3}$$

η being the dynamic viscosity of the liquid. In dimensionless units the equilibrium position is $\tilde{z} = 1$. At short times $t \sim 0$, $\tilde{z} \ll 1$, Eq. 5.2 is integrated once leading to $\tilde{z} \propto \tilde{t}^{1/2}$. The speed of rise is expected to diverge as $v \sim t^{-1/2}$. The divergence is solved by a cut-off time below which inertia plays a role and defines a maximal speed [109]. At large times, the square root behaviour vanishes and the system relaxes to equilibrium. At the late stage of the rise $\tilde{z}$ is close to 1 and is written as $\tilde{z} = 1 - \epsilon\tilde{z}_1$ with $\epsilon \ll 1$ which reduces Eq. 5.2 to $\tilde{z}_1' = -\tilde{z}_1$ at the first order in ϵ. The height of rise relaxes exponentially to equilibrium. Both asymptotic cases $t \sim 0$ and $t \sim \infty$ and the crossover from one to another are described by the Washburn law.
The system we are presenting here involves more free surfaces than the capillary tube and is intermediate between capillary rise and the spreading of a drop. The latter problem has been studied by several authors and has been summarized in a review by Oron *et al.* [110]. More recently Warren [111] performed an analysis of the power law exponents for different driving forces of the spreading and showed that these exponents are not only sensitive to the driving force: the condition of spreading from a reservoir at constant pressure and the condition of spreading at constant volume lead to different exponents for the same driving force. Indeed to take the example of Washburn's law, a reservoir of liquid is placed at one side of the capillary and ensures a constant pressure condition at the inlet of the capillary. In the case of the spreading of a drop on a wetting substrate, there is no pressure reservoir but only conservation of the volume of the drop during the spreading. A summary of the power law exponents is given in the Table 5.1

We restrict our discussions to capillary-driven spreading (gravity is neglected). In the presence of a reservoir the table indicates that a character-

[1]The full calculation will be displayed and discussed in Section 5.3

System	Reservoir		References
	Yes	No	
Capillary-driven radial spreading	–	1/7 (2-D) 1/10 (3-D)	Tanner [112], Cazabat [113]
Gravity-driven radial spreading	–	1/5 (2-D) 1/8 (3-D)	Cazabat [113], Lopez [114]
Capillary-driven flow in a tube	1/2	–	Washburn [108]
Inertial-Capillary flow in a tube	1	–	Quéré [109]
Capillary rise in rough tubes	1.4 - 2	–	Schäffer [115]
Capillary-driven flow between plates	1/2	–	Dreyer [116]
Capillary-driven flow in a wedge	1/2	2/5	Romero [117], Warren [111]
Capillary-driven flow on a stripe	1/2	1/5	Darhuber [118] Warren [111]
Spreading on groove network	1/2	1/3	Warren [111]
Spreading on rough substrates	–	1/4 - 2/5	Cazabat [113]
Electrocapillary flow on stripes	1/2	–	Ahmed [119]
Electrocapillary flow in open-channels	1/2	–	see Section 5.2.2

Table 5.1: Summary of the power-law exponents for the spreading in different systems. No reservoir means that the liquid volume is conserved during spreading while Reservoir means that the liquid spreads from a reservoir which supplies a constant pressure.

istic exponent of 1/2 is expected and observed in most of the systems: wetting and electro-wetting on stripe, capillary rise, flow in a wedge (triangular grooves)... It is thus natural to expect such an exponent in our experiments. However the discussion is much richer when the constant pressure condition is replaced by the constant volume condition. In this situation there is a strong difference in the exponent even for similar systems, like the wetting of a stripe (1/5) and in a wedge (2/5).

Several authors studied the spreading kinetics but fewer studied the receding dynamics. Attempts performed on the capillary fall showed that a power law exponent of 1/2 is recovered for the height as a function of time. For this particular system an overpressure maintained the liquid meniscus above Jurin's height and was released to study the relaxation to equilibrium. For other systems, like wetting on a stripe such a pressure pre-actuation is not possible since the free-surface would destabilize before the desired initial state is reached. Yet dynamics remain an important topic, particularly because advancing and receding display different properties as illustrated in these two typical examples:

1. for a drop sliding on an inclined surface a pearling instability at the rear of the drop is observed above a critical speed [120, 121]. The origin of the instability is due to a maximal speed that a receding line can sustain which does not exist for an advancing contact line;

2. in triangular grooves ongoing work showed that a wedge can be filled by electrowetting similarly to what has been done in the present work. When the voltage is turned down, depending on the switch of contact angle that is induced, the liquid finger either recedes or develops a pearling instability leading to disconnected drops in the channel. The dynamics of the emptying can thus be very different in the same system. In rectangular grooves such an instability is not expected theoretically. Indeed it can be shown that the wavelength of the most unstable mode depends on the opening angle of the triangular groove and diverges at 0 degree opening angle. Asymptotically, a zero degree opening angle corresponds to rectangular groove: no instability is expected and we did not observe it in our system. In practical cases it is sufficient that the wavelength of the instability be larger than the length of the channel

to avoid the instability.

Our system allows to perform a pre-actuation of the liquid in the channel and to study both advancing and receding dynamics.

5.2 Dynamics – Filling of the channel

We studied the dynamics of groove filling as a function of the applied voltage, the frequency of the voltage source and the dimensions of the channels. Drops were deposited on the grooves and the volume of fluid spread in the groove was always a small portion of the total volume. The mother drop is thus considered as a reservoir.

5.2.1 Experiments

As we have seen in Chap. 4, the frequency of the voltage source has an influence on the length of the liquid finger wetting the channel in the equilibrium state. Except right at the transition, the equilibrium length is given by the electrical length-scale λ. It has been demonstrated in Chap. 4 that the equilibrium length is the result of the electrical loss along the liquid finger. The voltage penetrates in the liquid only up to a length λ which limits the extension of the electrowetting effect and by consequence of the liquid finger to a length $\approx \lambda$.

In a first step, for simplicity, we will study the dynamics in the absence of electric loss along the liquid finger, *i.e.* working at low frequency of the voltage source ($f_1 = 1$ kHz). Indeed in this situation, the total length of the channel (2 mm) is smaller than the electric length scale λ: the voltage is thus constant all along the liquid finger.

In a second step we study the relaxation to equilibrium working with a voltage source at $f_2 = 20$ kHz. The analysis of the dynamics will then be performed in analogy with Washburn's model.

5.2.2 Low frequency, early stage of the spreading

The experiments are performed as follows. A drop of the solution is deposited on the surface. A voltage larger than the threshold voltage is applied briefly in order to induce the filling and to start the experiments with a Wenzel drop. A voltage step from 0 to U_0 is applied to the drop. The length of the liquid finger is recorded as a function of time via a Philips DICA camera at a frame rate close to 200 fps. The voltage is then turned back to 0 before the liquid finger reaches the end of the channel to avoid any pinning at the edge. Under these conditions, the equilibrium position is not reached, as displayed in Fig. 5.1. The dynamics depend on the value of the applied voltage:

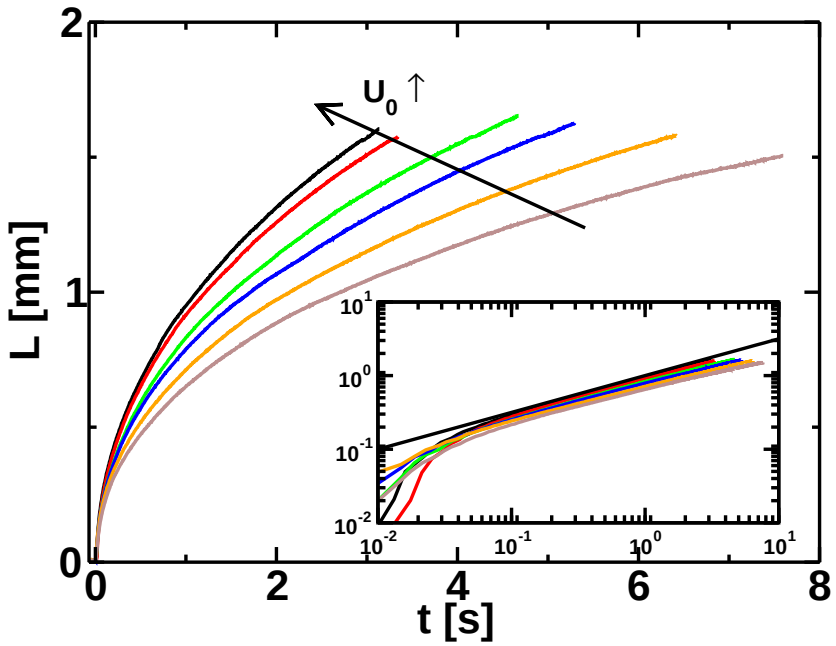

Figure 5.1: Filling dynamics in open micro-channels at 1 kHz for different applied voltages U_0 (60, 65, 70, 75, 80 and 85 V). The equilibrium position is not reached: the voltage is turned off before the liquid fills entirely the channel. Inset: the dynamics display a power-law behviour of the length as a function of time with an exponent 1/2.

1. for voltages below $\approx$ 45 V, no filling is observed as discussed in Chap. 4

(data not shown).

2. between 45 V and 60 V, the liquid finger reaches an equilibrium position determined by the electric loss. Since the relaxation to equilibrium will be studied in the next section, these data are netther discussed nor shown here.

3. above 60 V, the equilibrium length is not reached within the duration of the experiments. The spreading dynamics shows a dependence on the value of the applied voltage. In a logarithmic scale the data show a power-law behaviour of the form:

$$L^2(t) = \kappa \times t \tag{5.4}$$

on almost two orders of magnitude in time (see inset of Fig. 5.1). The experiments show that an increase of voltage leads to an increase of κ: the spreading in the channel becomes faster at higher voltages.

Analysis – Looking back to Washburn's analysis, a power-law exponent of 1/2 is the result of a constant driving force balanced by viscous dissipation [108, 109] and has been reproduced in many systems [111, 118, 117], especially in Ahmed *et al.*'s experiment of electrophoretic actuation on stripes [119]. In our case the length is smaller than λ which indicates that the voltage is approximately constant along the liquid finger: the electric loss is negligible and the contact angle of the liquid is homogeneous and determined without any ambiguity as Lippmann's angle at the applied voltage U_0. The electrocapillary forces are thus constant and uniform in all the system which ensures a constant driving force for the motion. The 1/2 power law is the sign of the spreading at constant pressure difference (or constant driving force) between the tip and the mother drop.
In a circular capillary tube the coefficient κ can easily be expressed analytically and is proportional to the cosine of the contact angle of the liquid in the tube $\cos\theta$ [108]. Decreasing the contact angle thus increases the value of κ to a maximum reached for 0 degree contact angle. In our case the analytical expression of κ requires the computation of the viscous dissipation in an open channel which is a problem that has not been addressed to the author's knowledge. However κ is expected to differ only via a numerical correction and the contact angle dependence should remain. Since we know

that electrowetting enhances the wettability of the surface and lowers the contact angle, the driving force of the spreading increases with an applied voltage which explains the variations of κ with the voltage.

Conclusions – In the absence of electric loss, a liquid finger under electrowetting conditions spreads in the grooves according to a power law behavior similar to capillary rise in a tube (in particular with an exponent 1/2: $L^2(t) = \kappa \times t$). The coefficient κ is voltage dependent as a result of the voltage dependence of the contact angle via Lippmann's equation. A more complete analysis on κ will be performed in the following section.

5.2.3 High frequency, equilibrium position

Working at 20 kHz the equilibrium length of the liquid finger is now close to one millimetre, smaller than the channel length. Therefore the liquid finger will reach the equilibrium length before the end of the channel. Upon increasing the voltage from 0 to U_0, the length of the liquid finger as a function of time is extracted from the images and as expected reaches a voltage dependent equilibrium position L_∞ as studied in Chap. 4 (see Fig. 5.2, Fig. 5.3, and Fig. 5.4).

This equilibrium length L_∞ is measured as a function of applied voltage for the different aspect ratios and gives the typical static plots shown in the Chapter 4. From all the data a single length scale $\lambda = 1.15/(1+2A)^{1/2}$ mm is determined (see Fig. 5.5). This length scale is determined from the static measurements and is used to rescale all the experimental lengths, using the corresponding value of the aspect ratio A.

When the data are plotted in a logarithmic scale we observe the typical power-law behaviour with 1/2 exponent at the early stage of the spreading(*i.e.* at small lengths). Eq. 5.4 is slightly modified:

$$L^2(t) \sim \kappa \times t,\ t \sim 0 \tag{5.5}$$

As before, the coefficient κ is a function of the applied voltage: increasing the voltage increases the value of κ. Thus in the early stage of the spreading the typical features observed at 1 kHz remain. The coefficient κ is now obtained

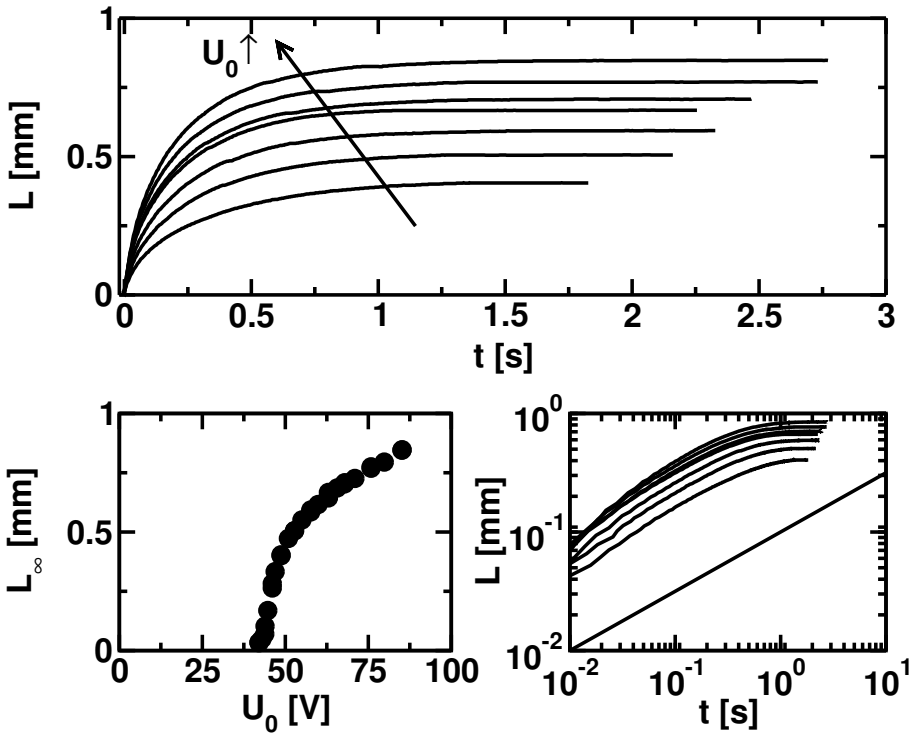

Figure 5.2: Filling of the channels at 20 kHz ($A = 1.33$). Top: length at $U_0 \in [49, 53, 58, 63, 68, 76, 85]$ V. The equilibrium length L_∞ is reached after a few seconds (bottom left). Bottom right: a power law exponent of 1/2 is recovered in the early times of the spreading.

as the slope of $L^2(t)$ at $t \sim 0$ and is plotted as a function of contact angle obtained from the electrowetting curve in Fig. 5.6. The coefficient κ is a linear function of the contact angle. At a threshold contact angle θ_T, κ is equal to zero; above the threshold the linear relationship between κ and $\cos\theta$ shows that the system acts as a pure capillary system where the driving force is proportional to the difference between the cosine of the contact angle and the cosine of threshold contact angle. From this an intrinsic penetration coefficient independent of the applied voltage (or on the contact angle) κ_0 can be extracted:

$$\kappa = \kappa_0 \times (\cos\theta_L(U_0) - \cos\theta_T) \tag{5.6}$$

When the voltage is above the threshold voltage of the filling, the coefficient κ is positive. When the voltage is below U_T, κ is negative which allows only

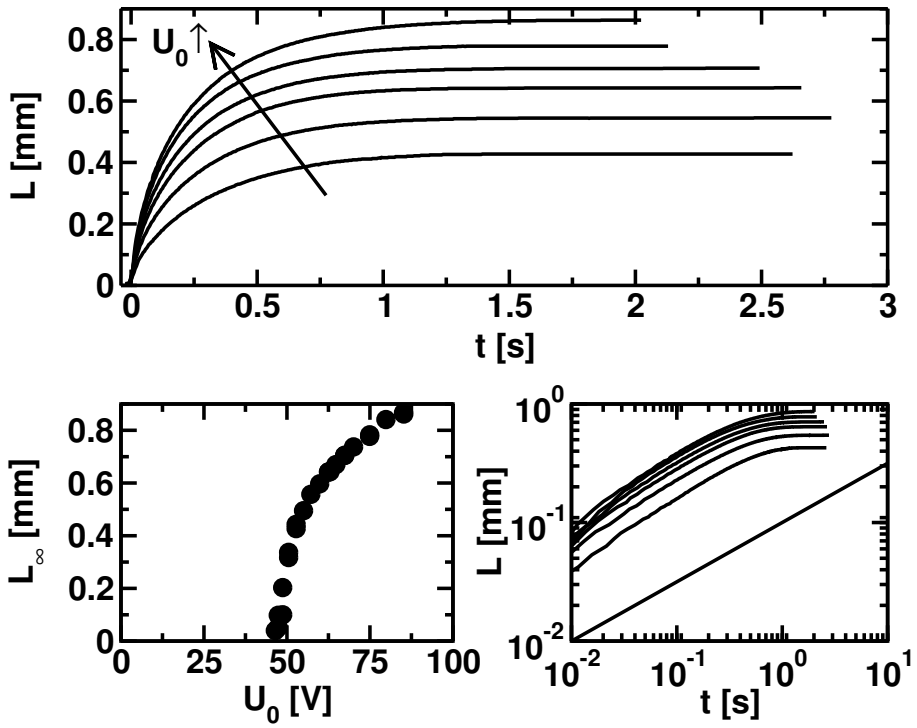

Figure 5.3: Filling of the channels at 20 kHz ($A = 1.00$). Top: length at $U_0 \in [53, 57, 62, 67, 75, 85]$ V. The equilibrium length L_∞ is reached after a few seconds (bottom left). Bottom right: the power law exponent of 1/2 is recovered in the early times of the spreading.

receding contact lines.

$$\kappa \geq 0 \leftrightarrow U_0 \geq U_T \tag{5.7}$$

It has thus been shown that κ is effectively linked to the contact angle: the dynamics of the filling at the early stage is explained by considering that the motion is driven by Lippmann's contact angle. This will have consequences in the following to explain the relaxation to equilibrium.

Note – Our system behaves similarly to capillary rise in a circular tube of radius r_t. Indeed, for a contact angle of 0 degrees in the tube, the coefficient κ_c is simply $\gamma r_t/2\eta$ which is usually corrected by the contact angle as $\kappa_c^\theta = \kappa_c \times \cos\theta$. In the case of a capillary tube, the filling is obtained at 0 pressure when the contact angle is smaller than 90 degrees. The threshold contact angle of filling in a tube is thus 90 degrees. This leads to the same expression

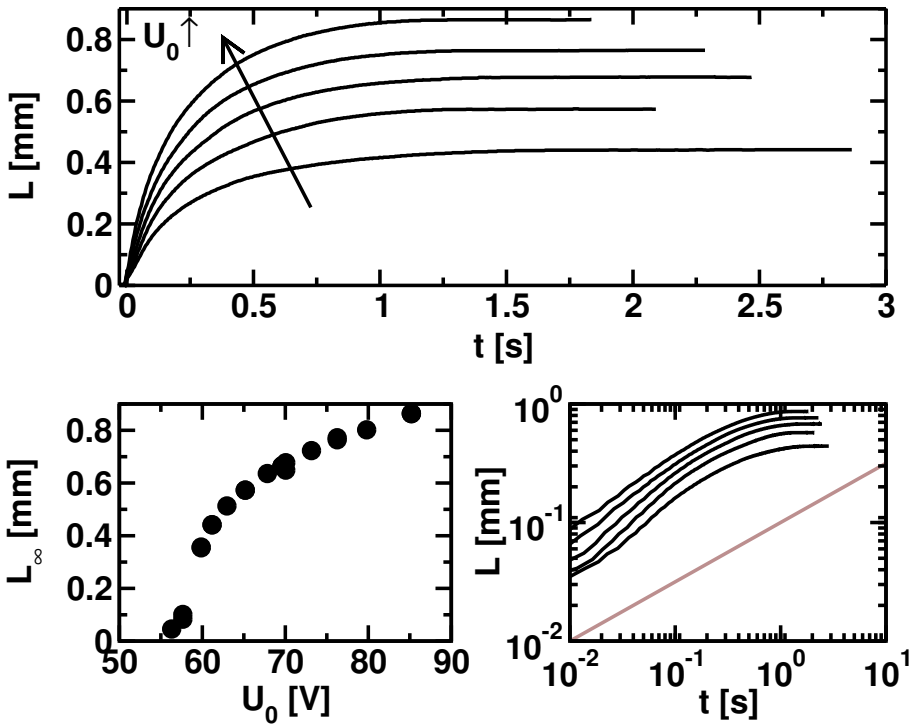

Figure 5.4: Filling of the channels at 20 kHz ($A = 0.66$). Top: length at $U_0 \in [61, 65, 70, 76, 85]$ V. The equilibrium length L_∞ is reached after a few seconds (bottom left). Bottom right: a power law exponent of 1/2 is recovered in the early times of the spreading.

as in Eq. 5.6 using $\cos\theta_T = 0$:

$$L^2 = \frac{\gamma r_t}{2\eta}\left(\cos\theta - \cos\frac{\pi}{2}\right) \times t \tag{5.8}$$

5.2.4 Conclusions

In the early filling stage, the spreading dynamics obtained in the absence of voltage loss is recovered: the pressure difference is thus constant which indicates that the voltage is constant and uniform. This result is in agreement with the fact that the lengths are smaller than the penetration length λ.
In addition to the value of the equilibrium length, the applied voltage determines the dynamics of the filling and gives a threshold for the filling via the penetration rate κ. κ is directly linked to the wettability change and is directly determined by the Lippmann contact angle. This ingredient will be the starting point of the full description of the filling dynamics hereafter.

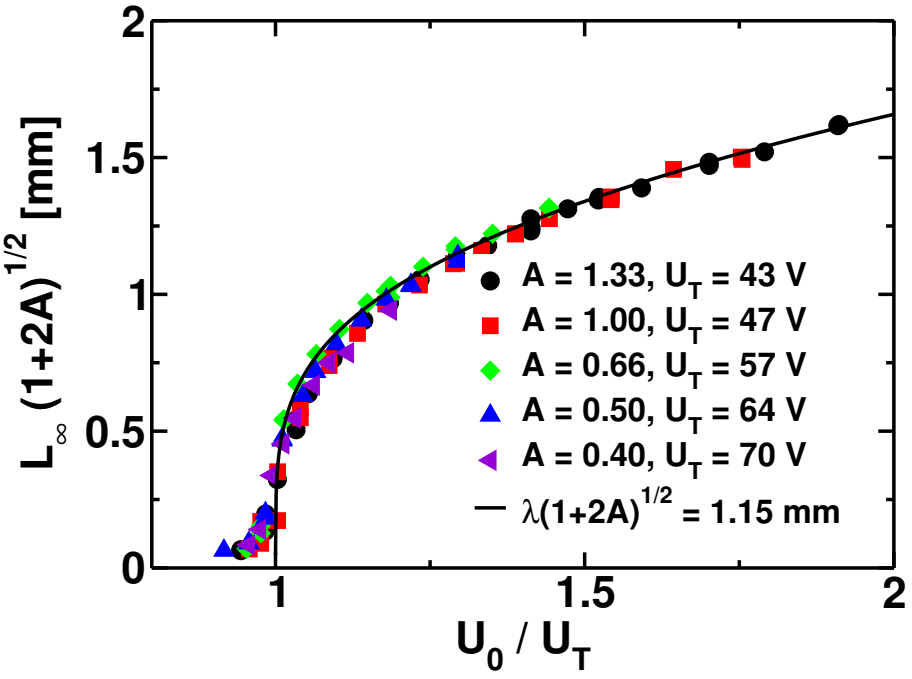

Figure 5.5: Equilibrium length L_∞ for the different aspect ratios. A single length scale λ is defined: $\lambda = 1.15/(1+2A)^{1/2}$ mm.

5.3 Modeling the dynamics

We are interested in modelling the full dynamics of the groove filling using electrowetting. The model based on capillarity is extended to the dynamics using the same tools as in the theoretical description of the filling of capillary tubes (see Washburn 5.19 and Quéré [109]). Indeed, similarly to Washburn, we expect (and observe) a saturation to a finite length. However the nature of the equilibrium length is different: the increase of hydrostatic pressure in Washburn's law is here replaced by a loss of voltage along the liquid finger. Instead of writing a force out of the electric loss we will consider that the driving force related to electrowetting is decreasing when the liquid finger increases: the basic idea will be to consider that the driving force is the contact angle at the tip of the finger which is determined by the local voltage at the tip from the Lippmann curve. First we will derive a simple hydrodynamic model to express the viscous dissipation in the case of open-air channels.

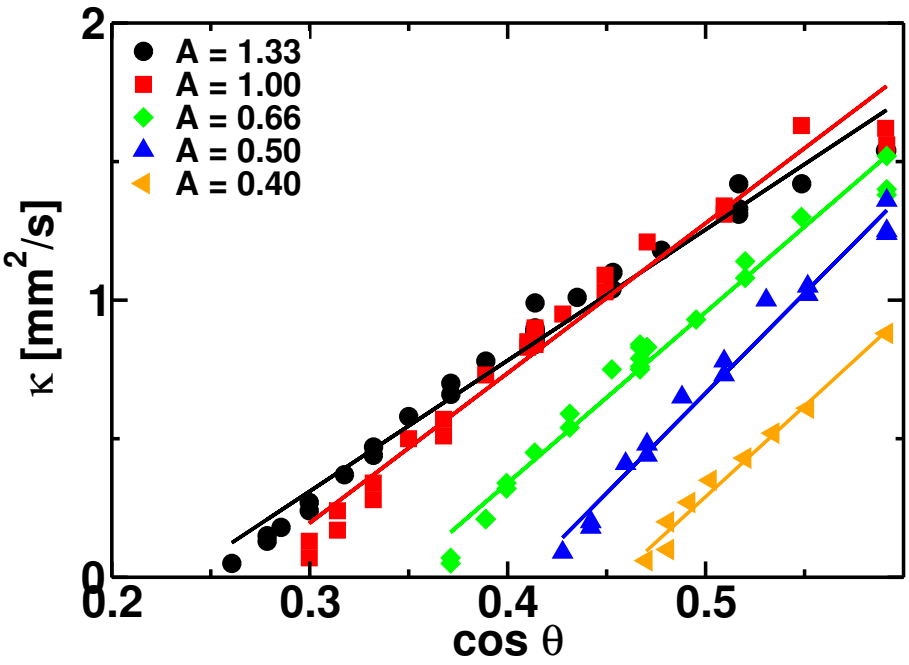

Figure 5.6: Propagation coefficient κ as a function of the contact angle obtained from the Lippmann curve. The propagation coefficient κ is proportional to $(\cos\theta_L - \cos\theta_T)$

5.3.1 Capillary flow in an open air rectangular channel

Writing the excess of energy required to increase the length L of a liquid finger at zero Laplace pressure by $\mathrm{d}L$ one finds:

$$\frac{\mathrm{d}E}{\mathrm{d}L\gamma\Sigma_{\mathrm{ls}}} = \frac{\Sigma_{\mathrm{lv}}}{\Sigma_{\mathrm{ls}}} - \cos\theta_Y \tag{5.9}$$

where Σ_{ls} is the surface area per unit of length which is wetted by the liquid and Σ_{lv} the surface per unit of length of the liquid / vapor interface. Defining $\cos\theta_T = \Sigma_{\mathrm{lv}}/\Sigma_{\mathrm{ls}}$, we obtain:

$$\frac{\mathrm{d}E}{\mathrm{d}L\gamma\Sigma_{LS}} = \cos\theta_T - \cos\theta_Y \tag{5.10}$$

In the case of a closed and circular capillary tube Σ_{LV} is zero thus $\cos\theta_T = 0$. The transition occurs at 90 degrees. In the case of a channel with rectangular cross-section and aspect ratio A one recovers the expression

$$\cos\theta_T = 1/(1+2A)$$

In order to determine the dynamics of the filling we balance the excess of capillary energy with the viscous dissipation. In the case of a closed circular capillary one has [109]

$$8\pi\eta LL' = -\frac{\mathrm{d}E}{\mathrm{d}L} = \gamma 2\pi r\cos\theta_Y \tag{5.11}$$

In our case the expression of the viscous dissipation has to be calculated and depends *a priori* on the dimensions of the channel. The calculation has to take the free-surface boundary into account and a non-slip boundary condition at the solid / liquid interface. In order to determine the viscous dissipation, we assume for simplification that the free-surface is flat which corresponds to a situation where the Laplace pressure in the channel is constant and equal to zero. We expect that the curvature of the free-surface will lead to a minor correction in the flow rate expression that can be included if necessary. The Stokes equation in a channel reads:

$$\frac{\partial^2 v_y}{\partial x^2} + \frac{\partial^2 v_y}{\partial z^2} = \frac{a}{\eta} \tag{5.12}$$

v_y being the speed in the direction y of the channel while x and z are the physical coordinates perpendicular to the flow and a is the pressure gradient along the channel. This equation has been already solved for the mechanical torsion of rectangular bars [122] or for flow in closed channel [123] using Fourier decomposition. Our boundary conditions

$$\begin{cases} v_y(x = \pm W/2, z) = 0 \\ v_y(x, z = 0) = 0 \\ \frac{\partial v_y}{\partial z}(z = D) = 0 \end{cases} \tag{5.13}$$

select different modes in the Fourier decomposition. Rescaling x and z by W and v_y by $v_0 = W^2 a/\eta$, one finds:

$$\frac{v_y(x,y)}{v_0} = \frac{4}{\pi^3}\sum_{n\in 2\mathbb{N}+1}\frac{(-1)^{(n-1)/2}}{n^3}\cos(n\pi x)\left(\frac{\cosh(n\pi(z-A))}{\cosh(n\pi A)} - 1\right) \tag{5.14}$$

Examples of computed profiles are given for $A \in \{0.4, 0.5, 0.66, 1.00, 1.33\}$. The first 25 terms of the sum have been taken into account. The velocity profile can then be integrated in order to find the flow rate $\mathcal{Q}$

$$\mathcal{Q} = W^2 v_0 \int_{x=-1/2}^{1/2}\int_{z=0}^{A}\frac{v_y(x,z)}{v_0}\mathrm{d}x\mathrm{d}z = W^2 v_0 F(A) \tag{5.15}$$

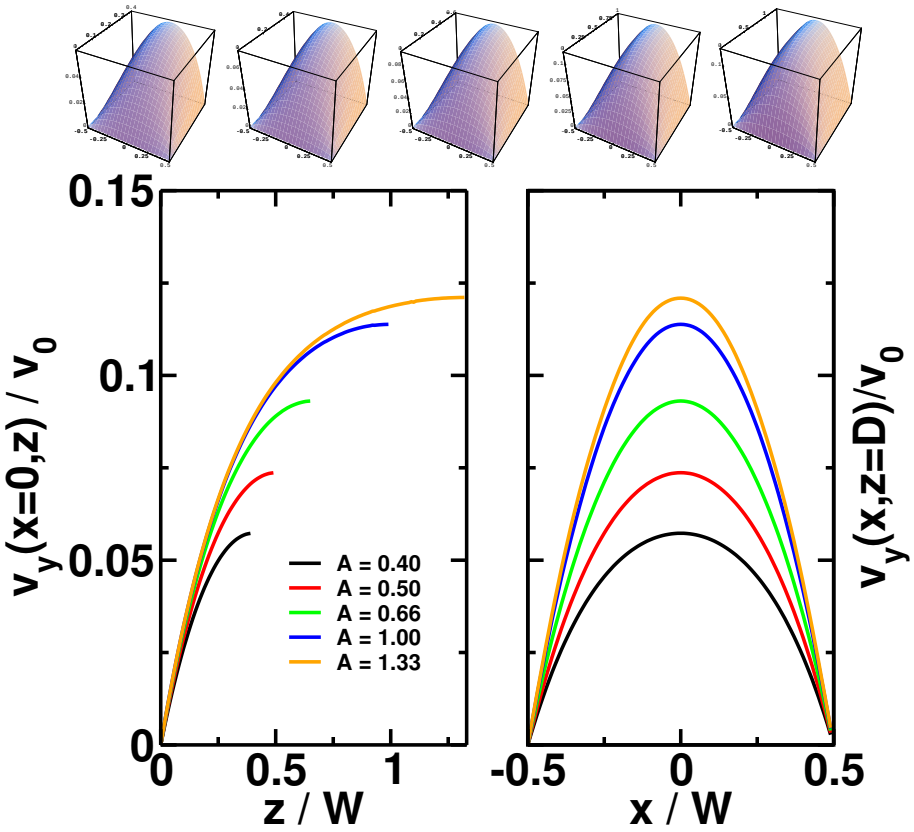

Figure 5.7: Flow profile in different rectangular open-channel. The free-surface is assumed to be flat during the flow.

where F is a function of A only integrating the flow field. $\mathcal{Q}$ is on the other hand equal to $W \times D \times \mathrm{d}L/\mathrm{d}t$:

$$W \times D \times \frac{\mathrm{d}L}{\mathrm{d}t} = \frac{W^4}{\eta} a F(A) \tag{5.16}$$

a is the pressure gradient $\delta P/L$ with $\delta P = \gamma(\cos\theta - \cos\theta_T)\frac{W+2D}{WD}$. After all, the length of the liquid finger follows the differential equation:

$$2L\frac{\mathrm{d}L}{\mathrm{d}t} = \kappa_0(\cos\theta - \cos\theta_T) \tag{5.17}$$

where:

$$\begin{cases} \kappa_0 &= \kappa^* \times G(A) \\ \kappa^* &= \frac{2\gamma D}{\eta} \\ G(A) &= F(A) \times \frac{1+2A}{A^3} \end{cases} \tag{5.18}$$

κ_0 and κ^* have the dimensions of a diffusion coefficient describing the way the liquid diffuses in this simple porous medium. κ_0 can be measured experimentally and κ^* is determined by the system parameters: with our parameters, $\kappa^* \approx 32$ mm^2/s. $G(A)$ is a geometrical correction associated to the laminar flow in the channel of aspect ratio A. Provided that L only is time dependent the integration of Eq. 5.17 leads to a square root behaviour:

$$L^2(t) = \kappa_0(\cos\theta_Y - \cos\theta_T)t \tag{5.19}$$

Electrowetting is included in this model considering that the filling is due to the wettability at Lippmann's contact angle θ_L and not Young's contact angle. The behaviour of the fluid under the conditions of eletrowetting is thus expected to follow a modified capillary rise equation:

$$L^2(t) = \kappa_0(\cos\theta_L - \cos\theta_T) \times t \tag{5.20}$$

The dependence on the voltage is only present in the contact angle. The coefficient κ_0 is found to be independent of the applied voltage and depends only on the aspect ratio of the channel and the hydrodynamical parameters of the liquid. A comparison between the calculated κ_0 and the experimental values of κ_0 is given in Fig. 5.8. Even though the exact shape of the curve is not reproduced the agreement is satisfactory in particular when considering that we use no fit parameters. The model gives thus a qualitative agreement for the dynamics: the power law behaviour and the values of the propagation coefficient κ_0 are consistent with experimental observations. The shape discrepancy may have several origins the most probable coming from the assumption of a flat free-surface. This simple equation is valid as long as the driving force of the invasion is constant: in the case of capillary rise this means until gravity counteracts the rising motion and stabilizes the liquid front at Jurin's height; in electrowetting, the counteracting force is replaced by the loss of voltage through the capacitive coupling: λ has been introduced in the static case as the length-scale over which the voltage penetrates the liquid finger. As long as $L \ll \lambda$, the voltage along the channel is constant and defines only one contact angle and the liquid filament has to increase following the square root law. The saturation to the finite length L_∞ is represented by the increase of the contact angle at the tip due to the voltage decrease. When it reaches the threshold contact angle the wetting is not favourable any more, the driving force is then going to zero which means

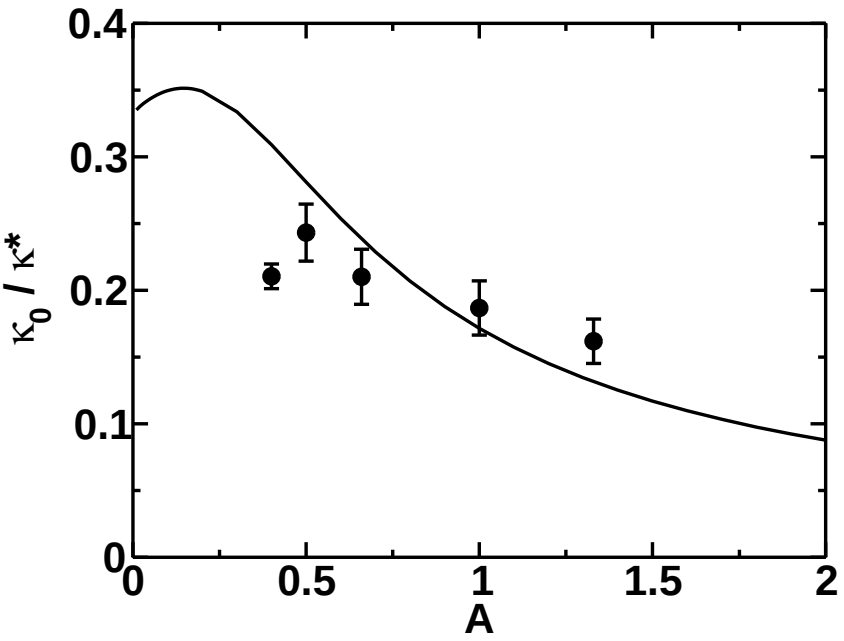

Figure 5.8: Comparison of κ_0 obtained experimentally with the model based on the computation of the fluid velocity: the full line corresponds to the computation of $G(A)$. $\kappa^* = (2\gamma D/\eta) \approx 32$ mm^2/s is obtained with the experimental values, $\eta = 80$ mPas, $\gamma = 65$ mN/m, $D = 20$ μm.

that the relaxation to the equilibrium will involve an exponential decay.

5.3.2 Relaxation to equilibrium

Washburn's law is obtained for gravity counteracting surface tension proportionally to the length of the liquid column. Here we make the assumption that the variation of the voltage at the end of the filament defines locally the wetting properties of the liquid in the channel and drive the liquid in the channel:

$$2L\frac{\mathrm{d}L}{\mathrm{d}t} = \kappa_0 \times (\cos\theta(x = L) - \cos\theta_T) \tag{5.21}$$

The value of $\cos\theta(x = L)$ is determined using the Lippmann curve for the local voltage at the tip $U(x = L)$ which has thus to be determined at any

time. So far we only know that at $t = 0$, $U(x = L = 0) = U_0$ and that at equilibrium $U(x = L_\infty) = U_T$.

In order to determined $U(L)$ we first discuss the two main time-scales in the system. The time scale of charging a liquid finger of length L is roughly determined by the RC constant τ_{el} of the liquid finger which is simply written as:

$$\tau_{\text{el}} = \frac{L}{\sigma W D} \times \frac{\varepsilon_0 \varepsilon_r (W + 2D) L}{D} = \frac{L^2}{\lambda^2} \times \frac{1}{\omega} \tag{5.22}$$

Since L is always smaller or of order λ, $\tau_{\text{el}} < 1$ ms in all the experiments. On the other hand the time scale for the finger motion τ_{hydro} is of the order 1 s. We thus have:

$$\tau_{\text{el}} \ll \tau_{\text{hydro}}$$

This implies that electrical equilibrium is fulfilled during the motion of the tip: the voltage in the finger is **instantaneously** redistributed during the motion as a result of the change in the boundary conditions at L. As a result the boundary condition of zero current at the tip is valid. In order to determine the voltage along the channel, we have to solve the electrical circuit presented in Chap. 4 (see also Appendix D):

$$\frac{\mathrm{d}^2 U}{\mathrm{d}X^2} = 2j \frac{U(X)}{\lambda^2} \tag{5.23}$$

without using the boundary condition $U(L) = U_T$ which is a condition of hydrodynamic equilibrium. The voltage along a liquid finger of length $L = \lambda \times l$ is thus a function of the position and of the length l:

$$\frac{U(x,l)^2}{U_0^2} = \frac{\cosh^2(x-l) - \sin^2(x-l)}{\cosh^2 l - \sin^2 l} \tag{5.24}$$

Eq. 5.24 is plotted in Fig. 5.9 for different liquid finger lengths and shows that the voltage decay along the liquid finger is increasing with increasing length. When $l \to \infty$, Eq. 5.24 provides $U(x,l) \sim U_0 \exp(-x)$ which is the classical exponential decay of a voltage along a coaxial cable using a boundary condition at infinity. The enveloppe of the extrema is obtained simply by taking $x = l$ in Eq. 5.24:

$$U(l,l)^2 = \frac{U_0^2}{\cosh^2 l - \sin^2 l} \tag{5.25}$$

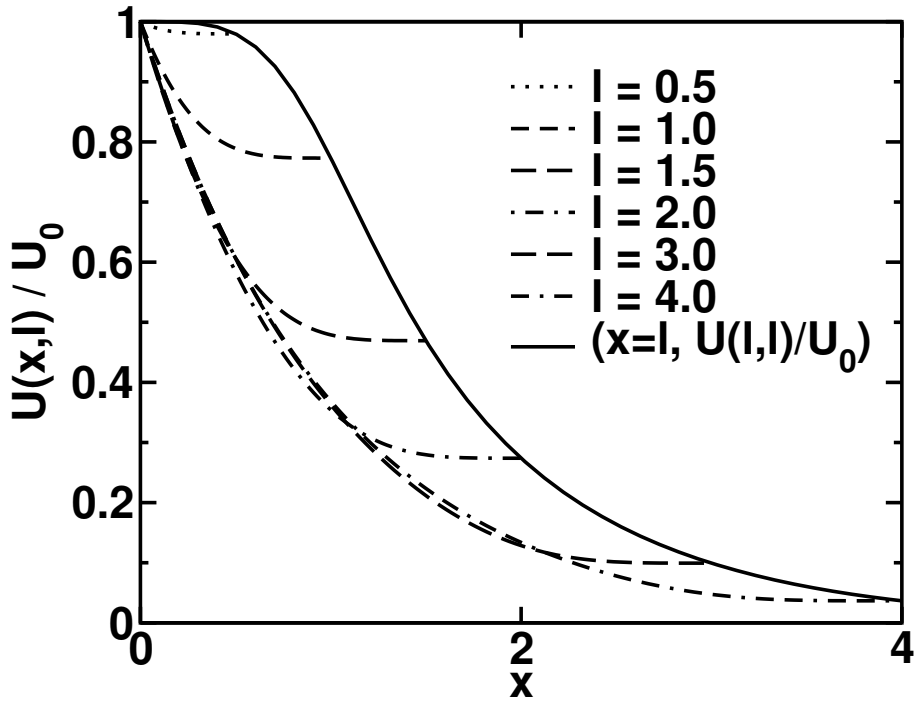

Figure 5.9: Voltage decay along the liquid finger for increasing dimensionless lengths(0.5 - 4). At small lengths, the voltage is close to the applied voltage U_0. When the length increases the voltage drop becomes increasingly significant. The full line is the envelope of the extrema $\{x = l, U(l,l)/U_0\}$.

At equilibrium the boundary condition used in the static case is recovered:

$$U(l_\infty, l_\infty)^2 = U_0^2 \times \frac{1}{\cosh^2 l_\infty - \sin^2 l_\infty} = U_T^2 \tag{5.26}$$

The voltage at the tip is equal to the threshold voltage which is only valid at equilibrium. The system is out of equilibrium as long as $U(l,l) > U_T$ and reaches equilibrium when $U(l,l) = U_T$ where $l = l_\infty$. The relationship between the voltage is system-dependent via the experimental Lippmann curve. From this analysis, the electric loss can be expressed as an opposing force for the fluid motion in the channel. Two situations have to be discussed, the ideal case of the Lippmann regime and the practical case we have here with the experimental relationship between the contact angle and the voltage.

Ideal case – In the ideal case, the contact angle is determined by Lippmann's equation: $\cos\theta = \cos\theta_Y + (U_0/U_L)^2$. Combining Eq. 5.21 and Eq. 5.25

one obtains:

$$2L\frac{\mathrm{d}L}{\mathrm{d}t} = \kappa_0 \times \frac{1}{U_L^2}\left(\frac{U_0^2}{\cosh^2 l - \sin^2 l} - \frac{U_0^2}{\cosh^2 l_\infty - \sin^2 l_\infty}\right) \tag{5.27}$$

The terms of the equations are then rearranged:

$$2L\frac{\mathrm{d}L}{\mathrm{d}t} = \kappa_0 \times \frac{U_0^2 - U_T^2}{U_L^2} - \kappa_0 \frac{U_0^2}{U_L^2} \times \left(\frac{\sinh^2 l - \sin^2 l}{\cosh^2 l - \sin^2 l}\right) \tag{5.28}$$

Eq. 5.28 is the exact analogue to Washburn's law. The first term in the equation is the driving force of the motion: the wettability at Lippmann's angle. The second term is an equivalent opposing force F_{el} which is here due to the electric loss along the finger which can be compared to the hydrostatic pressure in the Washburn law. The opposing force depends on the length of the liquid finger L/λ:

$$F_{\mathrm{el}} = \frac{2\gamma DG(A)U_0^2}{U_L^2} \times \left(\frac{\sinh^2 L/\lambda - \sin^2 L/\lambda}{\cosh^2 L/\lambda - \sin^2 L/\lambda}\right) \tag{5.29}$$

In the absence of electric loss, λ is infinite and F_{el} is equal to zero. In the balance of force the only remaining term is the electrowetting term which balances the viscous dissipation. In the early stage of the spreading, one has $L/\lambda \ll 1$ and $F_{\mathrm{el}} \propto (L/\lambda)^4$, the opposing force is negligible, see Fig. 5.10. It is only in the latest stage of the spreading that F_{el} becomes of the order of the driving force leading to an exponential relaxation.

Our practical case – In our case and for the regimes of voltage considered in the following the contact angle follows a simple linear law as a function of the applied voltage. It should be noticed that we are not in the Lippmann regime: here, above 40 V, we have a linear regime between the voltage and the contact angle which fits with:

$$\cos\theta_L - \cos\theta_Y = U_0/U_{LL} \tag{5.30}$$

where $U_{LL} = 122V$ is determined from a linear fit of the electrowetting curve. Eq. 5.21 can thus be re-written as

$$2ll' = \frac{\kappa_0}{\lambda^2}\frac{U_T}{U_{LL}}\left(\sqrt{\frac{\cosh^2(l_\infty) - \sin^2(l_\infty)}{\cosh^2 l - \sin^2 l}} - 1\right) \tag{5.31}$$

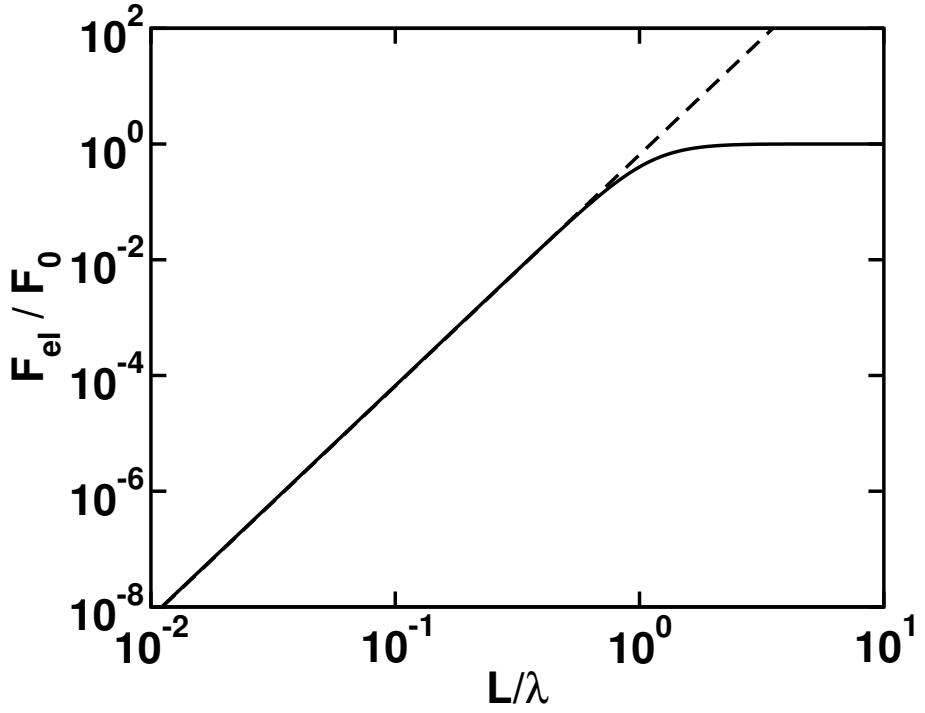

Figure 5.10: Equivalent counteracting force to the spreading F_{el} coming from the loss of voltage along the liquid finger. At short length, the opposing force scales as L^4 (dashed line). $F_0 = 2\gamma DG(A)U_0^2/U_L^2$

The parameter τ_{dyn}

$$\tau_{\text{dyn}} = \frac{\lambda^2}{\kappa_0}\frac{U_{LL}}{U_T} \tag{5.32}$$

is a time scale used as a fit parameter for the experimental data which roughly corresponds to the time required to diffuse to a length of order λ. Equation 5.31 is solved numerically. For each value of U_0 the value of τ_{dyn} is determined by the fit. This value is expected to be independent of the applied voltage. The fits of the experimental data by the model are displayed in Fig. 5.11 as well as the values obtained for the parameter τ_{dyn}. The fits and the experimental data are in perfect agreement indicating that the model used correctly describes the dynamics. Moreover τ_{dyn} is constant as soon as U_0 is sufficiently large compared to U_T. It should be noted here that for each model curve there is only one fit parameters, the time scale τ_{dyn}. The electrical length-scale is experimentally determined from the equilibrium length: $\lambda \times (1+2A)^{1/2} = 1.15$ mm is used for all fits using the corresponding value

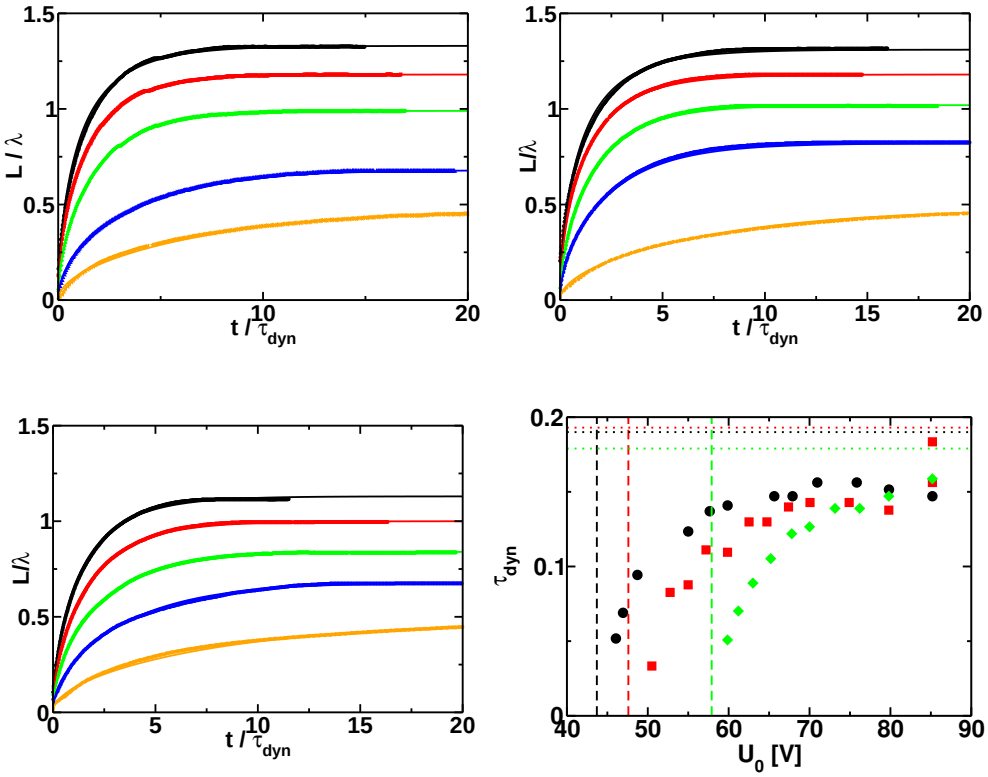

Figure 5.11: Fits of the experimental curves with the model curve. The only fit parameter is τ_{dyn}. The length is rescaled by λ. Top left, top right and bottom left: fits for different voltages and aspect ratios of 1.3 ($U_0 \in [46, 49, 58, 68, 85]$), 1.0 ($U_0 \in [50, 57, 64, 75, 85]$) and 0.66 ($U_0 \in [60, 63, 68, 76, 85]$) respectively. Bottom right: values of the fits used in the graphs. The model predicts that τ_{dyn} is time independent which is observed for voltages significantly above the threshold. The vertical dashed lines represent the position of the threshold for the different aspect ratios. The horizontal lines represent the expectations from Eq. 5.32 which are 20% off.

of A. Once this parameter is fixed the time-scale is changed in order to find the best fit with the experimental data. The variation of the time-scale τ_{dyn} then plotted as a function of the applied voltage. Considering the model, this time-scale is expected to be constant which is observed as soon as the voltages are far enough from the threshold voltages as displayed in Fig. 5.11. According to the previous work by Romero and Yost, our analysis is expected

to break-down close to the transition [117] which could explain the behaviour close to the threshold and the increase of the time scale. Another explanation could be that close to the threshold the driving force has become smaller than the pinning forces: the equilibrium length is thus not reached which leads to an error on the determination of $\tau_{\rm dyn}$. In the end the discrepancy between the experimental and "theoretical" time scales is around 20% which gives an extremely reasonable agreement considering the rough approximations made in the calculation of the flow rate in the channel. Moreover the values of $\tau_{\rm dyn}$ obtained in this way are consistent with the values obtained for κ_0 according to Eq. 5.32. It should also be noted that one can write an opposing force $F_{\rm el}$ similarly to the ideal case. Here the balance of forces involves the viscous dissipation $F_{\rm visc} = 2\eta LL'$, the driving force $F_{\rm wett} = 2\gamma DG(A)(\cos\theta_L - \cos\theta_T)$ and the opposing force:

$$F_{\rm el} = 2\gamma DG(A)\frac{U_0 - U(x=L)}{U_{LL}} \tag{5.33}$$

which can be written:

$$F_{\rm el} = 2\gamma DG(A)\frac{U_0}{U_{LL}}\left(1 - \frac{1}{\sqrt{\cosh^2(L/\lambda) - \sin^2 L/\lambda}}\right) \tag{5.34}$$

For $L \ll \lambda$, $F_{\rm el} \approx (L/\lambda)^4$ which indicates that the electric loss does not influence the spreading. At equilibrium one obtains $F_{\rm el}(L_\infty) = F_{\rm wett}$.

Note on the general case – When the relationship between $\cos\theta$ and U_0 is given by an increasing function $\mathcal{F}(U_0) = \cos\theta$ the opposing force reads:

$$F_{\rm el} = 2\gamma DG(A)\left(\mathcal{F}(U(x=L)) - \mathcal{F}(U_0)\right) \tag{5.35}$$

The function $U(x, L)$ do not depend on $\mathcal{F}$ as long as electrical equilibrium is reached. Then Eq. 5.24 determines fully $U(L, L)$. The only function that has to be determined is thus $\mathcal{F}(U_0)$, which is the Lippmann curve.

5.3.3 Discussions

The results and the model are in agreement under the assumption that the contact angle at the tip of the liquid finger drives the liquid motion. Our results indicate that the apparent contact angle is the right variable to study

in order to determine the wetting dynamics. This implies more generally that one does not have to consider the origin of the contact angle variation (electromechanical stress, Marangoni effect, chemical patterning of the surface, ...), the dynamics being determined by the value of the contact angle at the very position of the contact line. In his paper Jones [124] claims that *"Any or all of these mechanisms (causing the saturation) could simultaneously influence the contact angle and the electromechanical force"*. We expect that an analysis using Maxwell stress at the tip would deliver the same results to those obtained using a capillary viewpoint. However the description in terms of contact angle is convenient for the main reason described above: the contact angle is the sign of the local wettability of the surface. Here our argument is based on the assumption that the applied electric field effectively modulates the liquid / solid surface energies: the contact angle reflects the influence of electrical terms, however complicated they are. As long as the electric term can be writen as surface terms in the energy function (which leads to Lippmann's equation for small voltages) the apparent contact angle can be considered as the driving force of the liquid finger. Since capillary rise is driven by surface forces, it is natural to use the value of the contact angle as a boundary condition for the liquid rise (and thus as the driving force). The relevant contact angle is the contact angle at the tip of the liquid finger, which varies during the spreading from a value equal to the value of the mother drop's contact angle when the length of the liquid finger is small down to the threshold contact angle when the finger reaches equilibrium. This is expressed by the time dependence of $\cos\theta(x = L)$.

The model based on the contact angle description can be transposed to any other system which actively modulate the contact angle. As a simple illustration, we will consider the case of actuation in a close cylinder (capillary rise) of radius r_t. The transition occurs at 90 degrees contact angle: the actuation can be induced by the modulation of the contact angle if $\pi/2$ is within the range of accessible contact angles. The finite length effect in electrowetting is due to the electric loss described by the length-scale λ which in this case reads:

$$\lambda = \sqrt{\frac{T\sigma r_t}{\varepsilon_0 \varepsilon_r \omega}}$$

As a comparison, in the case of Marangoni actuation, the liquid can be heated

at one side of the capillary in order to decrease the contact angle while the substrate is maintained at constant temperature. For contact angle below 90 degrees the liquid rises. It is then equivalent to a thermally conducting rod that can exhibit thermal loss through the liquid / solid interface which reduces the Marangoni effect at the tip of the finger. In this case the temperature at the point x is given by a second order differential equation with real coefficient and a thermal length scale appears [125]:

$$\lambda_{\mathrm{Th}} = \sqrt{\frac{r_t \sigma_{\mathrm{Th}}}{h_{\mathrm{Th}}}}$$

where σ_{Th} is the thermal conductivity of the liquid and h_{Th} is the heat transfert coefficient at the solid / liquid interface. There is thus a direct link between the two systems:

$$\begin{cases} \sigma & \Leftrightarrow & \sigma_{\mathrm{Th}} \\ \varepsilon_0 \varepsilon_r \omega / T & \Leftrightarrow & h_{\mathrm{Th}} \end{cases} \tag{5.36}$$

In other words our model can be transposed to the case of thermal actuation when the liquid is heated from a point source, taking into account the finite thermal conductivity. However, the thermal system does not allow to actively change λ_{Th} which is given by the material contrary to the electric field actuation where the capacitive coupling is modulated by ω.

5.3.4 Conclusions

The filling dynamics of a microchannel under electrocapillary conditions has been investigated. It shows that the dynamics are close to the Washburn law:

1. the square root behaviour $L \propto t^{1/2}$ has the same origin as in the capillary rise, a constant driving force: in the absence of electric loss or at the early stage of filling the driving force is constant and determined by Lippmann equation.

2. the relaxation to equilibrium is modelled by a dynamic loss of voltage during the spreading which is shown to be linked to the change of contact angle. The effect of the electric loss is to decrease the driving force during the spreading. At equilibrium the driving force is 0. Formally the electric loss can be written as an increasing opposing force to the driving electrocapillary force.

These two elements are responsible for the Washburn like behaviour which can be derived analytically. A comparison with the experiments shows a nice agreement when the contact angle used for the computation is that obtained from the experimental Lippmann curve. The electric field only acts as a modification of the wetting properties: in the Lippmann regime the wettability is modified by a simple electrostatic interaction while in the saturation regime additional terms interplay.

5.4 Emptying

After having examined the filling dynamics, the dynamics of emptying are now studied using the same experimental tools.

5.4.1 Experimental results

The emptying is studied experimentally by looking at the length of a liquid finger when the voltage is quenched to 0 from different values U_0 (giving different initial lengths of the liquid finger). The experiments have been performed on channels with different aspect ratios on various drops. The length of the finger has been plotted as a function of time with a time origin taken when the length of the finger is equal to zero.
The length displays a slight increase at early times: this is an experimental artefact caused by the fast motion of the mother drop's contact line when the voltage is turned down. In the meantime the end of the liquid finger does not move. After this increase, the liquid in the channel starts to recede. The expected Washburn behaviour caracterized by a power law exponent of 1/2 has been observed with droplets of diameter much larger than the width of the channels (see Fig. 5.12). In other experiments however, the power law exponent slightly differs from this ideal case. The results are displayed in Fig. 5.13 to 5.15 for the aspect ratios of 1.3, 1.0 and 0.66. All the curves for the different initial length collapse on a master-curve which only depends on the geometry of the channels (and most likely also on the viscosity of the liquid): the original applied voltage has no influence except for setting up the original length of the liquid finger. The universal curve defines a power law exponent which appears to be close to 2/3 for all the aspect ratios studied here (see Fig. 5.16).

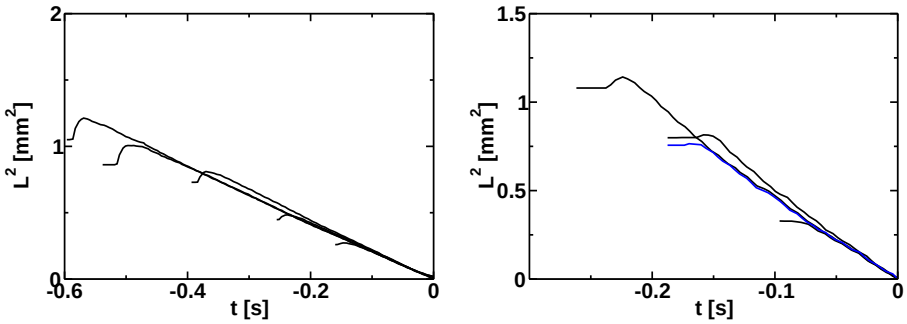

Figure 5.12: Emptying of the channel after filling. $A = 1.0$ and $A = 0.5$. The curves align on a universal curve for voltages between 60 - 90 V reproducing the expected Washburn law. $L^2 \propto t$

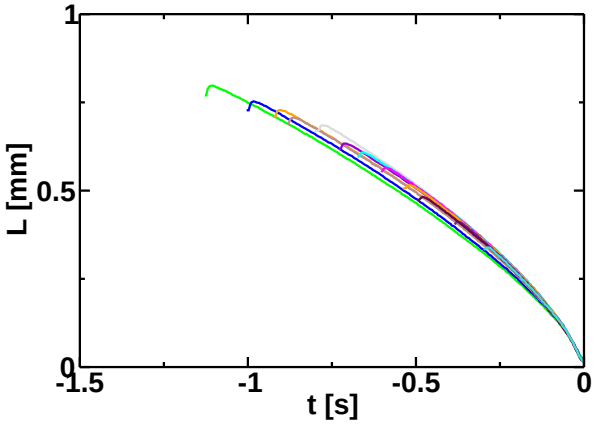

Figure 5.13: Emptying of the channel after filling. $A = 1.3$. The curves align on a universal curve for voltages between 60 - 90 V

In summary the behaviour of the liquid during the emptying does not depend on the electrical parameters of the sytem (voltage and frequency of the voltage source). The power law exponents varies in all the experiments (about 50 data sets on various aspect ratio) between 0.5 and 0.7 without a clear dependence on drop size.

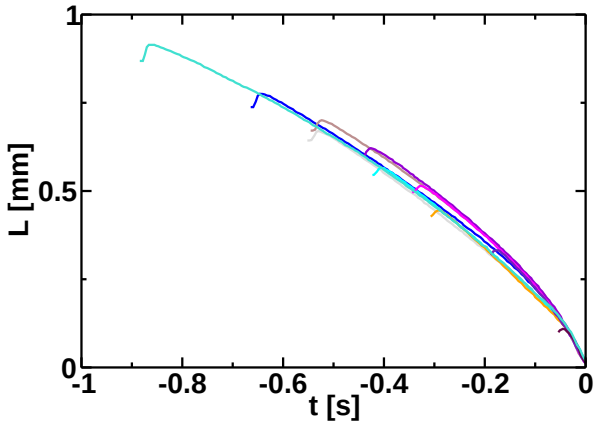

Figure 5.14: Emptying of the channel after filling. $A = 1.0$. The curves align on a universal curve for voltages between 60 - 90 V

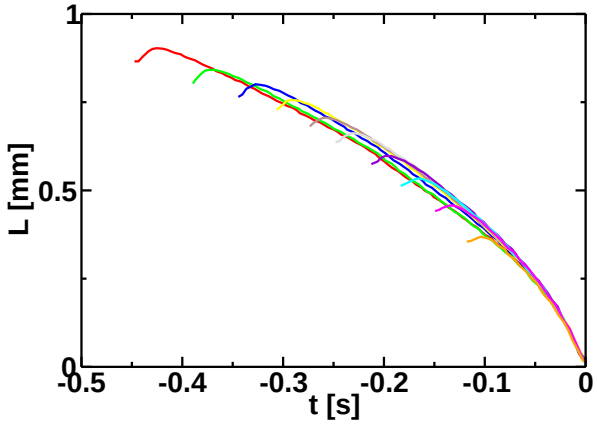

Figure 5.15: Emptying of the channel after filling. $A = 0.66$. The curves align on a universal curve for voltages between 60 - 90 V

5.4.2 Discussions

In the receding case the driving force is only linked to Young's contact angle since the voltage is 0. In other words the natural wetting properties of the system control the dynamics. With the typical dimensions of the channel and speed observed, small Reynolds number of order 10^{-4} indicates a lam-

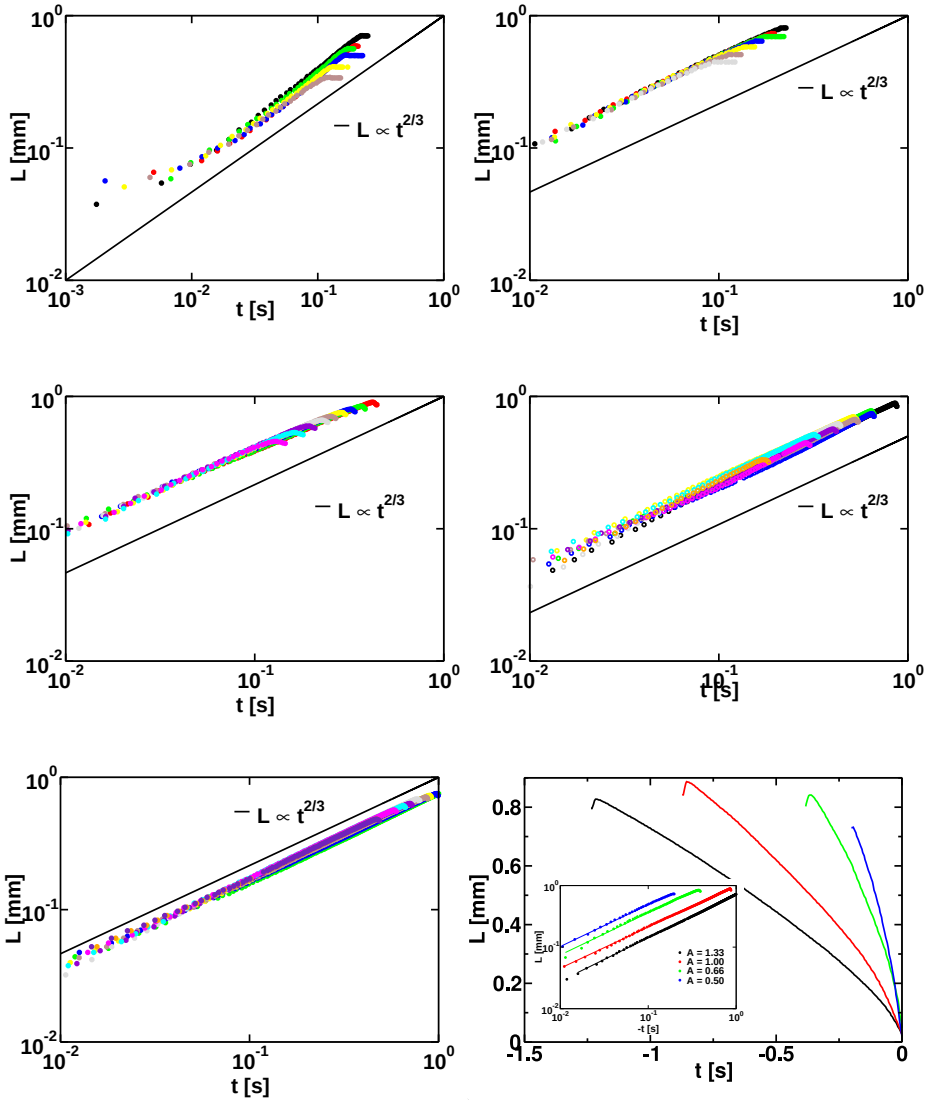

Figure 5.16: Power-Law behaviour at the capillary emptying: the exponent is close to 2/3 in all cases. From top to bottom and left to right, $A = 0.40$, 0.50, 0.66, 1.00, 1.33. The last graph shows the comparison for $A = 0.50$, 0.66, 1.00, 1.33.

inar flow in the channel with negligible inertia. The motion starts as soon as the driving force is settled: the time-scale of the acceleration is smaller than the camera frame rate and the liquid recedes immediately with a speed depending on its position in the channel. Indeed the speed at the length L

is fixed by the pressure gradient $\delta P/L$ where δP is constant: the pressure gradient only depends on L and the position $L(t)$ is thus a universal curve. The filling experiments could also have been performed by setting the voltage down to values below the threshold voltage. Under these conditions, one would have observed different curves depending on the voltage quench. Such experiments are not shown here.

While filling exhibits a power-law of 1/2 at the early stage, the receding exhibits different power law exponents between 0.5 and 0.7 for the whole range of the relaxation. The reason for the uncertainty on the exponent is yet unclear and should be the subject of a more accurate study. However, when one refers to other exponent caracterization in capillary spreading one observes that the determination of the exponent is relatively unaccurate. For example Cazabat and Cohen observed exponents between 0.094 and 0.125 for a spreading drop which gives an error bar of 23 %, and Chen about 30 % variation in the determination of the exponent (this figures are available in Ehrhard's paper [126]). Here 33 % error is in the same order of magnitude for the error bars. However one can wonder if the dispersion in the power law is not coming from a more fundamental problem. It has not been possible considering the experiment performed here to find a particular reason but some points should be investigated to improve the determination of the power-law:

1. Influence of the liquid finger free-surface. The flow rate in the channel is certainly modified by this additional free boundary and may lead to a different exponent than expected.

2. Influence of the motion of the mother drop contact line. The exponent 1/2 is expected not only for a reservoir at fixed pressure but also at a fixed position. The contact line of the drop is slighlty moving during the experiment which may influence the dynamics.

3. Influence of the drop configuration. It has been difficult to observe any influence of drop size but the variation of the drop shape in particular at the moment where the liquid finger's end is close to the drop may produce a counter acting pressure that can slow down the motion of the liquid finger leading to a smaller apparent power law exponent.

4. Variation of the mother drop pressure: while the drop recedes, the drop volume increases and thus its Laplace pressure decreases. The condition δP is constant does not hold any more. In the case of filling, one can write: $L' \propto 1/L$. Here we have $L \propto t^{2/3}$ thus $L' \propto L^{1/2}/L$. This means that the difference of pressure has to vary as $\delta P \propto L^{1/2}$. This is not the case: the conservation of the volume and the spherical cap assumption gives $\delta P \propto (V - WDL)^{-1/3}$ far from the simple scaling. Nevertheless the exponent 2/3 may arise from a crossover regime from a size-independent to a size dependent emptying.

5. Influence of contact angle. The viscous dissipation is maybe not correct in its form. Including a viscous dissipation at the contact line would be a solution. The contact angle is also sensitive to roughness. The roughness of the channel may change the non slip boundary condition.

Moreover some other explanations can already be discarded:

1. Contact angle hysteresis could have a role here. However one would expect an increase of the influence of hysteresis when the size decreases which has not been observed.

2. Influence of electrical charges. The charges trapped in the insulating layer may interact with the contact line which could result in slowing down the contact line. The flow of kept charges through the insulating layer after the voltage is set to zero is also a possibility. But no effect has been observed by changing the frequency of the voltage source.

5.5 Application to on-chip liquid cooling

The system presented here gives a nice tool for fluid actuation due to the reversibility of the flow. We studied this system as a way to perform on-chip liquid cooling. Electrowetting liquid cooling has in fact already been investigated in the drop geometry [127]. Using patterned electrodes a drop is moved by electrowetting to a hot spot on a chip. In contact with the hot-spot the drop temperature increases and after a given contact time the drop is removed from the hot spot and diluted in a reservoir at room temperature

at the side of the device[2]. There is thus a transfer of thermal energy from the hot spot to the outside leading to an integrated cooling system. The advantage is obvious: there is no mechanical part in this system and the flow is electrically controlled.
In our case the system is based on the actuation of fluid in microchannels. A reservoir is placed at the edge of the chip feeding microchannels etched directly in the silicon of the chip. When a hot spot is detected, the liquid actuation starts: the liquid fills the channels to the hot spot and heats up. The voltage is turned down, the liquid recedes to the reservoir and is cooled down. When the voltage increases, fresh water is again distributed to the hot spot. Preliminary calculations were performed to determine the cooling efficiency as a function of the frequency of liquid pulsation in the channels and seem to indicate that an actuation at a about 1 Hz would already give an efficient cooling [128]. This principle has been patented[3] and work is still in progress; only preliminary results are available.
The advantages of such a system can be discussed in terms of accessible sizes: liquid in 15 μm channels is easily actuated at the millimetre scale. In comparison a drop actuation on patterned substrates requires structures as wide as long (square electrodes) due to the round shape of the drop. To our knowledge no electrowetting system has yet presented actuation of 15 μm diameter drops. The channels can (easily) be patterned in between the natural structures of the chip and potentially not only in the surface but also in the three dimensions of the wafer, using existing technological solutions.

5.6 Conclusions

The dynamics of the filling and emptying of microchannels using electrowetting has been investigated. It shows that the filling behaviour follows capillary expectations and that electrical loss in the channel is the source of relaxation to equilibrium via a Washburn-like law. The optimal actuation for the liquid is obtained in the absence of electrical opposing force, leading to a 1/2 power law exponent. The influence of the dimensions of the channel

[2]Using a drop as a reservoir and a system based on the self-excited oscillations of the Chapter 3 would be a really nice solution to enhance the temperature homogenization !
[3]Patent PH NL040898EPP, *A cooling system for electronic substrates*

is obtained from our model and is similar to capillary rise. The system displayed here shows a fluid actuation over 1 mm in about 1 s for a liquid about 100 times more viscous than water. Under these conditions we expect to see an increased speed with water and an actuation over 1 cm in about 1 s or over 1 mm in 10 ms which is of particular interest for microfluidic applications. A system based on a water solutions would have to be closed in order to reduce evaporation. This experimental drawback is the main reason why such a situation has not been studied but would be interesting in the future since closed channels are more suitable for applications such as on-chip liquid cooling where a free-surface is not required.

The system is thus driven by electrocapillarity and has been fully modelled by the heterogeneous modulation of the surface tension by the applied electric field. In the presence of homogeneous fields, the system behaves just as a capillary system, using Lippmann's contact angle. When the loss of voltage along the channel is taken into account, the spreading stops at an equilibrium length where the speed of the contact line reaches zero. The filling dynamics depend on the electrical properties and the driving force for fluid motion is linked to the electrical forcing exerted by the voltage. This driving force acts at the tip of the liquid finger via the local electrowetting properties and vanishes at equilibrium. In the emptying a simple Washburn law is expected but the experiments showed a power law exponent distribution between 0.5 to 0.7.

The reversibility of the filling and emptying transition is a nice tool to provide a microfluidic pumping device. Indeed the typical actuation times are given by capillarity and one can make use of the ac-voltage for an optimal control of the kinetics. Moreover this simple system can also be completed by additional electrodes patterned in the substrates or coming on top. The finite length saturation can for instance be switched on and off via a careful choice of additional electrode positions. The maximal kinetics would then be maintained by suppressing the electric effects. In particular in closed channels, such a system could be used for on-chip liquid cooling. It has been shown recently that the typical flow rates obtained here are compatible with an efficient cooling in some applications [128].

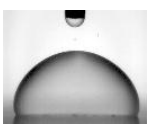

Chapter 6

Conclusions and Outlook

The main objective of this thesis was to actuate liquid at the millimetre and micrometer size, to switch between liquid morphologies and to induce motion of liquid structures on an active and controled way. Because we wanted to have scalable system, the basis of the actuation is a tunable modulation of capillary forces by a voltage supply achieved by the electrowetting effect.

Capillary transitions – Drops are known to display different shapes depending on the constraints of the substrate on which they are deposited. Morphological transitions have been predicted by different authors using pure capillary models: these different morphologies have also been observed using surfaces of different wettabilities. Here we have studied the influence of active wettablity changes on liquid behaviour by means of electrowetting: the modulation of the surface wettability induced by an applied electric field gives here a convenient way to reversibly actuate droplets. The influence of wettability on the liquid behaviour has been studied in three cases: i) drop deposition ii) drop oscillations and iii) open-capillary filling. The transitions expected are correctly observed and they are reversible which provides an interesting tool for microfluidics actuation. We have shown that the influence of the electric field is fully captured by considering a capillary system with an apparent contact angle according to the Lippmann curve. The transitions occurs when Lippmann's angle is equal to the threshold angle of the capillary transition, in the drop deposition, the oscillating drop and the channel filling systems. Moreover, the dynamics model of capillary filling also indicates that the dynamics of the electrowetting actuation is described in terms of apparent local contact angles. However the Lippmann's angle that has to be considered is obtained by taking into account the loss of voltage due to electric characteristics.

Electrical parameters – In addition to the capillary transitions, the influence of the electrical parameters on droplet actuation has been studied. Beyond the transitions the droplet behaviour is not only determined by the capillary parameters but also by the electrical parameters. In particular the choice of AC or DC current is fundamental. We have shown that drop os-

cillations can not occur for DC current: the condition $\chi \gg 1$ required for oscillations is not reached for DC where $\chi = 0$. Since $\chi \propto \omega$, we have an active control on this parameter using AC frequencies and therefore on the number of charges in the drop determined by χ. For channel filling the electric loss due to the capacitive coupling with the substrate was shown to be the source of a length-scale λ. $\lambda \propto \omega^{-1/2}$ is finite in AC fields and diverges in DC fields: a liquid drop should disappear entirely in the channel to form a liquid finger in DC fields; in AC fields λ determines the equilibrium length of the liquid finger in a channel.
Beyond the transition, the electrical parameters provide an additional control on the system (via χ or λ) and an additional degree of freedom for liquid manipulation compared to other systems, in particular to Marangoni actuation. Since the transitions we studied are capillary driven they can be induced in any system which shows an active change of the wettability. In particular, the drop deposition/detachment criterion could be investigated using the temperature dependence of surface tensions (and contact angles). This holds for the fluid actuation in capillaries that could be induced by Marangoni effect. But the contact angle modulation that can be achieved using Marangoni effect is much smaller than that based on electrowetting: Marangoni actuation is more sensitive to contact angle hysteresis. Moreover, the additional control on the fluid behaviour via the frequency dependence of λ or χ has no equivalent in Marangoni actuation.

In summary, we have shown that electrowetting is a convenient and versatile tool to induce and study capillary transitions. It not only allows to induce reversibly the transitions but also provides an additional control via the active choice of the electrical parameters which is of potential interest for microfluidics applications.

On-going and Future work – At this point, some elements related to this work are still under investigation, among them I will mention, the study of **mixing** efficiency in oscillating drops (group Physics of Complex Fluids, University of Twente – NL), the actuation of fluid in open-air **microchannels** with triangular cross-section (Max Planck Institute for Dynamics and self-organization, Göttingen – D) and the study of **on-chip liquid cooling** using electrowetting on drops or microchannels (University of Leuven –

Be) and of course the electrowetting fundamental problems still under debate, for example the contact angle saturation and the oil / water / solid interface. This work could be extended in different directions, **the deposition/detachment problem** could be studied using vesicles or cells. In this case, the additional constraints on the area of the body would probably modify the results. The stiffness of the vesicule and the strength of adhesion forces should have a role that could be interesting to study. One could then detect anormal cells which would have non-regular behavior. **The oscillations of a drop** could be studied when the drops are driven at a given frequency. It would be interesting to determine the amplitude of drop oscillations as a function of voltage frequency and see if resonance peaks can be observed. These peaks should be linked to the frequencies obtained in the self-excited mode. It could be interesting to use a sytem without electrode, a reversed system of oil drop in water. **The electroactuation** could be also studied in the case of close channels or capillaries. In this case the threshold is 90 degrees which gives a wide range of contact angles to study the dynamics. Moreover, more complex systems could be investigated in order to provide real microfluidic components.

Appendix A

Notations

A.1 List of symbols

Mathematical symbols

Symbol	Name	Caracteristics
j	Imaginary unit	$j^2 = -1$
e, exp	Exponential constant	$\ln e = 1$
π		≈ 3.14159
ϵ	"small" parameter	
$\Delta.$	Laplace-Beltrami operator	
$\|\ldots\|, \|\ldots\|$	Norm, modulus	

Physical symbols

Symbol	Name	Typical Value $\approx$	Unit
g	Acceleration of gravity	9.81	m/s^2
k_B	Boltzmann constant	1.38×10^{-23}	J/K
ε_0	Dielectric constant of vacuum	8.8×10^{-12}	F/m
t	Time		s
Θ	Temperature		K
x, y, z	Cartesian coordinates		
r, z	Cylindrical coordinates		

Fluid caracteristics

Symbol	Name	Typical Value ≈	Unit
ρ	Density	0.7 - 1.3	kg/m^3
σ	Electrical conductivity	0.01 - 1	S/m
γ	Surface tension	38 - 72	mN/m
η	Liquid viscosity	1 - 100	mPa×s
L_c	Capillary length	1-8	mm

Dimensionless numbers (typical speed v, length l)

Number	Name	Expression
Ca	Capillary Number	$\eta v/\gamma$
Bo	Bond Number	$\rho g l^2/\gamma$
We	Weber Number	$\rho v^2 l/\gamma$
Oh	Ohnesorge Number	$\eta/\sqrt{\rho l \gamma}$
Re	Reynolds Number	$\rho v l/\eta$
Li	Lippmann Number	$(\varepsilon_0 \varepsilon U^2/2T)/\gamma$
χ	Dimensionless Number	$2\pi f(R_0 C t_0^{\mu})^{1/(\mu+1)}$

Systems

Symbol	Name	Typical Value ≈	Unit
T	Thickness of insulating layer	1.1 ± 0.1	μm
r_e, (r_e^i)	Electrode radius (internal)	50 - 250	μm
z_e, z_s	Electrode, substrate altitude		mm
r_t	Capillary tube inner radius		mm
d, $d_{\max}$	Distance electrode / substrate	0.5 - 2	mm
F	Frequency of oscillations	10-150	Hz
W	Width of microchannels	15-50	μm
D	Depth of microchannels	10-20	μm
A	Aspect ratio D/W	0.20 - 1.33	–

Drops

Symbol	Name	Typical Value ≈	Unit
θ_Y	Young's contact angle	100 - 160	degrees
θ_L	Lippmann's contact angle	45 - 160	degrees
θ	Apparent contact angle		degrees
θ_a (θ_r)	Advancing (Receding) angle		degrees
$\gamma_{\text{sl,sv,lv}}$	Surface tensions		mN/m
V, Ω	Drop Volume	0.1 - 10	μL
S	Solid surface wetted by the drop	1	mm^2
Σ	Drop external surface	1 - 0	mm^2
h	Drop height	.5 - 8	mm
r_0	Drop Radius	0.1 - 2	mm
r_s	Radius of wetted surface	1	mm
$r_{\min}$	Minimal radius of a neck	0-0.5	mm
$r_{1,2}$	Parameters of Undoloids		
α	Tilt angle of undoloids	0- π	degrees
$E_{s,\Sigma}$	Surface energies		J
E_V	Body energies		J
P, δP	Pressure, pressure difference		Pa
M	Mean Curvature		m^{-1}
v_x, v_y, v_z	Liquid velocities		m.s^{-1}
$\mathcal{Q}$	Flow rate		$\text{m}^3.\text{s}^{-1}$
z_J	Jurin's Height		mm
L, L_∞	Length of liquid finger	0 - 2	mm
λ	Electrical lengthscale	0 - 10	mm
l	Rescaled length L/λ		–
$t_{0,1,2}$	Typical time		s
μ	Exponent of resistance divergence	0.8 -1.5	–
ν	Exponent of capillary breakup	2/3 - 1.0	–
κ , κ_0, κ^*	Propagation coefficient in channels		m^2/s

Electrical parameters

Symbol	Name	Typical Value ≈	Unit
ε_r	Relative permitivitty of SiO_2	2 - 4	–
U_0, U_T, $U(x)$	Voltage	0 - 120	V
f, f_T	Frequency of voltage (in AC)	1 - 30	kHz
ω	2πf		rad/s
τ	Electrical period	0.05 - 1	ms
C	Electrical capacitance	10^{-11} - 10^{-9}	F
R, R_d, R_n, R_m	Electrical resistance	1 - 10^5	Ω
Z	Electrical impedance		Ω
q	Electrical charge		C
Q, $Q_{\max}$	Dimensionless charge	Q/CU	–
I, I_0, $I_{\max}$, i	Electrical current		A

Miscellaneous

Symbol	Name	Typical Value ≈	Unit
τ_{el}	Electrical timescale		s
τ_{hydro}	Hydrodynamic timescale		s
τ_{dyn}	Dynamic timescale of channel filling		s
v_0	Typical speed		m/s
F_{visc}	Viscous force		N
F_{wett}	Capillary force		N
F_{el}	Electrical counteracting force		N
a	Pressure gradient		Pas/m
σ_{th}	Thermal conductivity		W/mK
h_{th}	Heat transfert coefficient		W/m^2K
λ_{th}	Thermal lengthscale		m

Appendix B

Material

All the experiments have been performed on silicon wafers (n+ arsenic doped, resistivity 1 – 5 m$\Omega\times$ cm).

B.1 Fluids

We usually used as a fluid for electrowetting mixtures of glycerol, water and salt (Sodium Chloride). Different ratio of glycerol water and salt have been used in order to control the viscosity and electrical conductivity of the fluid. As surrounding phase silicon oil has been used, either Wacker AK5 (viscosity $\approx$ 5 mPa $\times$ s)or Fluka DC200 (viscosity $\approx$ 10 mPa $\times$ s).

B.2 Processing of the silicon wafers

In all the experiments, we used conductive silicon wafer In order to produce topographies in the substrate, a positive mask for photolithography has first been designed processed in Dupont. The following steps have then been realized:

- A polymer resist is spin-coated on the wafer.
- The wafer is UV-illuminated through the mask and rinsed.
- The anisotropic ion etching steps [129] are performed.
- A silicon oxide layer has been thermally grown up to 1 μm on top of the wafers.

At the end of the process an additional hydrophobic coating has been formed using standard protocol [72].

- The silicon surface are carefully cleaned and activated using Piranha solution.
- The wafers are placed in a bath of OTS and solvent.
- The wafers are rinsed with chloroform.

The first time the substrates are used a special cleaning is applied in order to get rid of the excess of reactants at the surface. The wafers are thus

successively cleaned in ultrasonic bath of acetone (1 hour), ethanol (1 hour) and toluol (1 hour). In between each bath the samples are dried by nitrogen flow.

In order to control the sizes of the features etched in the wafer SEM pictures of a sample have been taken. Since the method is destructive the pictures have been taken only at the end of the experiments. The pictures presented here are given for the smallest and largest aspect ratio (Fig. B.1). The etching process could give different depth as a function of the aspect ratio of the features that are etched. It is not the case here and the final dimensions are the one that have been chosen. The roughness is the consequence of the etching process. It should be noticed that this roughness is anisotropic: it will influence marginally the flow along the channel.

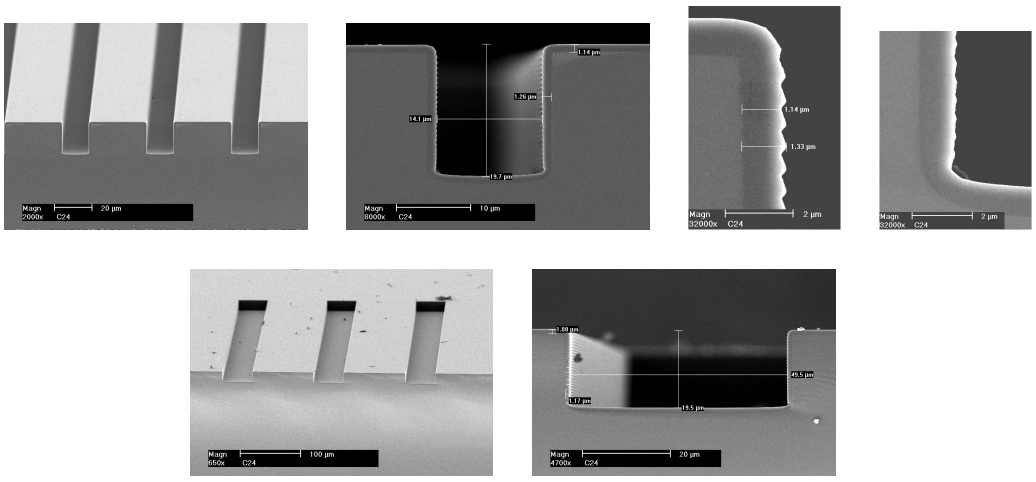

Figure B.1: Microchannels in silicon wafer (Top line $D = 20\mu$m, $W = 15\mu$m, $A = 1.33$, Bottom line: $D = 20\mu$m, $W = 50\mu$m, $A = 0.4$). The insulating layer is also visible.

B.3 Contact angle measurement

At the end of the process the static contact angles of water on the surface are 109 degrees advancing 102 degrees receding in air environment defining to a static hysteresis of 5-7 degrees B.2. All the contact angle have been measured using side view of a the sessile drop using OCA-30 hard- and software. The value of the contact angle is a good indication of the quality of

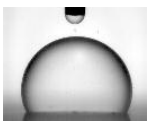

the layer as well as the small contact angle hysteresis. The physical origin of the hysteresis is probably the reorganization of the monolayer at the contact line [8].

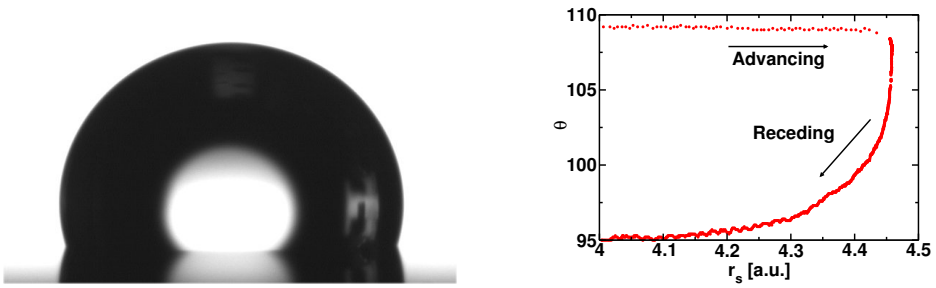

Figure B.2: Static hysteresis 109 - 105 degrees. r_s is the radius of the area wetted by the drop.

B.4 Preparation of samples for electrowetting

After one day in air it has been observed that the contact angle hysteresis was increasing leading to unreproducible results. In order to avoid this effect the samples are cleaned the day they are used in ultrasonic bath of acetone, ethanol and toluol a few minutes in each bath. The samples are then placed on a glass plate and glued to a copper wire using conducting epoxy or silver painting.

B.5 Electrowetting

The electrowetting set-up consist in a low frequency generator (Agilent) and an amplifier (Philips home made). The range of voltage accessible to the amplifier is 0-400 V (rms) but we used it only up to 125 V (rms). The rms values of the voltages are measured via a standard multimeter and the full signal is displayed on an oscilloscope (HP). The low frequency generator is connected to a computer and is driven in some case via a Labview routine.

Appendix C

Delaunay Surfaces

C.1 Unduloids

C.1.1 Introduction

Any axi-symmetric surface with a constant mean curvature is a so called Delaunay surface [73] as displayed in Fig. C.1. The subfamily of stretched Delaunay surface is the unduloid family.

The analytical expressions of these shapes are known and are given in the case of unduloids which are studied in the following. Some details on nodoids can be found in Martin Brinkmann's thesis [17] or in Langbein's book [74].

C.1.2 Parametrization

We have used the parametrization of the shape based on the maximal radius r_2 and the minimal radius r_1 of the unduloid for $r \in [r_1, r_2]$. The rest of the unduloid is obtained by symmetry and periodisation as displayed in the Fig. C.2:

$$\left\{ \begin{array}{rcl} u(r_1,r_2,r) & = & \arcsin\sqrt{\frac{r_2^2(r^2-r_1^2)}{r^2(r_2^2-r_1^2)}} \\ z(r_1,r_2,r) & = & r_2 E(u(r_2,r_1,r),k) \\ & & +r_1 F(u(r_2,r_1,r),k) \\ & & -\frac{(r_2^2-r_1^2)\cos u(r_1,r_2,r)\sin u(r_1,r_2,r)}{\sqrt{r_2^2\cos^2 u(r_1,r_2,r)+r_1^2\sin^2 u(r_1,r_2,r)}} \end{array} \right. \tag{C.1}$$

where $u \in [0, \pi/2]$, $(u(r_1, r_2, r_1) = 0)$ and $(u(r_1, r_2, r_2) = \pi/2)$; the elliptic integral E and F and k are defined as:

$$\left\{ \begin{array}{rcl} E(u,k) & = & \int_0^u \mathrm{d}v (1-k^2\sin^2 v)^{1/2} \\ F(u,k) & = & \int_0^u \mathrm{d}v (1-k^2\sin^2 v)^{-1/2} \end{array} \right. \tag{C.2}$$

$$k = \sqrt{\frac{r_2^2-r_1^2}{r_2^2}} \tag{C.3}$$

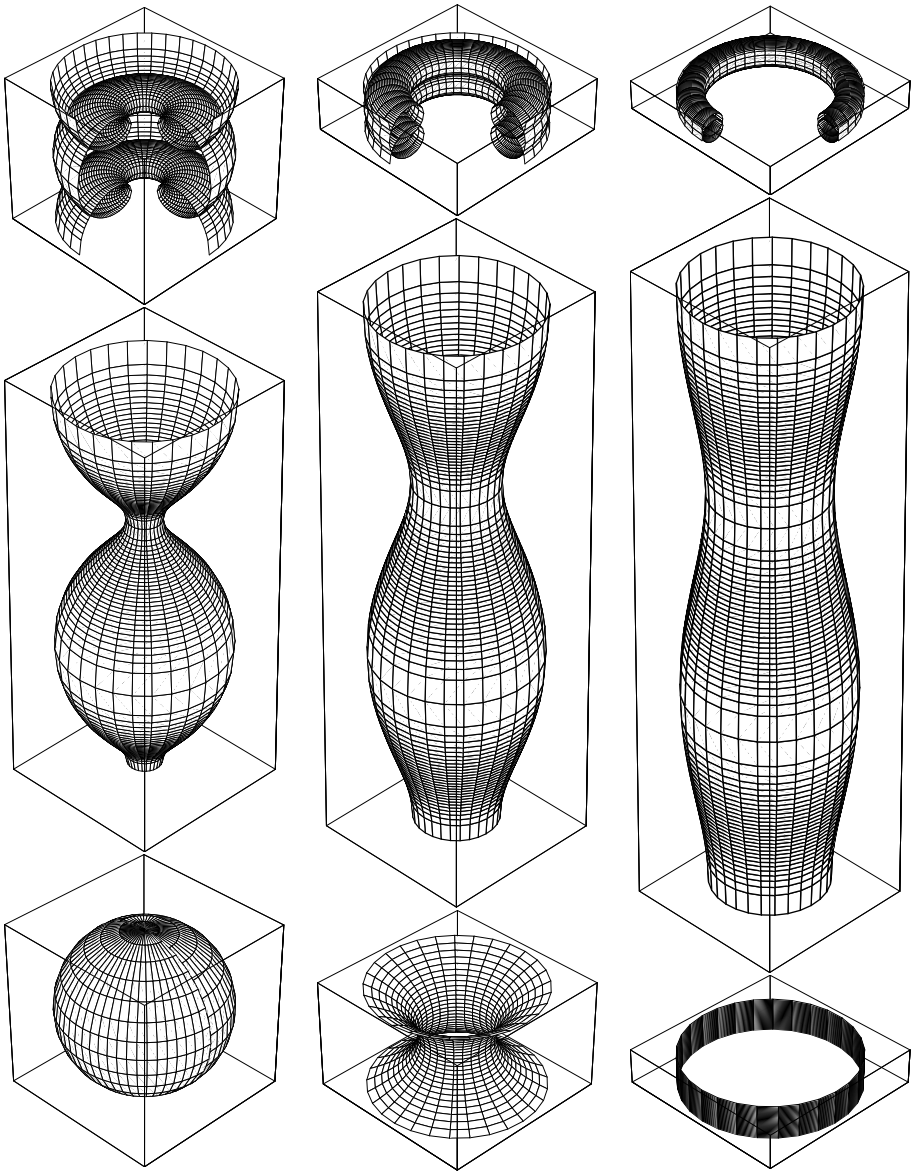

Figure C.1: Examples of Delaunay surfaces for different sets of parameters $\{r_1, r_2\}$. Top, from left to right: nodoids ($\{2, 10\}$, $\{5, 10\}$, $\{7, 10\}$); Midle, from left to right: unduloids ($\{2, 10\}$, $\{5, 10\}$, $\{7, 10\}$); Bottom, limiting shapes, from left to right: Sphere $\{r_1 = 0, r_2\}$, catenoid $\{r_1, r_2 = \infty\}$ and cylinder $\{r_1, r_2 = r_1\}$.

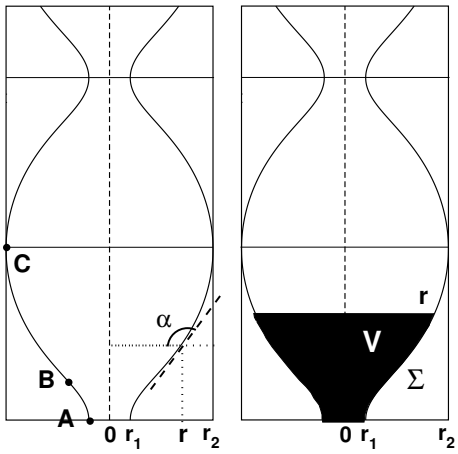

Figure C.2: Unduloid parameters: α is the tilt angle, V the volume and Σ the external surface area.

Point	Caracteristics	u	z	r
A	Minimal Radius	0	0	r_1
B	Inflexion Point	$\arcsin\sqrt{\frac{r_2}{r_2+r_1}}$		$\sqrt{r_1 \times r_2}$
C	Maximal radius	$\pi/2$	$r_2 E(\frac{\pi}{2}, k) + r_1 F(\frac{\pi}{2}, k)$	r_2

Table C.1: Special Points

C.1.3 Volume

The volume V of a portion of unduloid starting between $r = r_1$ and $r \in [r_1, r_2]$ is:

$$\begin{aligned} \frac{3}{\pi} \times V(r_1, r_2, r) &= (2r_2(r_1^2 + r_2^2) + 3r_1 r_2^2) \times E(u(r_1, r_2, r), k) \\ &\quad -r_2 r_1^2 F(u(r_1, r_2, r), k) \\ &\quad -(-r^2 + 2(r_1^2 + r_2^2) + 3r_1 r_2) \\ &\quad \times \frac{(r_2^2 - r_1^2)\cos u(r_1,r_2,r) \sin u(r_1,r_2,r)}{\sqrt{r_2^2 \cos^2 u(r_1,r_2,r) + r_1^2 \sin^2 u(r_1,r_2,r)}} \end{aligned} \tag{C.4}$$

The expression of the volume of a unduloid depends on its class. For example when the unduloid is limited by r_e at one side and r_s at the other side the expression for the un-necked unduloid at $\theta > \pi$ is:

$$V(r_1, r_2, r_e, r_s) = 2 \times V(r_1, r_2, r_2) - V(r_1, r_2, r_e) - V(r_1, r_2, r_s) \tag{C.5}$$

and for the necked unduloid at $\theta > \pi$:

$$V(r_1, r_2, r_e, r_s) = 2 \times V(r_1, r_2, r_2) + V(r_1, r_2, r_e) - V(r_1, r_2, r_s) \tag{C.6}$$

The volume in the other situation is determined by linear combination of the volume V.

C.1.4 Surface area

The surface area Σ of a portion of unduloid starting between $r = r_1$ and $r \in [r_1, r_2]$ is:

$$\Sigma(r_1, r_2, r) = 2\pi(r_2 + r_1) \times \left(r_2 E(u(r_1, r_2, r), k) - \frac{\sqrt{(r_2^2 - r^2)(r^2 - r_1^2)}}{r} \right) \tag{C.7}$$

The full expression depends on the class of the unduloid and is obtained similarly to the volume.

C.1.5 Tilt angle

The angle α made by the tangent to the unduloid surface to the horizontal plane which is related to contact angle is obtained by derivation of z with respect to r:

$$\frac{\mathrm{d}z}{\mathrm{d}r} = \frac{r^2 + r_1 r_2}{\sqrt{(r_2^2 - r^2)(r^2 - r_1^2)}} \tag{C.8}$$

leading to:

$$\cos\alpha(r_1, r_2, r) = \frac{(r_2 - r_1)\sin u(r_1, r_2, r)\cos u(r_1, r_2, r)}{\sqrt{r_2^2 \cos^2 u(r_1, r_2, r) + r_1^2 \sin^2 u(r_1, r_2, r)}} \tag{C.9}$$

C.2 Spherical cap

For clarity some mathematical expressions used in the manuscript are developed here for a drop of given volume V deposited on a flat substrate with a contact angle θ as displayed in Fig. C.3

$$\begin{array}{rcll} h(\theta, V) & = & \left(\frac{3V}{\pi}\right)^{1/3} & \times \frac{1-\cos\theta}{(2-3\cos\theta+\cos^3\theta)^{1/3}} \\ r_0(\theta, V) & = & \left(\frac{3V}{\pi}\right)^{1/3} & \times \frac{1}{(2-3\cos\theta+\cos^3\theta)^{1/3}} \\ r_s(\theta, V) & = & \left(\frac{3V}{\pi}\right)^{1/3} & \times \frac{\sin\theta}{(2-3\cos\theta+\cos^3\theta)^{1/3}} \\ S(\theta, V) & = & \pi\left(\frac{3V}{\pi}\right)^{2/3} & \times \frac{\sin^2\theta}{(2-3\cos\theta+\cos^3\theta)^{1/3}} \\ \Sigma(\theta, V) & = & 2\pi\left(\frac{3V}{\pi}\right)^{2/3} & \times \frac{1-\cos\theta}{(2-3\cos\theta+\cos^3\theta)^{1/3}} \end{array} \tag{C.10}$$

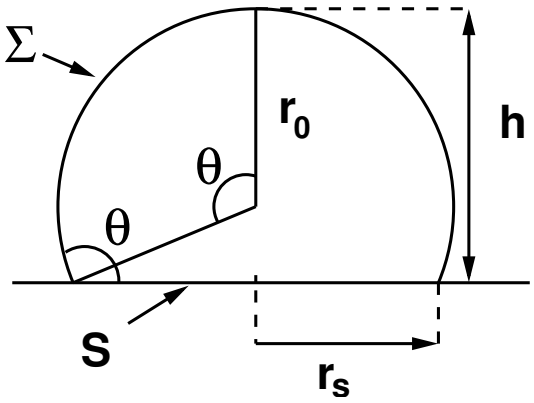

Figure C.3: Spherical cap

Appendix D

The free-ended coaxial cable

D.1 Physical description

We want to find the distribution of voltage along an electricaly conducting liquid finger of length L free to move surrounded by a insulating layer. The driving voltage U_0 at frequency ω is applied at one edge of the liquid finger at $X = 0$. The liquid conducitivity is σ, the insulating layer thickness is T, its dielectric constant $\varepsilon_0\varepsilon_r$. The channels depth and width are D and W. The liquid finger is assumed to be flat and we neglect the curvature at the tip in $X = L$. The system is equivalent to a free-ended coaxial cable described by the equivalent electrical circuit of Fig. D.2.

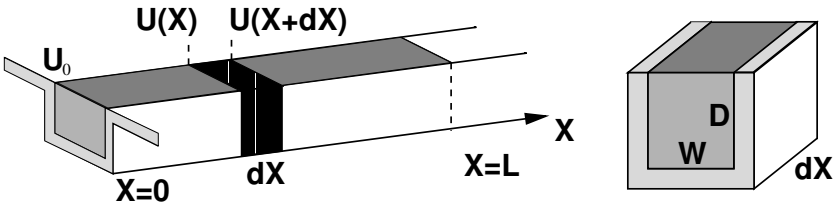

Figure D.1: Simple model for the liquid finger in a channel.

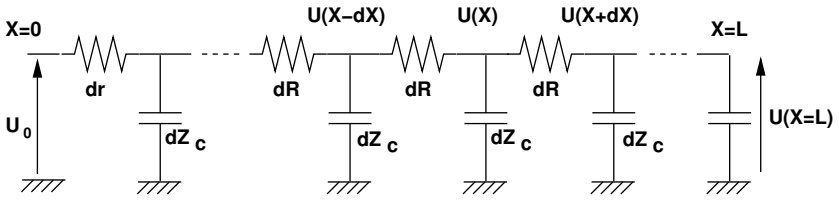

Figure D.2: Equivalent electrical circuit for the liquid finger.

$\mathcal{U}(x)$ is the complex voltage at X which depends on the voltage at $\mathcal{U}(X - \mathrm{d}X)$ and $\mathcal{U}(X + \mathrm{d}X)$ via:

$$\mathcal{U}(X)\left(2 + \frac{\mathrm{d}R}{\mathrm{d}Z_c}\right) = \mathcal{U}(X + \mathrm{d}X) + \mathcal{U}(X - \mathrm{d}X) \tag{D.1}$$

where $\mathrm{d}R = \mathrm{d}X/(\sigma W D)$ and $\mathrm{d}Z_c = T/(j\omega\varepsilon_0\varepsilon_r(W + 2D)\mathrm{d}X)$ are the resistance and capacitive impedance of a piece of liquid of length $\mathrm{d}X$. Using

$$\mathcal{U}(X + \mathrm{d}X) - 2\mathcal{U}(X) + \mathcal{U}(X + \mathrm{d}X) = \frac{\mathrm{d}^2\mathcal{U}}{\mathrm{d}X^2}(\mathrm{d}X)^2$$

Eq. D.1 reduces to:

$$\frac{\mathrm{d}^2\mathcal{U}(X)}{\mathrm{d}X^2} = 2j\frac{\mathcal{U}(X)}{\lambda^2} \tag{D.2}$$

where

$$\lambda = \sqrt{\frac{2T\sigma}{\omega\varepsilon_0\varepsilon_r}\frac{WD}{(W+2D)}}$$

D.2 Solution

$\mathcal{U}(x)$ is a **complex** function of the real variable x (j being the complex unit $j^2 = -1$) and $U(x) = \|\mathcal{U}(x)\|$ the physical amplitude of the voltage. x is the dimensionless coordinate along the groove X/λ. $\mathcal{U}(x)$ fulfils:

$$\frac{\mathrm{d}^2\mathcal{U}(x)}{\mathrm{d}x^2} = 2j\mathcal{U}(x)$$

$\mathcal{U}(x)$ is decomposed on a basis of exponential function:

$$\mathcal{U}(x) = \mathcal{A} \times \mathrm{e}^{r_1 x} + \mathcal{B} \times \mathrm{e}^{r_2 x}$$

where $\{r_1, r_2\}$ are the complex roots of the characteristic equation $r^2 - 2j = 0$: $r_1 = 1 + j$ and $r_2 = -1 - j$ and $\mathcal{A}$ and $\mathcal{B}$ complex values determined by the boundary conditions. We define $A = \|\mathcal{A}\|$ and $B = \|\mathcal{B}\|$.

Condition 1 – Electrical equilibrium reads $\frac{\mathrm{d}U}{\mathrm{d}x}_{(x=l)} = 0 \Leftrightarrow \frac{\mathrm{d}\mathcal{U}}{\mathrm{d}x}_{(x=l)} = 0$ leading to:

$$\mathcal{B} = \mathcal{A} \times \mathrm{e}^{2(1+j)l} \Rightarrow \mathcal{U}(x) = \mathcal{A} \times \mathrm{e}^{l}\,\mathrm{e}^{jl} \times \left(\mathrm{e}^{x-l}\mathrm{e}^{j(x-l)} + \mathrm{e}^{l-x}\mathrm{e}^{j(l-x)}\right)$$

and thus:

$$U(x) = A \times \mathrm{e}^{l} \times \left\|\mathrm{e}^{x-l}\mathrm{e}^{j(x-l)} + \mathrm{e}^{l-x}\mathrm{e}^{j(l-x)}\right\|$$

Condition 2 – Using the second boundary condition $U(x = 0) = U_0 \Leftrightarrow \|\mathcal{U}(x = 0)\| = U_0$, one finds:

$$A \times \mathrm{e}^{l} = \frac{U_0}{\|\mathrm{e}^{-l}\mathrm{e}^{-jl} + \mathrm{e}^{l}\mathrm{e}^{jl}\|}$$

Hence:

$$\frac{U(x)}{U_0} = \left\|\frac{\mathrm{e}^{x-l}\mathrm{e}^{j(x-l)} + \mathrm{e}^{-(x-l)}\mathrm{e}^{-j(x-l)}}{\mathrm{e}^{-l}\mathrm{e}^{-jl} + \mathrm{e}^{l}\mathrm{e}^{jl}}\right\|$$

then,

$$\frac{U(x)}{U_0} = \left\|\frac{\cos(x-l)\cosh(x-l) + j\sin(x-l)\sinh(x-l)}{\cos(l)\cosh(l) + j\sin(l)\sinh(l)}\right\|$$

$$\left(\frac{U(x)}{U_0}\right)^2 = \frac{\cos^2(x-l)\cosh^2(x-l) + \sin^2(x-l)\sinh^2(x-l)}{\cos^2(l)\cosh^2(l) + \sin^2(l)\sinh^2(l)}$$

Since $\forall x \in \mathbb{R}$, $\cosh^2(x) - \sinh^2(x) = 1$, and $\cos^2(x) + \sin^2(x) = 1$,

$$\frac{U(x)}{U_0} = \sqrt{\frac{\cosh^2(x-l) - \sin^2(x-l)}{\cosh^2(l) - \sin^2(l)}}$$

This equation is used when the liquid finger is out of hydrodynamical equilibrium.

Condition 3 – At equilibrium, $l = l_\infty$ is determined by $U(x = l_\infty) = U_T$ leading to:

$$\frac{U_0}{U_T} = \sqrt{\cosh^2(l_\infty) - \sin^2(l_\infty)}$$

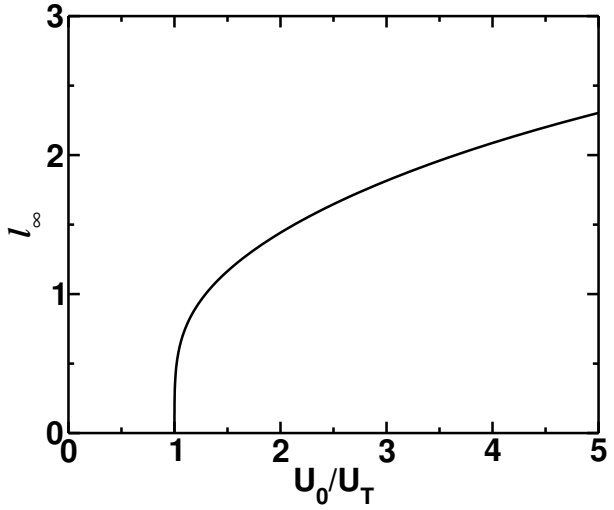

Figure D.3: Equilibrium length as a function of the applied voltage.

Asymptotic – The development in Taylor series for $l_\infty \sim 0$ gives:

$$\sqrt{\cosh^2(l_\infty) - \sin^2(l_\infty)} = 1 + \frac{1}{3}l_\infty^4 - \frac{11}{210}l_\infty^8 + \mathcal{O}(l_\infty^{12})$$

Therefore for $U_0 - U_T \sim 0^+$, $l_\infty \sim 3^{1/4}\left(\frac{U_0}{U_T} - 1\right)^{1/4}$.

For $l_\infty \sim \infty$, the hyperbolic cosine dominates: $\frac{U_0}{U_T} \sim \frac{e^{l_\infty}}{2} \Leftrightarrow l_\infty \sim \ln\left(2\frac{U_0}{U_T}\right)$.

Bibliography

[1] P. G. de Gennes, Françoise Brochard-Wyart, and David Quéré. *Gouttes, bulles, perles et ondes*. Belin, 2002.

[2] Lord Rayleigh. On the capillary phenomena of jets. *Proc. R. Soc. London Ser*, A 29(71), 1879.

[3] Lord Rayleigh. On the instability of a cylinder of viscous liquid under capillary force. *Phil. Mag. S. 5*, 34(207):145–154, 1892.

[4] Lord Rayleigh. On the instability of a cylindrical fluid surfaces. *Phil. Mag. S. 5*, 34(207):177–181, 1892.

[5] P. G. de Gennes. Wetting : statics and dynamics. *Rev. Mod. Phys*, 57(827), 1985.

[6] E. B. Dussan and R.T.-P. Chow. On the ability of drops or bubbles to stick on non-horizontal surfaces of solids. *J. Fluid Mech.*, 137:1–29, 1983.

[7] E. B. Dussan. On the ability of drops or bubbles to stick on non-horizontal surfaces of solids. part 2. small drops or bubbles having contact angles of arbitrary size. *J. Fluid Mech.*, 151:1–20, 1985.

[8] J. Z. Chen, S. M. Troian, A. A. Darhuber, and S. Wagner. Effect of contact angle hysteresis on thermocapillary droplet actuation. *J. Appl. Phys.*, 97(01):4906, 2005.

[9] A. B. D. Cassie and S. Baxter. Wettability of porous surfaces. *Trans. Faraday Soc.*, 40:546–551, 1944.

[10] R. N. Wenzel. Resistance of solid surface to wetting by water. *Ind. Eng. Chem.*, 28:988–994, 1936.

[11] A. Otten and S. Herminghaus. How plants keep dry: a physicist's point of view. *Langmuir*, 20(6):2405, 2004.

[12] R. Blossey. Self-cleaning surfaces - virtual realities. *Nature Materials*, 2:301–306, 2003.

[13] J. Bico, U. Thiele, and D. Quéré. Wetting of textured surfaces. *Colloids and Surfaces A*, 206:41–46, 2002.

[14] A. Lafuma and D. Quéré. Superhydrophobic states. *Nature Material*, 2:457–460, 2003.

[15] J. Jopp, H. Grüll, and R. Yerushalmi-Rozen. Wetting behavior of water droplets on hydrophobic microtextures of comparable sizes. *Langmuir*, 20:10015–10019, 2004.

[16] K. Okumura, F. Chevy, D. Richard, D. Quéré, and C. Clanet. Water spring : a model for bouncing drops. *Europhys. Lett*, 62(2):237–243, 2003.

[17] M. Brinkmann. *Benetzung lateral strukturiert Oberflächen*. PhD thesis, MPI für Kolloid - und Grenzflächenforschung, Golm - D, 2002.

[18] M. Brinkmann and R. Lipowsky. Wetting morphologies on substrates with striped surface domains. *J. Appl. Phys.*, 92(8):4296–4306, 2002.

[19] H. Gau, S. Herminghaus, P. Lenz, and R. Lipowsky. Liquid morphologies on structured surfaces: From microchannels to microchips. *Science*, 283:46–49, 1999.

[20] S. Herminghaus, Hartmund Gau, and Wolfgang Mönch. Artificial liquid microstructures. *Adv. Mater*, 11(16):1393–1395, 1999.

[21] R. Lipowksy. Structured surface and morphological wetting transitions. *Interface Science*, 9:105–115, 2001.

[22] A. Valencia, M. Brinkmann, and R. Lipowsky. Liquid brigdes in chemically structured slit pores. *Langmuir*, 17:3390–3399, 2001.

[23] N.A. Patankar and Y. Chen. Numerical simulation of droplet shapes on rough substrates. *Modeling and Simulation of Microsystems*, Proceedings:116–119, 2002.

[24] A. O. Parry, E. D. Macdonald, and C. Rascón. Droplet shapes on structured substrates and conformal invariance. *J. Phys.: Condens. Matter*, 13:383–402, 2001.

[25] R. Seemann, M. Brinkmann, E. J. Kramer, F. F. Lange, and R. Lipowsky. Matching surface topography and wettability: A new route to open microfluidic systems. *PNAS*, 102(6):1848–1852, 2005.

[26] P. O. Swain and R. Lipowsky. Contact angles on heterogeneous surfaces: A new look at cassie's and wenzel's laws. *Langmuir*, 14:6772–6780, 1998.

[27] L. M. Peurrung and D. B. Graves. Film thickness profiles topographies in spin-coating. *J. Electrochem. Soc*, 138:2115–2124, 1991.

[28] M.M.J. Decré and J.-C. Baret. Gravity driven flows of viscous liquids over two-dimensional topographies. *J. Fluid Mech.*, 487:147–166, 2003.

[29] D. C. Duffy, H. L. Gillis, J. Lin, N. F. Sheppard Jr, and G. J. Kellogg. Microfabricated centrifugal microfluidic systems: characterization and multiple enzymatic assays. *Anal. Chem.*, 71:4669–4678, 1999.

[30] A. A. Darhuber and S. M. Troian. Principle of microfluidic actuation by modulation of surface stress. *Annu. Rev. Fluid Mech.*, 37:425–55, 2005.

[31] O. Sandre, L. Gorre-Talini, A. Ajdari, J. Prost, and P. Silberzan. Moving droplets on asymmetrically structured surfaces. *Phys. Rev. E*, 60(3):2964–2972, 1999.

[32] J. Lee, B.He, and N. A. Patankar. A roughness-based wettability switching membrane device for hydrophobic surfaces. *J. Micormech. Microeng*, 15:591–600, 2005.

[33] Anton A. Darhuber, Joseph P. Valentino, Sandra M. Troian, and Sigurd Wagner. Thermocapillary actuation of droplets using microheater arrays. *J. Microelectromechanical Systems*, 12(6):873–879, 2003.

[34] A. Wixforth, C. Gauer, J. Scriba, M. Wassermeier, and R.Kirchner. Flat fluidics: A new route toward programable biochips. In *Microflu-*

idics, BioMEMS and Medical Microsystems, volume 4982 of *Proceedings of SPIE*, pages 235–242, 2003.

[35] F. Mugele, A. Klingner, J. Buehrle, D. Steinhauser, and S. Herminghaus. Electrowetting: a convenient way to switchable wettability patterns. *J. Phys. Cond. Matter*, 17(559-576), 2005.

[36] R. P. Feynman, R. B. Leighton, and M. Sands. *Le cours de physique de Feynman - Electromagnétisme 1.* InterEdition, 1979.

[37] M. W. J. Prins, W. J. J. Welters, and J. W. Weekamp. Fluid control in multichannel structures by electrocapillary pressure. *Science*, 291:277–280, 2001.

[38] T. Jones and K.-L. Wang. Frequency-dependent electromechanics of acqueous liquids: Electrowetting and dielectrophoresis. *Langmuir*, 20:2813–2818, 2004.

[39] P. Tabeling. *Introduction à la microfluidique.* Belin, 2003.

[40] C. T. O'konski and H. C. Thacher. The distortion of aerosol droplets by electrical field. *J. Phys. Chem*, 57:955–958, 1953.

[41] A. Bateni, S. S. Susnar, A. Amirfazli, and A. W. Neumann. Development of a new methodology to study drop shape and surface tension in electric field. *Langmuir*, 20:7589–7597, 2004.

[42] O. D. Velev, B. G. Prevo, and K. T. Bhatt. On-chip manipulation of free droplets. *Nature*, 426:515–516, 2003.

[43] A. Torkkeli. *Droplet Microfludics on planar surface.* PhD thesis, Helsinki University of Technology, Helsinki - Finland, 2003.

[44] T. Jones. On the relationship of dielectrophoresis and electrowetting. *Langmuir*, 18:4437–4443, 2002.

[45] S. K. Cho, H. Moon, and C. J. Kim. Creating, transporting, cutting, and merging liquid droplets by electrowetting-based actuation for digital microfluidic circuits. *J. Microelectromechanical systems*, 12(1):70–80, 2003.

[46] M. Bienia, C. Quillet, and M. Vallade. Modification of drop shape controlled by electrowetting. *Langmuir*, 19:9328–9333, 2003.

[47] A. Klingner, S. Herminghaus, and F. Mugele. Self-excited oscillatory dynamics of capillary bridge in electric field. *Appl. Phys. Lett*, 81(23):4187–4189, 2003.

[48] A. Klingner and F. Mugele. Electrowetting-induced morphological transitions of fluid microstructures. *J. Appl. Phys.*, 95:2918, 2004.

[49] Robert A. Hayes and B. J. Feenstra. Video-speed electronic paper based on electrowetting. *Nature*, 425:383–385, 2003.

[50] F. Mugele and J.-C. Baret. Electrowetting: from basics to applications. *J. Phys. Cond. Matter*, 17:R705–R774, 2005.

[51] M. G. Lippmann. Relation entre les phénomènes électriques et capillaires. *Ann. Chim. Phys*, 5:494, 1875.

[52] Alexandre Froumkine. Couche double, électrocapillarité, surtension. *Actualités scientifiques et industrielles*, 373(1):5–36, 1936.

[53] B. Berge. Electrocapillarité et mouillage de films isolants par l'eau. *C. R. Acad. Sci. III*, 317:157, 1993.

[54] E. Seyrat and R. A. Hayes. Amorphous fluoropolymers as insulators for reversible low-voltage electrowetting. *J. Appl. Phys.*, 90(3):1383–1386, 1999.

[55] T. Krupenkin, S. Yang, and P. Mach. Tunable liquid microlens. *Appl. Phys. Lett.*, 82(3):316–318, 2003.

[56] B. Berge and J. Peseux. Variable focal length controlled by an external voltage: application of electrowetting. *Eur. Phys. J.*, E(3):159–163, 2000.

[57] M. G. Pollack, R. B. Fair, and A. D. Shenderov. Electrowetting-based actuation of liquid droplets for microfluidic applications. *Appl. Phys. Lett*, 77(11):1725–1726, 2000.

[58] A. Quinn, R. Sedev, and J. Ralston. Influence of electrical double layer in electrowetting. *J. Phys. Chem. B*, 107:1163–1169, 2002.

[59] A. Quinn, R. Sedev, and J. Ralston. Contact angle saturation in electrowetting. *J. Phys. Chem. B*, 109:6268–6275, 2005.

[60] B. Shapiro, H. Moon, R. L. Garell, and C.-J. Kim. Equilibrium behaviour of sessile drop under surface tension, applied external fields and material variations. *J. Appl. Phys.*, 93(9):5794–5811, 2003.

[61] M. Vallet, M. Vallade, and B. Berge. Limiting phenomena for the spreading of water on polymer films by electrowetting. *Eur. Phys. J. B*, 11:583–591, 1999.

[62] A. Klingner. *Änderung der Flüssigkeitsmorphologie durch elektrische Felder zur Anwendung in der Mikrofluidik.* PhD thesis, University of Ulm, Ulm - D, 2004.

[63] M. Bienia. *Etude de déformation de goutte et de film mince induite électriquement.* PhD thesis, Université Joseph Fourrier, Grenoble 1 - F, 2005.

[64] J. Eggers. Nonlinear dynamics and breakup of free-surface flows. *Rev. Mod. Phys.*, 69(3):865–929, 1997.

[65] R. Finn. *Equilibrium capillary surfaces.* Springer-Verlag, 1986.

[66] H. H. Chen and M. P. Brenner. The optimal faucet. *Phys. Rev. Lett.*, 92(16):6106, 2004.

[67] G. Taylor. Disintegration of water drops in an electric field. *Proc. R. Soc. Lond. A*, 280:383–397, 1964.

[68] R. Hartman. *Electrohydrodynamic atomization in the cone-jet mode.* PhD thesis, Univeristy of Delft - NL, 1998.

[69] Y. Xia, K. E. Paul J. A. Rogers, and G. M. Whitesides. Unconventional methods for fabricating and patterning nanostructures. *Chem. Rev.*, 99:1823–1848, 1999.

[70] Anton A. Darhuber, Sandra M. Troian, and Sigurd Wagner. Physical mechanisms governing pattern fidelity in microscale offset printing. *J. Appl. Phys.*, 90(7):3602–3609, 2001.

[71] K. Brakke. The surface evolver. *Exp. Math.*, 1(2):141, 1992.

[72] J. Sagiv. Organized monolayers by adsorption. 1. formation and structure of oleophobic mixed monolayers on solid surfaces. *J. Am. Chem. Soc.*, 102(92), 1980.

[73] C. Delaunay. Sur la surface de révolution dont la courbure moyenne est constante. *J. math. pures et appliquées*, 6:309–319, 1841.

[74] D. Langbein. *Capillary Surfaces*. Springer, 2002.

[75] P. Lenz, C. Bechinger, C. Schäfle, P. Leiderer, and R. Lipowsky. Perforated wetting layers from periodic patterns of lyophobic surface domains. *Langmuir*, 17:7814–7822, 2001.

[76] M. Brinkmann and J.-C. Baret. In preparation. 2005.

[77] H. J. J. Verheijen and M. W. J. Prins. Reversible electrowetting and trapping of charge : model and experiments. *Langmuir*, 15:6616–6620, 1999.

[78] J. R. Lister and H. A. Stone. Capillary breakup of a viscous thread surrounded by another viscous fluid. *Phys. Fluids*, 10(11):2758–2764, 1998.

[79] R. F. Day, E. J. Hinch, and J. R. Lister. Self-similar pinchoff of an inviscid fluid. *Phys. Rev. Lett.*, 80(4):704–707, 1998.

[80] D. Leppinen and J. R. Lister. Capillary pinch-off in inviscid fluids. *Phys. Fluids*, 15(2):568–578, 2003.

[81] J. C. Burton, J. E. Rutledge, and P. Taborek. Fluid pinch-off dynamics at nanometer length scales. *Phys. Rev. Lett.*, 92(24):4505, 2004.

[82] J. Eggers. Universal pinching of 3d axisymmetric free-surface flow. *Phys. Rev. Lett.*, 71(21):3458–3460, 1993.

[83] A. U. Chen, P. K. Notz, and O. A. Basaran. Computational and experimental analysis of pinch-off and scaling. *Phys. Rev. Lett.*, 88(17):4501, 2002.

[84] I. Cohen and S. R. Nagel. Testing for scaling behavior dependence on geometrical and fluid parameters in the two fluid drop snap-off problem. *Phys. Fluids*, 13(12):3533–3541, 2001.

[85] I. Cohen, M. P. Brenner, J. Eggers, and S. R. Nagel. Two fluid drop snap-off problem: Experiments and theory. *Phys. Rev. Lett.*, 83(6):1147–1150, 1999.

[86] W. W. Zhang and J. R. Lister. Similarity solutions for capillary pinch-off in fluids of differing viscosities. *Phys. Rev. Lett.*, 83(6):1151–1154, 1999.

[87] J. D. Romano and R. H. Price. The conical resistor conundrum: A potential solution. *Am. J. Phys.*, 64(9):1150–1153, 1996.

[88] F. Mugele and S. Herminghaus. Electrostatic stabilization of fluid microstructures. *Appl. Phys. Lett*, 81(12):2303–2305, 2002.

[89] A. G. Bailey. *Electrostatic spraying of liquids*. Research studies press, 1988.

[90] N. K. Nayyar and G. S. Murty. The stability of a dielectric liquid jet in the presence of a longitudinal electric field. *Proc. R. Soc. London Ser. A*, 75(369), 1960.

[91] X. Zhang and O. A. Basaran. Dynamics of drop formation from a capillary in the presence of electric field. *J. Fluid Mech.*, 326:239–263, 1996.

[92] D. A. Saville. Electrohydrodynamic stability: Fluid cylinder in longitudinal electric fields. *Phys. Fluids*, 13(12):2987–2994, 1970.

[93] S. Sankaran and D. A. Saville. Experiments on the stability of a liquid bridge in an axial electric field. *Phys. Fluids*, 5(4):1081–1083, 1993.

[94] D. A. Saville. Stability of electrically charged viscous cylinder. *Phys. Fluids*, 14(6):1095–1099, 1971.

[95] A. El Magd A. Mohamed and El Sayed F. El Shehaweney. Nonlinear electrohydrodynamics rayleigh-taylor instability ii. a perpendicular field producing surface charge. *Phys. Fluids*, 26(7):1724–1730, 1983.

[96] J.-W. Ha and S.-M. Yang. Deformation and breakup of newtonian and non-newtonian conducting drops in an electric field. *J. Fluid Mech.*, 405:131–156, 2000.

[97] C. L. Burcham and D. A. Saville. the electrohydrodynamic stability of a liquid bridge: microgravity experiments on a bridge suspended in a dielectric gas. *J. Fluid Mech.*, 405:37–56, 2000.

[98] J.-C. Baret. Dynamics of self-excited droplet oscillations in electrowetting. Technical Report TN-2003/00985, Philips Research, Eindhoven - NL, 2003.

[99] S. Schiaffino and A. A. Sonin. Molten droplet deposition and solidification at low weber number. *Phys. Fluids*, 9(11):3172–3186, 1997.

[100] P. Paik, V. K. Pamula, M. G. Pollack, and R. B. Fair. Electrowetting-based droplet mixers for microfluidic systems. *Lab Chip*, 3:28–33, 2003.

[101] P. Paik, V. K. Pamula, and R. B. Fair. Rapid droplet mixer for digital microfluidic systems. *Lab Chip*, 3:253–259, 2003.

[102] D. R. Steinhauser. Elektrowetting in fluid-fluid systemen. Master's thesis, University of Ulm, Ulm - D, 2004.

[103] M. Brinkmann, R. Blossey, S. Arscott, C. Druon, P. Tabouier, S. Le Gac, and C. Rolando. Microfluidic design rule for capillary slot-based electrospray sources. *Appl. Phys. Letters*, 85(11):2140–2142, 2004.

[104] C. Quillet and B. Berge. Investigation of effective interface potentials by electrowetting. *Europhys. Lett*, 60:99–105, 2002.

[105] J. Buehrle, S. Herminghaus, and F. Mugele. Interface profiles near three-phase contact lines in electric fields. *Phys. Rev. Lett.*, 91(08):6101, 2003.

[106] M. Morita, T. Koga, H. Otsuka, and A. Takahara. Macroscopic-wetting anisotropy on the line-patterned surface of fluoroalkylsilane. *Langmuir*, 21:911–918, 2005.

[107] R. E. Matick. *Transmission lines for digital and communication networks*. IEEE PRESS, 1969.

[108] E. W. Washburn. The dynamics of capillary flow. *Phys. Rev.*, 17(3):273, 1921.

[109] D. Quéré. Inertial capillarity. *Europhys. Lett.*, 39(5):533–538, 1997.

[110] A. Oron, S. H. Davis, and S. G. Bankoff. Long-scale evolution of thin liquid films. *Rev. Mod. Phys*, 69:931–980, 1997.

[111] P. B. Warren. Late stage kinetics for various wicking and spreading problems. *Phys. Rev. E*, 69(04):1601, 2004.

[112] L. H. Tanner. The spreading of silicone oil drops on horizontal surfaces. *J. Phys. D: Appl. Phys.*, 12:1473–1485, 1979.

[113] A. M. Cazabat and M. A. Cohen-Stuart. Dynamics of wetting: effects of surface roughness. *J. Phys. Chem.*, 90:5845–5849, 1986.

[114] J. Lopez, C. A. Miller, and E. Ruckenstein. Spreading kinetics of liquid drops on solid. *J. Colloid and Interface Sci.*, 56(3):460–468, 1976.

[115] E. Schäffer and P. Wong. Dynamics of contact line pinning in capillary rise. *Phys. Rev. Lett.*, 80(14):3069, 1998.

[116] M. Dreyer, A. Delgado, and H.-J. Rath. Capillary rise of liquid between parallel plates under microgravity. *J. Coll. Interface Science*, 163:158–168, 1994.

[117] L. A. Romero and F. G. Yost. Flow in an open channel capillary. *J. Fluid Mech.*, 322:109–129, 1996.

[118] A. A. Darhuber, S. M. Troian, and W. W. Reisner. Dynamics of capillary spreading along hydrophilic microstripes. *Phys. Rev. E*, 64:031603, 2001.

[119] R. Ahmed, D. Hsu, C. Bailey, and T. B. Jones. Dispense picoliter droplets using dielectrophoretic (dep) microactuation. In *First International Conference on Microchannels and minichannels*, 2003.

[120] T. Podgorski, J.-M. Flesselles, and L. Limat. Corners, cusps and pearls in running drops. *Phys. Rev. Lett.*, 87:036102, 2001.

[121] E. Rio, A. Daerr, B. Andreotti, and L. Limat. Boundary conditions in the vicinity of a dynamic contact line: exprerimental investigation of viscous drops sliding down an inclined plane. *Phys. Rev. Lett.*, 94(024503), 2005.

[122] S. P. Timoshenko and J. N. Goodier. *Theory of elasticity*. McGraw Hill Classic textbook reissue, 1970.

[123] J. G. Knudsen and D. L. Katz. *Fluid dynamics and heat transfer*. Robert E. Krieger publishing compagny, 1979.

[124] T. Jones. An electromechanical interpretation of electrowetting. *J. Micromech. Microeng.*, 15:1184–1187, 2005.

[125] H. Y. Wong. *Heat Transfert for engineers*. Longman group, 1977.

[126] P. Ehrhard. Experiments on isothermal and non-isothermal spreading. *J. Fluid Mech.*, 257:463–483, 1993.

[127] V. K. Pamula and K. Chakrabarty. Cooling of integrated circuits using droplet-based microfluidics. pages 84–87, 2003.

[128] G. Van der Veken. Electronics cooling by means of electro-static actuated liquid through micro channels. Master's thesis, Katholieke Universiteit Leuven, Heverlee - Be, 2005.

[129] A. Alami, F. C. van den Heuvel, A. Kemmereen, F. Roozeboom, and J. Verhoeven. Anisotropic reactive ion etching of high aspect ratio pore and trench arrays in silicon for integrated mos decoupling capacitors. Technical Report PR-TN-2003/00250, Philips Research, Eindhoven - NL, 2003.

Acknowledgments

During these three years of PhD I have had the possibility to work in different environments which has the advantage that I met a lot of people with different ways of working. The drawback is that my acknowledgment list is going to look endless...

Before really starting, I want to thank people who took time to work on GNU projects and open source softwares[1], this thesis has been written using LaTeX, most of the grahics have been produced with Grace-5.1.12[2], the sketchs have been drawn with XFig-3.2.4[3] either in a Linux environment or under Microsoft Windows using Cygwin-2.416[4].

Now, I can thank the people that I know... I thank all my colleagues from Philips for their enthousiasm and their help, starting with my room-mates Dirk-Jan van Dam and Jacqueline van Driel and the different group leaders, Marteen Buijs, Frits Dijksmann, Ad Leenaars and Christopher Busch, who have been all really supportive. I am gratefull to those who helped me with the wafers, from the photolithography mask (Jos van de Ven) via the etching process (Anton Kemmeren, Emil Van Thiel) to the monolayer formation (Dirk Burdinski). I also thank Martin Vernhout and Albert Geven for introducing me to LabView and helping me interfacing my set-up with my PC. Thanks also to Jurgen Rusch for his help with image processing and his expertise of Linux. I also thank Céline Nicole and Geert van der Veken for their contribution to the thermal cooling using microchannels, Clemens Lasance for giving me the opportunity to interact with the people from CFD-ACE+ and Martin Hack for his help with viscosity measurements and inkjet experiments. Thanks also to Johan Feenstra, Rob Hayes, Stein Kuiper and Menno Prins for interesting comments and discussions on electrowetting; having so many experts in the field is simply amazing. I also think to Margotza and Ula and I wish them good luck for the end of their PhD ! Good luck also to my football team the "Materiaalmannen" for the next season ! I met in the University of Ulm really nice and motivated people, my room-mate Anne-Marie with whom it was so easy to speak french that my german improved only a little, Manfred Hörger, Udo Krafft whose technical expertise makes

[1] http://www.gnu.org

[2] http://plasma-gate.weizmann.ac.il/Grace/

[3] http://www.xfig.org

[4] http://www.cygwin.com

everything possible and all the students who made my stay over there so nice, Anke, Thomas, Lothar, Sarah, Rolf, Dagmar, Jürgen and of course Alex who introduced me to a very friendly football team ! The experiments I performed in the University of Twente would have never been possible without the help of Helmut, Benjamin and Renske. Thanks a lot ! I also want to thank the people from Göttingen, Krishnacharya with whom it was nice to work on the wetting of channels, good luck with the end of your PhD and Martin Brinkmann who took so much time introducing me to the theory of axisymmetric constant mean curvature surfaces and with whom I really enjoy to work; I have really learned a lot from our discussions and not only on a professional point of view ! I also have a special thought for Emmanuelle and Anne remembering the time we spent together writing our respective thesis and a very special thought for Sandrine and her patience when I decide at late hours to make soap or fluid experiments in the kitchen or in the bathroom ! Thanks for your support in all occasions; I will try to support you the same way when your turn to write down your thesis will come !
Finally my next lines are going to Michel Decré who should have understood now that it is really pleasant to work with him. I already noticed this point during my engeneering traineeship a couple of years ago and I had a perfect confirmation during my thesis. He also introduced me to people who took an essential part in my thesis: Ralf Seemann and Stephan Herminghaus supervised me on the project on electrowetting on structured substrates. I really enjoyed all the positive imagination and ideas that you can have and I learned a lot working in your group in Ulm and Göttingen ! I am just still disappointed on my badminton level but I will continue to work on that ! And of course I thank Frieder Mugele who first introduced me to the potential of electrowetting and who has then accepted to be my PhD promotor here in the Netherlands. It was not only interesting and motivating to work with you on a scientific level but also on a personal level. Everything is going so smoothly with you, and I am really happy to be one of your PhD student.

You all contributed to my vision of science and of a scientist's life.
Thank you ! Merci ! Bedankt ! Danke !